Nitrogen doped zirconia (N-YSZ): preparation, characterization and electrode processes

vom Fachbereich Biologie und Chemie

der Justus-Liebig-Universität Gießen

zur Erlangung des Grades

Doktor der Naturwissenschaften

-Dr. rer. nat.-

genehmigte

Inaugural-Dissertation

von

M.Sc. Ilia Valov

geboren am 12.04.1972 in Sofia, Bulgarien

Gießen 2006

Dekan   Prof. Dr. Peter Schreiner

1. Gutachter   Prof. Dr. Jürgen Janek

2. Gutachter   Prof. Dr. Martin Lerch

Arbeit eingereicht am 24. April 2006

Tag der mündlichen Prüfung: 9. Juni 2006

Arbeit veröffentlicht in der Gießener Elektronischen Bibliothek (GEB)

Danksagung

Zusammenfassung

Die Defektstruktur, die Transporteigenschaften und die Elektrodenkinetik von stickstoffdotiertem yttrium-stabilizeirten Zirkonoxid (YSZ) werden systematisch untersucht, um die Elektrochemie von Stickstoff in ionischen Festkörper besser zu verstehen.

Der Einfluss von Stickstoff auf die Defektstruktur von reinem $ZrO_{2-\delta}$ und YSZ wurde untersucht. Auf der Basis der Defektgleichgewichte und der entsprechenden Brouwer-Annahmen werden die Kroeger-Vink Diagramme konstruiert, und die Defektstruktur dieser Festelektrolyten wird diskutiert. Die Thermodynamik von elektrochemischen Zellen des Typs $M/MX/X_2(Me)$ wird analysiert. In einer $E/\lg a_{X_2}$ Auftragung kann ein invarianter Punkt identifiziert werden, der der freien Enthalpie der Zusammensetzung MX bei $T = 0$ K entspricht.

Die Herstellung von stickstoffdotierten dünnen YSZ-Schichten mittels gepulste Laserdeposition (PLD) wird systematisch als Funktion der Temperatur, des Gasdrucks, des Abstands zwischen dem Target und dem Substrat und des Yttrium-Gehalts untersucht. Die Oberflächenmorphologie, die Gitterstruktur und der Stickstoffgehalt dieser Schichten werden mittels AFM, HRSEM, XRD, SIMS, XPS und optischer Spektroskopie ermittelt. Die YSZ:N Schichten zeigen eine flache Oberflächentopographie und sind kristallin, wobei die Schichten eine kleine Abweichung der Gitterparameter aus der idealen kubischen Struktur aufweisen, die für die stickstoffdotierten Schichten am deutlichsten ist. Wir berichten ebenfalls über einen Orientierungseffekt des Hintergrundgases während des Depositionsprozesses auf die Struktur der Schichten. Ein maximaler Stickstoffgehalt von 14 Atom-% wurde an einer 7YSZ-Probe gemessen. Die mit 7 Atom-% Yttriumoxid dotierten YSZ:N Schichten zeigen deutlich andere Eigenschaften. Die Resultate von Röntgenspektroskopie (XPS) und optischer Spektroskopie weisen auf einen anderen Valenzzustand und/oder andere Positionen der Stickstoffatome hin.

Die Kinetik der elektrochemischen Reduktion von Stickstoff wurde mittels potentiodynamischer und potentiostatischer Polarisationsmethoden an Mikroelektroden untersucht. Die geeigneten Arbeitsbedingungen (Elektrodenmaterial,

Elektrolyt und Temperaturbereich) sind experimentell bestimmt worden. Die Ergebnisse der elektrochemischen Experimente weisen auf einen komplexen Mechanismus hin, der mehrere Reduktionsschritte durchläuft. Durch Anwendung des "Konzepts der stöchiometrischen Zahl" konnte der Mechanismus dieser Reaktion ermittelt werden. Als geschwindigkeitsbestimmender Schritt wird der Schritt $N_2^- + e^- = N_2^{2-}$ vorgeschlagen. Wir haben auch den Einbau von Stickstoff in YSZ-Schichten und Einkristallen mittels SIMS nachgewiesen. Die *in-situ* durchgeführten XPS-Analysen ermöglichten es erstmalig, die elektrochemische Stickstoffreduktion während kathodischer Polarisation nachzuweisen. Dies stellt den ersten *in-situ* Beweis der elektrochemischen Reaktivität von Stickstoff dar.

In der vorliegenden Arbeit wird bestätigt, dass der Stickstoff auch aus der Luft in YSZ eingebaut werden kann, ohne den Elektrolyten zu reduzieren. Die Experimente in Ammoniak-Gas zeigen, dass der Stickstoffeinbau deutlich schneller abläuft verglichen mit dem Einbau aus einer N_2-Gasatmosphäre. Darüber hinaus konnte eindeutig bewiesen werden, dass der Prozess von Stickstoffeinbau von der Oberflächenkinetik gehemmt wird und nicht von der Diffusion der schon reduzierten Spezies ins Festelektrolyt.

Die Transporteigenschaften von dünnen YSZ:N Schichten werden als Funktion des Stickstoffgehalts untersucht. Die Aktivierungsenergien der ionischen Leitfähigkeit nehmen deutlich zu mit steigender Stickstoffkonzentration. Auf der Basis der Auswertung der Impedanzspektren wird gezeigt, dass der Ionen-Transport in der Korngrenzen, für Schichten mit höcherem Stickstoffgehalt, die Diffusion limitiert.

Abstract

The defect structure, the transport properties and the electrode kinetics of nitrogen-doped zirconia is investigated in order to explore the electrochemistry of nitrogen in the solid state.

Firstly the influence of nitrogen on the defect structure properties of pure $ZrO_{2-\delta}$ and yttria stabilized zirconia (YSZ) is studied. On the basis of the defect equilibria and the appropriate Brouwer approximations the Kroeger-Vink diagrams are constructed and the defect structure of these materials is discussed. The thermodynamics of electrochemical cells of the type $M/MX/X_2(Me)$, is analyzed and we found an invariant point in the $E/\lg a_{X_2}$ plot corresponding to the free enthalpy of formation of the compound MX at $T = 0$ K.

The preparation of nitrogen-doped YSZ thin films by pulsed laser deposition (PLD) is systematically studied as a function of the temperature, gas pressure in the deposition chamber, distance between the target and the substrate and the yttria content. The surface morphology, the structure and the nitrogen content of these films are analyzed by AFM, HRSEM, XRD, SIMS, XPS and optical spectroscopy. Both nitrogen-doped (YSZ:N) and nitrogen free YSZ films prepared by PLD shown a flat surface topography and crystalline structure, but the films show a slight distortion of the fluorite-type cubic cell, mostly pronounced for the nitrogen-doped samples suggesting a possible order of the nitrogen ions in the films but also can be a result of the nano-sized grain structure. An orientation dependence of the films from the background gas is also reported. The maximal nitrogen content of 14 at.% was measured for the 7YSZ:N sample. The 7YSZ:N films show a different behavior than YSZ:N films with lower or higher yttria content. The XPS and optical absorption experiments suggest an other charge or an other position of the nitrogen ions in the 7YSZ:N lattice.

The kinetics of the electrochemical reduction of nitrogen on micro-electrodes is studied by potentiodynamic (LSV, CV) and steady state (potentiostatic, galvanostatic) polarization techniques. The appropriate electrode material, electrolyte and temperature are experimentally determined and discussed. The results clearly show a complicated multi-step charge transfer controlled process.

Applying the concept of the stoichiometric number we suggest a mechanism for the cathodic electrochemical reduction of nitrogen where as a rate determining step we suggest the intermediate reaction: $N_2^- + e^- = N_2^{2-}$ with a stoichiometric number $\nu = 3$. In addition we confirmed the nitrogen incorporation into YSZ thin films and as well in single crystals by SIMS analysis. Spatially resolved XPS studies during cathodic polarization confirmed for the first time *in-situ* the electrochemical reactivity of nitrogen.

In this work we demonstrate that nitrogen can be incorporated upon cathodic polarization in YSZ even from the air. The experiments in ammonia gas phase show that the nitrogen incorporation proceeds much easier than from N_2 gas and thus we suggest that nitrogen incorporation is limited by the surface reaction and not by the diffusion into the bulk.

The transport properties of YSZ:N thin films as a function of the nitrogen content show an increase in the activation energies of the total ionic conductivity with increasing nitrogen content. On the basis of the decovolution of the impedance spectra we conclude that for films with higher nitrogen content the ionic transport in the grain boundaries limits the diffusion.

Contents

1 Introduction

1.1 Overview

For a number of reasons the heterogeneous kinetics of nitrogen incorporation into oxides is a subject of growing interest. Oxinitrides have recently been studied as new pigments [1,2] and materials for UV optics [3] or as nitrogen electrolytes [4]. We are interested in the reactivity of molecular nitrogen towards oxygen ion conducting solid electrolytes. The reason for this interest is twofold: Firstly, nitrogen is usually regarded as an inert component in most electrochemical high temperature applications, and possible reactions between nitrogen gas and oxide electrolytes are neglected. Secondly, the study of the interaction of molecular nitrogen with ionic solids is an important prerequisite for the development of any electrochemical device working with nitrogen containing atmospheres.

Countless studies exist on the chemical reactivity of molecular nitrogen in general. The most important heterogeneous chemical reaction with molecular nitrogen is probably the catalytic ammonia synthesis via the Haber-Bosch process and thus numerous publications can be found [5]. In the present context of solid state electrochemistry on the mobility of nitrogen in oxide phases only a small number of reports were found in the literature [4,6–9]. Most of the existing papers deal with thermal [4,6,7,10–17] or plasma [18] based incorporation, and only [19] reports on the ZrN phase formation upon cathodic polarization experiments.

It is well known that nitrogen may replace oxygen partially in solid electrolytes on the basis of zirconium(IV)-dioxide at very high temperatures under reducing conditions. Under equilibrium conditions at 2000 °C, an upper solubility of nitrogen in ZrO_2 of 4.7 wt% has been reported [15]. But neither a detailed

discussion on the incorporation mechanism has been given nor has a systematic experimental study been performed.

Zirconia stabilized by doping with aliovalent ions is a ternary compound from the thermodynamic point of view. Fixing temperature, atmospheric pressure and the concentration of the metal dopant (usually yttrium, scandium or calcium), only the chemical potential (i. e. the partial pressure) of oxygen remains as a single thermodynamic degree of freedom. As a function of the oxygen partial pressure the oxygen content in the compound varies, and the non-stoichiometry δ can be defined as the deviation of the oxygen content in $Zr_{1-x}Y_xO_{2-\frac{x}{2}-\delta}$ from the stoichiometric formula $Zr_{1-x}Y_xO_{2-\frac{x}{2}}$ containing only Zr^{4+} and Y^{3+}. Doping with trivalent yttrium reduces the oxygen content of the cubic lattice of the fluorite type, and thus, leads to the creation of oxygen vacancies with high concentration ($[Y'_{Zr}] = 2[V_O^{\bullet\bullet}]$). These vacancies become mobile at elevated temperatures between 300 °C and 400 °C and increase the intrinsic ionic conductivity of zirconia. As the dopant concentration is typically between 5 and 13 mol% Y_2O_3, the small non-stoichiometry corresponding to vacancy concentration in the range 10^{-3} mol.cm^{-3} $- 10^{-4}$ mol.cm^{-3} [20] does not influence the ionic conductivity. On the other hand, it leads to measurable changes of the electronic transport properties, since the intrinsic concentration of electronic defects is very low (band gap E_g = 4 eV - 5 eV) [21,22]. The oxidation or reduction of YSZ (accompanied by oxygen incorporation or release) can be formulated by the heterogeneous oxygen equilibrium (using the Kroeger-Vink notation):

$$O_2(gas) + 2V_O^{\bullet\bullet}(YSZ) + 4e^-(YSZ) \rightleftharpoons 2O_O^{\times}(YSZ) \qquad (1.1)$$

Thus, high oxygen activities (oxidizing conditions) lead to p-type electronic conductivity whereas low oxygen activities (reducing conditions) provide n-type charge carriers. A detailed analysis of the electronic properties of YSZ has been reported by Park and Blumenthal [23].

Introducing nitrogen as a fourth component adds an additional thermodynamic degree of freedom and has to be accounted by an additional reaction. The nitrogen incorporation in the anion sublattice at high temperatures proceeds under reducing conditions according to:

$$N_2(gas) + 2V_O^{\bullet\bullet}(YSZ) + 6e^-(YSZ) \rightleftharpoons 2N'_O(YSZ) \qquad (1.2)$$

assuming that trivalent nitrogen anions (N^{3-}) are incorporated. Combining eqs. 1.1 and 1.2 without a net reduction step, i.e. without the generation of n-type charge carriers, the partial substitution of oxygen by nitrogen can be formulated as:

$$N_2(\text{gas}) + 3O_O^\times(\text{YSZ}) \rightleftharpoons 2N_O'(\text{YSZ}) + V_O^{\bullet\bullet} + 3/2O_2(\text{gas}) \qquad (1.3)$$

According to eq. 1.3 the number of anion vacancies can be increased by substitution of oxygen by nitrogen. And as the oxygen ions, nitrogen ions may also be mobile via jumps into vacant lattice sites and cause a partial nitrogen ion conductivity.

Mainly due to the much larger binding energy of N_2 the Gibbs reaction energy ΔG_N° of eq. 1.2 is probably much higher (less negative) than the Gibbs reaction energy ΔG_O° of eq. 1.1 (comparing the free enthalpy of formation of ZrN and ZrO_2, one finds a much higher value for the nitride) and the concentration of nitrogen ions will be quite small in thermodynamic equilibrium under normal conditions. In order to support the nitrogen incorporation, we may either increase the electron or the vacancy concentration, as suggested by eq. 1.2. In YSZ the concentration of vacancies is fixed by the dopant and only the electron concentration remains as variable. Whereas the dopant concentration cannot be increased significantly, the electron concentration grows by orders of magnitude with decreasing oxygen partial pressure, i.e. under strongly reducing conditions. The high temperature synthesis [4] is based on such strongly reducing conditions, i.e. high temperatures and the presence of carbon as a reducing agent. In any case, the idea to use eq. 1.3 as a basis for an anion exchange without introducing additional electrons is almost hypothetical. At a given pressure p_{N_2} only one specific p_{O_2} will keep the electronic concentration constant.

In this work the electrochemical polarization of YSZ is explored as a possible alternative for the shift of the heterogeneous nitrogen equilibrium (1.3), which allows the control of the oxygen activity and the supply with electrons directly via the applied electric potential in an electrochemical cell of the type:

$$(+) \ \text{Me} \ / \ \text{Zr} \ / \ ZrO_2 \ / \ \text{YSZ} \ / \ \text{Me}(N_2) \ (-)$$
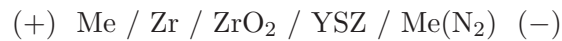
The application of a cathodic potential to the right electrode supplies electrons

and shifts the nitrogen equilibrium towards the right side of eq. 1.2:

$$N_2(gas) + 2V_O^{\bullet\bullet} + 6e^-(Me) \rightleftharpoons 2N_O'(YSZ) \tag{1.4}$$
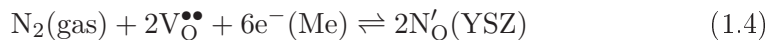
Even small cathodic voltages correspond to extremely strong reducing conditions (i.e. low oxygen activities), which cannot be achieved via conventional chemical techniques. At 1000 K a cathodic voltage step of 50 mV corresponds to a change of the oxygen activity by one order of magnitude.

1.2 Aim of the work

The aim of this thesis is firstly to analyze and compare the defect structures of zirconia and nitrogen doped zirconia. On the basis of the chemical reactions describing the defect formation the Kroeger-Vink diagrams for these systems are constructed at constant nitrogen respectively oxygen pressures, thus predicting and differentiating their defect-related properties. The thermodynamics of $Zr/ZrO_2/O_2$ and $Zr/ZrN/N_2$ systems is also discussed.

A second point is the preparation and characterization of thin N-doped YSZ layers on different substrates via pulsed laser deposition (PLD). A systematic study was performed in order to determine the structure, morphology, and nitrogen content of N-YSZ films as a function of the variation of nitrogen pressure, yttria content and temperature. The latter serves as a base for optimization and standardization of the deposition parameters.

An important part of the thesis is the study of the kinetics of reduction processes of nitrogen, its electrochemical behavior, the electrode properties and reactivity of molecular nitrogen on YSZ or nitrogen doped YSZ and the influence of the incorporated nitrogen ions on the transport properties of the material.

The thesis is exposed as follows:

In the theoretical part the defect-structure of nitrogen-free and nitrogen-doped zirconia is discussed as a function of the variable gas (oxygen or nitrogen) activity. According to the appropriate Brouwer approximations the Kroeger-Vink diagrams are constructed. In addition the thermodynamics of

the cells $Zr/ZrN/Me(N_2)$ and $Zr/ZrO_2/Me(O_2)$ is discussed and the current state of knowledge about the nitrogen electrode is summarized. At the end of this part the general concepts of the ionic transport and the electrochemical surface charge transfer theory are presented.

In the experimental part the basics of the main preparation and analytical techniques used for the deposition and characterization of the samples are described as well as the experimental equipment and the experimental conditions in general. In the following chapters are presented the results and discussions on the preparation and characterization of the nitrogen doped samples by PLD, the transport properties and the electrode processes. The individual experimental details are given separately in each section. At the end the results are briefly summarized.

2 Theory

2.1 Defect structures and properties of ZrO_2, YSZ, ZrO_2:N and YSZ:N

In order to analyze the defect structure of nitrogen-doped zirconia in more detail we construct the Kroeger-Vink diagram for both nitrogen-free and nitrogen-doped ZrO_2, respectively YSZ at constant nitrogen and variable oxygen activity as well for a constant oxygen and variable nitrogen activity. In table 2.1 below the systems are listed with the thermodynamic variables to be kept constant in order to define the systems thermodynamically: Increasing the number of

Table 2.1: Defect models for zirconia based oxygen solid electrolytes

System	Components	thermodynamic parameters to be fixed			
ZrO_2	2	T	a_{O_2}	-	-
(Zr, MeO_2)	3	T	a_{O_2}	$x(Me)$	-
$(Zr, Me)(O, N)_2$	4	T	a_{O_2}	$x(Me)$	a_{N_2}

components we also increase the number of thermodynamic variables to be fixed. The temperature and the cation dopant concentration are easily fixed, and to ensure constant gas pressures is also experimentally possible.

2.1.1 Pure ZrO_2

Undoped ZrO_2 is usually a crystalline material (an amorphous phase has also been reported [24, 25]) appearing at three different modifications (monoclinic, tetragonal, and cubic) depending on the temperature and the applied pressure

but a high pressure orthorhombic phase has also been reported [26]. Up to 1170 °C the stable crystallographic structure is of monoclinic symmetry. It shows n-type conductivity [27–30] with a band gap (E_g) of about 5 eV. Nevertheless different values for E_g varying from 4 eV up to 7 eV have been reported [31,32]. At higher temperatures (1170 °C - 2370 °C) the tetragonal structure becomes stable and above 2370 °C the fluorite type cubic lattice is the stable one. The crystallographic structure influences the dominant type of point defects in the lattice and their mobility, respectively the electric properties. In the tetragonal and the cubic phase the lattice allows oxygen ions to move between tetrahedral positions resulting in a high ionic (anion) conductivity. The electron/hole conductivity has a negligible influence ($\sigma_{total} \simeq \sigma_{ion}$). In the monoclinic structure the electronic conductivity is dominant. A detailed analysis and discussion of the crystallographic structures, the corresponding point defect structures and defect-related properties of ZrO_2 are given in [20,32–39].

ZrO_2 is a non-stoichiometric compound with an oxygen deficiency (or metal excess), and the chemical formula is typically written as $ZrO_{2-\delta}$, where δ varies with the oxygen partial pressure in the order of 10^{-4} [40]. A variety of point defects were considered for the correct modelling of undoped $ZrO_{2-\delta}$. Some authors proposed a Schottky-type disorder [41], involving oxygen and zirconium vacancies as the predominant ionic defects ($Zr_{Zr}^{\times} + 2O_O^{\times} \rightleftharpoons V_{Zr}'''' + 2V_O^{\bullet\bullet} + ZrO_2$). Douglass and Wagner [34] suggest anion Frenkel-type defects where the oxygen ion is moving to an interstitial position leaving a vacancy ($O_O^{\times} + V_I^{\times} = V_O^{\bullet\bullet} + O_i''$), confirmed also by [42]. Kroeger [43] and also Poulton [44] have postulated an interaction between zirconium and oxygen vacancies, forming a negatively charged associate of the type $(V_O^{\bullet\bullet}V_{Zr}'''')''$. A detailed review of the latter is given by Nowotny [33].

From the point of view of the technical application the most important phase is the cubic one as it provides the highest anion conductivity. We consider only this cubic phase, stable at temperatures above 2373 °C, where the majority defects are of anion Frenkel-type. Possible majority point defect pairs in pure cubic ZrO_2 are given in the table below.

Because of the formal charge 4+ of zirconium, it is unlikely to expect zirconium ion mobility, and no reports have been found presuming a cation con-

Table 2.2: Possible point defect pairs in pure $ZrO_{2-\delta}$

Defects	$V_O^{\bullet\bullet}$	$h^\bullet$	$Zr_i^{\bullet\bullet\bullet\bullet}$
O_i''	$\times$	$\times$	-
e^-	$\times$	$\times$	-
V_{Zr}''''	-	-	$\times$

ductivity. Thus we exclude the cations as possible mobile charge carriers from further consideration. The tracer-diffusion coefficient of ^{96}Zr in stabilized cubic zirconia has been measured by Kilo et. al [45, 46].

2.1.2 The Kroeger-Vink diagram for ZrO$_{2-\delta}$

At the point of exact 1:2 stoichiometry we can safely assume that the Frenkel-type anion disorder dominates over the electron-hole disorder, where both of them are significantly larger than the Schottky type disorder ($K_F > K_e \gg K_S$). The Frenkel defect formation can be written as:

$$O_O^\times + V_i^\times \rightleftharpoons V_O^{\bullet\bullet} + O_i'' \qquad \text{with} \quad K_\text{F} = [V_O^{\bullet\bullet}][O_i''] \qquad (2.1)$$

where K_F is the equilibrium constant. The electron-hole disorder with its corresponding equilibrium constant (K_e) is given by:

$$e_\text{VB}^\times + h_\text{CB}^\times \rightleftharpoons e_\text{CB}' + h_\text{VB}^\bullet \qquad \text{with} \quad K_\text{e} = [e'][h^\bullet] \qquad (2.2)$$

The charge neutrality condition requires:

$$2[O_i''] + [e'] = 2[V_O^{\bullet\bullet}] + [h^\bullet] \qquad (2.3)$$

<u>*Near stoichiometric region:*</u> $[V_O^{\bullet\bullet}] = [O_i'']$

At slightly reducing conditions the oxygen excorporates from the crystal lattice leaving electrons and oxygen vacancies behind, thus causing a reduction of the material according to the equation:

$$O_2 + 2V_O^{\bullet\bullet} + 4e^- \rightleftharpoons 2O_O^\times \qquad (2.4)$$

The equilibrium constant is given as:

$$K_{\mathrm{O}} = \frac{[\mathrm{O_O^\times}]^2}{[\mathrm{V_O^{\bullet\bullet}}]^2 [\mathrm{e}']^4} \cdot \mathrm{a}_{\mathrm{O_2}}^{-1} \tag{2.5}$$

The Brouwer approximation for the near stoichiometric region assumes $[\mathrm{V_O^{\bullet\bullet}}] = [\mathrm{O_i''}]$. The concentration of the both defect species can then be expressed by K_{F} according to eq. 2.1:

$$[\mathrm{V_O^{\bullet\bullet}}] = [\mathrm{O_i''}] = K_{\mathrm{F}}^{1/2} \tag{2.6}$$

In this region the concentrations of oxygen-related ionic defects do only slightly depend on the oxygen partial pressure. In contrast the dependence of the electron and hole concentrations on $a_{\mathrm{O_2}}$ can be calculated from equation 2.5 assuming that the concentration of the oxygen ions on regular sites is constant ($[\mathrm{O_O^\times}] = $ const.). The concentration of oxygen vacancies can then be substituted by the Frenkel constant (see eq. 2.6).

$$[\mathrm{e}'] = \frac{[\mathrm{O_O^\times}]^{1/2}}{(K_{\mathrm{O}} \cdot K_{\mathrm{F}})^{1/4}} \cdot a_{\mathrm{O_2}}^{-1/4} \quad \text{and} \quad [\mathrm{h}^\bullet] = \frac{K_{\mathrm{e}} \cdot (K_{\mathrm{O}} \cdot K_{\mathrm{F}})^{1/4}}{[\mathrm{O_O^\times}]^{1/2}} \cdot a_{\mathrm{O_2}}^{1/4} \tag{2.7}$$

In a $\lg [\mathrm{def}]/\lg a_{\mathrm{O_2}}$ plot the electron concentration decreases with increasing oxygen activity with a slope of $-1/4$ and the hole concentration increases with a slope of $1/4$, see fig. 2.1.

Strongly reducing conditions: $2[\mathrm{V_O^{\bullet\bullet}}] = [e']$

The Brouwer approximation assumes that the charge of the increasing number of oxygen vacancies is compensated by electrons. Combining equations 2.1, 2.2 and 2.5 one can calculate the dependence of the different defect species on the oxygen activity:

$$[\mathrm{V_O}^{\bullet\bullet}] = \frac{[\mathrm{O_O^\times}]^{1/3}}{2^{2/3} K_{\mathrm{O}}^{1/6}} \cdot a_{\mathrm{O_2}}^{-1/6} \quad \text{and} \quad [\mathrm{O_i''}] = \frac{2^{2/3} \cdot K_{\mathrm{F}} \cdot K_{\mathrm{O}}^{1/6}}{[\mathrm{O_O^\times}]^{1/3}} \cdot a_{\mathrm{O_2}}^{1/6} \tag{2.8}$$

and

$$[\mathrm{e}'] = \frac{(2 \cdot [\mathrm{O_O^\times}])^{1/3}}{K_{\mathrm{O}}^{1/6}} \cdot a_{\mathrm{O_2}}^{-1/6} \quad \text{and} \quad [\mathrm{h}^\bullet] = \frac{K_{\mathrm{O}}^{1/6} \cdot K_{\mathrm{e}}}{(2 \cdot [\mathrm{O_O^\times}])^{1/3}} \cdot a_{\mathrm{O_2}}^{1/6} \tag{2.9}$$

In this region the oxygen vacancy and electron concentrations differ by a factor of two but decrease both with a slope of $-1/6$ towards higher oxygen activities. The concentration of oxygen interstitials differs also by factor of two from the

hole concentration, and both increase with a slope of $1/6$.

Strongly oxidizing conditions: $2[O_i''] = [h^\bullet]$

The Brouwer approximation requires the charge of the major ionic defects (oxygen interstitials) to be compensated by holes, and their concentration is twice as high as the interstitial oxygen concentration. Combining eqs. 2.1 and 2.2 one obtains the defect concentrations as a function of the oxygen activity:

$$[O_i''] = \frac{K_e^{2/3} \cdot K_O^{1/6} \cdot K_F^{1/3}}{2^{2/3} \cdot [O_O^\times]^{1/3}} \cdot a_{O_2}^{1/6} \quad \text{and} \quad [V_O^{\bullet\bullet}] = \frac{(2 \cdot K_F)^{2/3} \cdot [O_O^\times]^{1/3}}{K_O^{1/6} \cdot K_e^{2/3}} \cdot a_{O_2}^{-1/6}$$

$$(2.10)$$

respectively for electrons and holes:

$$[h^\bullet] = \frac{K_e^{2/3} \cdot K_O^{1/6} \cdot (2 \cdot K_F)^{1/3}}{[O_O^\times]^{1/3}} \cdot a_{O_2}^{1/6} \quad \text{and} \quad [e'] = \frac{(K_e \cdot [O_O^\times])^{1/3}}{K_O^{1/6} \cdot (2 \cdot K_F)^{1/3}} \cdot a_{O_2}^{-1/6}$$

$$(2.11)$$

On the basis of equations 2.7, 2.8 and 2.9 for reducing conditions and equations 2.10, 2.11 for oxidizing conditions the Kroeger-Vink diagram for ZrO$_2$ at given temperature can be constructed.
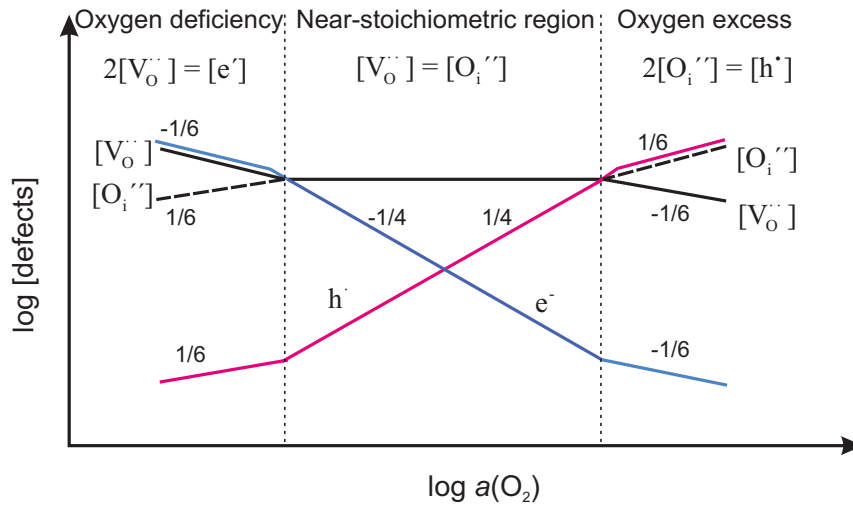
Fig. 2.1: Kroeger-Vink diagram for undoped ZrO$_2$ (T = const)

According to Xue [20] the stoichiometric point at 1100 °C is found at $a_{O_2} = 10^{-3}$. In addition, Xue determined the deviations from stoichiometry in the

range $10^{-11} < a_{O_2} < 1$.

2.1.3 Yttria-stabilized zirconia (cation doping strategy)

Pure $ZrO_{2-\delta}$ conducts oxygen only at elevated temperatures (practically above 700 °C). Because of the low vacancy concentration ($V_O^{\bullet\bullet}$ is in the range of 10^{-3} to 10^{-5} mol.cm^{-3}) [20,40] the ionic conductivity is not sufficient concerning practical applications. To increase the vacancy concentration (respectively the oxygen conductivity) and to stabilize the cubic structure, ZrO_2 is doped with different metal oxides introducing aliovalent cations into the crystal lattice. Typical doping agents used for ZrO_2 solid electrolytes are Y_2O_3, CaO, Sc_2O_3, MgO, CeO_2 and Gd_2O_3. Among them Sc_2O_3 leads to the highest conductivity but because of its lower price and only slightly worse doping effect Y_2O_3 has been found to be the most attractive dopant. Added to ZrO_2 in amounts of 1 mol% up to 20 mol% it stabilizes the tetragonal, respectively the cubic structure of zirconia, depending on the yttria content [47]. The addition of 3 mol% to 5 mol% Y_2O_3 stabilizes the tetragonal structure. Dopant concentrations of 5 mol% up to 8 mol% result in a mixture of tetragonal and cubic phases. Above 9 mol% only the cubic fluorite-type structure is present at room temperature. Because of its mechanical stability and the high concentration of vacancies yttria stabilized zirconia (YSZ) is the most widely used solid oxygen ion electrolyte.

By introducing yttrium oxide (Y_2O_3) into the lattice of zirconia, Y^{3+} substitutes Zr^{4+} in the cation sublattice creating a negative relative charge. To compensate this charge one oxygen vacancy is created for each incorporated Y_2O_3 "molecule". This substitution process is usually denoted as:

$$Y_2O_3 \xrightarrow{2ZrO_2} 2Y'_{Zr} + 3O_O^{\times} + V_O^{\bullet\bullet} \tag{2.12}$$

The charge balance requires $2[V_O^{\bullet\bullet}] = [Y'_{Zr}]$, so the concentration of the created vacancies is only half the concentration of the incorporated yttrium ions.

2.1.4 The Kroeger-Vink diagram for YSZ

To create the Kroeger-Vink diagram we can simply upgrade the diagram constructed for the pure ZrO_2 (fig. 2.1). The values of mass-action constants

(K_F; K_e and K_O) for the case of the pure substance remain unchanged for YSZ in a first order approximation, where of course the concentrations of the species will differ. The equilibrium reactions and their mass-action expressions for YSZ are the same as for the pure oxide (see eqs. 2.4 and 2.5). The charge neutrality condition is now given by the equation:

$$[Y'_{Zr}] + 2[O''_i] + [e'] = 2[V_O^{\bullet\bullet}] + [h^\bullet] \tag{2.13}$$

The solution of Y$_2$O$_3$ causes an increase of the vacancy concentration (see eq. 2.12). According to eq. 2.1 the increase of $[V_O^{\bullet\bullet}]$ will cause a decrease of oxygen interstitials as K_F is assumed to remain unchanged. Doping with 10 mol% yttria will create 10 mol% oxygen vacancies, which is about 4 orders of magnitude higher than the vacancy concentration $[V_O^{\bullet\bullet}]$ in the pure material. Both concentrations remain constant in a wide range of oxygen partial pressures, ensuring high oxygen ion conductivity and a small electronic transference number.

Near-stoichiometric region: ($[Y'_{Zr}] = 2[V_O^{\bullet\bullet}]$)

In the case of YSZ, because of the high concentration of the dopant, the effect of a deviation from the stoichiometry can be completely neglected. As the Y$_2$O$_3$ concentration is constant, the concentrations of oxygen vacancies and interstitials are basically independent on the partial pressure. The electron and the hole concentrations depend on the oxygen activity as derived from eq. 2.5:

$$[e'] = \frac{(2 \cdot [O_O^\times])^{1/2}}{K_O^{1/4} \cdot [Y_{Zr}']^{1/2}} \cdot a_{O_2}^{-1/4} \quad \text{and} \quad [h^\bullet] = \frac{K_O^{1/4} \cdot K_e \cdot [Y_{Zr}']^{1/2}}{(2 \cdot [O_O^\times])^{1/2}} \cdot a_{O_2}^{1/4} \tag{2.14}$$

The resulting slopes of the electron/hole dependencies remain $-1/4$ or $1/4$, respectively (as for pure ZrO$_2$), but the lines shift in vertical direction (for electrons to lower and for holes to higher concentration values) parallel to the lines drawn for pure zirconia. The stoichiometric point does not move on the concentration axis, but is shifted towards lower partial pressures of oxygen.

Strongly reducing conditions: $2[V_O^{\bullet\bullet}] = [e']$

The vacancy concentration increases and it is not any more fixed by the dopant by very low a_{O_2}. The compensation of the additional charge involves now electrons, as the concentration of $[Y'_{Zr}]$ ions is not sufficient. Thus, the Brouwer approximation in this region is formulated as $2[V_O^{\bullet\bullet}] = [e']$. The latter happens

at much lower oxygen partial pressures (than in the case of pure ZrO_2), when the concentration line of $[V_O^{\bullet\bullet}]$ for YSZ crosses the line drawn for the pure substance. The slope of the dependencies of the defect species can be calculated in accordance with eq. 2.8 and eq. 2.9:

$$[O_i''] \propto a_{O_2}^{1/6}; \quad [V_O^{\bullet\bullet}] \propto a_{O_2}^{-1/6} \quad \text{and} \quad [h^\bullet] \propto a_{O_2}^{1/6}; \quad [e'] \propto a_{O_2}^{-1/6} \qquad (2.15)$$

and have the values of $-1/6$ for electrons and oxygen vacancies and $1/6$ for holes and oxygen interstitials, respectively.

Strongly oxidizing conditions (oxygen excess): $\quad [Y_{Zr}'] = [h^\bullet]$
At sufficiently high oxygen activities the hole concentration approaches the doping level, and the Brouwer approximation in this region is formulated as $[h^\bullet] = [Y_{Zr}']$. The concentration of vacancies and oxygen interstitials can be calculated according to eq. 2.5:

$$[V_O^{\bullet\bullet}] = \frac{[O_O^\times] \cdot [Y_{Zr}']^2}{K_O^{1/2} \cdot K_e^2} \cdot a_{O_2}^{-1/2} \quad \text{and} \quad [O_i''] = \frac{K_F \cdot K_O^{1/2} \cdot K_e^2}{[O_O^\times] \cdot [Y_{Zr}']^2} \cdot a_{O_2}^{1/2} \qquad (2.16)$$

The concentration of $V_O^{\bullet\bullet}$ decreases with $-1/2$ and those of O_i'' increase with $1/2$ in the logarithmic plot with increasing a_{O_2}. The concentrations of electrons and holes remain constant ($[e'] = $ const. and $[h^\bullet] = $ const.).

Extremely high oxygen activities: $\quad (2[O_i''] = [h^\bullet])$
The concentration of oxygen interstitials exceeds $[Y_{Zr}']$ and the defect structure is dominated by $(2[O_i''] = [h^\bullet])$.

$$[V_O^{\bullet\bullet}] \propto a_{O_2}^{-1/6}; \quad [O_i] \propto a_{O_2}^{1/6} \quad \text{and} \quad [e'] \propto a_{O_2}^{-1/6}; \quad [h^\bullet] \propto a_{O_2}^{1/6} \qquad (2.17)$$

The vacancy and electron concentrations decrease with -1/6 and the concentrations of oxygen interstitials and holes increase with $1/6$ as in the case of the pure ZrO_2 (logarithmic plot).
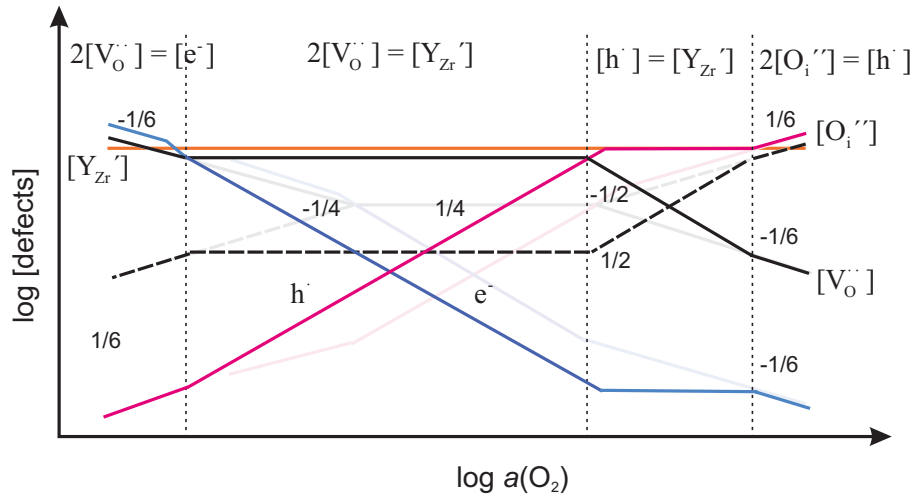
Fig. 2.2: Kroeger-Vink diagram for yttria stabilized zirconia (YSZ)

2.1.5 Nitrogen stabilized zirconia (anion doping strategy)

In analogy to cation doping one can choose an anion doping strategy, but it has much less been practiced than cation doping. This alternative allows to create new point defects in the crystals substituting ionic species from the anion sub-lattice with more or less negatively charged anions. In the case of zirconia we introduce an extra negative charge by doping with anions negatively charged relative to the oxygen ion, which has to be compensated either by electron holes or by creating new oxygen vacancies. Lerch [13, 14] studied intensively the nitridation of ZrO$_2$, the phase formation and the phase transitions in the ZrO$_2$ − Zr$_3$N$_4$ system. He studied in details the dark colored rhombohedral β − phases. Depending on the nitrogen content the β phases are ordered as follows: β − Zr$_7$O$_8$N$_4$; β' − Zr$_7$O$_{11}$N$_2$; β'' − Zr$_7$O$_{9.5}$N$_{3.0}$. The highest nitrogen content is observed in the pale yellow colored cubic γ − phase with the stoichiometric formula Zr$_2$ON$_2$. At temperatures below 1000 °C N-doped ZrO$_2$ exists as a phase mixture of monoclinic ZrO$_2$, and β- and γ-phases until the Zr$_3$N$_4$ compound is achieved. At elevated temperatures (above 1000 °C) nitrogen stabilizes the tetragonal or the cubic structure depending on its content. A detailed analysis of the phase stability and structural transitions in these systems can

be found in [11,14,39,48,49]. The substitution of oxygen by nitrogen proceeds according to the reaction:

$$N_2 + 3O_O^\times \longrightarrow 2N_O' + V_O^{\bullet\bullet} + 3/2O_2 \qquad (2.18)$$
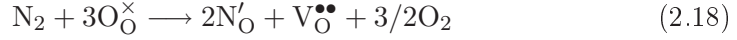
at low oxygen partial pressures. We should note that nitrogen substitution is not energetically preferable. Comparing the free enthalpy of formation of ZrO_2 and ZrN (data on the Zr_3N_4 are still not available) one can easily find that the oxide is thermodynamically much more stable than the nitride. So we can firstly assume that the oxinitride formation can only be achieved at extremely low oxygen activities, and secondly that the nitrides and the oxinitrides will convert to oxides easily if exposed to oxygen atmosphere. Nevertheless the latter process takes place only at elevated temperatures where oxygen and nitrogen ions are mobile. Even at intermediate temperatures (up to 600 °C) the rate of the re-oxidation reaction is relatively low, as kinetic difficulties also appear (the diffusion coefficient of N^{3-} ion is three to four orders of magnitude lower than that of O^{2-}). Thus, zirconium oxinitrides are in air metastable at low temperatures.

The Zr-O-N is a ternary system with the components Zr, O and N, which can thermodynamically be fixed only if we keep three variables constant besides the pressure - the temperature, the oxygen activity and the nitrogen activity.

2.1.6 The Kroeger-Vink diagram for $ZrO_{(2-\delta)(1-x)}N_{4x/3}$

The Kroeger-Vink diagram can be constructed as in the case of YSZ on the basis of the ZrO_2 diagram. Whereas we can assume a constant yttrium concentration in YSZ, due to the small vapor pressure of yttrium, it is more reasonable to consider the nitrogen partial pressure at the given temperature rather than the nitrogen concentration in the solid. The electroneutrality condition is:

$$[N_O'] + 2[O_i''] + [e'] = 2[V_O^{\bullet\bullet}] + [h^\bullet] \qquad (2.19)$$

The reactions of oxygen incorporation and excorporation and the corresponding mass-action expressions are the same as in the cases of pure zirconia and

YSZ (see equations 2.4 and 2.5). Additionally we have to formulate the reaction of nitrogen incorporation/excorporation related with oxygen evolution and incorporation via the chemical potentials of the both gases. Nitrogen reacts according to:

$$N_2 + 6e' + 2V_O^{\bullet\bullet} \rightleftharpoons 2N_O' \quad \text{with} \quad K_N = \frac{[N_O']^2}{[V_O^{\bullet\bullet}]^2 \cdot [e']^6 \cdot a_{N_2}} \tag{2.20}$$

Combining this equation with eq. 2.4 we obtain the chemical equation of the overall exchange reaction.

$$N_2 + 3O_O^{\times} \rightleftharpoons 2N_O' + V_O^{\bullet\bullet} + 3/2O_2 \tag{2.21}$$
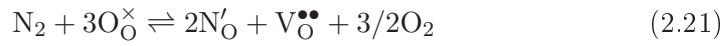
with equilibrium constant:

$$K_{O,N} = \frac{K_N}{K_O^{3/2}} = \frac{[N_O']^2 \cdot [V_O^{\bullet\bullet}] \cdot a_{O_2}^{3/2}}{[O_O^{\times}]^3 \cdot a_{N_2}} \tag{2.22}$$

Depending on the chemical potentials of both components (μ_{N_2} and μ_{O_2}) reaction 2.21 will proceed to the right (substitution of oxygen by nitrogen) or to the left (substitution of nitrogen by oxygen) side. If a high concentration of nitrogen in zirconia is achieved, we expect K_O to differ from the value for ZrO$_2$ and YSZ, but here we assume that it is constant.

Near-stoichiometric region: $[V_O^{\bullet\bullet}] = [O_i''];\ (a_{N_2} = \text{const.})$

Near to the stoichiometric point of pure ZrO$_2$ the concentration of the main defect species is determined by the intrinsic equilibrium and the Brouwer approximation is formulated as in the case of pure zirconia, $[V_O^{\bullet\bullet}] = [O_i'']$. The concentrations of vacancies and interstitials remain independent from the oxygen activity. The electrons and holes depend on a_{O_2} as follows:

$$[e'] = \frac{[O_O^{\times}]^{1/2}}{(K_O \cdot K_F)^{1/4}} \cdot a_{O_2}^{-1/4} \quad \text{and} \quad [h^{\bullet}] = \frac{K_e \cdot (K_O \cdot K_F)^{1/4}}{[O_O^{\times}]^{1/2}} \cdot a_{O_2}^{1/4} \tag{2.23}$$

There is no qualitative difference to the same regions in pure ZrO$_2$ or YSZ. According to equations 2.22 and 2.24 the increase of the nitrogen ion concentration is proportional to the decreasing oxygen activity to the power of $-3/4$:

$$[N_O'] = \frac{K_{O,N}^{1/2} \cdot [O_O^{\times}]^{3/2} \cdot a_{N_2}^{1/2}}{K_F^{1/4}} \cdot a_{O_2}^{-3/4} \tag{2.24}$$

In reducing atmosphere we assume two possible conditions for the nitrogen incorporation into the lattice. As postulated the nitrogen partial pressure is constant, but we have to consider a different values for this pressure. To substitute oxygen by nitrogen we should achieve conditions where the chemical potential of nitrogen exceeds those of oxygen. Comparing the standard free enthalpy of formation of ZrN and ZrO_2, one finds a much smaller value (less negative) for the nitride, mainly caused by the large binding energy of the nitrogen molecule. Thus, the nitrogen concentration in YSZ is very small in thermodynamic equilibrium under normal conditions.

At reducing conditions we discuss the defect formation reactions for two general conditions: $a_{N_2} \gg a_{O_2}$ (*Variant A*) and $a_{N_2} \leq a_{O_2}$ (*Variant B*) leading to the construction of two different Kroeger-Vink diagrams.

Reducing conditions: variant A $[N'_O] = 2[V_O^{\bullet\bullet}]$; $(a_{N_2} = \text{const.})$
The nitrogen incorporation into $ZrO_{(2-\delta)(1-x)}N_{\frac{4x}{3}}$ at low oxygen pressures proceeds under the assumption that the nitrogen activity is constant but higher than the oxygen activity. In this case we assume that the lattice oxygen will be directly displaced by nitrogen (eq. 2.21) without reduction of zirconia. As discussed above nitrogen acts as a dopant creating one additional oxygen vacancy for two N'_O ions. Both $[V_O^{\bullet\bullet}]$ and $[N'_O]$ are dependent on the oxygen partial pressure and the Brouwer approximation in this region is formulated as: $[N'_O] = 2[V_O^{\bullet\bullet}]$. As the chemical equation involves no electrons or holes their concentration remains constant. The defect concentration dependence on the oxygen partial pressure is calculated from equation 2.22:

$$[N'_O] = K_{O,N}^{1/3} \cdot [O_O^\times] \cdot a_{N_2}^{1/3} \cdot 2^{-1/3} \cdot a_{O_2}^{-1/2} \tag{2.25}$$

and

$$[V_O^{\bullet\bullet}] \propto a_{O_2}^{-1/2} \quad \text{and} \quad [O_i''] \propto a_{O_2}^{1/2} \tag{2.26}$$

$$[e'] = \text{const.} \quad \text{and} \quad [h^\bullet] = \text{const.} \tag{2.27}$$

The process of oxygen displacement will complete with either Zr_3N_4 or ZrN formation.

Reducing conditions: variant B $[e'] = 2[V_O^{\bullet\bullet}]$; $(a_{N_2} = \text{const.})$
If the nitrogen activity is not sufficiently high to ensure a direct substitution

of oxygen by nitrogen the decrease of oxygen activity will cause a reduction of the initial material. In this case the Brouwer approximation is defined as $[e'] = 2[V_O^{\bullet\bullet}]$ and the oxygen evolution is dominant. The defect determining equations are identical with those for pure ZrO₂ (see eqs. 2.8 and 2.9):

$$[V_O^{\bullet\bullet}] \propto a_{O_2}^{-1/6}; \quad [O_i''] \propto a_{O_2}^{1/6} \quad \text{and} \quad [e'] \propto a_{O_2}^{-1/6}; \quad [h^\bullet] \propto a_{O_2}^{1/6} \tag{2.28}$$

The concentration of the nitrogen ions will change according to:

$$[N_O'] = \frac{K_N^{1/2}}{K_O^{2/3}} \cdot [O_O^\times]^{4/3} \cdot 2^{-4/3} \cdot a_{N_2}^{1/2} \cdot a_{O_2}^{-2/3} \quad \text{or} \quad [N_O'] \propto a_{O_2}^{-2/3} \tag{2.29}$$

The nitrogen ions are incorporated but their concentration is not sufficient to govern the defect formation.

Strongly reducing conditions: variant B $[N_O'] = 2[V_O^{\bullet\bullet}]; \quad (a_{N_2} = \text{const.})$
If the oxygen activity decreases to sufficiently low values the nitrogen incorporation takes place and the Brouwrer approximation will be changed to $[N_O'] = 2[V_O^{\bullet\bullet}]$. The dependence of the defects formation on the oxygen activity is the same as in the case of *variant A*.

$$[N_O'] \propto a_{O_2}^{-1/2} \quad \text{and} \quad [V_O^{\bullet\bullet}] \propto a_{O_2}^{-1/2} \quad \text{and} \quad [O_i''] \propto a_{O_2}^{1/2} \tag{2.30}$$

$$[e'] = \text{const.} \quad \text{and} \quad [h^\bullet] = \text{const.} \tag{2.31}$$

Oxidizing conditions $[h^\bullet] = 2[O_i'']; \quad (a_{N_2} = \text{const.})$
At oxidizing conditions the concentration of N_O' drops with the increasing oxygen activity until the nitrogen is fully replaced by oxygen in zirconia and the Kroeger-Vink diagram for $ZrO_{(2-\delta)(1-x)}N_{4x/3}$ in this region is reduced to the diagram for the pure substance. At high oxygen activities the oxygen excess controls the defect structure and we calculate:

$$[V_O^{\bullet\bullet}] \propto a_{O_2}^{-1/6}; \quad [O_i''] \propto a_{O_2}^{1/6} \quad \text{and} \quad [e'] \propto a_{O_2}^{-1/6}; \quad [h^\bullet] \propto a_{O_2}^{1/6} \tag{2.32}$$

with slopes equal to those for pure ZrO₂. The concentration of nitrogen ions drops with a slope $-2/3$ according to:

$$[N_O'] = \frac{K_N^{1/2} \cdot K_e^{1/3} \cdot a_{N_2}^{1/2} \cdot [O_O^\times]^{1/3}}{K_F^{1/3} \cdot K_O^{2/3}} \cdot a_{O_2}^{-2/3} \tag{2.33}$$
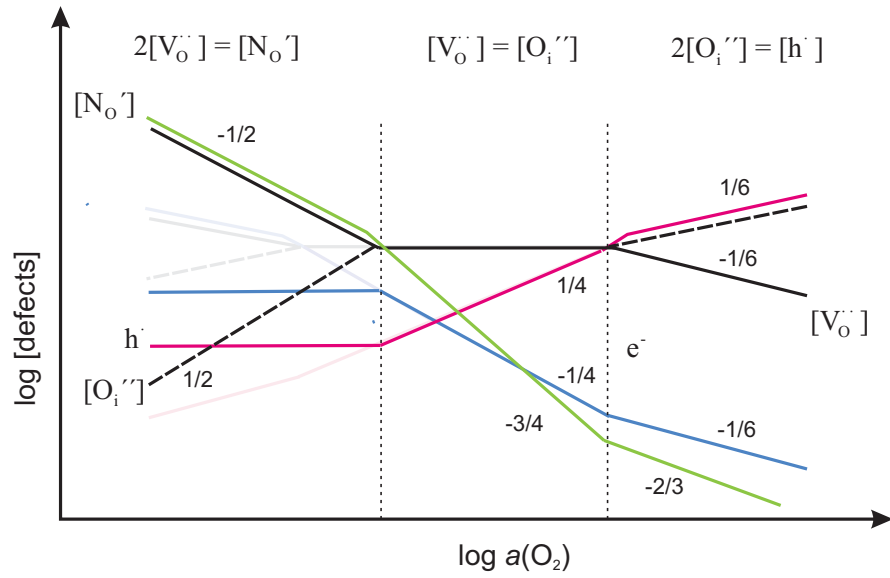
Fig. 2.3: Kroeger-Vink diagram for $\mathrm{ZrO}_{(2-\delta)(1-x)}\mathrm{N}_{4x/3}$ at constant high nitrogen pressure (variant A)
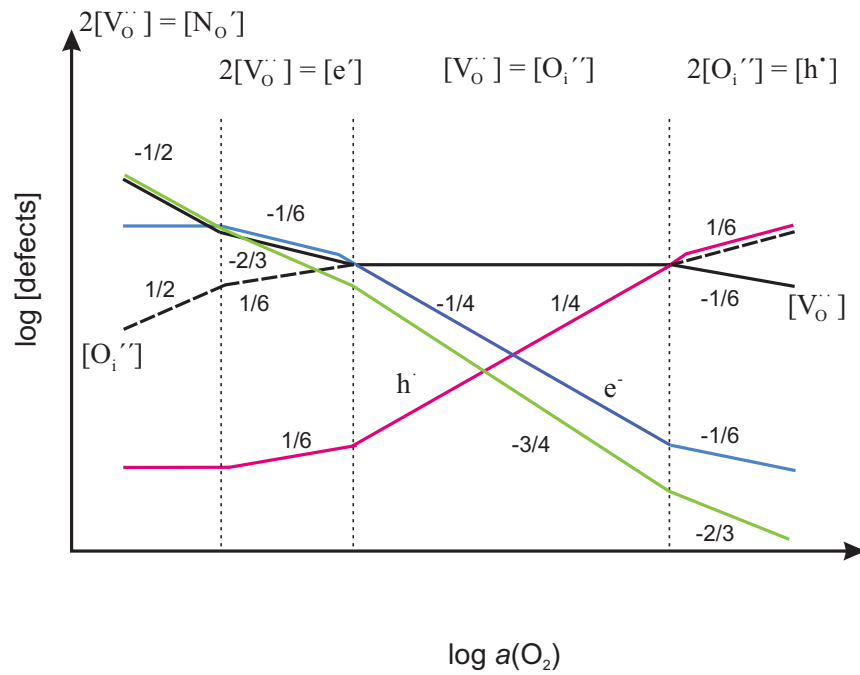
Fig. 2.4: Kroeger-Vink diagram for $\mathrm{ZrO}_{(2-\delta)(1-x)}\mathrm{N}_{4x/3}$ at constant low nitrogen pressure (variant B)

The diagrams present the both cases where the nitrogen partial pressure in the oxygen deficient region is higher (*Variant A*) or lower (*Variant B*) than the oxygen partial pressure. For the determination of the concentration dependence of defect species and Brouwer approximations by variation of the oxygen pressure, it is important to consider the nitrogen pressure. It is convenient and also useful to present the dependence of the defect structure of $\mathrm{ZrO}_{(2-\delta)(1-x)}\mathrm{N}_{\frac{4x}{3}}$ on both oxygen and nitrogen activities in a three-dimensional plot. The plot is shown in figure 2.5. The diagram reproduces the surface determined by the
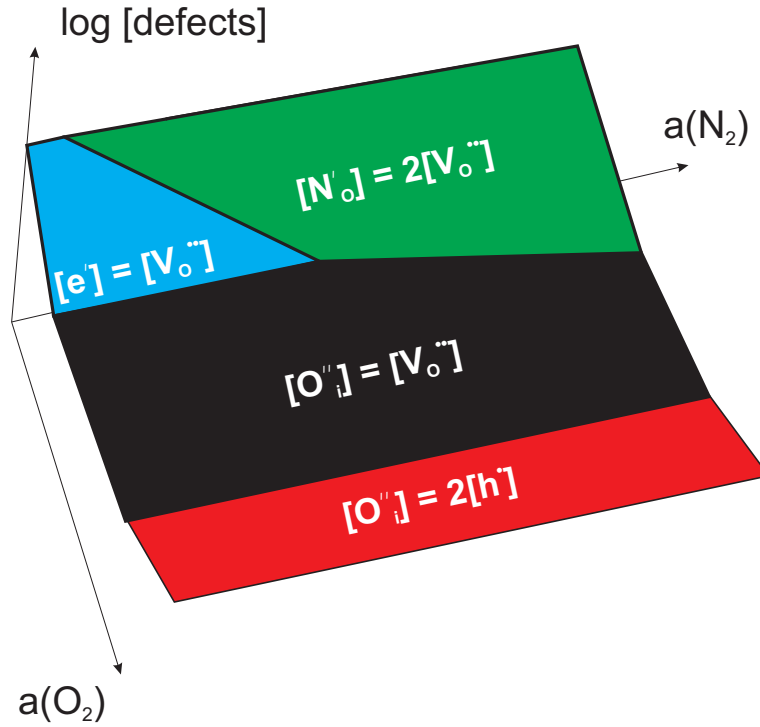
Fig. 2.5: Three dimensional presentation of the "surface" of a Kroeger-Vink diagram determined by the major defects for $\mathrm{ZrO}_{(2-\delta)(1-x)}\mathrm{N}_{4x/3}$ as a function on both oxygen and nitrogen activities

major defects at different Brouwer approximations by variation of nitrogen and oxygen activities. In this way one can easily take out a slice at a certain oxygen (or nitrogen) activity and determine the defect structure of the oxide.

2.1.7 Nitrogen doped YSZ

As discussed in the previous section $ZrO_{(2-\delta)(1-x)}N_{4x/3}$ is usually black (at least of dark color) and combines ionic and electronic conductivity, because the material is partially reduced. The re-oxidation at higher temperatures (above approx. 400 °C) results in de-nitridation of the samples thus diminishing the anion doping effect, respectively decreasing the ionic conductivity. On the other hand there is also a limit in the cation doping of YSZ. It has been found that Y_2O_3 segregates on the surface of zirconia with the time. This effect is much more pronounced when yttria concentration is higher than 13 mol% [50]. The segregation of yttria (a poor conductor) lowers the the effective vacancy concentration in the bulk. It is reasonable to combine both cation and anion doping in order to obtain a stable defect structure. Depending on the yttria (alternatively MgO and CaO) content both tetragonal and cubic fluorite-type structure can be stabilized by doping with nitrogen [4, 6–8, 12, 14, 51].

2.1.8 Kroeger-Vink diagram for N-doped YSZ

To construct the Kroger-Vink diagram for nitrogen doped YSZ we can use the diagram for YSZ (fig. 2.2) combining it with that for $ZrO_{(2-\delta)(1-x)}N_{4x/3}$ (fig. 2.4). As in the case of the Zr-O-N system we assume that the nitrogen partial pressure is fixed, while the oxygen pressure varies. The electroneutrality condition includes the intrinsic defects and both dopant species:

$$[N'_O] + [Y'_{Zr}] + 2[O''_i] + [e'] = 2[V^{\bullet\bullet}_O] + [h^\bullet] \tag{2.34}$$

The reactions and their mass-action constants are the same as for pure ZrO_2 and YSZ (see equations 2.2, 2.4 and 2.5) but we add reaction 2.20 to the oxygen reaction to obtain eq. 2.21 accounting for the nitrogen influence on the defect speciation.

Combining the doping effect of both species (Y'_{Zr} and N'_O) we create more oxygen vacancies in the crystal lattice. An advantage of the combined anion-cation doping is reducing the segregation of yttria which happens as mentioned above at concentrations higher than 13 mol% Y_2O_3. We can keep the yttria

concentration at lower levels (up to 10 mol%) increasing further the number of oxygen vacancies by addition of nitrogen anions.

Dopant (cation) controlled region $[Y'_{Zr}] = 2[V_O^{\bullet\bullet}]$; $(a_{N_2} = \text{const.})$
According to the expressions for the equilibrium constants K_O and K_e (equations 2.2 and 2.5) the line for the electron concentration will be shifted parallel to the initial one (the one for pure ZrO₂) towards lower values and those for the holes to higher values. Thus the crossing between these two lines (the intrinsic stoichiometric point) will be shifted towards lower oxygen partial pressures. The Brouwer approximation can be defined as: $[Y'_{Zr}] = 2[V_O^{\bullet\bullet}]$. The concentrations of oxygen vacancies and interstitials are constant and the electron and hole concentrations decrease/increase with slopes $-1/4$ respectively $1/4$ according to equation 2.5 as in the case of pure ZrO₂:

$$[e'] = \frac{[O_O^\times]^{1/2}}{K_O^{1/4} \cdot 2^{1/2} \cdot [Y'_{Zr}]^{1/2}} \cdot a_{O_2}^{-1/4} \quad \text{and} \quad [h^\bullet] = \frac{[O_O^\times]^{1/2}}{K_O^{1/4} \cdot 2^{1/2} \cdot K_e \cdot [Y'_{Zr}]^{1/2}} \cdot a_{O_2}^{1/4}$$
(2.35)

There are no qualitative differences between the same regions for nitrogen doped ZrO₂ or YSZ.

According to equations 2.22 and 2.24 the increase of the nitrogen ion concentration is proportional to the decreasing oxygen activity to the power of $-3/4$:

$$[N'_O] \propto a_{O_2}^{-3/4}$$
(2.36)

Reducing conditions: Variant A $[N'_O] = 2[V_O^{\bullet\bullet}]$; $(a_{N_2} = \text{const.})$
As in $ZrO_{(2-\delta)(1-x)}N_{4x/3}$ depending on the particular value of the nitrogen pressure ($a_{N_2} \gg a_{O_2}$ or $a_{N_2} \leq a_{O_2}$) we have two possible routes to incorporate nitrogen into the lattice. _Variant A_ concerns the case - $a_{N_2} \gg a_{O_2}$. The Brouwer approximation takes the form $[N'_O] = 2[V_O^{\bullet\bullet}]$. Respectively in the first route nitrogen directly substitutes oxygen:

$$N_2 + 3O_O^\times = 2N'_O + V_O^{\bullet\bullet} + 3/2O_2$$
(2.37)
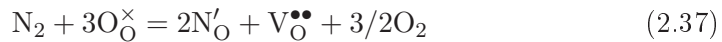
and the concentration of the defect species is calculated according to equation 2.22, where the nitrogen ions and oxygen vacancy concentration increases with a slope of $-1/2$ and oxygen interstitials decrease with $1/2$ towards lower oxygen activities in logarithmic scale:

$$[V_O^{\bullet\bullet}] \propto a_{O_2}^{-1/2} \quad [N'_O] \propto a_{O_2}^{-1/2} \quad \text{and} \quad [O_i''] \propto a_{O_2}^{1/2}$$
(2.38)

$$[e'] = const. \quad \text{and} \quad [h^\bullet] = const. \tag{2.39}$$

The process will continue until oxygen is fully displaced by nitrogen in the anion sublattice.

Reducing conditions: Variant B $[e'] = 2[V_O^{\bullet\bullet}]; \; (a_{N_2} = \text{const.})$

Variant B concerns the case of insufficient nitrogen activity. The nitrogen chemical potential is too low and nitrogen ions cannot be incorporated in YSZ. Due to the decreasing oxygen activity the material is reduced and the Brouwer approximation is defined as for pure ZrO_2 - $[e'] = 2[V_O^{\bullet\bullet}]$. The concentration of nitrogen ions changes according to:

$$[N_O'] = \frac{K_N^{1/2}}{K_O^{2/3}} \cdot [O_O^\times]^{4/3} \cdot 2^{-4/3} \cdot a_{N_2}^{1/2} \cdot a_{O_2}^{-2/3} \quad \text{or} \quad [N_O'] \propto a_{O_2}^{-2/3} \tag{2.40}$$

The concentration dependencies of the other ionic species are identical with those of pure zirconia:

$$[V_O^{\bullet\bullet}] \propto a_{O_2}^{-1/6}; \quad [e'] \propto a_{O_2}^{-1/6}; \quad [O_i''] \propto a_{O_2}^{1/6}; \quad [h^\bullet] \propto a_{O_2}^{1/6} \tag{2.41}$$

Strongly reducing conditions: Variant B $[N_O'] = 2[V_O^{\bullet\bullet}]; \; (a_{N_2} = \text{const.})$

At strongly reducing conditions the incorporated nitrogen ions become dominant as defect determining species and the Brouwer approximation changes to $[N_O']$ = $2[V_O^{\bullet\bullet}]$. The dependencies of the concentrations of defects on the decreasing oxygen activity are given as:

$$[N_O'] \propto a_{O_2}^{-1/2}; \quad [V_O^{\bullet\bullet}] \propto a_{O_2}^{-1/2} \quad \text{and} \quad [O_i''] \propto a_{O_2}^{1/2} \tag{2.42}$$

$$[e'] = \text{const.} \quad \text{and} \quad [h^\bullet] = \text{const.} \tag{2.43}$$

Oxidizing conditions (oxygen exsess) $[h^\bullet] = [Y_{Zr}']; \; (a_{N_2} = \text{const.})$

At oxidizing conditions the defect formation is independent on the nitrogen species and follows those of YSZ. The Brouwer approximation changes to $[h^\bullet]$ = $[Y_{Zr}']$. The oxygen defects change their concentrations according to eqs 2.16:

$$[V_O^{\bullet\bullet}] \propto a_{O_2}^{-1/2} \quad \text{and} \quad [O_i''] \propto a_{O_2}^{1/2} \tag{2.44}$$

with slopes -1/2 and 1/2 for vacancies and interstitials respectively, whereas

$$[e'] = const. \quad \text{and} \quad [h^\bullet] = const. \tag{2.45}$$

$$[N'_O] = K_e^{1/2} \cdot K_O^{1/4} \cdot K_{O,N}^{1/2} \cdot [O_O^\times] \cdot a_{N_2}^{1/2} \cdot a_{O_2}^{-1/2} \tag{2.46}$$

the lines of electronic defects keep going constant and the nitrogen ion concentration decreases with slope of -1/2 until the intrinsic disorder starts to dominate over the extrinsic one.

Strongly oxidizing conditions (oxygen excess) $[h^\bullet] = 2[O_i'']$; $(a_{N_2} = \text{const.})$
At strongly oxidizing conditions as in YSZ and in pure ZrO$_2$ the Brouwer approximation changes to $2[O_i''] = [h^\bullet]$ and the dependencies of defects on the oxygen pressure are:

$$[V_O^{\bullet\bullet}] \propto a_{O_2}^{-1/6}; \quad [O_i''] \propto a_{O_2}^{1/6} \quad \text{and} \quad [e'] \propto a_{O_2}^{-1/6}; \quad [h^\bullet] \propto a_{O_2}^{1/6} \tag{2.47}$$

The concentration of nitrogen is proportional to the oxygen activity powered to -2/3:

$$[N'_O] = \frac{K_N^{1/2} \cdot K_e^{1/3} \cdot a_{N_2}^{1/2} \cdot [O_O^\times]^{1/3}}{K_F^{1/3} \cdot K_O^{2/3}} \cdot a_{O_2}^{-2/3} \tag{2.48}$$

On the basis of these calculations the Kroeger-Vink diagrams for nitrogen doped YSZ is constructed.
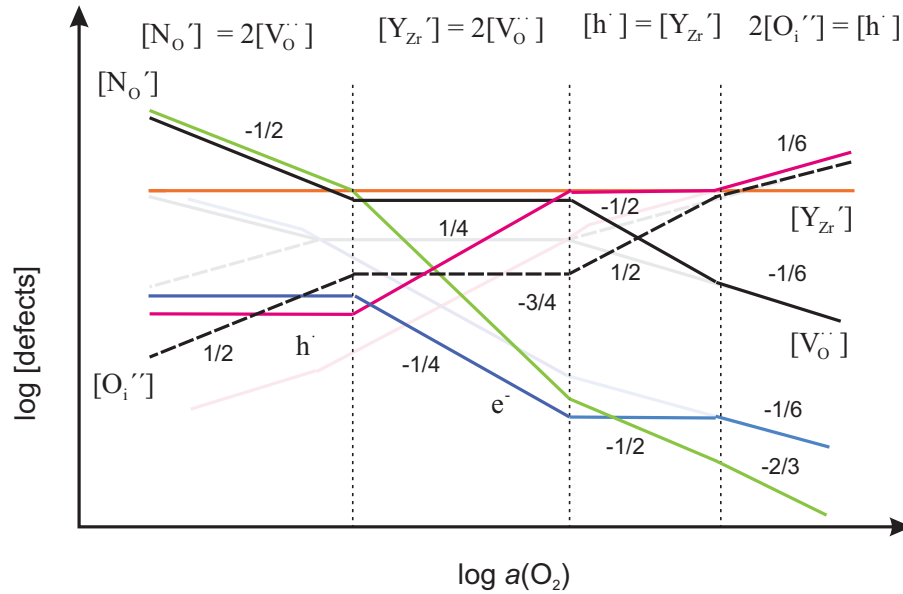
Fig. 2.6: Kroeger-Vink diagram for N-doped YSZ at constant nitrogen pressure (Variant A)

Exposing N-YSZ at variable nitrogen and constant oxygen pressure the electroneutrality conditions did not change:
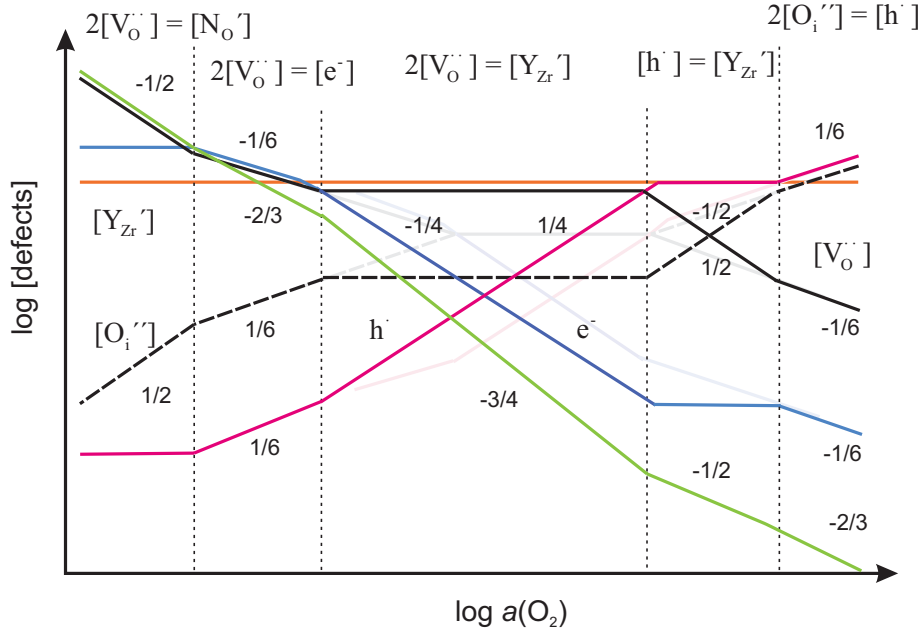
Fig. 2.7: Kroeger-Vink diagram for N-doped YSZ at constant nitrogen pressure (Variant B)

Electroneutrality conditions

$$[N_O'] + [Y_{Zr}'] + [e'] + 2[O_i''] = 2[V_O^{\bullet\bullet}] + [h^\bullet] \tag{2.49}$$

High nitrogen pressure $2[V_O^{\bullet\bullet}] = [N_O']; \ (a_{O_2} = \text{const.})$

At high nitrogen pressures oxygen ions are substituted and the formation of oxygen vacancies is determined mainly by the nitrogen N^{3-} ions. The Brouwer approximation is formulated as $2[V_O^{\bullet\bullet}] = [N_O']$. The concentration of N_O' increases according to:

$$[N_O'] = \frac{2[O_O^\times] \cdot K_N^{1/3}}{K_O^{1/2} \cdot a_{O_2}^{1/2}} \cdot a_{N_2}^{1/3} \quad \text{or} \quad [N_O'] \propto a_{N_2}^{1/3} \tag{2.50}$$

The oxygen vacancies and interstitials also depend on the nitrogen partial pressure:

$$[V_O^{\bullet\bullet}] = \frac{[O_O^\times] \cdot K_N^{1/3}}{K_O^{1/2} \cdot a_{O_2}^{1/2}} \cdot a_{N_2}^{1/3} \quad \text{or} \quad [V_O^{\bullet\bullet}] \propto a_{N_2}^{1/3} \tag{2.51}$$

$$[O_i''] = \frac{K_F \cdot K_O^{1/2} \cdot a_{O_2}^{1/2}}{[O_O^\times] \cdot K_N^{1/3}} \cdot a_{N_2}^{-1/3} \quad \text{or} \quad [O_i''] \propto a_{N_2}^{-1/3} \tag{2.52}$$

The concentration of electrons and holes is given by:

$$[e'] = K_N^{-1/6} \cdot a_{N_2}^{-1/6} \quad \text{and} \quad [h^\bullet] = K_e \cdot K_N^{1/6} \cdot a_{N_2}^{1/6} \qquad (2.53)$$

In this region the defect structure is governed by the nitrogen ions and the cation doping effect is less important.

<u>*Low nitrogen pressures*</u> $2[V_O^{\bullet\bullet}] = [Y_{Zr}']$; ($a_{O_2} = $ const.)

At low nitrogen pressures the concentration of N_O' decreases. The $V_O^{\bullet\bullet}$ concentration is determined only by the cation doping. The Brouwer approximation is defined as in the case of YSZ: $2[V_O^{\bullet\bullet}] = [Y_{Zr}']$. The concentration of nitrogen ions decreases with a slope of $1/2$:

$$[N_O'] = \frac{K_N^{1/2} \cdot [O_O^\times]^{3/2}}{1/2^{1/2} \cdot [Y_{Zr}']^{1/2} \cdot K_O^{3/4} \cdot a_{O_2}^{3/4}} \cdot a_{N_2}^{1/2} \quad \text{or} \quad [N_O'] \propto a_{N_2}^{1/2} \qquad (2.54)$$

The concentrations of the oxygen vacancies and interstitials, as well of electrons and holes remain independent from the nitrogen activity.

$$[V_O^{\bullet\bullet}] = const.; \quad [O_i''] = const.; \quad [e'] = const. \quad \text{and} \quad [h^\bullet] = const. \qquad (2.55)$$

The resulting Kroeger-Vink diagram (fig. 2.8) is simple but indicates the region of possible application of anion doped YSZ.

In figure 2.9 we present the three dimensional plot of the dependence of the major defects on both nitrogen and oxygen partial pressures for YSZ:N. Discussing the defect formation and defect related properties of N-YSZ in this section we have assumed that the nitrogen ions are formally incorporated as N^{3-}. This assumption may not always be correct. The nitrogen incorporated in YSZ provides a new 2p electronic level positioned at higher energies than the 2p level of oxygen. Thus in case of oxidation of the initial material firstly the electrons provided by N^{3-} will be consumed. The latter will result in a complete change of the defect model, because nitrogen can be present as $N_O^\times$ (i.e. valence state of $2-$) and then forms a "neutral" dopant. Further oxidation may even result in positively charged nitrogen defects which then leads to a much more complicated defect behavior. More detailed studies on the transport properties of YSZ:N at different temperatures and gas activities are necessary in order to define precisely the region of stability of YSZ:N doped with trivalent nitrogen ions.
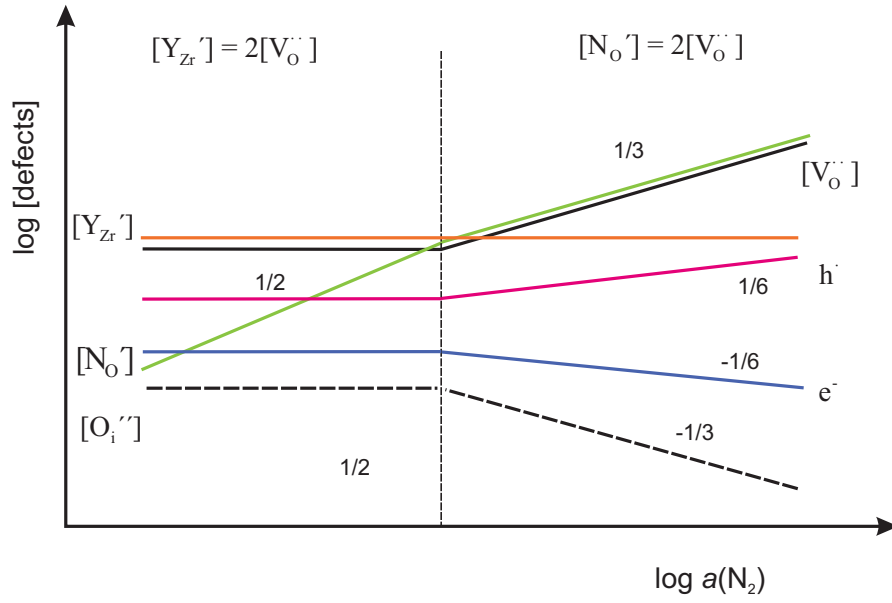
Fig. 2.8: Kroeger-Vink diagram for N-doped YSZ at constant oxygen and variable nitrogen pressure

Constructing the diagram for the behavior of YSZ:N in dependence on the nitrogen pressure (at constant a_{O_2}) we should also be very careful in the selection of the oxygen partial pressure, in view of the YSZ:N behavior at variable oxygen pressure (diagrams 2.6 and 2.7). If the O_2-pressure provides oxidizing conditions, nitrogen will easily be replaced by oxygen. The most reasonable region for nitrogen incorporation is at reducing conditions as shown in fig. 2.7 where the concentration of nitrogen ions is high, ensuring a region with a pronounced anion doping effect.

2.2 Expected differences in chemical and physical properties

The main physical properties of zirconia doped and undoped with nitrogen as density, hardness etc. do not differ drastically. They show similar behavior at room temperature and are chemically inert. Only concentrated hot acids are able to corrode these materials. However there are some differences: as reported by Lerch [14] the X-ray diffraction studies show a shift of the cell parameters towards lower values if ZrO_2 or YSZ are doped with nitrogen. The
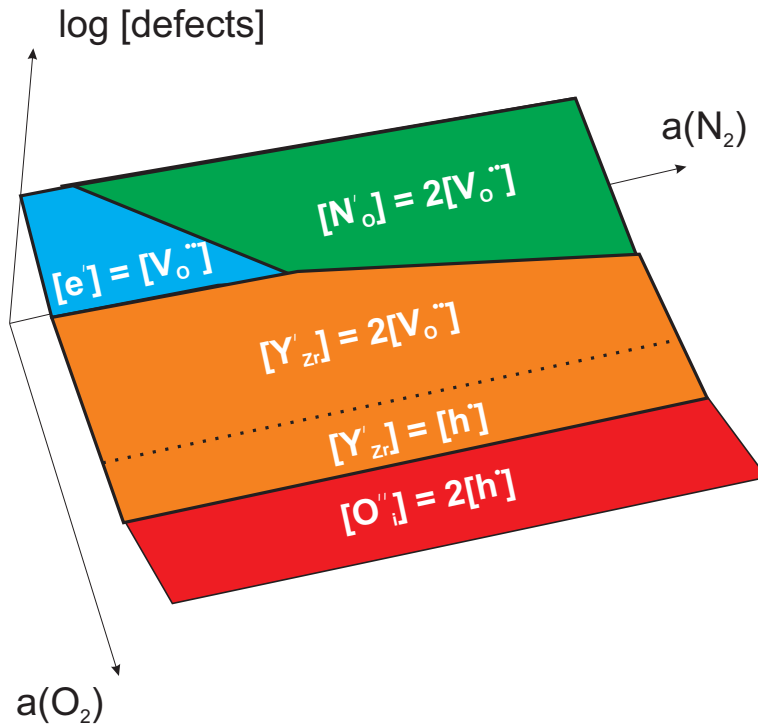
Fig. 2.9: Three dimensional presentation of the "surface" of a Kroeger-Vink diagram determined by the major defects for YSZ:N as a function on both oxygen and nitrogen activities

band structure also differs. Theoretical calculations show, that nitrogen creates donor levels within the band gap of zirconia ($E_g \approx 5$ eV) resulting in a smaller band gap ($E_g \approx 1$ eV) and respectively in differences in the electronic properties [52]. As it will be discussed later the spectroscopic studies show a shift of the optical band edge towards higher wave lengths and an adsorption maximum at about 500 nm in the nitrogen-doped material.

From the analysis of the defect structure of N-doped ZrO_2 and YSZ we expect a deviation in the chemical behavior and the defect-related properties of these materials from those of pure oxides. We assume that the nitrogen ions are a possible alternative in the doping strategy, introduced additionally to Y_2O_3 to prevent the use of high concentrations of yttria as a dopant leading to its segregation on the surface or in the bulk of the material, but keeping high oxygen vacancy concentration.

However, there is a principle difference in Y^{3+} and N^{3-} as doping agents. It

consists in their chemical stability and mobility within zirconia. The yttrium ion mobility is much lower (1.7×10^{-13} cm^2s^{-1} at 1600 °C) [45] compared to the nitrogen mobility at the same temperature (1.79×10^{-6} cm^2s^{-1}) [53, 54]. The cation doping effect is stable in a wide range of oxygen partial pressures (see fig. 2.2), i.e Y_2O_3 acts as an inert dopant and its undesirable effects (like segregation, diffusion, etc.) are detectable only on the long time scale and at elevated temperatures, whereas nitrogen doping cannot ensure a constant vacancy concentration even at reducing conditions, because it is dependent on the nitrogen partial pressure.

Nitrogen is much less reactive than oxygen but nevertheless it cannot be treated as inert at higher temperatures and its interactions and electrochemical reactions should not be neglected or underestimated in particular under reducing conditions. As both nitrogen and oxygen are involved in the thermodynamic equilibria and the defect formation they should always be considered together. As the formal valence state of nitrogen can vary from 3− up to 5+, special attention is required regarding the defect charge and the formulation of the defect equilibria. Nevertheless nitrogen doping offers the opportunity to manage different properties of the same material by variation of the oxygen/nitrogen ratio where one of these components is kept constant.

N-doped zirconia is a perspective solid electrolyte material, but should be used only in a controlled atmosphere.

2.3 Thermodynamics of the systems Zr/ZrO$_2$ and Zr/ZrN

The thermodynamic properties of the pure system Zr/ZrO_2 in O_2 atmosphere are determined by the equilibrium reaction:

$$\text{Zr} + \text{O}_2 = \text{ZrO}_2 \tag{2.56}$$

where the mass-action constant can be written as:

$$\exp\left(-\frac{\Delta_r G_{\text{O}}^{\circ}}{RT}\right) = K = \frac{a_{\text{ZrO}_2}}{a_{\text{Zr}} \cdot a_{\text{O}_2}} \tag{2.57}$$

with a standard free enthalpy of formation ($a_{\text{ZrO}_2} = a_{\text{Zr}} = 1$)

$$\Delta_r G_{\text{O}}^{\circ} = -RT \ln K = RT \ln a_{\text{O}_2}^* \qquad (2.58)$$

As the activity of ZrO$_2$ and Zr are assumed to equal unity, the mass-action constant defines the activity a_{O_2} (i.e. the partial pressure) of oxygen. The free enthalpy of formation can also be related to the standard electromotive force (denoted further as *emf* or E) of the electrochemical cell:

$$\Delta_r G_{\text{O}}^{\circ} = -nFE^{\circ} \qquad (2.59)$$

where F is the Faraday constant and n is the number of electrons involved in the reaction. The combination of equations 2.58 and 2.59 results in the expression relating the *emf* with the thermodynamic quantities:

$$E^{\circ} = -\frac{RT}{4F} \ln a_{\text{O}_2}^* \qquad (2.60)$$

where four electrons are required to complete the reaction.

This relation is the formal basis of potentiometric oxygen sensors: we measure the emf of an electrochemical cell using an oxygen conducting solid electrolyte (an important requirement is that the transference number of the oxygen ions must be $t_{\text{O}^{2-}} \cong 1$) between two electrodes exposed to different oxygen activities (partial pressures) $a_{\text{O}_2}^*$ and a_{O_2}, where $a_{\text{O}_2}^*$ is a fixed reference. The emf formed is a result of the difference in the chemical potential of oxygen on the both sides of the symmetrical cell $(\text{O}_2)^{\text{ref}}\text{Me}/\text{YSZ}/\text{Me}(\text{O}_2)$:

$$E = E_{(\text{O}_2/\text{O}^{2-})}^{\circ} + \frac{RT}{4F} \ln \frac{a_{\text{O}_2}}{a_{\text{O}^{2-}}} - E_{(\text{O}_2/\text{O}^{2-})}^{\circ *} - \frac{RT}{4F} \ln \frac{a_{\text{O}_2}^*}{a_{\text{O}^{2-}}} \qquad (2.61)$$

As the standard half cell potentials $\text{E}_{(\text{O}_2/\text{O}^{2-})}^{\circ}$ and $\text{E}_{(\text{O}_2/\text{O}^{2-})}^{\circ *}$ of the oxygen reaction on the both sides are equal and $[\text{O}^{2-}]$ in the solid electrolyte is constant and fixed by the dopant, the only variable that determines the electromotive force is the oxygen activity:

$$E = \frac{RT}{4F} \ln \frac{a_{\text{O}_2}}{a_{\text{O}_2}^*} \qquad (2.62)$$

Figure 2.10 represents the dependence of the emf on the activity of oxygen in the temperature range 400 K - 1400 K relative to the constant oxygen pressure
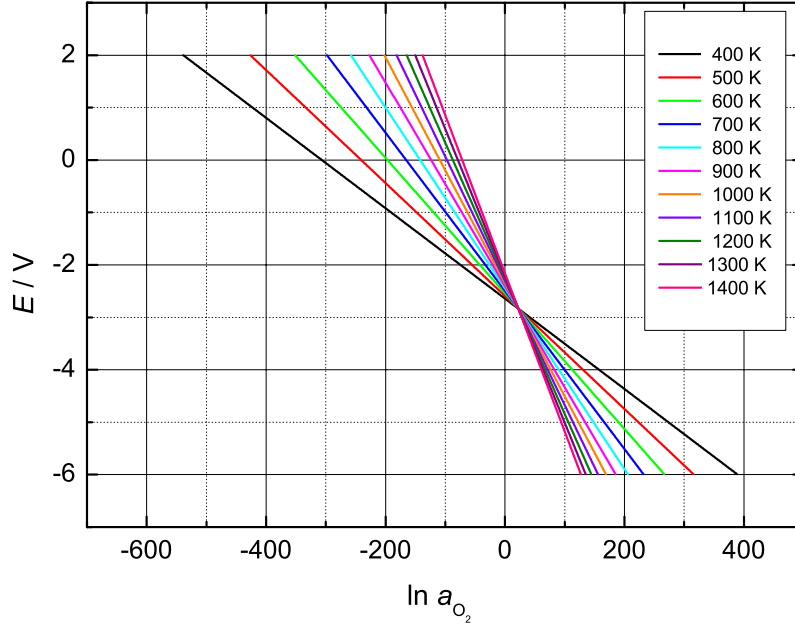
Fig. 2.10: Calculated dependence of the emf of the $Zr/ZrO_2/O_2$ cell on the oxygen activity a_{O_2} at various temperatures.

provided by the Zr/ZrO_2 half cell. The different emf values correspond to the change in the Gibbs energy by variation of the conditions and can directly be obtained from the thermodynamic data available in the literature [55]. The calculated potentials are highly positive as the oxygen activities are extremely low (10^{-43} at 700 K).

In fig. 2.10 it can be seen that the isothermal lines cross at an invariant point with the potential value E = -2.835 V and $a_{O_2} = 4.19 \times 10^9$. At this point neither the equilibrium activity nor the equilibrium potential depend on the temperature. Substituting this emf value in equation 2.59 we have calculated the value of the free enthalpy of formation ΔG_O° and after a comparison with the literature data we found that this value coincides exactly with the value of the Gibbs energy of the system at the temperature $T = 0$ K. We confirmed the latter also theoretically. The total emf of the cell consists of the difference in the free enthalpy terms of the right and the left side of the cell or we also

can express it in terms of the electrical potential difference. We consider the following cell: $\mathrm{Pt^I/Zr/ZrO_2/O_2(Pt^{II})}$ under the following assumptions:

- the charge carriers are only oxygen ions ($t_{\mathrm{O^{2-}}} \approx 1$) and the transfer number remains constant with the time

- there is no gradient of the electrochemical potential in the solid electrolyte, i.e. $\nabla \tilde{\mu}_{\mathrm{O^{2-}}} = 0$

In this case the measured potential difference between the both ends of this cell presents the reversible (Nernst) emf of the system. If the transference number of the oxygen ions deviates from unity, i.e. if the electrons or other ions also contribute to the total conductivity, the measured voltage will be lower than the Nernst voltage.

On the left side of the cell we assume that the electrochemical potential of the electrons in platinum and in zirconium are equal as both of them are metals. At the $\mathrm{Zr/ZrO_2}$ boundary we can formulate the thermodynamic equilibrium:

$$\mathrm{ZrO_2 + 4e^- = 2O^{2-} + Zr} \tag{2.63}$$

On the right side of the cell the following equilibrium is established:

$$\mathrm{O_2 + 4e^- = 2O^{2-}} \tag{2.64}$$

On the basis of these two equilibria representing the processes on the both sides of the electrochemical cell we mathematically express the equilibrium via the chemical/electrochemical potentials of the species:

$$\mu_{\mathrm{ZrO_2}} + 4\tilde{\mu}_{\mathrm{e-}}(\mathrm{Pt^I}) + 2\tilde{\mu}_{\mathrm{O^{2-}}}(\mathrm{Pt^{II}}) = \mu_{\mathrm{Zr}} + 2\tilde{\mu}_{\mathrm{O^{2-}}}(\mathrm{Pt^I}) + 4\tilde{\mu}_{\mathrm{e-}}(\mathrm{Pt^{II}}) + \mu_{\mathrm{O_2}}(\mathrm{Pt^{II}}) \tag{2.65}$$

As there is no gradient of the the electrochemical potential of oxygen ions on the both sides they can be eliminated from equation 2.65. Further assuming that $\tilde{\mu}_{\mathrm{i}} = \mu_{\mathrm{i}} + zF\phi$ and $\mu_{\mathrm{i}} = \mu_{\mathrm{i}}^{\circ} + RT \ln a_{\mathrm{i}}$ we rewrite eq. 2.65:

$$\mu_{\mathrm{ZrO_2}}^{\circ} + RT \ln a_{\mathrm{ZrO_2}} + 4\tilde{\mu}_{\mathrm{e-}}(\mathrm{Pt^I}) = \mu_{\mathrm{Zr}}^{\circ} + RT \ln a_{\mathrm{Zr}} + 4\tilde{\mu}_{\mathrm{e-}}(\mathrm{Pt^{II}}) + \mu_{\mathrm{O_2}}^{\circ} + RT \ln a_{\mathrm{O_2}}(\mathrm{Pt^{II}}) \tag{2.66}$$

After rearrangement and assuming that the activity of ZrO_2 and Zr is unity we
obtain:

$$4\widetilde{\mu}_{e-}(Pt^I) - 4\widetilde{\mu}_{e-}(Pt^{II}) = \underbrace{-\mu^\circ_{ZrO_2} + \mu^\circ_{Zr} + \mu^\circ_{O_2}}_{-\Delta_r G^\circ} + RT \ln a_{O_2}(Pt^{II}) \qquad (2.67)$$

$$4\left[\mu_{e-}(Pt^I) - F\phi(I) - \mu_{e-}(Pt^{II}) + F\phi(II)\right] = -\Delta_r G^\circ + RT \ln a_{O_2}(Pt^{II}) \quad (2.68)$$

The chemical potential of the electrons in the platinum metal is equal on both
sides of the cell and can be eliminated and as final result we obtain:

$$4F\left[\phi(II) - \phi(I)\right] = -\Delta_r G^\circ + RT \ln a_{O_2}(Pt^{II}) \qquad (2.69)$$

and

$$E = \phi(II) - \phi(I) = \frac{-\Delta_r G^\circ}{4F} + \frac{RT}{4F} \ln a^{II}_{O_2} \qquad (2.70)$$

or writing the equation as a function of the emf:

$$\ln a_{O_2} = \frac{\Delta_r G^\circ}{RT} + \frac{4F}{RT} \cdot E \qquad (2.71)$$

Considering equation 2.71 for two different temperatures T_1 and T_2 the invariant
point denoted by "$\star$" should fulfill two requirements:

1. $\ln a^\star_{O_2}(T_1) = \ln a^\star_{O_2}(T_2) = \ln a^\star_{O_2}$

2. $E^\star(T_1) = E^\star(T_2) = E^\star$

Applying these assumption to eq. 2.71 we obtain:

$$\frac{\Delta_r G^\circ(T_1)}{RT_1} + \frac{4F}{RT_1} \cdot E^\star(T_1) = \frac{\Delta_r G^\circ(T_2)}{RT_2} + \frac{4F}{RT_2} \cdot E^\star(T_2) \qquad (2.72)$$

or

$$\frac{T_2 \Delta_r G^\circ(T_1)}{T_2 T_1} - \frac{T_1 \Delta_r G^\circ(T_2)}{T_2 T_1} = E^\star \cdot 4F \left(\frac{T_1 - T_2}{T_2 T_1}\right) \qquad (2.73)$$

Multiplying the both sides of eq. 2.73 by T_2T_1 we obtain:

$$4F \cdot E^\star = -\frac{T_2 \Delta_r G^\circ(T_1 = 0)}{T_2} = -\Delta_r G^\circ(T_1 = 0) \qquad (2.74)$$

or

$$E^\star = -\frac{\Delta_r G^\circ(T = 0)}{4F} = -\frac{\Delta_r H^\circ(T = 0)}{4F} \qquad (2.75)$$

All lines must necessarily cross (fig. 2.10) at one point where the emf and the oxygen activity do not depend on the temperature. This point has the coordinates: $E^\star = \frac{-\Delta_r H^\circ_{(T=0)}}{4F}$ and $\ln a^\star_{O_2} = \frac{\Delta S^\circ_{(T=0)}}{R}$.

If the requirement $t_{ion} \approx 1$ or at least $t_{ion} = $ const. is satisfied this method can be applied for estimating standard thermodynamic quantities by electrochemical measurements performed at different temperatures.

Analyzing the thermodynamic data for the system Zr/ZrN we calculate the conditions of formation and stability of ZrN in nitrogen atmosphere in the same way as for the Zr/ZrO_2 system. The equilibrium reaction is:

$$\text{Zr} + 1/2\text{N}_2 = \text{ZrN} \quad \text{with} \quad K_N = \frac{a_{ZrN}}{a_{Zr}} \cdot a_{N_2}^{-1/2} \tag{2.76}$$
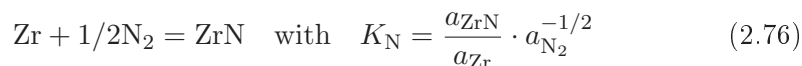
and the relation between the standard Gibbs energy and the electromotive force in this case is given:

$$\Delta G^o_N = -nFE = -RT \ln K_N = -RT \ln \frac{a_{ZrN}}{a_{Zr} \cdot a_{N_2}^{1/2}} \tag{2.77}$$

or

$$E = -\frac{RT}{6F} \ln a^*_{N_2} \tag{2.78}$$

The calculated emf as a function of the nitrogen activity at different temperatures is presented in fig. 2.11. The lines drawn for various temperatures cross at a point with the coordinates $E^\star = 1.256$ V and $a^\star_{N_2} = 2.57 \times 10^9$ values corresponding to the free enthalpy of formation at $T = 0$ K.

On the basis of the thermodynamic analysis, comparing the standard emf of the Zr/ZrN and Zr/ZrO_2 systems we easily see that zirconia is much more stable than zirconium nitride. The substitution of oxygen by nitrogen in the oxide phase requires strongly reducing atmospheres and high temperatures.

2.4 Transport properties of solid electrolytes

The thermodynamics and the defect structure of nitrogen-doped zirconia determine its conductivity. In fully oxidized YSZ all ions (i.e. O^{2-}, Zr^{4+} and Y^{3+}) exist only in one valance state and band-band transitions of electrons/holes are not expected and thus, YSZ is found to be a purely oxygen ion conductor.
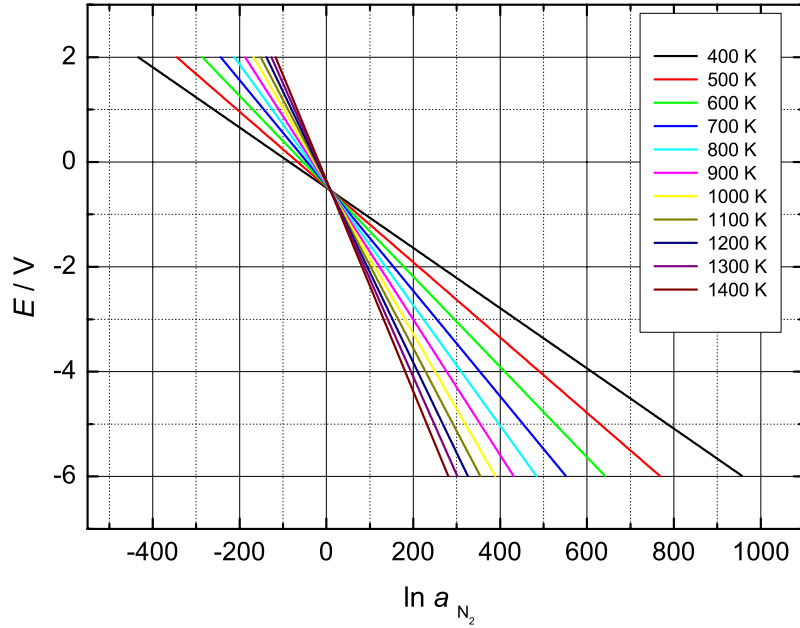
Fig. 2.11: Calculated dependence of the e.m.f. of the system $Zr/ZrN/N_2$ on the nitrogen activity a_{N_2}.

Diffusion in a chemical potential gradient:

In general, the mobility of particle of sort i is given as:

$$b_i = \frac{|\overrightarrow{v}|}{|\overrightarrow{F}|} \tag{2.79}$$

where b_i is the mechanical mobility of particle i, $\overrightarrow{v}$ is the velocity of this particle and $\overrightarrow{F}$ is the driving force. The molar flux of particles of one sort is proportional to the concentration multiplied by the velocity, i.e. $\overrightarrow{j_i} = c_i \cdot \overrightarrow{v_i}$, the total flux of particles driven by the chemical potential gradient is given by:

$$\overrightarrow{J_i} = c_i \cdot b_i \cdot \nabla\mu \tag{2.80}$$

Assuming only one dimensional diffusion of the particles we combine the Fick's first law ($J_i = -D_i \, \partial c_i/\partial x$) with the equation $\mu_i = \mu_i^\circ + RT \ln c_i$ and we obtain the final expression relating the chemical diffusion coefficient to the mobility of these particles, known as Nernst-Einstein equation is:

$$D_i' = b_i \cdot RT \tag{2.81}$$

The diffusion coefficient determined has to be corrected by the term $d \ln a / d \ln c$ accounting the inequality between the activity a and the concentration c, often denoted as a thermodynamic factor. Then the chemical diffusion coefficient is given by:

$$D_i' = D_i \cdot \frac{d \ln a_i}{d \ln c_i} \tag{2.82}$$

where D_i is the self-diffusion coefficient.

Diffusion in an electrical potential gradient:

If the driving force is not the gradient of the chemical potential, but an electric filed, the force $\overrightarrow{F}$ acting on a particle of sort i is given by the product of the particle's charge and the electric potential gradient, i.e. $\overrightarrow{F} = -z_i \cdot e \nabla \phi$. Combining equations 2.79 and 2.81 the total flux can be expressed as:

$$\overrightarrow{J_i} = -c_i \cdot b_i \cdot z_i F \nabla \phi = -D_i \frac{c_i \cdot z_i \cdot F}{RT} \nabla \phi \tag{2.83}$$

In analogy to equation 2.79 the mobility of particles of sort i in electric filed gradient (i.e. the electrical mobility) is given by:

$$u_i = \frac{\overrightarrow{v_i}}{\overrightarrow{E}} = |z_i| \cdot F \cdot b_i \tag{2.84}$$

The total flux in electric field can also be defined as $\overrightarrow{j_i} = \overrightarrow{i}/z_i F$. On the other hand at not too strong electric fields the current density i can also be expressed using the conductivity according to the Ohm's law: $\overrightarrow{i} = \sigma \overrightarrow{E}$ or $\overrightarrow{i} = -\sigma_i \nabla \phi$, where σ_i is the partial conductivity of particles i. Thus the molar flux $\overrightarrow{j_i}$ is given by:

$$\overrightarrow{J_i} = -\frac{\sigma_i}{z_i F} \nabla \phi \tag{2.85}$$

Combining this equation with equation 2.83 we obtain the following relation between the conductivity and the self-diffusion coefficient, respectively the mobility:

$$\sigma_i = c_i \cdot b_i \cdot z_i^2 F^2 = c_i \cdot u_i \cdot z_i F = D_i \frac{c_i \cdot z_i^2 F^2}{RT} \tag{2.86}$$

Diffusion in an electrochemical potential gradient:
If both chemical and electrical potential gradients are present, then the force acting is the electrochemical potential gradient. In this case the particles flux is given by:

$$\overrightarrow{J_i} = -c_i \cdot b_i' \nabla \mu - c_i \cdot b_i'' z_i F \nabla \phi = -c_i \cdot b_i \cdot \nabla \widetilde{\mu} \tag{2.87}$$

Here we assume that the mechanical mobility of the particles in a chemical potential gradient (b'_i) are equal to the mobility of these particles in an electric filed gradient (b''_i) because only under this assumption the flux at equilibrium condition can equal zero, i.e. $\nabla\widetilde{\mu} = 0$. Combining equations 2.87, 2.81 and 2.86 we obtain for the total flux of particles of sort i in an electrochemical potential gradient the relation:

$$\overrightarrow{J_i} = -\frac{c_i D_i}{RT}\nabla\widetilde{\mu} = -\frac{\sigma_i}{z_i^2 F^2}\nabla\widetilde{\mu} \tag{2.88}$$

As usual more than one species are mobile the total conductivity σ (as σ is a measurable quantity of the total flux) is a sum of all partial conductivities:

$$\sigma = \sum_{i=1}^{n}\sigma_i \tag{2.89}$$

where n is the total number of charge carriers. Thus, the ratio of partial conductivity σ_i of particles of the type i to the total conductivity σ is known as the transference number of this particle:

$$t_i = \frac{\sigma_i}{\sum\limits_{i=1}^{n}\sigma_i} \tag{2.90}$$

The transference number shows the part of the total charge carried by a particular sort of particles (electrons or ions). As the ions can be charged positively and as well negatively the sum $t_+ + t_- = 1$, where t_+ denotes the sum of the transference numbers of all cations and t_- denotes the sum of all anions.

Some specifics of the ionic movement in solids

The diffusion of ions in solids has some specifics compared to their diffusion in liquids. Firstly we cannot differentiate if the ion moves or the vacancy. Secondly the ions cannot move freely in the crystal lattice. There are only a limited number of free positions (vacancy or interstitial place) for the jump to occur. Thus, increasing the number of vacancies we increase the probability that the jump will successful. The ability for an ionic movement is characterized by the jump frequency. It is defined as the number of jumps per unit time and is denoted by ω. The jump frequency is related to the activation energy (for the jump) by:

$$\omega = \nu \cdot \exp\left(-\frac{\Delta G^{\neq}}{RT}\right) = \underbrace{\nu \cdot \exp\left(\frac{\Delta S^{\neq}}{k}\right)}_{\omega_0} \cdot \exp\left(-\frac{\Delta H^{\neq}}{kT}\right) \tag{2.91}$$

where ν is the Debye frequency, $\Delta S^{\neq}$ and $\Delta H^{\neq}$ are the migration entropy and the migration enthalpy respectively. As the entropy term is not temperature dependent we can combine the first two terms of equation 2.91:

$$\omega = \omega_0 \cdot \exp\left(-\frac{E_A}{kT}\right) \tag{2.92}$$

The self-diffusion coefficient can be then expressed by:

$$D_i = \frac{n \, r^2}{2d} \, \omega = \underbrace{\frac{1}{6} \, r^2 \, \omega_o}_{D_i^\circ} \cdot \exp\left(-\frac{E_A}{kT}\right) = D_i^\circ \, \exp\left(-\frac{E_A}{kT}\right) \tag{2.93}$$

where $1/6$ in D_i° term accounts for the three dimensional diffusion ($1/6 = n \, /2 \, d$) for a mean random walk, r is the single jump distance, n is number and d is the dimensionality. The number 2 accounts that the ion can move in both right and left direction from its initial position.

Combining equations 2.86 and 2.93 we obtain the relation between the conductivity, the self-diffusion coefficient and the activation energy for ionic jump:

$$\sigma_i = D_i^\circ \frac{c_i \cdot z_i^2 F^2}{RT} \exp\left(-\frac{E_A}{RT}\right) = \frac{\sigma_i^\circ}{T} \exp\left(-\frac{E_A}{RT}\right) \tag{2.94}$$

Thus, we can determine the activation energy, and respectively the diffusion coefficient by a measurement of the temperature dependance of conductivity. The experimental data presented in the plot $\ln \sigma_i T \; vs. \; 1/T$ consists of points laying on a straight line with a slope E_A/R with an intercept on a y-axis σ_i°.

Often in the solid state studies more than one species are mobile and the measured conductivity represents the sum of the individual conductivities σ_i. One of the possible experimental ways to determine the individual diffusion coefficient of particles of sort i is by tracer diffusion experiments. The tracer diffusion coefficient D_i^* is related to the self-diffusion coefficient D_i according to:

$$D_i^* = f \cdot D_i, \; where \; f \equiv \frac{(\overline{R_n^2})_{tracer}}{(\overline{R_n^2})_{regular}} \tag{2.95}$$

Here $\overline{R_n^2}$ is the mean random walk of respectively the tracer ion and of the regular ions.

2.5 The Me(N$_2$) electrode

The electrochemical behavior of nitrogen in equilibrium with its ionic species has been studied so far mostly in liquid electrolytes. Neutral atomic nitrogen has the ground state electronic configuration: $1s^2 2s^2 2p^3$, where the 2p energy level is only half occupied. This electronic structure determines the stability of nitrogen molecule $(\sigma_s^b)^2\ (\sigma_s^*)^2\ (\pi_{y,z}^b)^4\ \sigma_x^b)^2$ with completely filled bonding orbital and completely empty $\pi_{x,y}^*$ and σ_x^* anti-bonding orbital. The electronic structure of the nitrogen atom determines the possible valence states of the nitrogen ion. All valence states between 5+ and 3− are accessible involving the electrons of the 2s and 2p levels. The standard electrode potentials of some nitrogen species in aqueous solutions according to [56] are given in the figure 2.12 below.
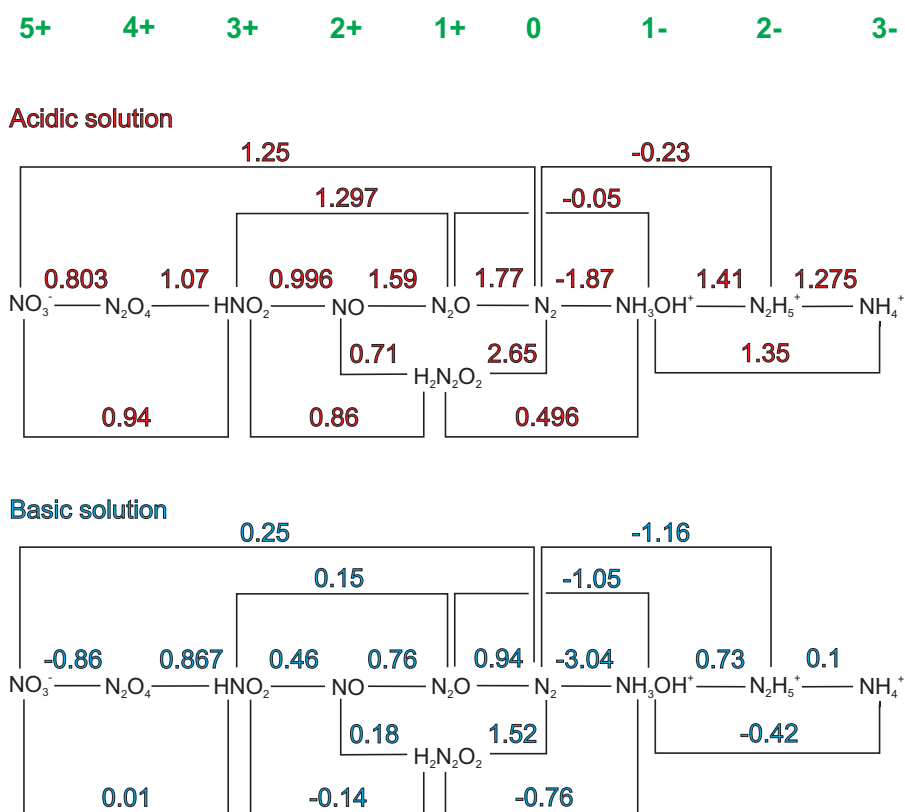
Fig. 2.12: Standard half cell potentials of various nitrogen species in aqueous media at room temperature.

The electrochemical behavior of nitrogen is complicated and involves complex ions formed by its interaction with oxygen, hydrogen or hydroxyl species.

Electrode systems involving only a simple redox system of the type nitrogen ion/nitrogen have not been reported for liquid systems.

The only studies reporting the reversible nitrogen half cell potential of the simple redox couple N^{3-}/N_2 have been published by Ito [57] and Goto [58]. They investigated the behavior of the nitrogen electrode in the $LiCl - KCl - Li_3N$ molten electrolyte system at nickel and titanium electrodes and have determined for the electrode potential $E = 0.382 + \frac{RT}{6F} \cdot \ln p_{N_2} - \frac{RT}{3F} \cdot \ln a_{N^{3-}}$ versus Li^+/Li reference electrode[1].

To our knowledge no reports on the N^{3-}/N_2 electrode in solid state systems exist. Studies on the reduction of NO_x gases on solid electrolytes of different compositions [59, 60] can be found but nitrogen is usually regarded as inert towards solid electrolytes and only Wilcockson [19] briefly reports about the ZrN formation during electrochemical polarization of YSZ in nitrogen atmosphere.

In order to discuss the nitrogen electrode on solid electrolytes and the redox reaction(s) of nitrogen we firstly formulate the equilibrium chemical reaction and the equilibrium electrochemical potential equations for the N^{3-}/N_2 redox couple on the N-doped YSZ solid electrolyte system. As discussed in section 2.1.5 nitrogen can be incorporated chemically and as well electrochemically according to reaction:

$$N_2(gas) + 2V_O^{\bullet\bullet}(YSZ) + 6e'(Me) \rightleftharpoons 2N_O'(YSZ) \qquad (2.96)$$
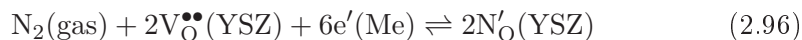
The only difference with equation 1.2 is the source of electrons. In the case of eq. 1.2 they are provided by the electrolyte while in eq. 2.96 they are supplied by the metal electrode. The Nernst-type equation for the half cell can then be formulated as:

$$E_{N^{3-}/N_2} = E^\circ_{N^{3-}/N_2} + \frac{RT}{6F} \ln \frac{[N_O']^2}{[V_O^{\bullet\bullet}]^2 \cdot a_{N_2}} \qquad (2.97)$$

where $E^\circ_{N^{3-}/N_2}$ is the standard electrochemical potential of the redox couple. Practically this value is the only unknown parameter in the equation, because we can easily calculate the number of oxygen vacancies, nitrogen ions and we can determine the particular nitrogen pressure. Nevertheless the situation is more complicated than eq. 2.97 shows. Nitrogen doped YSZ is a quaternary

---

[1]Li^+/Li standard redox potential is -3.06 V vs SHE in aqueous solution and approximately -3 V in non-aqueous media

compound and its potential is a mixed (corrosion) potential, where all the ions are involved in the potential determining reaction and we cannot exclude an interaction between the individual ionic components i.e. between the oxygen- and nitrogen ions. So we cannot expect that the measured equilibrium electro-chemical potential is formed only on the basis of N^{3-}/N_2 reaction.

In respect to a possible practical use of any type of electrode working with molecular nitrogen, the thermodynamics of the nitrogen half cell is only one part of the problem. Without a reasonably fast kinetics, an equilibrium potential may never be achieved. The understanding of this process requires detailed studies on the kinetics of the charge transfer process(es) during the oxidation and the reduction of nitrogen species.

2.6 Theory of charge transfer and multi electron exchange processes

2.6.1 The Butler-Volmer equation

An equation describing the relation between the overpotential η and the current density i for the charge-transfer controlled electrode reactions was derived in the first decades of the 20$^{\text{th}}$ century and is known today as the Butler - Volmer equation. It has been derived and experimentally confirmed by Butler [61, 62] and Volmer [63] in the 30th years of the 20$^{\text{th}}$ century starting from the empirical Tafel law suggested in 1905 by J. Tafel [64]. Here we present the derivation of this fundamental equation from energy/potential curves as suggested in 1935 by Horiuti and Polanyi [65].

The diagram 2.13 presents the potential energies of a particle being discharged according to the equation $Ox + ze^- = Red$ as a function of its distance from the electrode surface. Curve 1 represents the potential energy of an ion geometrically situated at the outer Helmholz plane (OHP) of the electrical double layer (EDL). It is assumed that no ligand or solvent molecules are present near and bonded to the reacting particle. Curve 2 is the potential energy of an atom on the surface of the metal electrode. We formulate the following equations describing the consequence of the reaction:
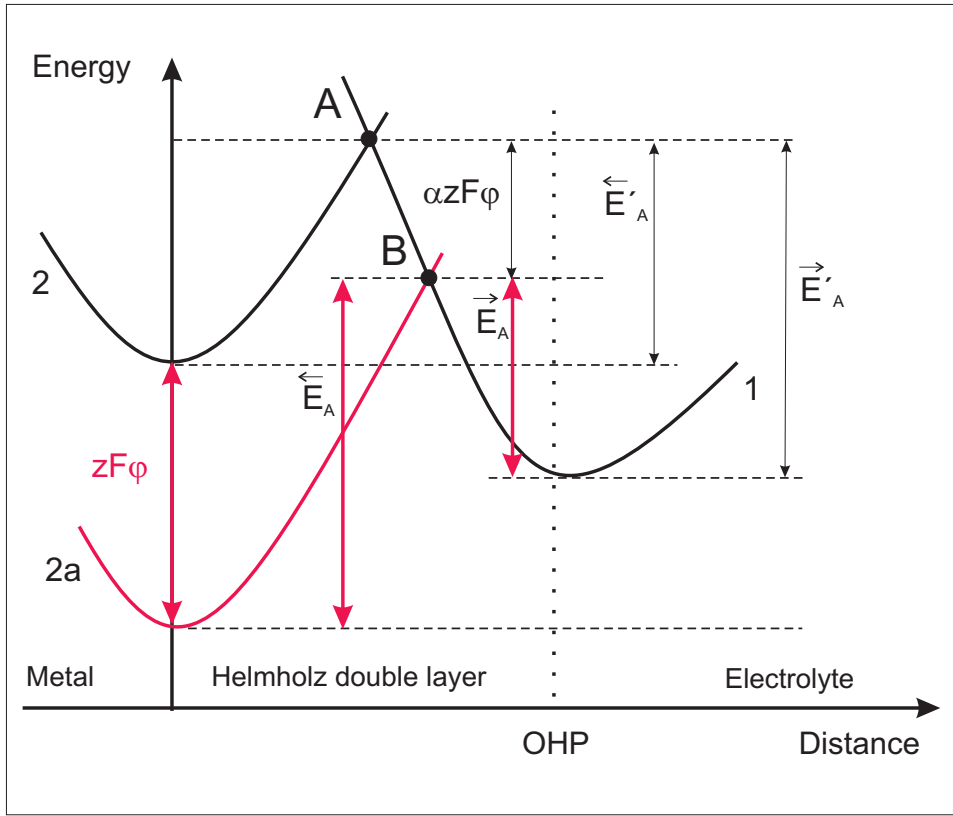
Fig. 2.13: Potential energy versus distance from the electrode surface. Curve 1 represents the potential energy of an atom on the surface of a metal electrode. Curves 2 and 2a represent the pot. energy of an ion without and with electrode/electrolyte potential difference.

$$Ox_{(solution)} \xrightarrow{diffusion} Ox_{(OHP)}$$

$$Ox_{(OHP)} + ze^-_{metal} \xrightarrow{charge\ transfer} Red_{(metal)}$$
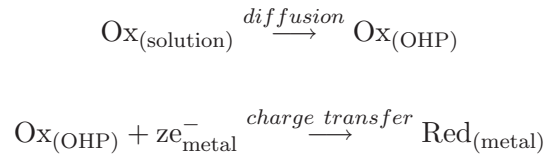
The reaction rate for the forward direction (reduction) is determined according to the chemical kinetic theory as:

$$\overrightarrow{v}_0 = \overrightarrow{k} \cdot c_{ox} \cdot \exp\left(-\frac{\overrightarrow{E}'_A}{RT}\right) \tag{2.98}$$

where C_{Ox} is the concentration of the reacting species, $\overrightarrow{E}'_A$ is the activation energy of the reaction, assuming no externally applied potential difference between the electrode and the electrolyte. R is the gas constant and T is the

temperature in Kelvin. $\overrightarrow{k}$ is a constant, defined as:

$$\overrightarrow{k} = \aleph \frac{kT}{h} \tag{2.99}$$

here h - is the Plank constant, $\aleph$ is a transmission coefficient, representing the probability of charge transmittance, k is the Boltzmann constant. Analogously we define the rate of the same reaction in the reverse (oxidation) direction:

$$\overleftarrow{v}_0 = \overleftarrow{k} \cdot c_{\text{red}} \cdot \exp\left(-\frac{\overleftarrow{E}'_{\text{A}}}{RT}\right) \tag{2.100}$$

Further we assume we charge negatively the electrode. The applied potential difference enhance the rate of reduction and lowers the rate of oxidation reaction.

In fig.2.13 the applied potential shifts the initial potential energy curve 2 vertically by $zF\varphi$ to the new position 2a. The shift also changes the intercept point with curve 1 (from point A to point B). As a result the activation energy of the reduction process changes from $\overrightarrow{E}'_A$ to $\overrightarrow{E}_A$ and is defined as:

$$\overrightarrow{E}_A = \overrightarrow{E}'_A - \alpha zF\varphi \tag{2.101}$$

For the oxidation the expression is:

$$\overleftarrow{E}_A = \overleftarrow{E}'_A + zF\varphi - \alpha zF\varphi = \overleftarrow{E}'_A + (1-\alpha)zF\varphi \tag{2.102}$$

The term α is defined as "transfer coefficient" and depends on the shape of the potential curves. It represents this part of the applied potential energy, used in the charge transfer in the forward, respectively for $(1-\alpha)$ in the backward reaction or we can write: $\alpha = \frac{change\ in\ activation\ energy}{change\ in\ potential}$. The transfer coefficient (firstly introduced by Volmer [63] *as symmetry factor*) can also be understand as a change in the geometrical position (in the double layer) of the intercept point (the energetic maximum) of the potential curves.

It follows that every change in the energetic conditions of the charge transfer reflects in a change of the geometrical coordinates of the maximum (situated between the planes in the Helmholz part of the EDL). In the case as presented in fig.2.13 the applied potential shifts the maximum into the direction of the electrolyte. It corresponds to a lower activation energy for the forward (reduction) and a higher activation energy for the backward (oxidation) reaction.

Equations 2.101 and 2.102 are further transformed assuming that the Galvani-potential (φ) can be expressed in terms of the electrode potential ε (measured versus a given reference scale) plus a constant Const., depending on the choice of the reference electrode ($\varphi = E + Const.$):

$$\overrightarrow{E}_A = \overrightarrow{E}'_A - \alpha zF \cdot Const. - \alpha zFE \tag{2.103}$$

or

$$\overrightarrow{E}'_A = \underbrace{\overrightarrow{E}_A + \alpha zF \cdot Const.}_{\overrightarrow{E}} + \alpha zFE \tag{2.104}$$

and for the oxidation process we obtain:

$$\overleftarrow{E}_A = \overleftarrow{E}'_A + (1-\alpha)zF \cdot Const. + (1-\alpha)zFE \tag{2.105}$$

or

$$\overleftarrow{E}'_A = \underbrace{\overleftarrow{E}_A - (1-\alpha)zF \cdot Const.}_{\overleftarrow{E}} - (1-\alpha)zFE \tag{2.106}$$

Substituting equations 2.104 and 2.106 in equations 2.98 and 2.100 we obtain:

$$\overrightarrow{v} = \overrightarrow{k} \cdot c_{ox} \cdot \exp\left(-\frac{\overrightarrow{E} + \alpha zFE}{RT}\right) \tag{2.107}$$

$$\overleftarrow{v} = \overleftarrow{k} \cdot c_{red} \cdot \exp\left(-\frac{\overleftarrow{E} - (1-\alpha)zFE}{RT}\right) \tag{2.108}$$

It is well known that the rate of any chemical reaction can be expressed by the charge passed through the system: $v = i/zF$, where i is the current density. Combining this expression with the rate constants $\overrightarrow{k}$ and $\overleftarrow{k}$ together with the first part of the exponential term: $\exp\left(-\frac{\overrightarrow{E}}{RT}\right)$, respectively $\exp\left(-\frac{\overleftarrow{E}}{RT}\right)$ in k_1 and k_2 one obtains the reaction rate in electric units:

$$\overrightarrow{i} = zFk_1 c_{ox} \cdot \exp\left(-\frac{\alpha zF}{RT}E\right) \tag{2.109}$$

$$\overleftarrow{i} = zFk_2 c_{red} \cdot \exp\left(\frac{(1-\alpha)zF}{RT}E\right) \tag{2.110}$$

On the other hand the potential ε at given current can be presented as a sum of an equilibrium potential ε_r and the polarization $\Delta\varepsilon$ ($E = E_r + \Delta E$ or $\Delta E = $

$\varepsilon - \varepsilon_r$). ΔE is commonly known as the overpotential (or overvoltage) and is typically denoted as η. After substitution of the latter in equations 2.109 and 2.110 we can finally derive:

$$\overrightarrow{i} = zFk_1c_{ox} \cdot \exp\left(-\frac{\alpha zFE_r + \alpha zF\eta}{RT}\right) \tag{2.111}$$

$$\overleftarrow{i} = zFk_2c_{red} \cdot \exp\left(\frac{(1-\alpha)zFE_r + (1-\alpha)zF\eta}{RT}\right) \tag{2.112}$$

We rearrange equations 2.111 and 2.112 assuming that:

$$\overrightarrow{i}_0 = zFk_1c_{ox} \cdot \exp\left(-\frac{\alpha zF}{RT}E_r\right) \tag{2.113}$$

and

$$\overleftarrow{i}_0 = zFk_2c_{red} \cdot \exp\left(\frac{(1-\alpha)zF}{RT}E_r\right) \tag{2.114}$$

where i_0 is an important electrochemical characteristic - the exchange current and is defined as the current at $\eta = 0$:

At equilibrium $E = E_r$ and respectively the sum of electrical current in both directions is zero, it follows that $\overrightarrow{i}_0 = \overleftarrow{i}_0$ respectively $\overrightarrow{i} = \overleftarrow{i}$, so that the total current of the system equals zero. The latter does not mean that $\overrightarrow{i}$ or $\overleftarrow{i}$ are zero, but their sum is zero. Assuming positive currents for the oxidation and negative currents for the reduction processes the total current is given as:

$$i = \overleftarrow{i} - \overrightarrow{i} = \overrightarrow{i}_0 \cdot \exp\left(-\frac{\alpha zF}{RT}\eta\right) - \overleftarrow{i}_0 \cdot \exp\left(\frac{(1-\alpha)nF}{RT}\eta\right) \tag{2.115}$$

or:

$$i = \overleftarrow{i} - \overrightarrow{i} = i_0 \left[\exp\left(\frac{(1-\alpha)nF}{RT}\eta\right) - \exp\left(-\frac{\alpha zF}{RT}\eta\right)\right] \tag{2.116}$$

Equation 2.116 is known as the Butler-Volmer equation and describes the current dependence on the applied potential. It is a general equation of the charge transfer theory and is valid for all cases of electrochemical reactions, where the effect of the double layer structure can be neglected.

Three limiting cases can be considered:

1. If the applied net current is zero ($i = 0$), it follows that $\overrightarrow{i} = \overleftarrow{i}$, the overvoltage is also zero ($\eta = 0$). In this case from the Butler-Volmer equation can directly be derived the Nernst equation.

2. If $i \neq 0$ and $|\eta| \gg RT/F$. Assuming $\overrightarrow{i} \gg \overleftarrow{i}$ the cathodic current dominates and the first term of eq. 2.116 can be neglected and we obtain:

$$i = \overrightarrow{i} \cong i_0 \cdot \exp\left(-\frac{\alpha z F}{RT}\eta\right) \tag{2.117}$$

If we solve this equation with respect to η we obtain the well known Tafel equation:

$$\eta = \underbrace{\frac{RT}{\alpha z F}\ln i_0}_{a} - \underbrace{\frac{RT}{\alpha z F}}_{b}\ln i = a + b\ln i \tag{2.118}$$

The coefficient b is used to determine the transfer coefficient α, which is characteristic for the symmetry of the energy barrier of the charge transfer. The coefficient a includes in addition the term of the exchange current i_0, which characterizes the catalytic activity of the electrode material.

3. If $i \neq 0$ and $|\eta| \ll RT/F$ (close to equilibrium). In this case both cathodic and anodic terms have to be taken into account. Assuming that the charge transfer coefficient α has a constant value of 0.5, we can express the equation by the function $\sinh[x] = \frac{e^x - e^{-x}}{2}$. One can rewrite eq. 2.116 as:

$$i = 2i_0 \cdot \sinh\left[\frac{zF\eta}{2RT}\right] \tag{2.119}$$

Under the conditions of very small deviations from equilibrium ($\eta \ll \frac{RT}{F}$) we can approximate that $\sinh[\frac{zF}{RT}\eta] \cong \frac{zF}{RT}\eta$. The latter results to:

$$i = \frac{i_0 z F}{RT}\ \eta = \frac{1}{R_p}\ \eta \tag{2.120}$$

where $\frac{RT}{i_0 z F}$ is often denoted as polarisation resistance (R_p) in analogy with the Ohm's law.

The Butler-Volmer equation has been applied numerous electrochemical processes (metal deposition, corrosion etc.), but it has also some disadvantages:

1. It applies only to a single charge transfer step. Thus, all involved electrons have to be transferred in a single act.

2. The equation neglects and thus cannot describe or predict the effect of the electrolyte (attractive or repulsive interactions between the reacting species and the surrounding environment) on the charge transfer process.

3. The equation cannot explain the effects of the structure of the electrical double layer on the kinetics of the processes.

4. It does not include the dependence of the transfer coefficient α on the overvoltage (η).

The Butler-Volmer equation had been modified for more complicated cases taking into account the double layer effects (Frumkin correction) or for the case that both charge transfer kinetics and diffusion control the overall reaction rate. The microscopic theory developed by Marcus predicts well the dependence of the transfer coefficient on the overpotential. A detailed analysis of these special cases is given in ref. [66, 67]. The general charge transfer theory was continuously developed and adapted to cases where more than one electron exchange step is present, as shown in the following.

2.6.2 Multi-step charge transfer

Many electrode processes involve an exchange of more than one electron, transferred in more than one elementary act (multi-step transfer). This problem is not concerned by the Butler-Volmer equation and requires a more advanced formal concept. Lets assume an electrochemical reaction $(\mathrm{Ox} + \mathrm{ze}^- = \mathrm{Red})$ consists of n single electron exchange steps:

$$
\begin{array}{cccccc}
\mathrm{Ox} & + & \mathrm{e}^- & \xrightarrow{i_1} & \mathrm{R}_1 & (\text{Step 1}) \\
\mathrm{R}_1 & + & \mathrm{e}^- & \xrightarrow{i_2} & \mathrm{R}_2 & (\text{Step 2}) \\
\ldots\ldots & \ldots\ldots & \ldots\ldots & \ldots\ldots & \ldots\ldots & \ldots\ldots \\
\mathrm{R}_x & + & \mathrm{e}^- & \xrightarrow{i_n} & \mathrm{Red} & (\text{Step n})
\end{array}
$$
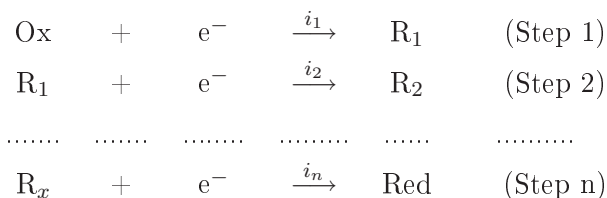
Each step is characterized by its own reaction rate i.e. current (i), overvoltage (η) and according to eq. 2.120 its polarization resistance (R_p) if near to equilibrium $(|\eta| \ll RT/F)$. When a steady state condition is reached the concentration of intermediates do not change with the time, and the current, overvoltage, and polarization resistance of the individual steps are equal: $(i_1 = i_2 \ldots = i_n); (\eta_1 = \eta_2 \ldots = \eta_n); (R_{p1} = R_{p2} \ldots = R_{pn})$. In the case of equal rate of all the individ-

ual steps near to equilibrium the average current $\bar{i}$ is defined with the equation:

$$\bar{i} = \frac{\sum\limits_{i=1}^{n} \eta_i}{\sum\limits_{i=1}^{n} R_{pi}} \tag{2.121}$$

Respectively $\frac{\eta_1}{R_{p1}} = \frac{\eta_2}{R_{p2}} \dots = \frac{\eta_n}{R_{pn}}$. However the individual steps are concerned as parallel to each other as the electrons flow through the interface. Thus, the current of the overall redox reaction is defined as a sum of all the individual stages or $i_{\text{total}} = i_1 + i_2 + \dots + i_n = n\bar{i}$. Substituting the latter in eq. 2.121 the current of the overall reaction near to equilibrium is:

$$i_{\text{total}} = \frac{\sum\limits_{i=1}^{n} \eta_i}{n \sum\limits_{i=1}^{n} R_{pi}} \tag{2.122}$$

If the polarization resistance of one of the steps (let assume step m, where m $1 < m < n$) is much higher than those for any from the other steps ($R_{pm} \gg R_{pn}$ $[n \neq m]$) than we can safely assume:

$$\sum\limits_{i=1}^{n} R_{pi} = R_{p1} + R_{p2} + \dots R_{pn} \approx R_{pm} \tag{2.123}$$

Respectively the overpotential of the slower step (for systems either far or near to equilibrium) will be much higher than the others ($\eta_m \gg \eta_n$ $[m \neq n]$) and thus determines the overpotential, respectively the current (i.e. the reaction rate) of the total reaction ($\eta_{reaction} \approx \eta_m$) because all other individual terms become insignificant. In this case equation 2.122 changes to:

$$i_{\text{total}} = \frac{\eta_m}{n R_{pm}} \tag{2.124}$$

The reaction rate of step m will control the rate of the overall reaction and respectively the current $i = n i_m$ and since $i_m = \overrightarrow{i}_m - \overleftarrow{i}_m$ the total current is $i = n(\overrightarrow{i}_m - \overleftarrow{i}_m)$.

The step controlling the rate of one multi-step reaction is denoted as rate determining step (RDS). All other reaction steps are considered as reversible (diffusion controlled), very near to individual stage equilibrium and according to the first sequence of Butler-Volmer equation (see page 46) the dependance of the concentration of the reacting species on the potential can be described by the

Nernst equation. At applied potential E the concentration of the intermediate species R_1 (see eq.2.6.2) is given by:

$$E = E_1^\circ + \frac{RT}{F} \ln \frac{c_{ox}}{c_{r_1}} \tag{2.125}$$

or

$$c_{r_1} = \underbrace{\exp\left(\frac{F}{RT} \cdot E_1^\circ\right)}_{k_1} \cdot c_{ox} \cdot \exp\left(-\frac{F}{RT} \cdot E\right) \tag{2.126}$$

where E_1° is the standard half cell potential of the couple $[\mathrm{ox}/\mathrm{r}_1]$ and k_1 is constant at given temperature. Respectively the concentration of the species r_2 is defined as:

$$c_{r_2} = k_2 \cdot c_{r_1} \cdot \exp\left(-\frac{F}{RT} \cdot E\right) \tag{2.127}$$

or

$$c_{r_2} = k_1 \cdot k_2 \cdot c_{ox} \cdot \exp\left(-\frac{F}{RT} \cdot 2E\right) \tag{2.128}$$

Thus the concentration of species of the step before the rate determining step is defined:

$$c_m = k_m \cdot c_{m-1} \cdot \exp\left(-\frac{F}{RT}\, E\right) = \prod_{i=1}^{m} k_i \cdot c_{ox} \cdot \exp\left(-\frac{F}{RT}\, mE\right) \tag{2.129}$$

as m steps are involved. The rate determining step is far from equilibrium (irreversible process controlled by the electron(s) transfer) and obeys the Butler-Volmer equation. For the cathodic reaction (see eq. 2.111) it is written as:

$$\overrightarrow{i}_{RDS} = k_m \overrightarrow{k}\, c_m \cdot \exp\left(-\frac{\alpha F}{RT}\, \eta\right) = \prod_{i=1}^{m} k_i \overrightarrow{k}\, c_{ox} \cdot \exp\left(-\frac{(m+\alpha)F}{RT}\, \eta\right) \tag{2.130}$$

and for the backward reaction(oxidation)the equation takes the form:

$$\overleftarrow{i}_{RDS} = \prod_{i=m+1}^{n} k_i \overleftarrow{k}\, c_{red} \cdot \exp\left(\frac{(n-m-\alpha)F}{RT}\, \eta\right) \tag{2.131}$$

Because the rate of the overall reaction is determined only by the RDS the experimental i/η dependance will also follow eq. 2.116:

$$i = i_0 \left[\exp\left(\frac{(n-m-\alpha)F}{RT}\, \eta\right) - \exp\left(-\frac{(m+\alpha)F}{RT}\, \eta\right)\right] \tag{2.132}$$

Additionally we formulate the most important criteria for a multi-step reaction:

1. The sum of the transfer coefficients for the cathodic and the anodic reaction $\alpha + (1 - \alpha)$ differs from 1 in case that multi-step process controlled by the charge transfer is present.

2. More than one Tafel slope can appear on $\eta/\ln i$ plot. The latter suggests either that the reaction mechanism changes depending on the overpotential or that more than one charge transfer steps with approximately equal currents are present.

3. On the potentiodynamic i/E curves (cyclovoltammetry, linear sweep voltammetry, polarography) it is possible to detect the individual peaks characterizing the different intermediate steps.

It is of theoretical interest but also from a practical importance to determine the mechanism and the rate determining step(s) of one particular chemical/electrochemical reaction. One of the possible ways to do it is to determine the stoichiometric number of the reaction.

2.6.3 The concept of stoichiometric number

The concept of the stoichiometric number was originally introduced by Horiuti and Ikusima [68] in 1939 and further developed by Horiuti [69,70], Riddiford [71], Ehrenburg [72,73], Losev [74–76], Parsons [77], Frumkin [78], Krishtalik [79] and Bockris [67,80]. It has been successfully applied to different systems in catalysis, but also in electrochemical studies, e.g. in ammonia synthesis, oxygen reaction, hydrogen evolution etc. [70,81–83]. It was recently applied by Athanasiou et. al and Wang et. al [84,85] in their study on the mechanism of the oxygen reaction at palladium/LSM electrodes on YSZ electrolyte. The theory was originally derived by the authors during the studies on different possible mechanism of the simple hydrogen reaction: $H_2 + 2e^- = H_2$. The experiments were performed with deuterium ions as a tracers in order to compare the results from the electrochemical measurements with the isotope analysis. Thus they confirmed that to create a hydrogen molecule (H_2) the reaction $H + e^- = H$ should proceed twice. Thus Horiuti defined the stoichiometric number as the number of steps to occur for every act of a complete chemical/electrochemical reaction. It is suggested, that each reaction can proceed (but not necessarily) via different routes, involving the creation and consumption of different intermediates. The lifetime of the intermediates can be shorter or longer, but in the steady state their concentration is constant. The total sum of all intermediates created in all

possible routes and steps equals zero, as the intermediates itself are not a final product.

Within the concept of the stoichiometric number the steady state condition of a single route reaction is expressed as:

$$n_i = \sum_{s=1}^{S} \nu_{s,i} b_{s,i} = 0 \qquad i = 1........I \qquad (2.133)$$

Here S denotes the total number of reaction steps, and I is the number of different independent intermediates. Then n_i is the total number of intermediate i created in all S steps, $b_{s,i}$ is the stoichiometric coefficient of intermediate i in step s, and $\nu_{s,i}$ is the number of times of step s to occur within the total process. To define a certain mechanism we firstly formulate a set of chemical equations for the possible elementary reaction steps involving the intermediate species. By applying the steady state condition (eq. 2.133) to the possible reaction routes one can determine the number of alternative solutions corresponding to independent pathways. P is the number of the independent reaction mechanisms:

$$P = S - I \qquad (2.134)$$

Let us consider the hydrogen electrode reaction as an example. Three equations describe the possible reaction routes:

1. $H^+ + e^- = H_{ad}$

2. $H_{ad} + H_{ad} = H_2$

3. $H^+ + H_{ad} + e^- = H_2$

The steady state condition can be formulate as defined in eq. 2.133. As we have only one intermediate species we can neglect the index i. In the first step (1) the stoichiometric coefficient of the intermediate (H_{ad}) is $b_1 = 1$. In reaction (2) the stoichiometric coefficient of the intermediate is $b_2 = -2$. In the third reaction the number of the intermediate is $b_3 = -1$. The steady state condition results as:

$$\nu_1 - 2 \cdot \nu_2 - \nu_3 = 0$$

The number of involved reaction steps is $S = 3$; the number of intermediates is $I = 1$ and it follows for the number of independent solutions $P = 2$. The solutions require a certain sequence of steps to occur in order to obtain the final product of the reaction. The possible independent solutions are $\{\nu_1 = 1; \nu_2 = 0; \nu_3 = 1\}$ and $\{\nu_1 = 2; \nu_2 = 1; \nu_3 = 0\}$. The solutions can also be represented as vectors with the following coordinates: $K^1 \equiv (1, 0, 1)$ and $K^2 \equiv (2, 1, 0)$, corresponding to the reaction mechanisms:

| H$^+$ | + | | e$^-$ | = | H$_{ad}$ | | 2H$^+$ | + | 2e$^-$ | = | 2H$_{ad}$ |
| H$^+$ | + | H$_{ad}$ | + e$^-$ | = | H$_2$ | | 2H$_{ad}$ | | | = | 2H$_2$ |

We can apply any linear mathematical operation for these vectors and the results will satisfy the requirements of eq. 2.133, as for example (2,0,2), (4,2,0) or $(\frac{1}{2}, 0, \frac{1}{2})$. The selection of a certain route or set of consecutive steps as a mechanism of the reaction has to be based on additional experimental or theoretical knowledge on the intermediate steps. Without such additional information no mechanism can be ruled out.

Further we can denote the stoichiometric number of a single step "s" in the route "r" by $\nu^r_{s,i}$ as suggested by Horiuti [70] and modify eq. 2.133:

$$\sum_{s=1}^{S} b_{s,i} \nu^r_{s,i} = 0 \qquad i = 1.....I, \quad r = 1.....R \qquad (2.135)$$

The progress of the reaction via certain route can be characterized by the reaction rate V^r specific for each route. Then the reaction rate of the step "s" is formulated as:

$$V_s = \sum_{r=1}^{R} \nu^r_{s,i} V^r \qquad i = 1.....I, \quad s = 1.....S \qquad (2.136)$$

V_s is the net rate of step "s" and V^r is the net rate through route "r".

Concerning a single step of the route in the terms of the generalized statistical mechanical theory of rate [69] one can denote as $(In_{s,i})$, $(*)$, and $(F_{s,i})$ the initial, critical, and final particular state respectively of set of particles (intermediates) of sort i. Their chemical potential (μ_i) is different and thus resulting in a free enthalpy decrease $(\Delta G_s = \mu_s^{In} - \mu_s^F)$ passing from the initial to the final state. The total Gibbs energy decrease in the step "s" in route r will be:

$$-\Delta G^r_i = -\sum_{s=1}^{S} \nu^r_{s,i} \Delta G^r_{s,i} \qquad r = 1.....R \qquad (2.137)$$

It is further assumed that if the rate of a single reaction step s in route r is much slower than all others (i.e. it is the rate determining step) the overall reaction reaction rate is determined by this step, t.e. direction $(V_s^r = V)$, or according to eq. 2.136 it follows that $\nu_s^r \ V^r = V$. We can also rewrite this equation by $V = i/zF$, and as an end result we obtain the result as derived by Horiuti [70]:

$$\nu(\alpha_c + \alpha_a) = n \tag{2.138}$$

where ν is the stoichiometric number, n is the number of exchanged electrons, α_c is defined as $(\alpha_c = -\frac{RT}{F}\frac{\partial \ln \overrightarrow{i}}{\partial \ln \eta})$ and α_a as $(\alpha_a = \frac{RT}{F}\frac{\partial \ln \overleftarrow{i}}{\partial \ln \eta})$. α_c and α_a are also often denoted as *apparent transfer coefficients*. Combining the classical Butler-Volmer equation 2.116 with equation 2.138 we derive the form of the charge transfer equation often used in the electrochemical analysis of the mechanism of the reactions:

$$i = i_0(e^{\frac{\alpha_a F}{RT}\eta} - e^{-\frac{\alpha_c F}{RT}\eta}) \tag{2.139}$$

The theory was further developed especially for the case when the reaction rate of a single route reaction, consists of more then two intermediate steps, is determined by one of them - the rate determining step (further denoted as RDS). [66,80]. The set of reaction steps is formulated as:

$$
\left.
\begin{aligned}
Ox \quad &+ e^- = R_1 \\
R_1 \quad &+ e^- = R_2 \\
&\dots\dots \\
&\dots\dots \\
R_{m-1} &+ e^- = R_m
\end{aligned}
\right\} m \ steps \ before \ RDS
$$

$$
\nu(R_m + e^- = R_{m+1}) \ \left.\right\} RDS \ repeated \ \nu \ times
$$

$$
\left.
\begin{aligned}
R_{m+1} &+ e^- = R_{m+2} \\
&\dots\dots \\
&\dots\dots \\
R_{n-1} &+ e^- = \ R_n
\end{aligned}
\right\} (n - m - \nu) \ steps \ after \ RDS
$$
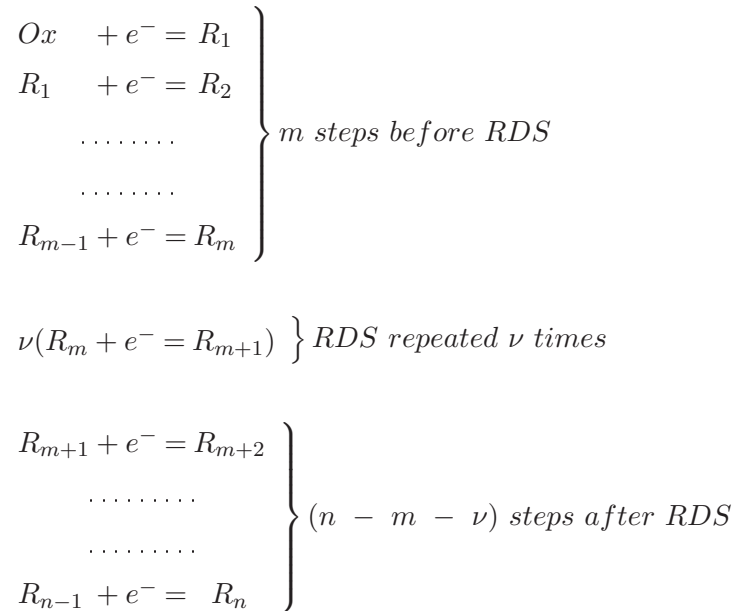
According to the charge transfer theory for a multi-step processes (see page 48) the concentration of the species c_m is given according to the Nernst equation

by:

$$c_m^{\nu} = k_m \cdot c_{m-1} \cdot \exp\left(-\frac{F}{RT}\,E\right) = \prod_{i=1}^{m} k_i \cdot c_{ox} \cdot \exp\left(-\frac{F}{RT}\,mE\right) \quad (2.140)$$

The concentration is raised to ν^{th} power, because the RDS is repeated ν - times. The Butler-Volmer equation for the current voltage dependance of the rate determining step involving only a single electron transfer takes in this case the form:

$$\overrightarrow{i}_{RDS} = \overrightarrow{k}\,c_m \cdot \exp\left(-\frac{\alpha F}{RT}\,\eta\right) = \overrightarrow{k} \cdot K^{\frac{1}{\nu}} c_{ox}^{\;\frac{1}{\nu}} \cdot \exp\left(-\frac{(\frac{m}{\nu}+\alpha)F}{RT}\,\eta\right) \quad (2.141)$$

where $K = \prod_{i=1}^{m} k_i$.

For the backward reaction (oxidation) the equation has the form:

$$\overleftarrow{i}_{RDS} = \overleftarrow{k}\left(\prod_{i=m+1}^{n} k_i\right)^{\frac{1}{\nu}} c_{red}^{\;\frac{1}{\nu}} \cdot \exp\left(\frac{(\frac{n-m}{\nu}-\alpha)F}{RT}\,\eta\right) \quad (2.142)$$

The coefficients $\left(\frac{m}{\nu}+\alpha\right)$ and $\left(\frac{n-m}{\nu}-\alpha\right)$ are exactly the same coefficients α_c and α_a as defined in equation 2.138. Thus the Tafel equation 2.118 is modified to:

$$\eta = \frac{RT}{\alpha_c F}\ln i_0 - \frac{RT}{\alpha_c F}\ln i \quad (2.143)$$

$$\eta = -\frac{RT}{\alpha_a F}\ln i_0 + \frac{RT}{\alpha_a F}\ln i \quad (2.144)$$

for the reduction and oxidation processes respectively. Evaluating the Tafel slope for one multi-step reaction we determine not the transfer coefficients α or $1-\alpha$ but the apparent transfer coefficients α_c and α_a.

In order to determine the mechanism of one electrochemical multi-step reaction one should proceed via following steps:

1. According to equations 2.133 and 2.134 to evaluate the most probable routes that the particular reaction could follow.

2. According to equation 2.138 (after we determine the apparent transfer coefficients from the experiment) we can easily calculate the stoichiometric number ν if the total number of exchanged electrons n is known.

3. As an additional further criterium serves the relation:

$$\frac{\alpha_c}{\alpha_a} = \frac{m + \alpha}{n - m - \alpha} \tag{2.145}$$

According to this equation, assuming that usally $\alpha_{RDS} \approx 0.5$ we can calculate the number of steps before and after the RDS and accordingly to complete the evaluation of mechanism of the reaction.

Of course there exist much more complicated electrochemical reactions where the number of electrons transferred in RDS is different as 1 ($n \geq 2$). In this cases the apparent transfer coefficients are defined as $\alpha_c = (\frac{m}{\nu} + n\alpha)$ and $\alpha_a = (\frac{m-n}{\nu} - n\alpha)$, where n is the number of electrons transferred in RDS.

In some reactions there also could exist two or more irreversible steps each having a comparable rate. Then each partial reaction is characterized by its own apparent transfer coefficient and exchange current. In this case the Butler-Volmer equation has much more complicated form and the analysis of $\ln i/\eta$ plots requires additional experiments and/or involves other methods of detecting and quantifying the intermediate species [71, 73–76]

Applying properly the concept of stoichiometric number we can determine the mechanism of certain electrochemical reaction. This method is often used for kinetic studies in electrochemistry and in chemical catalysis.

3 Experimental techniques and equipment

3.1 Experimental methods for preparation and characterization

3.1.1 Pulsed laser deposition (PLD)

The ongoing miniaturization in modern technology requires more and more precision of the dimension control during the deposition process and nowadays many materials are typically of micro- or of nanometer size. In thin film technology the thickness of a single layer varies typically from 10 μm down to approximately 20 nm. One of the most flexible thin film deposition techniques is the pulsed laser deposition (PLD). It is conceptually very simple: pulsed laser radiation (in UV range) hits the surface of certain material (the target). The material absorbs the photon energy, vaporizes and "explodes" in the form of a thermal plasma cloud reaching the substrate surface, forming a thin layer on it. A simple schematic presentation is shown in figure 3.1. The photon source is typically an eximer laser with a wavelength varying between 196 nm (ArF source) and 308 nm (XeF), but sometimes TEA-CO_2 lasers or Nd-YAG lasers are also used. The pulse duration is typical 10 ns to 20 ns. The repetition rate can vary from 1 Hz up to 50 Hz. The deposited films are usually crystalline and have an orientation relationship to the substrate. The properties of the layers prepared via PLD depend strongly on the deposition conditions. The crystallinity and sometimes the size of the grains depend on the *substrate temperature*. The higher the temperature the higher is the surface diffusivity, and thus the possibility for obtaining a high quality crystalline structure. However
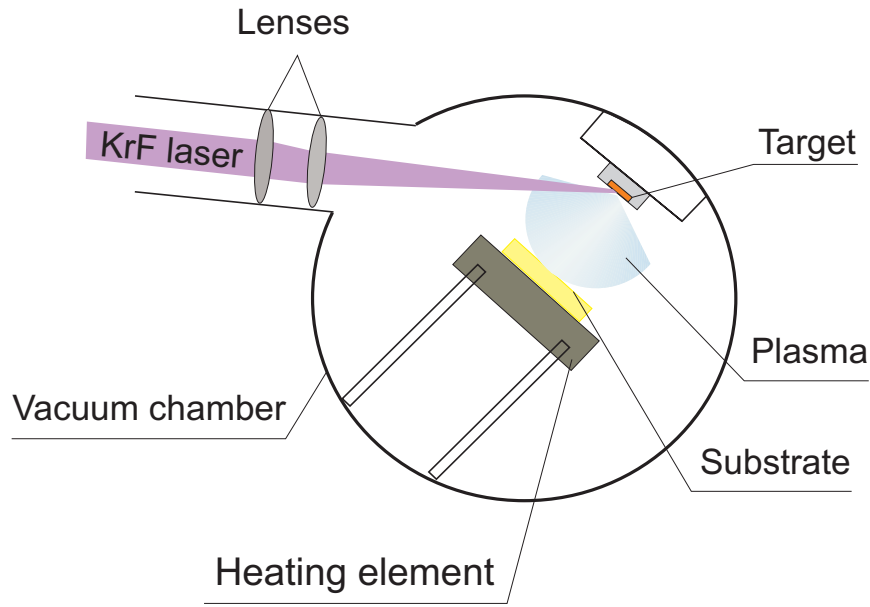
Fig. 3.1: Schematic presentation of the design of pulsed laser deposition chamber

the deposition rate is lowered by re-evaporation in the case of higher substrate temperatures.

The distance between the target and the substrate also influences the surface morphology and the layer structure. If the distance is too large the particles in the plasma cloud loose kinetic energy and can agglomerate resulting in porous, droplet-containing films. Additionally, because of the loss in kinetic energy the particles cannot move or rearrange on the substrate surface.

The gas ambient (background gas) plays an important role in the deposition process. For example, the deposition of oxides in argon atmosphere leads to more or less reduced films with a non-stoichiometric oxygen content. Reactive gases as hydrogen, oxygen, nitric oxides or even nitrogen are activated due to their interaction with the plasma and may be incorporated in the layer.

The gas pressure is also an important parameter influencing (enhancing) the rate of incorporation of molecules or ions from the gas phase into the films. On the other hand exceeding certain pressure results in a fast particle segregation, respectively in a poor film quality.

The density of the target is another important requirement for obtaining

high quality films. As the UV radiation vaporizes only the first atomic layers the photon energy is not equally dispersed only on the surface but also in the near subsurface layers. Thus, the plasma explosion creates cavities in the target material and forms larger particles (droplets). These droplets may be deposited on the substrate and lower the quality of the growing film.

As a broad variety of inorganic materials absorb in the UV range, the pulsed laser deposition is applied to the preparation of thin films of many oxides, nitrides, carbides and metals (excluded are only materials with a band gap larger than the wavelength of the laser which cannot absorb the photon energy). The PLD technique ensures a good adhesion, orientational growth (certain materials but not necessarily), flat structure and morphology repeating the surface morphology of the substrate.

The most serious disadvantage is that it cannot be used to cover large surfaces. Typically the area of the deposited film with a homogeneous thickness is limited to about 1 square centimeter. With some modifications this area can be enlarged to 5 cm^2 or even 10 cm^2 but not more. The latter limits the industrial application of this method. The film thickness is also limited to approximately 5 μm, otherwise the deposition time becomes too long. Also the deposition of thicker films results in an increasing amount of droplets. Additionally the droplets grow faster (because of geometric reasons) than the film, resulting in a poor quality of the films prepared at longer deposition times. The growth rate of approximately 1 μm/h is also relatively low compared with rates typical for other thin film techniques (CVD, PVD, magnetron sputtering etc.). A detailed description of the principles of the PLD technique and further applications are given in [86,87].

For our experiments a KrF excimer laser (Lambda Physik, Germany, wavelength $\lambda = 248$ nm, pulse duration $\tau = 25$ ns) with an energy of 200 mJ was used for the ablation process in a high vacuum chamber. The evaporated species were deposited onto the substrates fixed at a distance of approx. 4 cm from the target surface. The deposition was carried out typically for 180 min and the substrate temperature was maintained at 500 ℃. The thickness of the films was then approximately 3 μm. Films were deposited in either an oxygen or an argon atmosphere at a pressure of 4 Pa and in nitrogen atmospheres varying from 2

Pa to 8 Pa.

3.1.2 Characterization of the samples

YSZ thin films prepared by PLD in different gas atmospheres as well single crystalline samples have been analyzed by SIMS, XPS, UPS, AFM and HRSEM as surface sensitive methods in order to characterize their surface morphology, chemical composition and nitrogen content and also to detect locally nitrogen incorporated during electrochemical experiments with micro-electrodes. X-ray diffraction and optical spectroscopy as volume sensitive methods complete the set of characterization techniques. In the following sections we briefly summarize the basic principles and the quality of information we obtain from these methods.

Time-of-Flight Secondary Ion Mass Spectrometry (ToF-SIMS)

ToF-SIMS is a powerful technique for obtaining elemental information on the surfaces and near-surface regions of vacuum-compatible solids. It is often applied to the determination of concentration profiles, surface (ion mapping) and depth distribution of elements, tracer diffusion experiments and local changes in the chemical composition. The resolution of this method is in the nanometer range and only the Auger spectroscopy provides more detailed and laterally resolved information. SIMS is capable of detecting all elements, of differentiating between isotopes and of determining concentrations over a wide range, in most cases down to the ppm level. It provides chemical information as a function of both vertical and horizontal coordinates. The basic principles of the SIMS analysis are schematically presented in figure 3.2. The surface of the sample being analyzed is bombarded by primary ions (in the present case Ga^+ ions) of kinetic energy up to 25 keV. The primary ions penetrate the sample to a depth of approximately 10 nm (at 10 keV) and cause the ejection (sputtering) of material from the sample surface. The sputtered secondaries are neutral or charged clusters with kinetic energies in the order of 10 eV. By bombarding the sample its surface is charged by the primary ions which is compensated by an electron source. Secondary ions that are generated by a pulse of gallium ions are extracted perpendicular to the sample surface with an electrical potential of 2 kV. The ions of given
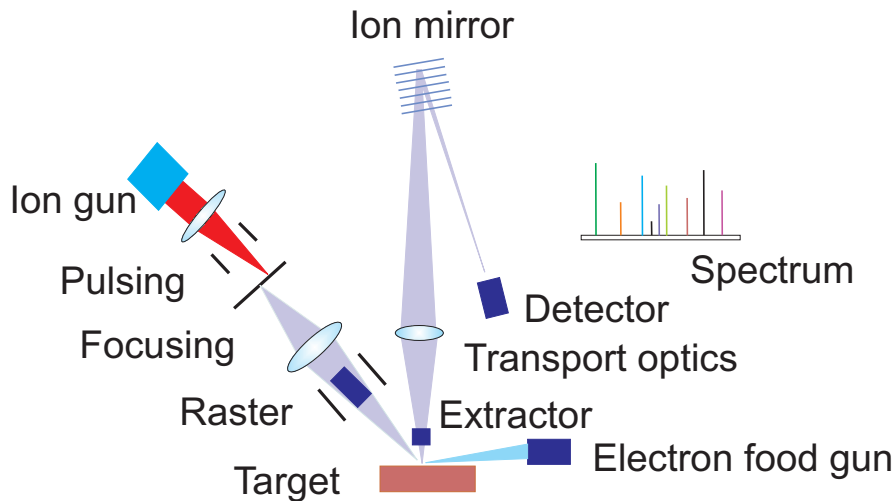
Fig. 3.2: Schematic presentation of the SIMS analysis (adapted from ION-TOF GmbH)

mass/charge ratio are separated according to their velocity. Secondary ions, even of the same type, are emitted, however, with a range of energies, and hence, after extraction they possess a range of velocities. The ion mirror (an electrostatic mirror) compensates to a first order for this spread of velocities: ions with slightly higher velocities penetrate further into the field than the slower ions, with the result that ions of the same mass but different energies arrive at the detector at the same time. Arriving at the detector, the secondary ions are counted and their arrival times are recorded. In this way a complete mass spectrum is acquired for every scan. The recorded spectra can be presented either as an intensity of a particular mass signal as a function of time (depth profile) or as an ion map of the surface (secondary ion image). The particles reaching the detector do not carry any information about the chemical bonds or valence state of the ions from the matrix. As a simple particular example: we usually analyze the ZrN secondaries to determine the nitrogen concentration in YSZ:N but this doesn't mean that we determine ZrN as chemical composition.

In ToF-SIMS the surface must also be sputtered (in the present case by Cs^+ ions) to obtain the depth distribution of the elements. The sputter rate depends on the source but has usually a value of about 1 μm per hour. The major problem of SIMS is to calculate the concentrations of elements from the intensity of their mass signal. For this purpose we need a calibration standard of known

concentration. Such standards are not universal and are specified only for a particular chemical composition and matrix. More detailed descriptions of SIMS and its application in tracer diffusion studies can be found in [88–90].

Our samples were analyzed by time-of-flight secondary ion mass spectrometry (ToF-SIMS IV, ION-ToF, Muenster, Germany), in the following abbreviated simply as SIMS, with the following typical parameters: a beam of Ga^+ ions with an energy of 25 keV, rastered over 100 μm $\times$ 100 μm, was used to generate secondary ions for the analysis ($I_{Ga} = 1$ pA). Sputter etching of the surface was carried out with a beam of Cs^+ ions of energy of 2 keV, rastered over 300 μm $\times$ 300 μm ($I_{Cs} = 150$ nA). The charge compensation was achieved by flooding the surface with electrons ($I_e > 1$ μA) of energies less than 20 eV. We quantified the nitrogen concentrations in our thin films by comparing the intensity ratios I ($^{90}Zr^{14}N^-$) / I ($^{96}Zr^{16}O^-$) with the ratio determined from an N-implanted sample, i.e. YSZ:N with known nitrogen content. The experimental error is very small and of this reason is not given in the figures.

Photo Electron Spectroscopy (XPS, UPS)

The X-ray photo electron spectroscopy (XPS) and the ultraviolet photo electron spectroscopy (UPS) are used for determining the valence state of the elements as well as the nature of the chemical bonds, i.e. the electronic structure, in the compound. The sample irradiation either by X-rays or by UV light causes an excitation of the system due to photon absorption and subsequent emission of photo electrons. The emitted photo electrons are collected by a semi-spherical analyzer, where depending on their kinetic energy the electrons follow longer (those with higher kinetic energy) or shorter (electrons with lower kinetic energy) routes before reaching the detector. Thus the arriving position is specific for each chemical element and electronic core level. The intensity of the particular signals depends on the number of collected photo electrons. At present XPS is the most versatile and generally applicable technique in the surface analysis. Detailed reviews on the basic principles and applications of XPS and UPS can be found in [91, 92].

X-ray Photoelectron spectroscopy (XPS) was carried out with a VG Instru-

ments equipment. The measurements were performed at room temperature with Mg K_α radiation at 1253.6 eV with a line width of 0.7 eV. As UV source a He I radiation with photon energy $h\nu$ = 21.21 eV was used. A hemispherical CLAM-type electron energy analyzer was used. The analysis chamber was equipped with an ion pump and a liquid nitrogen-cooled titanium sublimation pump, thus enabling a residual gas pressure of less than 10^{-8} Pa. To account for the charging effects of the insulating YSZ:N films at room temperature all spectra are calibrated with respect to the carbon C1s peak. The concentrations of the elements are evaluated as relative concentrations in at-%.

The *in-situ* XPS and SPEM measurements were performed at the synchrotron Elettra in Trieste, Italy. A simple schema of the experimental setup is given in figure 3.3. As working electrode we used Ir tip with a diameter at the contact point of approximately 100 μm and as a solid electrolyte a 9.5YSZ single crystal with (111) orientation. The counter electrode was a platinum paste burned on the back side of the crystal at 250 °C for 2 hours. The applied voltages vary in the range $\pm$ 3 V. The working temperature was in the range 300 °C to 500 °C measured at the upper side of the filament.
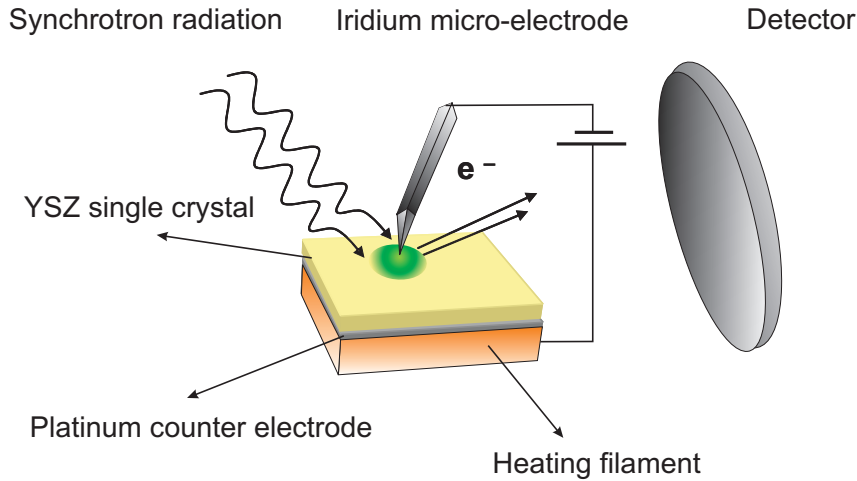
Fig. 3.3: Schematic presentation of the experimental setup for the SPEM and XPS experiments at the synchrotron Trieste, Italy

The X-ray beam allows a spatial resolution of approximately 100 nm. The photon energy is 640.0 eV and the overall energy resolution of the analyzer is <0.5 eV, sufficient to monitor energy shifts of 0.1 eV. The XPS spectra were

acquired with a VSW Class 150 16-channel electron energy analyzer.

Before the XPS and UPS measurements, the samples were sputtered with Ar^+ ions to remove the contaminants from the sample surface.

Atomic Force Microscopy

The atomic force microscope (AFM) was developed in the early eighties on the basis of the scanning tunnel microscope. It consists of scan head with a cantilever at the bottom on which a small tip (usually silicon) is mounted. This tip scans the surface of the sample where its movements in x, y and z directions are recorded and controlled via two or three piezo elements (depending on the construction). The piezo elements transform the mechanic steps in electric signals and create a digital image of the surface topography. The exact positioning of the tip and in some arrangements the z-axes are controlled by a laser. The lateral image resolution is in the nanometer range where specially designed AFM's also work at atomic resolution, but this feature depends on the model of the scan head, the tip, the quality of the electromagnetic shielding, the mechanical stability and the atmosphere. In fig. 3.4 a schematic picture of the AFM is given. The advantage of AFM compared with other high resolution microscopes
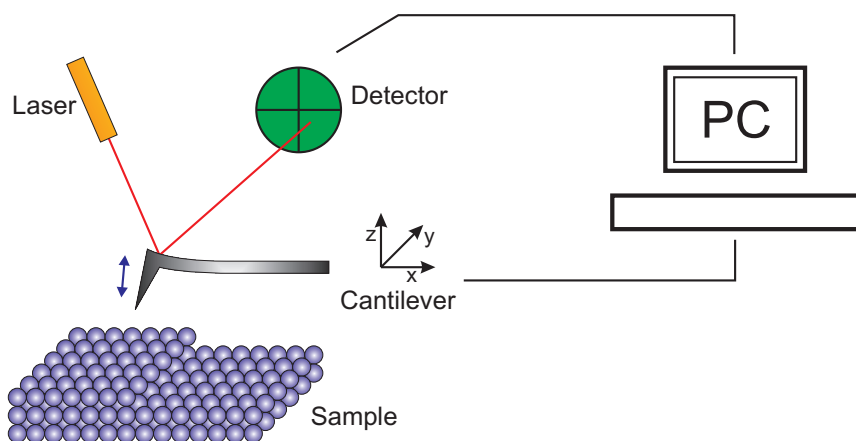
Fig. 3.4: Schematic presentation of atomic force microscope

(HRSEM, STM etc.) is its ability to work with both conductive and insulating materials without damaging or modifying the surface of the samples. The 3D

digital storage and imaging allows rotation the figure thus observing all details three dimensionally where the information from the sample surface once saved can be recalled at any time.

The atomic force microscope used for the surface imaging was a Q-scope 250 (Quesant, USA) with a head designed for a scan area from 200 nm × 200 nm up to 80 μm × 80 μm. The lateral resolution is approximately 1 nm, and the resolution of the z-axis is approximately in the same range. The measurements were performed in the non-contact mode with the following typical scan parameters: a scan rate of 0.5 Hz to 3 Hz, integral and proportional gain in the range 250 to 400 and image resolution 300 dpi to 600 dpi.

High Resolution Scanning Electron Microscopy

The scanning electron microscope (SEM) constructs the surface image by collecting electrons reflected from the sample after electron irradiation. The electrons are emitted by a cathode (Schottky emitter) in ultra high vacuum at a temperature of about 1800 °C. As the wavelength of the electrons is much smaller than of visible light, SEM achieves a resolution in the nanometer range. The magnification can be varied over a wide range (from 10 times up to approximately 250 000 times). Depending on the type of the interaction of the primary electrons with the sample surface we distinct elastic (results in the secondary electrons image) and inelastic (results in back scattered electrons image) interactions, providing different imaging modes.

As disadvantages of this method we can point out the charging effects if the sample is an insulator or poorly conductive and the fact that the sample is practically reduced, sometimes even destroyed at the contact point of the electron beam with the surface. Insulating samples must be covered with thin (a few nanometer) conducting films (usually from Pt or Au) before imaging.

We used a high resolution scanning electron microscope (LEO Gemini 982 equipped with an EDX (Oxford Instruments, INCA Energy) detector. The maximal energy resolution is 200 eV at maximum 1024 channels. The electron source is a Schottky field emitter with an acceleration voltage in the range of

0.2 keV up to 30 keV. The maximal lateral resolution achieved is approximately 2 nm.

X-ray Diffraction (XRD)

The X-ray diffraction analysis is the most widely used method for the determination of the crystal structure of solids. The X-ray irradiation penetrates the crystal and is reflected depending on order the atoms in the lattice and the distance between atomic planes. The wave length λ, the distance between the lattice planes d and the diffraction angle θ are related according to the Bragg equation:

$$n\lambda = 2d\sin\theta \tag{3.1}$$

The lattice constants a, b and c for the cubic, tetragonal and orthorhombic structures can be calculated according to the following equations:

Cubic structure:

$$sin^2\theta = \frac{\lambda^2}{4a^2} \cdot (h^2 + k^2 + l^2) \tag{3.2}$$

Tetragonal structure:

$$sin^2\theta = \frac{\lambda^2}{4a^2} \cdot \left(h^2 + k^2 + \frac{a^2 \cdot l^2}{c^2}\right) \tag{3.3}$$

Orthorhombic structure:

$$sin^2\theta = \frac{\lambda^2}{4} \cdot \left(\frac{h^2}{a^2} + \frac{k^2}{b^2} + \frac{l^2}{c^2}\right) \tag{3.4}$$

where h, k and l are the lattice plane indices.

The X-ray studies of the samples were performed with a θ-2θ diffractometer (Siemens D500) with Cu-K$_\alpha$ radiation at room temperature.

Optical Spectroscopy

The optical (UV and/or VIS) spectroscopy provides information on the excitations of valence electrons. It can also dynamically follow the changes in the material if the start and the intermediate (or end) product absorb the light in different ranges of the spectrum. The absorption is generally described by:

$$I = I_0 \exp\left(-\alpha d\right) \tag{3.5}$$

where I_0 is the initial light intensity; I is the transmitted light intensity; α is the absorption coefficient (a function of the wavelength) and d is the thickness of the material. From the absorption spectra we can determine the position of the optical band edge and the position of the doping levels in the band gap. For optimal results it is required that the sample thickness should not exceed a certain value (depending on the specific material), allowing a transmitted light with sufficiently high intensity to reach the detector.

The optical measurements were performed with a spectrometer Lambda 900 (Perkin-Elmer) in the range of 200 nm - 860 nm with a resolution of 1 nm and a scan rate of 250 nm/min. As light sources served a deuterium lamp emitting in the UV range (below 320 nm) and a tungsten-halogen lamp in the Vis/NIR-range (above 320 nm). As detectors we used a PbS-cell (in the range of 860 nm to 3300 nm) and a photo photomultiplier (in the range of 200 nm to 860 nm).

3.1.3 Electrochemical methods

A variety of electrochemical methods were developed in the last century involving different techniques of collecting, transforming and interpreting the current-voltage characteristics of the studied systems. These methods supply direct information on the change of the electrochemical characteristics of the electrode during its polarization or on the bulk properties of conducting materials. In the following section we briefly review the fundamentals and applications of those methods which are further applied in our studies.

Electrochemical impedance spectroscopy

The electrochemical impedance spectroscopy (EIS) studies the response of the system on the applied alternate current/voltage. In analogy to the Ohm's law the equation relating the voltage, the current and the AC resistance is written as: $E = I\,Z$, where Z is the impedance or the AC equivalent of resistance. The

AC current wave is given by the equation:

$$I(t) = A \sin \omega t + \theta \tag{3.6}$$

where $I(t)$ is the AC current at time t, A is the maximum amplitude, ω is the radial frequency ($\omega = 2\pi f$) and θ is the phase shift in radians. The impedance Z is presented as a complex number and has a real and imaginary part.

The impedance of the main circuit elements are given in the table below.

Circuit element	Impedance equation	
Resistance (R)	$Z = R + 0i$	$i = \sqrt{-1}$
Capacity (C)	$Z = 0 - i/\omega C$	$\omega = 2\pi f$
Inductance (L)	$Z = 0 + i\,\omega\,L$	$\omega = 2\pi f$

We combine the circuit elements either connecting them in series or in parallel. In the case of connection in series the combined impedance is the linear sum of all individual impedance values $Z = \sum\limits_{i=1}^{n} Z_i$. If connected in parallel the total impedance is calculated according to the relation is $Z^{-1} = \sum\limits_{i=1}^{n} Z_i^{-1}$. The equivalent circuit describing the response of the whole electrochemical system contains different sub-circuits connected in series and/or in parallel. The recorded experimental results are presented typically either in a complex plane (Nyquist plot) or as a logarithmic function of the frequency or the phase shift (Bode plot).

A detailed review of the impedance spectroscopy technique and its application in solid state electrochemical studies can be found in [93]

In our experiments we used EG&G (Princeton Applied Research, USA) potentiostat/galvanoctat model 285 equipped with an impedance analyzer working in a frequency range between 5 MHz and 1 mHz.

Steady state polarization measurements

The steady state polarization measurements are the most widely used technique for the qualitative and quantitative electrochemical characterization of redox systems. There are two general types of steady state experiments - galvanostatic and potentiostatic. In the galvanostatic mode we record the potential

response of the system as a function of the applied current. Conversely in the potentiostatic experiments we set a constant potential value and measure the current as a function of the applied potential. The recorded current-voltage data are presented as E/i plots where the current values are usually normalized to a unity electrode area (current density). Each electrode reaction taking place on the electrode surface causes generally an exponential increase of the current by increasing the potential. Above a certain potential value, because of charge transfer difficulties or diffusion problems the recorded currents do not change anymore with the potential increase. This region is called *limiting current* and characterizes the situation where a maximum of the electrochemical reaction rate is achieved. A further increase of the current is possible only of another redox reaction with more positive/negative standard electrochemical potential starts. The galvanostatic mode is suitable for coulometric studies, and for determining the current efficiency of particular reaction or to optimize the parameters of the process i.e it requires at least basic knowledge on the investigated system. The potentiostatic mode is often used for kinetic experiments or for basic studies on less known systems. The potentiodynamic (time dependent) experiments are based on the potentiostatic technique but the input potential values vary (usually linearly) with the time.

Considering electrochemical reactions two general cases can be distinguished: processes where the rate-limiting factor is diffusion (in case that no migration or convection effects are present) of the reacting species to or from the electrode surface and processes limited by the charge transfer rate.

Reversible (diffusion controlled) reactions

The electrochemical behavior of the first group is described by the combination of the Nernst equation and Fick's first law. The steady state condition requires that all the characteristics of the system, i.e. potential, current, concentration profiles etc. are time-independent. The equilibration time depends on the mobility of reacting species and on the total conductivity of the electrolyte. A direct relation between the reaction rate (i.e. the current) and the potential is obtained after a solution of Fick's first law (the total concentration of the

species is time independent). The total flux of species i is given as:

$$J_i = -D_i \frac{\partial c_i}{\partial x} = -D_i \frac{c_i^0 - c_i^s}{\delta} \qquad (3.7)$$

where J_i is the flux given in moles per unit cross-sectional area per unit time; D_i is the diffusion coefficient in $\mathrm{cm^2 s^{-1}}$ (in SI units - $\mathrm{m^2 s^{-1}}$); δ is the thickness of the diffusion layer; c_i^0 and c_i^s are the volume, respectively near-surface concentration of the particular species. The flux can also be written in electrical units for the charged species, and thus equation 3.7 takes the form:

$$i_i = z_i F D_i \frac{c_i^0 - c_i^s}{\delta} \qquad (3.8)$$

The maximal current is achieved when $c^s = 0$ and in this case equation 3.8 can be formulated as:

$$i_d = z_i F D_i \frac{c^0}{\delta} \qquad (3.9)$$

where i_d denotes the diffusion-limited current. Combining both equations we obtain:

$$\frac{i_i}{i_d} = 1 - \frac{c_i^s}{c_i^0} \qquad (3.10)$$

To obtain the final relation between the current and the overpotential we define the Nernst equation for the system in equilibrium state where no net current flows and for another system with applied constant current where the potential is shifted but the reversibility of the electrode process is still preserved.

$$E = E^\circ + \frac{RT}{zF} \ln c^0 \quad \text{and} \quad E_i = E^\circ + \frac{RT}{zF} \ln c^s \qquad (3.11)$$

The overpotential η_d controlled by diffusion is now defined as:

$$\eta_d = E_i - E = \frac{RT}{zF} \ln \frac{c^s}{c^0} \qquad (3.12)$$

By substitution of equation 3.10 in equation 3.12 we obtain:

$$\eta_d = \frac{RT}{zF} \ln \left(1 - \frac{i}{i_d} \right) \quad \text{or alternatively} \quad i = i_d \left[1 - \exp \left(\frac{zF}{RT} \, \eta_d \right) \right] \qquad (3.13)$$

On the basis of this equation the recorded experimental data are presented in plot of η_d versus $\ln \left(1 - i/i_d \right)$. The slope of the resulting straight line gives directly RT/zF and one can easy calculate the number of exchanged electrons z.

*Irreversible (charge transfer controlled) reactions*

The theory of charge transfer has already been considered in chapter 2.6.1 (see p. 42) and here we present only the equations and relations directly applicable to the evaluation of the kinetic parameters. According to the Butler-Volmer equation (see p. 46) at equilibrium conditions (no current is applied to the electrodes) both cathodic and anodic current are equal and define the exchange current density (i_0). By evaluation of the recorded experimental data in E/i plot we can generally differentiate three regions: *the first region* is the non-Tafel region. According to equation 2.120 (p. 47) the current depends virtually linear on the potential and the plot η/i results in a straight line with a slope $\frac{RT}{i_0 zF}$ often denoted as polarization resistance. *The second region* is the Tafel region where the current grows logarithmically with the increasing potential. The Tafel plot ($\eta/\ln i$) is a straight line with a slope $b = \frac{RT}{\alpha zF}$ and an intercept on the current axes at $\eta = 0$ equal to $a = -\frac{RT}{\alpha zF}\ln i_0$. Dividing a by b we directly determine the exchange current density i_0. Knowing the number of the electrons involved in the reaction we can further calculate the transfer coefficients α and $1-\alpha$ respectively for the cathodic and the anodic processes. In the case of multi-step processes where the electrons are transferred in different steps on the current voltage curves we detect only the slowest transfer process which determines the overall reaction rate. As discussed in section 2.6.3, the kinetic parameters determined from the Tafel plot refer to the rate-determining reaction and the calculated transfer coefficients are then called apparent transfer coefficients (α_c or α_a). The existence of more than one slope on the Tafel plot demonstrates either the change of the reaction mechanism with the increase of the overvoltage or the existence of two or more reactions with comparable rates. A complete treatment of these problems as well as mathematical solutions of equations for two or more charge transfer steps with equal rates, following or preceding chemical reactions etc. can be found in the review literature [66, 67, 94–96]. *The third region* is at much higher overvoltages, where the electrochemical process is limited by diffusion.

We performed our steady state measurements in the high temperature electrochemical cell described in details in section 3.2.1 below (p. 79). As current/voltage source a combined multi functional source/meter from Keithley

Model 2400 allowing 2, 3 and 4 point measurements in the voltage range $\pm$ 200
V with a maximal current of 1.05 A was used. For additional resistance mea-
surements of samples with high impedance we operated with a Keithley multi
meter Model 2700.

Dynamic polarization measurements (CVA, LSV)

The principles of potentiodynamic measurements are based on a linear varia-
tion of the applied potential (voltage ramp). The recorded current signals are
a function of the input potential. The formal name of this method is *linear po-
tential sweep chronoamperometry* but it is much more popular as **linear sweep
voltammetry** (LSV). A simple picture of the potential sweep and the resulting
current/voltage curve are presented in figure 3.5 The curve starts at time $t = 0$
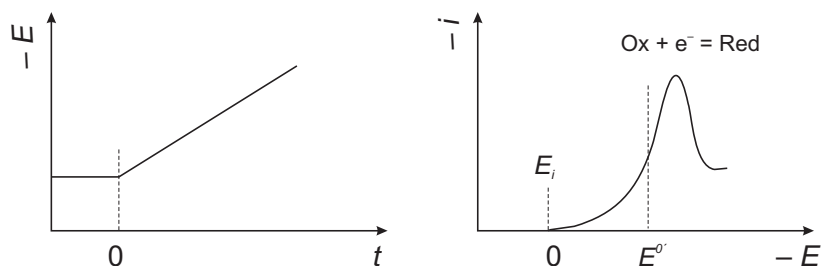
Fig. 3.5: Linear potential sweep (left) and resulting $E - i$ curve

corresponding to the initial potential value E_i. With $E^{\circ\prime}$ is denoted the formal
potential of the electrode [96]. The peak maximum corresponds to a limiting
current either of diffusive or of charge transfer nature.

If one continues the sweep but in the reverse direction towards the initial
potential value the resulting potential/time curve has a triangle form. This
reversal technique is known as *cyclic voltammetry* (CV). In this case the current
response has the form shown in figure 3.6 if a Faradaic process is included. The
forward sweep is identical to the one recorded in the LSV. The difference is
the reverse sweep where the redox process also reverses its direction leading to
the appearance of a new peak but with positive current. The number of the
peaks depends on the number of redox processes on the electrode/electrolyte
interface. As the LSV is basically a partial CV it is usually applied to systems
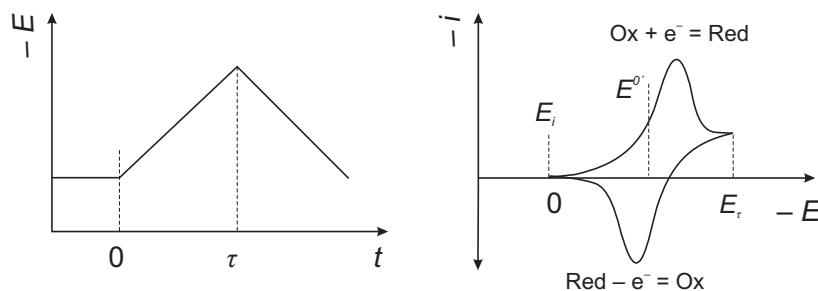
Fig. 3.6: Cyclic potential sweep (left) and resulting $E - i$ curve

where the reduction/oxidation of the already existing species during the reverse scan should be retarded.

In modern electrochemistry both methods have found wide application in the field of analytical electrochemistry to obtain qualitative and quantitative information on the redox processes. At the current level of technical instrumentation the potential can be varied with a sweep rate v ranging from 10 mV/s to 1000 V/s for conventional electrodes and up to 10^6 V/s using ultra micro electrodes. The practical potential resolution is 20 mV difference between two neighboring peaks (at sweep rates above 100 V/s the resolution is higher - 10 mV). A lower limit of 10 mV/s is defined, as below this rate the diffusion processes cannot be described any more with the equations derived for the time dependent current. In the next section the basics of the CV technique are given but we do not completely follow the mathematical solution of the diffusion equations. Only the initial boundary conditions and the most often used criteria for the experimental data evaluation are presented.

Reversible (Nernstian) systems

We firstly define the potential of the electrode at time t as:

$$E(t) = E_i - vt \tag{3.14}$$

where E_i is the initial potential in V; v is the sweep rate in V/s and t is the time in seconds. If we assume that the charge transfer at the electrode surface is much faster than the diffusion of the reacting species, the diffusion equations

derived for the steady state conditions (see p. 69) cannot be applied. The Nernst equation can be formulated as:.

$$\frac{c_{\text{ox}}(0,t)}{c_{\text{red}}(0,t)} = f(t) = \exp\left(\frac{zF}{RT} \cdot (E_i - vt - E^{\circ\prime})\right) \tag{3.15}$$

The dependence of the current on the reactant concentration (for example by cathodic process) is then given by equation 3.16

$$\bar{I}(t) = zFAD_{\text{ox}}\left[\frac{\partial \bar{c}_{\text{ox}}(x,t)}{\partial x}\right]_{x=0} \tag{3.16}$$

where $\bar{i}(t)$ is the average current at time t; z is the number of the exchanged electrons; F the Faraday constant; D_{ox} the diffusion coefficient of the oxidized species; A is the electrode surface.

The solution of this equation was presented by Randles [97] and Sevcik [98] who mathematically derived the final results known as Randles-Sevcik equation. It describes the relation of the peak current to the applied potential sweep rate.

$$I = zFAc_{\text{ox}}^0(\pi D_{\text{ox}}\sigma)^{1/2}\chi(\sigma t) \tag{3.17}$$

In equation 3.17 c_{ox}^0 denotes the bulk concentration of the oxidized species; σ is defined as $\sigma = \frac{zF}{RT}v = \frac{zF}{RTt}(E_i - E(t))$. The solution of the integral equation results in the function $\chi(\sigma t)$ and has been analytically derived, resulting in a set of $\chi(\sigma t)$ values, where the maximum of the function $\pi^{1/2}\chi(\sigma t)$ corresponds to the peak current on the voltammogram and for diffusion limited processes was found to be 0.4463. Thus the final form of Randles-Sevcik equation is:

$$\boxed{I_p = 0.4463\left(\frac{F^3}{RT}\right)^{1/2}z^{3/2}AD_{\text{ox}}^{1/2}C_{\text{ox}}^0v^{1/2}} \tag{3.18}$$

Irreversible systems

By the same mathematic treatment but with other boundary conditions the equation for irreversible processes has been derived in the form:

$$I = zFAC_{\text{ox}}^0D_{\text{ox}}^{1/2}v^{1/2}\left(\frac{\alpha zF}{RT}\right)^{1/2}\pi^{1/2}\chi(bt) \tag{3.19}$$

where α is the transfer coefficient and b is a time dependent parameter defined as $b = \frac{\alpha zF}{RT}v = \frac{\alpha zF}{RTt}(E_i - E(t))$. All other symbols are equal to those described in equation 3.17. The mathematical solution of the integral equation

for $\chi(bt)$ results in series of values with a maximum of the function $\pi^{1/2}\chi(bt)$ at $\pi^{1/2}\chi(bt) = 0.4958$. Substituting this value in equation 3.19 we obtain the final form of the Randles-Sevcik equation for the peak current for irreversible systems:

$$I_p = 0.4958 A c_{\text{ox}}^0 D_{\text{ox}}^{1/2} \left(\frac{\alpha z^3 F^3}{RT} \right)^{1/2} v^{1/2} \tag{3.20}$$

It should be mentioned that all mathematical equations and criteria presented are valid in the case the forward sweep as well as in the case of the reverse sweep (CV).

Based on equations 3.18 and 3.20 a number of criteria have been proposed for the evaluation of experimental results. In figure 3.7 the most important characteristics derived from the voltammetric curve are depicted.
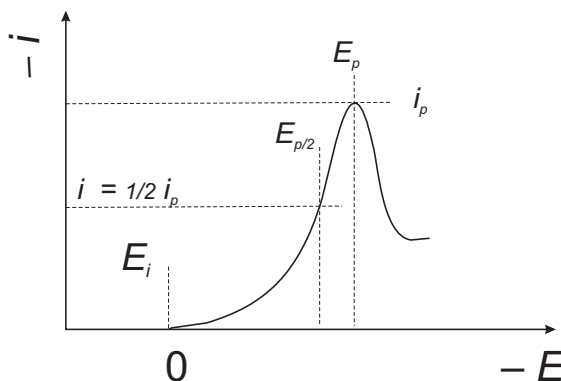
Fig. 3.7: Important characteristics of voltammetric curves

The peak potential (E_p) and the peak current (I_p or i_p) are the most important data used in the further analysis. Sometimes the peak maximum is not pronounced and the accuracy in the determination of the peak position is not sufficient. In this case the half peak potential ($E_{p/2}$) is often used, being defined as the potential value at the half of the peak current (E at $i = \frac{1}{2}i_p$).

One of the most important information which is derived from LSV and CV concerns the reversibility of the electrode process. The plot of the peak current versus the square root of the sweep rate ($i_p/v^{1/2}$) should result in a straight line, if a Randles-Sevcik equation applies. The slope of the line is a criterion for an irreversible (lower slope value) or for a reversible processes. In the case of

mixed control (charge transfer + diffusion) two different regions with different slopes can be clearly distinguished showing the transition of the limiting factor. However this criteria is not always useful *a priori* as it requires the knowledge of all variables in the Randles-Sevcik equation. The reversibility of a process can be checked much easier by investigating the shift in the peak position (current and potential) with a variation of the sweep rate. The peak potential E_p of diffusion controlled processes is almost independent on the sweep rate whereas the peak current increases rapidly. For irreversible processes both current and peak potential shift with the sweep rate but the current dependence is not strongly pronounced. Additionally the CV provides a clear criteria defined by the potential difference between the cathodic and the anodic peaks: $E_{p,c} - E_{p,a} = \frac{2.3RT}{zF}$ or $\frac{59}{z}$ mV at 25 °C. $E_{p,c}$ and $E_{p,a}$ are the cathodic and anodic peak potentials respectively.

For irreversible systems we can calculate the kinetic parameters of the reaction according to the following relations:

$$E_p / \ln v = \frac{RT}{2\alpha z F}$$

$$E_p^2 - E_p^1 = \frac{RT}{2\alpha z F} \ln \frac{v_2}{v_1}$$

Other relations have also been derived and successfully applied to both reversible and irreversible systems in studies of various adsorption processes. As the adsorption on the electrode surface is always related to the capacity of the double layer a very practical application finds the relation for the determination of the electrical double layer capacity:

$$i_c = C_{dl} \cdot \left(\frac{dE}{dt} \right) \tag{3.21}$$

where i_c is the non-Faradaic (capacity) current in mA.cm^{-2}; C_{dl} is the double layer capacity in F.cm^{-2} and dE/dt is the sweep rate v in mV.s^{-1}. To apply this equation we record the current/voltage characteristics for various sweep rates in the non-Faradaic region (i.e. there is no electrochemical reaction and the whole current is used to charge only the EDL). In the plot of current vs. sweep rate at given potential (i/v) for a number of v values the experimental points lie on a straight line and the slope gives the capacity of the double layer.

The peak current is proportional directly to the sweep rate in contrast to the Faradaic current which is proportional to the square root of the sweep rate.

A general review of the theoretical basics of these experimental techniques including application examples and complete description of the formal relations can be found in [96, 99].

The potentiodynamic experiments in this thesis were performed in a high temperature electrochemical cell (section 3.2.1, p. 79) with a EG & G (Princeton Applied Research, USA) potentiostat/galvanoctat model 283 with a frequency response detector Model 1025 (frequency range 5 MHz $\div$ 1 mHz). The applied sweep rates were varied in the range from 20 mV/s up to 1000 mV/s.

3.1.4 Application of conventional electrochemical methods in solid state electrochemistry

Considering the electrochemical processes on the interface (or contact point) electrode/solid electrolyte we have to check carefully whether there is a general difference with the conventional electrode/liquid electrolyte systems well known from liquid electrochemistry and whether the general equations and relations are valid and applicable to solid state electrochemistry. Considering the equations of the Butler-Volmer or the diffusion kinetics we find no term that excludes a specific physical state (gas, liquid or solid) of the reacting species or the electrode material. Thus all thermodynamics are identical for all systems. The microscopic theory of the electron transfer developed by Marcus is also independent from a specific physical state [100, 101]. The processes of gas corrosion and the growth of passive films in corrosion atmosphere are also treated according to the general electrochemical theory. So there is no theoretical reason to suppose deviations from the classical theory for the electrode/solid electrolyte systems. However we should not forget some specifics of the solid conductors and the difficulties which may arise by the theoretical treatment and practical application of the classical electrochemical theory on the solid state processes if the defect formation and the defect related properties are not accounted. An attention should be payed for each individual solid system. The general equations are valid but corrections are possible concerning the particular systems. Thus, Fleig discusses

the oxygen incorporation in the LSM (lanthanum strontium manganate)/YSZ system and suggests a correction in the main charge transfer equation for this mixed ionic/electronic conductor presuming an existence of O^- species as a stable surface intermediate diffusing freely in the LSM and being further reduced to O^{2-} in the volume of the solid [102]. However reviewing the solid state electrochemistry literature from the past 50 years the electroanalytical methods are widely applied and the results and their interpretation are in agreement with the classical electrochemical theory.

## 3.2 Microprobe station set up and experimental design

The experiments we have performed required specific experimental conditions where special attention was paid to the following parameters: **a)** The oxygen activity should be kept as low as possible. According to the thermodynamics in the presence of both oxygen and nitrogen the oxygen redox reaction should be preferred and precedes the nitrogen reaction. Just after the oxygen activity becomes negligible (i.e. reducing conditions) the nitrogen reaction will take place. For this reason we should provide an atmosphere where the initial oxygen activity is kept extremely low. **b)** We should be able to change precisely the position of the working electrode on the electrolyte surface but not to allow oxygen to penetrate into the cell. **c)** We should have a visual control during the experiments when adjusting the electrode position or to detect and record any change in the optical properties or in the surface morphology of our samples. **d)** To study the nitrogen reaction it is important to eliminate all other possible concurrent chemical and/or electrochemical reactions.

The second point in our studies concerns the spatial resolution in the positioning of the working electrode. We investigate the electrochemical nitrogen reduction and local incorporation into oxygen conducting solid electrolytes and we need precisely (in the micrometer range) to adjust the electrode position (the point of contact) depending on the surface topography. As the commercially available furnaces and cells for high temperature experiments could not meet

our requirements we have designed and produced an electrochemical cell of our
own, able to ensure the working conditions for the studies we have performed.

3.2.1 Electrochemical cell with micro-manipulators

The electrochemical cell was placed on a small carrier in the middle of a micro
probe station PM5 (SUISS, Germany) designed for the microelectronic industry
but adapted by us for high temperature electrochemical experiments. The micro
probe station (fig. 3.8) is equipped with four micro manipulators allowing a
precise movement and positioning of the electrodes - two on each side. An optical
microscope with a digital video camera allows to control visually the samples
and electrode movements. The whole setup is insulated from external vibrations.
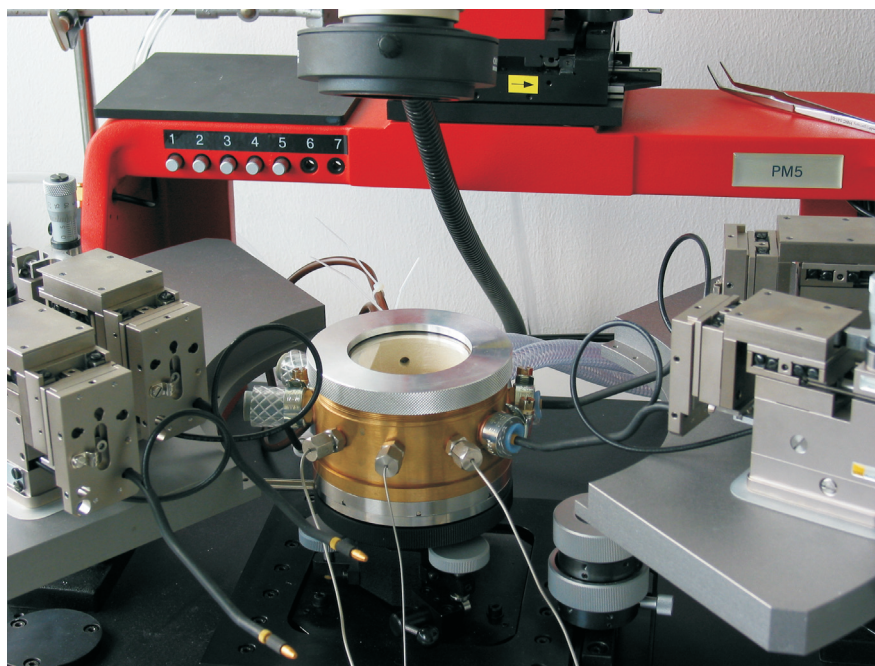
Fig. 3.8: Micro probe station with micro manipulators and optical microscope. In the
middle the heating chamber with the electrochemical cell is placed

The micro manipulators have three high resolution positioning screws with 100
tpi (threads per inch) and allow precise movements in X,Y and Z direction.
They are fixed to the main body of the microprobe station by a vacuum system.

The electrochemical cell we have designed is gas tight and water-cooled. It
can be used at temperatures up to 850 °C where the temperature limit depends

only on the power of the heating element. In figure 3.9 a cross section and top view of the cell are presented.
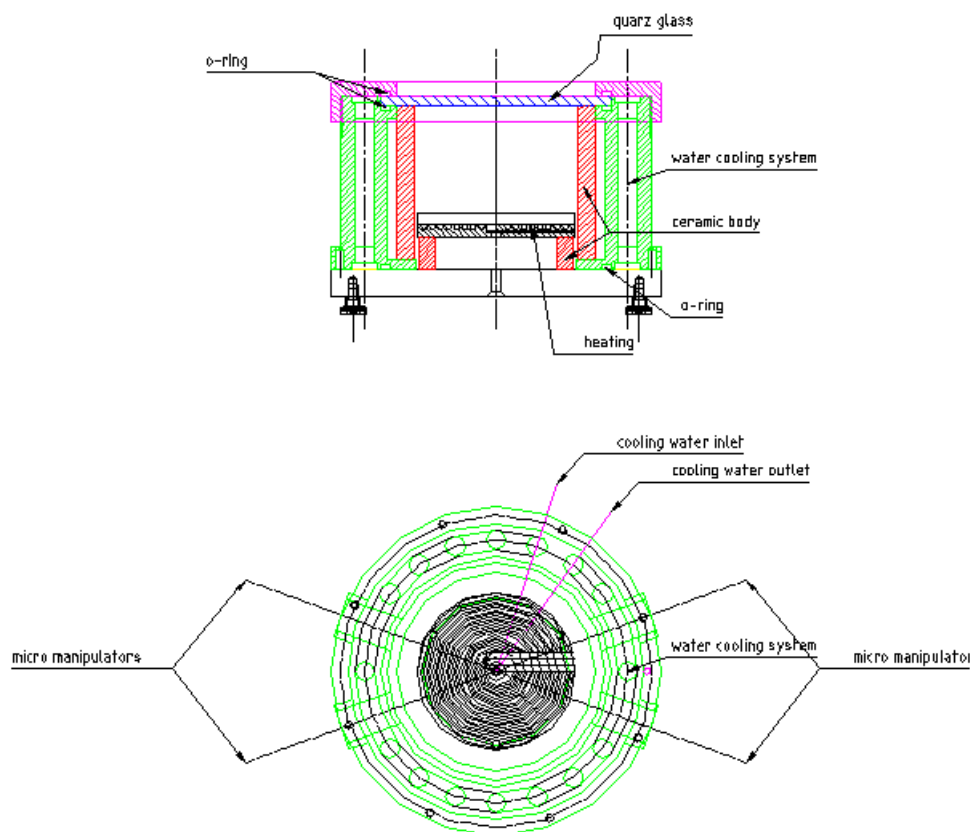
Fig. 3.9: Schematic presentation of the design of the electrochemical cell for high temperature experiments. The cell is gas tight and water cooled.

The cell consists of an outer body made from brass with channels for the water cooling and an inner body made of "Pythagoras", a ceramic material being stable up to temperatures of 1200 °C. On each side of the cell body we have placed two inlets for the arms of the micro manipulators. At the bottom the heating element and the thermoelement are situated, covered by a thin alumina plate which ensures an electrical insulation of the samples. The upper side is closed with a 3 mm thick silica glass disc in order to have visual access to the samples during the experiments. The gas inlet is attached at the upper side of the body and the gas outlet near to the bottom. This arrangement ensures a constant heat distribution on the sample surface in the cell because the hot gas moves from the bottom in direction to the top, meeting and mixing with

the cooler incoming gas. Thus the cold gas will be firstly heated before reaching the sample surface.

3.2.2 Experimental design and electrochemical cell arrangement

In our studies we have worked with two different arrangements of the electrochemical cell. The first one is the classical three electrode electrochemical cell equipped with working, reference and counter electrode. The second one is the two electrode cell, where the counter electrode has a surface much larger (more than 5 orders of magnitude) than the working electrode, thus preventing the polarization of the counter electrode. As the counter electrode (Zr/ZrO_2) provides a fixed oxygen activity, i.e. a reference potential we use it also as a reference electrode.

Three electrode electrochemical cell

The three electrode arrangement of our electrochemical cell designed for solid electrolytes is shown in figure 3.10. There are two possibilities to contact the electrolyte - either with all three electrodes placed on the surface or with the counter electrode at the lower side of the solid and the reference and the working electrode on the upper side. As the surface properties usually differ from the bulk properties these arrangements are not equal and they both have one serious disadvantage - the distance between the reference and the working electrode is too large. In liquids the reference electrode should be as close as possible to the working electrode in order to reduce the IR drop but it should not influence the electric field between the working and the counter electrode. In solid state electrochemistry the position of the reference electrode is often placed at a large distance from the working electrode and in some arrangements it is even placed on the side of the counter electrode. Such electrochemical cell cannot be used for precise electrochemical studies and the potential values measured can serve only as an approximate orientation. The positioning of the reference electrode accounting for the specifics of the solid electrolytes is critically discussed in [103, 104]. In the first paper the suggested distance range varies between 50 μm and 2500 μm. In the second paper the dependence of measured potential values
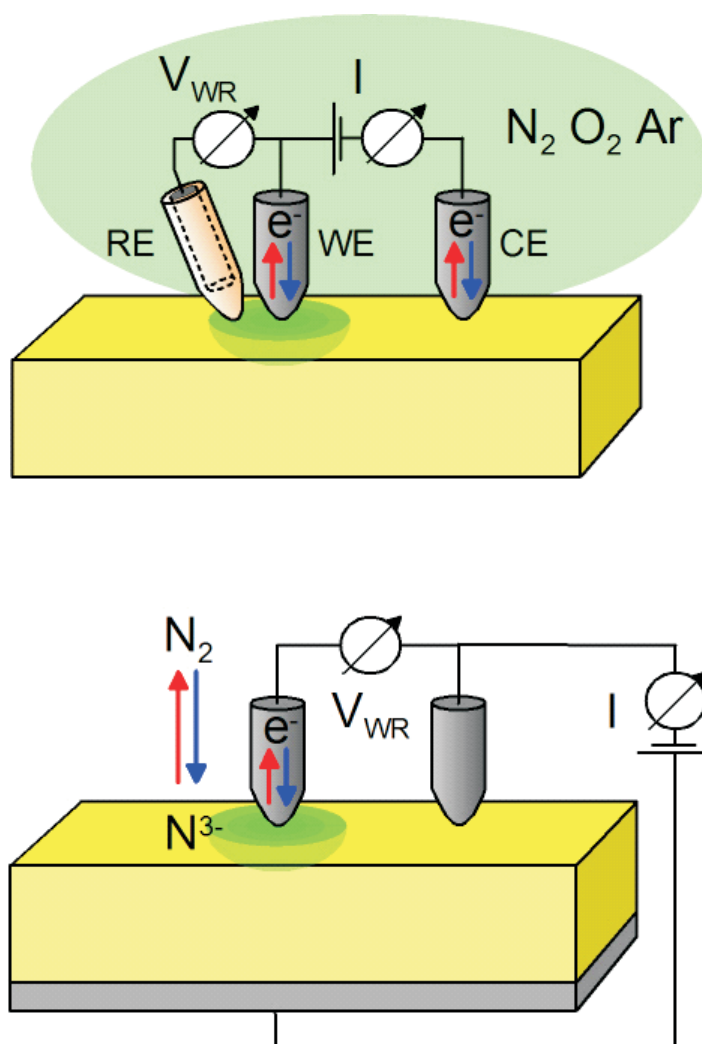
Fig. 3.10: Schematic presentation of two designs of three electrode electrochemical cell for high temperature experiments.

on the distance reference-working electrode was studied by application of micro structured electrodes and the suggested value is a few microns. The proposed distance is most appropriate in order to prevent a large IR contribution. As our studies are concentrated on the kinetics of the processes, a large distance between the reference and the working electrodes is not acceptable and we have tried to place our reference electrode as near as possible to the working electrode. However, because of geometric reasons a distance smaller than approximately 0.5 mm could not be achieved. We worked with this electrode arrangement in the experiments on the incorporation of nitrogen in single crystals and bulk samples

but for the precise kinetic studies we have used the two electrode arrangement which has some important advantages, discussed in the following section.

Two electrode electrochemical cell

The two electrode electrochemical cell has found its application mostly in very sensitive kinetic studies (usually on micro electrodes). Practically the counter electrode serves also as a reference electrode. There are some special requirements which should be fulfilled in using the two electrode arrangement. Firstly, the reaction taking place on the counter electrode should be reversible and at or very near to the equilibrium state. Secondly the difference in the electrode areas of the working and the counter/reference electrodes should be large enough to ensure low polarization of the counter electrode. In praxis a difference of at least two orders of magnitude is essential. Our two electrode cell arrangement is shown in figure 3.11.
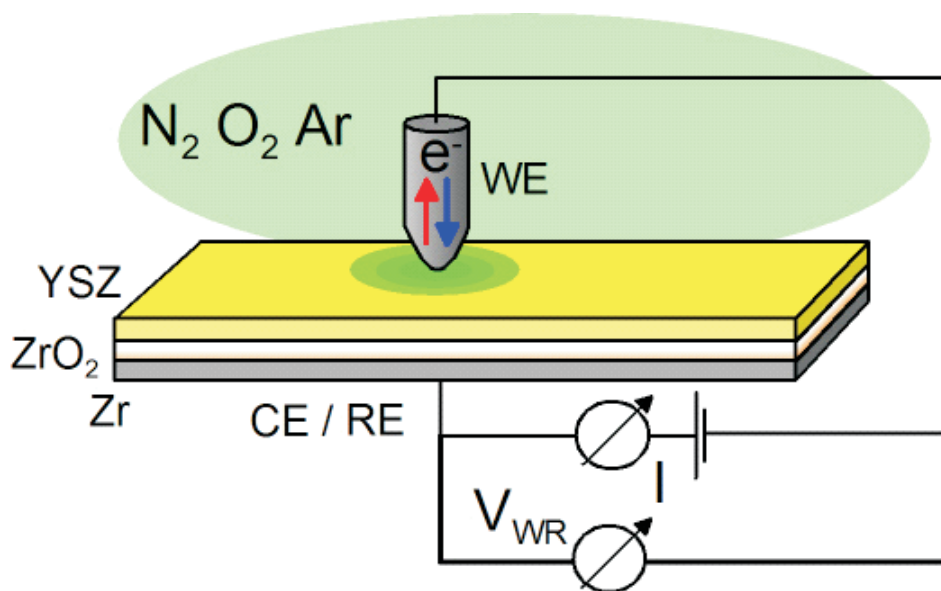

Fig. 3.11: Schematic presentation of a two electrode electrochemical cell for high temperature experiments.

As counter and reference electrode we use a zirconium metal plate with a geometric surface of 1 cm^2 covered with a thin (up to 3 μm) ZrO_2 film. Thus, we use Zr/ZrO_2 reference electrode with fixed oxygen partial pressure also as a

counter electrode. The working electrode is a micro electrode with a diameter of about 3 to 10 μm or a surface area of approximately 10^{-6} cm^2. If we apply a current of 10 μA to both electrodes, the current density on the working electrode will equal 10 A/cm^2 where current density on the counter electrode is only 10^{-5} A/cm^2. So the current density differs by six orders of magnitude and the polarization will have a negligible effect on the counter/reference electrode.

Micro vs. macro electrodes

In the following chapter we compare the advantages and disadvantages of the micro- and the macro-electrodes. We discuss the different possible contacting between the electrodes and the solid electrolyte. A special attention was paid to determine the current (voltage) distribution at the contact point between a micro-electrode and YSZ. Generally we expect that the electrochemical reactions involving the gas phase proceed at the triple phase boundary. However we cannot exclude competitive reactions as reduction of the electrolyte or reduction of the gas molecules at the bare metal surface of the electrode. As the electrochemical characteristics show the total current (voltage) including all these processes the knowledge on the distribution of the electric field will suggest which part will have the major contribution. We applied the finite element simulation method (FEM) to simulate the field distribution.

We have performed almost all our experiments with micro electrodes. *The micro-electrodes* have some advantages making their application in solid state electrochemistry especially attractive and successful. The term "micro" electrode and suitable applications of micro electrodes in studies on electrochemical systems are discussed by Schultze et. al [105]. The maximum diameter for one electrode still to be a micro electrode is defined as 10^{-2}cm. The main advantage is the low ohmic drop even in electrolytes with high ohmic resistance. According to Ohms law ($U = IR$) we minimize the influence of the electrolyte resistance (assuming constant R) by minimizing the current as an absolute value. In spite of the low current values we can work at high current densities, as the small current is applied to a very small electrode surface. Another advantage is the possibility for the local positioning on the electrolyte surface. The micro elec-

trode technique has been successfully developed and applied in the solid state electrochemistry by Fleig [106–109] for impedance studies, e.g. on the contribution of grain boundaries to the total impedance of solid electrolytes.

There is another specific problem we should discuss in applying micro electrodes to solid electrolytes. It is especially important in the case of studies with pure oxygen ion conductors that the electrochemical reaction of the gas reduction and incorporation into the oxide takes place only at the triple phase boundary. We assume two possible situations: **(a)** The electrode has an ideally perfect contact to the electrolyte. Applying a negative potential to the working electrode the current lines are not homogeneously distributed along the whole geometric interface. The edge effect is strongly pronounced and we expect to have a much larger contribution of the Faradaic current from the edges than from the middle of the electrode. This is clearly confirmed by finite element method (FEM) simulations of the current distribution on a micro electrode interface. The highest current density is, as expected, concentrated near to the electrode edge. In the middle of the interface the distribution is homogeneous but the intensity of the current density is much lower. In the real experimental conditions such current density distribution supports the reaction on the triple phase boundary. Concerning the incoming electrochemical signal it is important that recording the current - voltage characteristics we collect the data from the whole electrode surface. Assuming an ideal electrode/electrolyte contact and purely ion conducting electrolyte the active surface where the gas reduction takes place is only a small part of the whole electrode geometric area. If no direct charge transfer between the electrode and the electrolyte takes place (reduction of the electrolyte) than the recorded E/i characteristics will fully represent the electrochemical reaction on the three phase boundary, but if the inner electrode surface also contributes to the total current signal than we record a mixed signal dependent on the perimeter/surface ratio. By minimization of the diameter of the electrode we increase the contribution of the triple phase boundary as the ratio R will increase ($R = \frac{2\pi r}{\pi r^2} = 2/r$). So in order to ensure optimal conditions where the recorded electrochemical signal represents mainly the redox reaction on the three phase boundary we should minimize as much as possible the diameter of the working electrode. **(b)** The electrode surface is
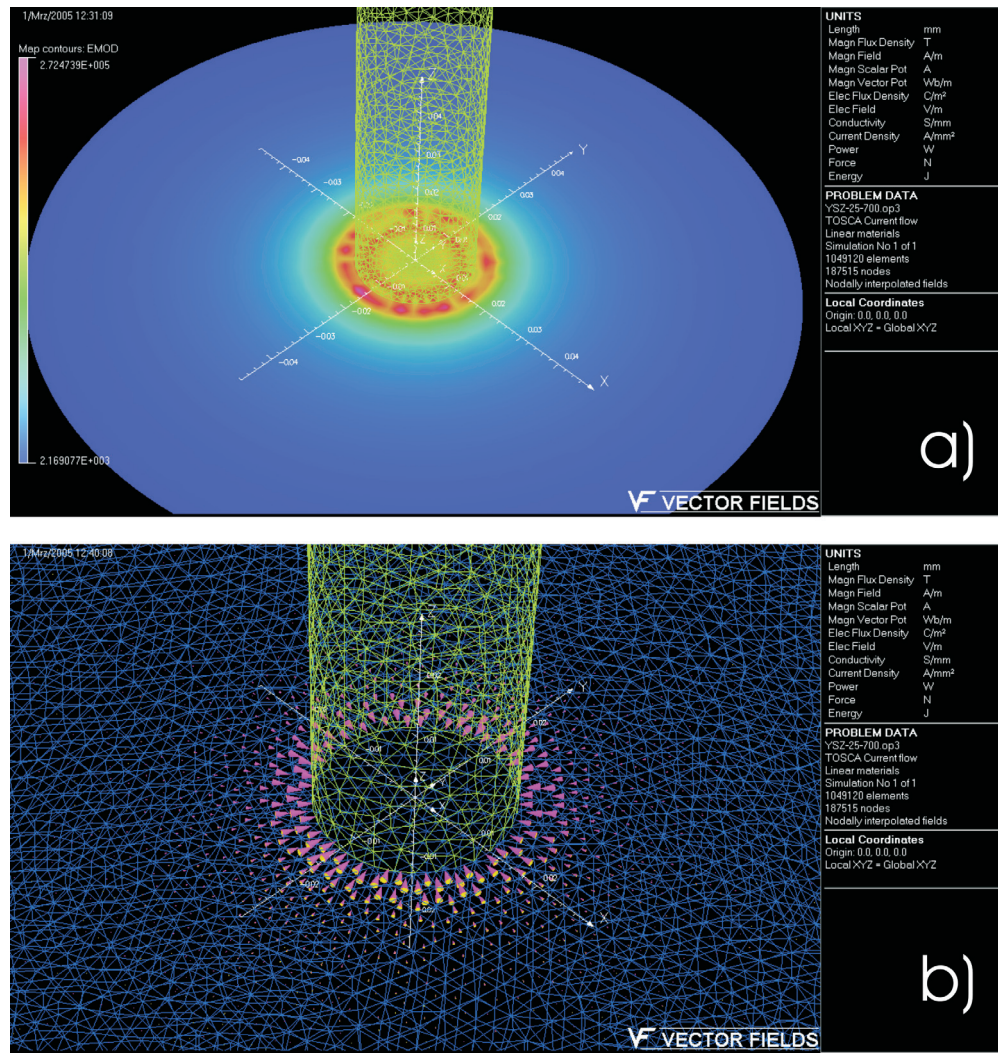
Fig. 3.12: Current distribution at a micro electrode in contact with YSZ solid electrolyte. a) the current density; b) current vector orientation; $T = 700$ °C; $U = 3$V

not perfectly contacted, i.e. there are only local points of contact and the interface must be treated as a sum of many triple phase contacts. In this situation the contribution part of the triple phase boundary is much larger and the noise caused by the possible undesired electrolyte reduction is minimized.

Another point for discussion is the orientation of the current lines. The knowledge on the direction of the current lines allows to predict the direction of movement of the reduced/oxidized species and the distribution of these species on the surface and in the bulk. In figure 3.13 the FEM computations show the orientation of the current vectors. On the simulation the current density is
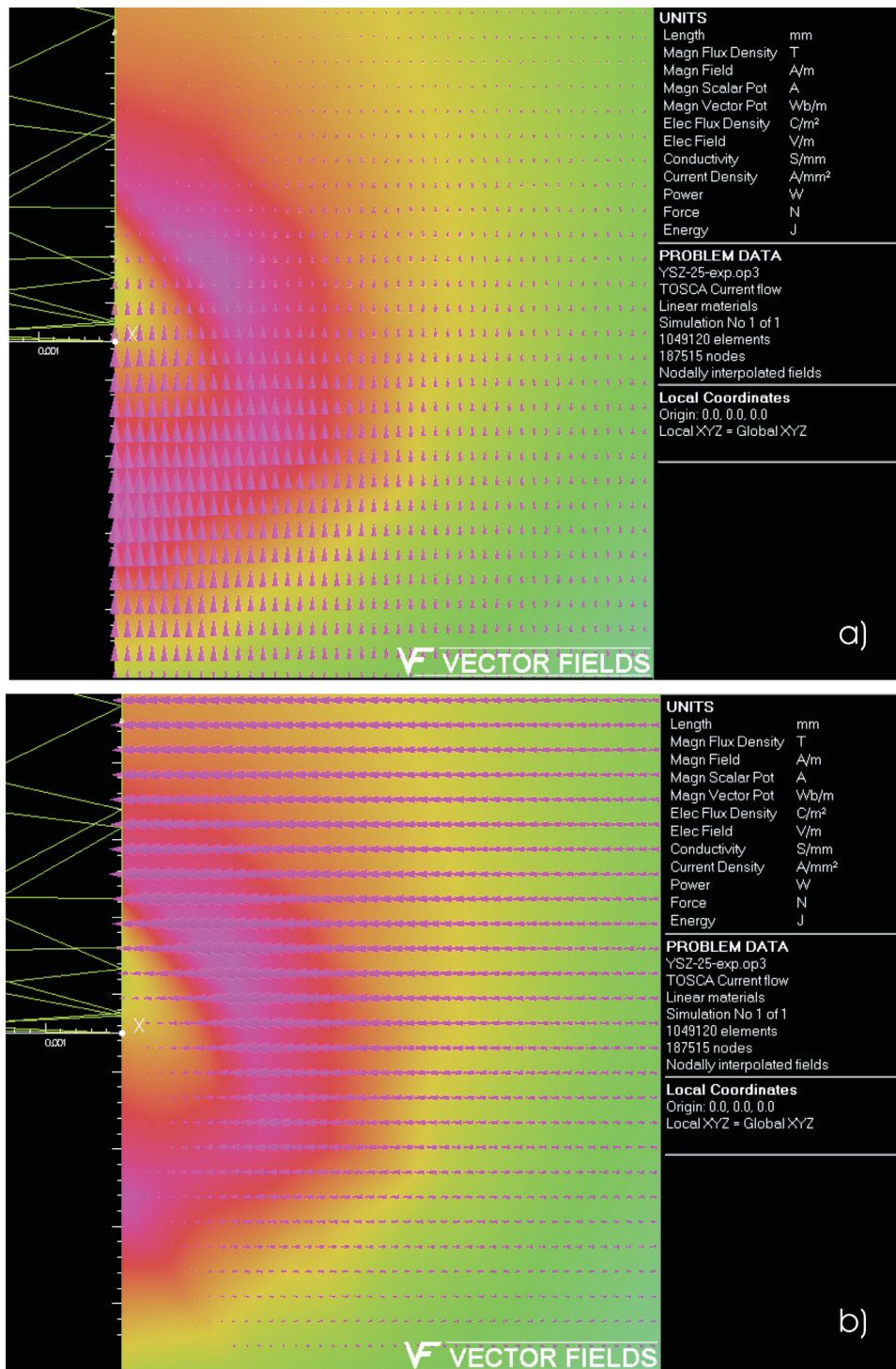
Fig. 3.13: FEM simulation of the current vectors, their orientation and intensity

given as background color and the size of the triangles (representing the current vectors) is proportional to their density. It can be seen that the lateral component is strongly pronounced on the gas/electrolyte side left to the point contact whereas the perpendicular vector orientation is stronger on the side of the electrode/electrolyte contact. From this figure we can conclude that both the orientation of the current lines and their density confirms a sufficiently large contribution of the redox reaction on the triple phase boundary.

We should point out some problems in the application of micro electrodes. As the whole contact surface is in micrometer range, even small non-contacting areas represent a high percentage of the total surface and lead to large deviations in the calculation of the current densities. Additionally, by repositioning the electrode during the experiment or by changing the experimental conditions (for example - rising the temperature) the electrode may be deformed depending on the electrode material and the applied pressure, thus leading to a wrong estimation of the contact surface. Additional problems may appear if dense electrodes contact the electrolyte perfectly. In this case the perimeter/surface ratio R is low and the contribution part of the triple phase boundary (the redox reaction) to the total current response will be small.

The application of *macro electrodes* has also some advantages. They are easy to be prepared. Even if small areas do not contact the electrolyte surface, this will present only a negligible part from the total geometric surface and will not influence the measured electrochemical characteristics. Another advantage compared to micro-electrodes is that the total amount of the reacted substance is much larger and it is much easier to be detected or measured by different analytical methods, and small imperfections will not cause drastic errors in the data evaluation. The disadvantages on the other side are - poor spatial resolution and a serious additional polarization due to the ohmic drop in the electrolyte.

The selection of the size of the working electrode depends strongly on the particular system and the main purpose of the experiment. Due to the high resistance of the solid electrolytes, the comfort to work in two electrode cell and the possibility to move freely the working electrode on the electrolyte surface we have chosen to use micro electrodes in most of the present studies.

4 Plasma-chemical preparation of thin nitrogen doped YSZ layers

The preparation of metal nitrides or nitrogen enriched oxide films via pulsed laser deposition has been already studied [110–113] for different oxide systems but the preparation of nitrogen doped ZrO_2 is reported only by Zhu [114]. In the present work we have systematically studied the influence of the deposition conditions on the nitrogen incorporation into thin films YSZ. We deposited films of ZrO_2 and YSZ in nitrogen ambient in order to test if nitrogen can be incorporated into the oxide films during the deposition and to observe if the properties of the doped material change. We also used the PLD for the preparation of thin film electrolytes (2 μm to 3 μm) for our electrochemical experiments. In this chapter we report on the results of our studies on the influence of the deposition conditions.

Experimental details

As target materials were used either pure ZrO_2 or ZrO_2 doped with 3, 5, 7, 9.5 or 13 mol% Y_2O_3 with a purity of 99.99 % excluding Hf (the hafnium content corresponds to max. 1 mol%) produced by HTM Reetz (Germany). In the following text we denote them as 3YSZ, 5YSZ, 7YSZ, 9.5YSZ and 13YSZ, respectively. The nitrogen doped YSZ films are denoted as 3YSZ:N, 5YSZ:N, 7YSZ:N, 9.5YSZ:N and 13YSZ:N. As substrate materials we used: (a) polished sapphire crystals with (0001) orientation of the surface[1], (b) (0001) orientated sapphire with a thin (approx. 50 nm) film GaN and (c) YSZ single crystals. The size of the substrates was typically 10 mm × 10 mm and the thickness of the films was homogenous over this area. The background gases (Messer, Germany)

---

[1]Some of the films for the optical absorption experiments were deposited on silica glass substrates.

supplied to the PLD chamber had a purity of 99.5 % (O_2), of 99.99 % (N_2) and of 99.996 % (Argon) respectively .

4.1 Surface morphology and structure of PLD deposited thin films

4.1.1 AFM surface imaging

All films deposited under the given conditions show a smooth surface with only a small number of pores or droplets. An AFM image of the surface of a 7YSZ:N film deposited on a sapphire substrate is shown in fig. 4.3.
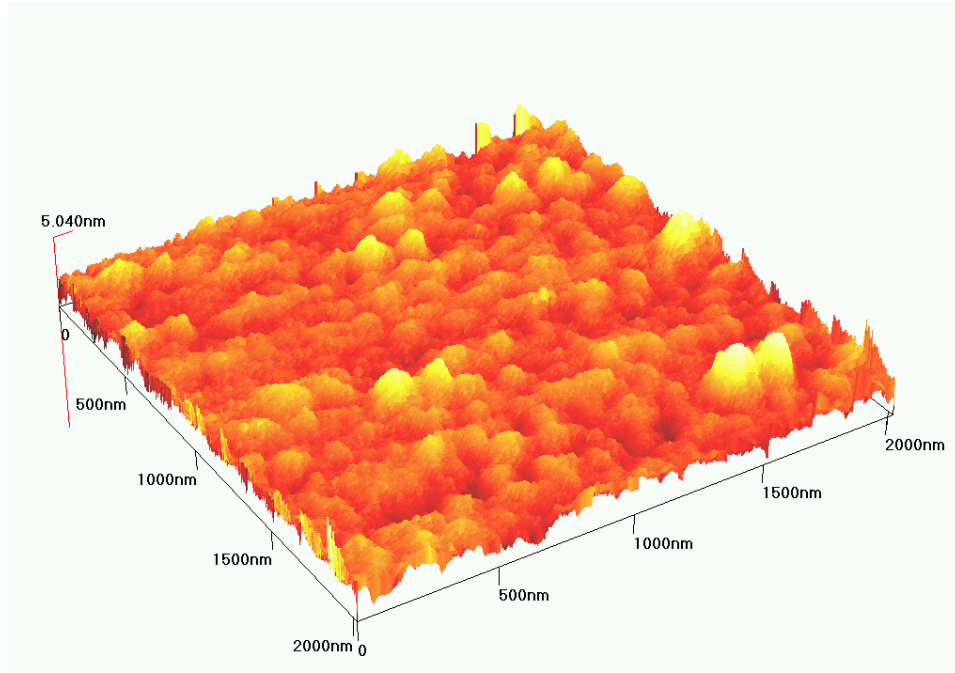
Fig. 4.1: AFM image of a 7YSZ:N film deposited on sapphire (0001). Deposition conditions: $p(N_2)$ = 4 Pa, T = 500 °C, d = 4 cm.

The morphology of the film repeats on the large scale the morphology of the substrate. The grain size at the surface varies in the range of 30 nm up to approximately 90 nm, with an average hight of 4 nanometers. We found no difference in the surface morphology of the YSZ films deposited in nitrogen or in oxygen atmosphere. We also found no significant influence of the yttria content
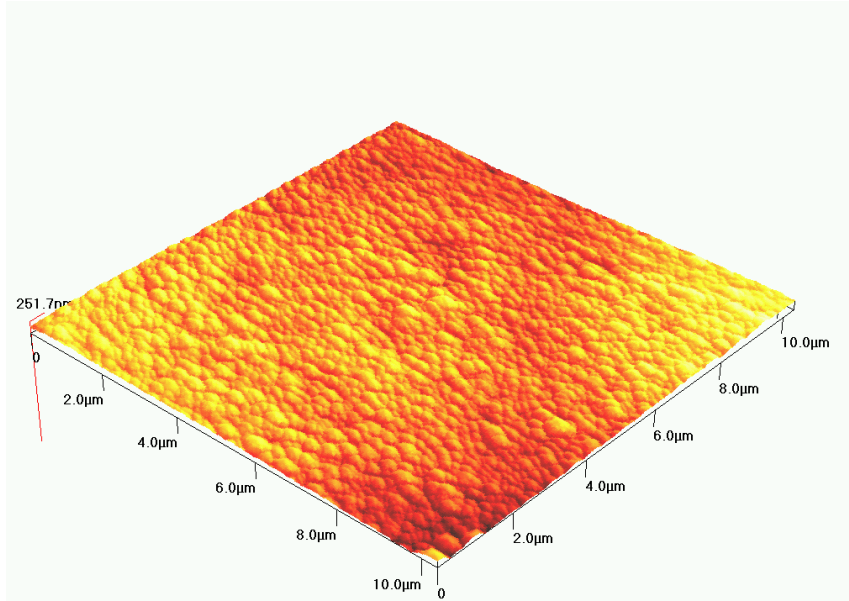
Fig. 4.2: AFM image of 7YSZ:N film deposited on a Zr substrate. Deposition conditions: $p(N_2) = 4$ Pa, $T = 500$ °C, $d = 4$ cm.
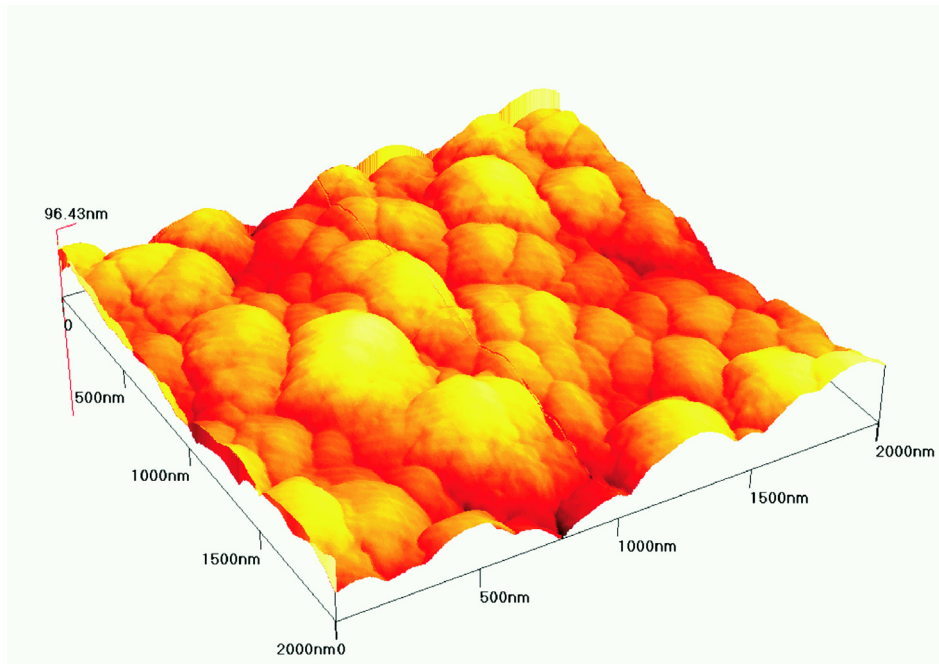
Fig. 4.3: AFM image of a 7YSZ:N film deposited on a Zr substrate. Deposition conditions: $p(N_2) = 4$ Pa, $T = 500$ °C, $d = 4$ cm.

and the deposition parameters, i.e. temperature, pulse energy and gas pressure on the film surface morphology.

However the grain size vary depending on the substrate. The layers deposited on a sapphire or YSZ single crystals substrates are of the same grain size, whereas films deposited on a quartz glass or Zr metal substrates show a much larger grain size varying in the range 100 nm up to approximately 250 nm. This effect is not surprising as the effect of the substrate surface on the film morphology is well known.
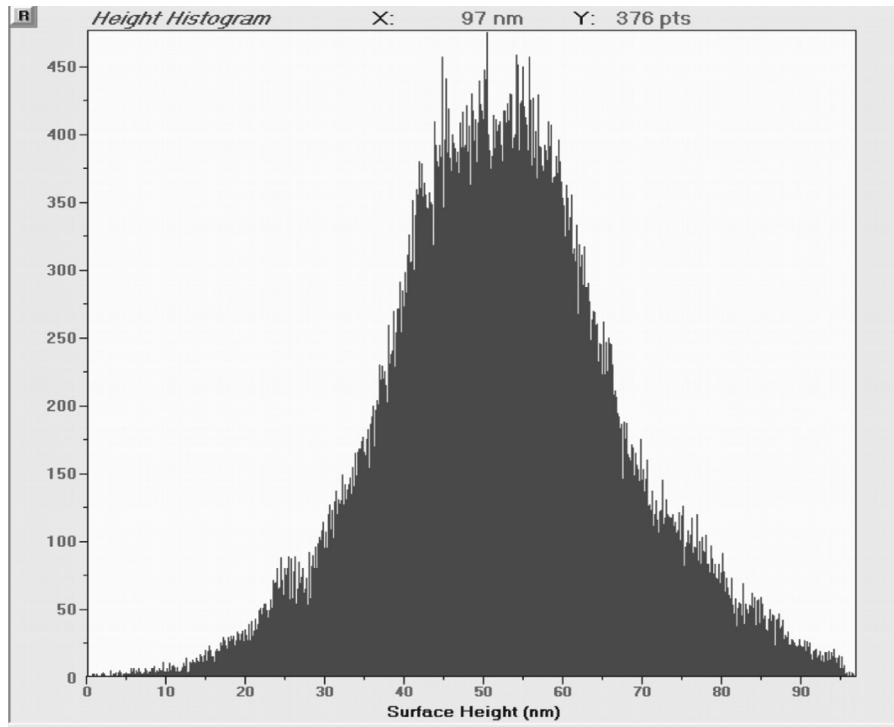
Fig. 4.4: Hight histogram of 7YSZ:N film. Deposition conditions: $p(N_2) = 4$ Pa, $T = 500\,°C$, $d = 4$ cm.

The height histogram presented in figure 4.4. The computed roughness parameters are $RMS = 14.56$ nm, $R_p = 44.57$ nm and $R_t = 96.7$ nm, where RMS is the root mean square roughness, R_p is the maximum peak and R_t is the maximum difference between the highest peak and the maximum valley measurement. It shows that the film is of a very good quality with a roughness in the nm range. Nevertheless as discussed in section 3.1.1, droplet particles also

occur especially if the deposition temperature drops below 400 °C. No significant difference in the film topography was found by variation of the working parameters (temperature, gas pressure, dopant concentration, substrate).

4.1.2 HRSEM

Additional to the AFM we controlled the surface and thickness of the PLD deposited films by high resolution scanning electron microscopy. The surface images of YSZ films with and without incorporated nitrogen are shown in fig. 4.5. The surface morphology of the both layers does not show a substantial
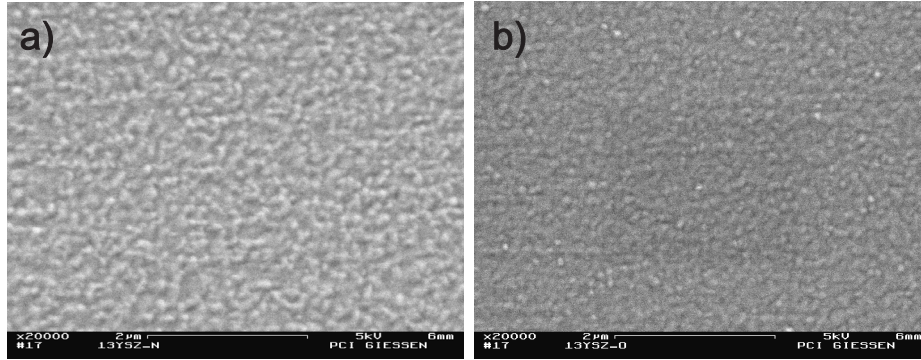
Fig. 4.5: HRSEM image of the surface of a) 13YSZ:N deposited at $p(N_2) = 4$ Pa and b) 13YSZ layers deposited at $p(O_2) = 4$ Pa on a (0001) orientated sapphire substrate. T = 500 °C, $d = 4$ cm.

difference. However the YSZ films deposited in an oxygen atmosphere are characterized by a slightly smaller average grain size of 40 nm, whereas the films deposited in nitrogen have an average grain size of 55 nm.

The films are virtually free of pores and perfectly dense, which is an important prerequisite for both the SIMS and optical experiments. The HRSEM image of a bilayer cross section consisting of one 9.5YSZ:N and one 9.5YSZ film (each with a thickness of approx. 1 μm) deposited on sapphire is shown in fig. 4.6.

The AFM images prove that both nitrogen-free and nitrogen-doped films have the same microstructure at the surface. The roughness of the films lies in the nm range, and thus, is very small compared to the thickness of the films in the micron range. The concentration of pores and droplets is small, and we interpret
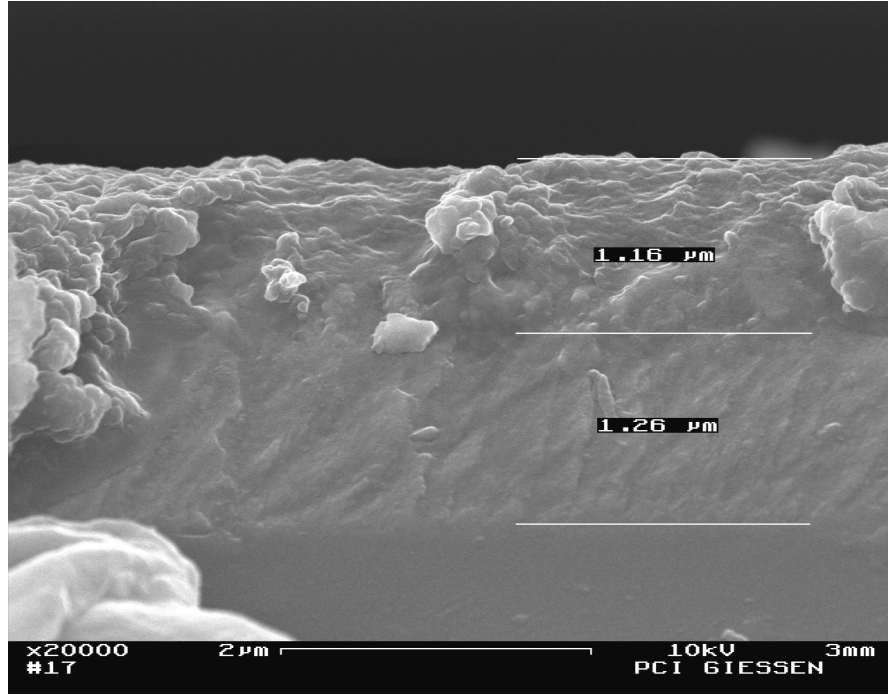
Fig. 4.6: HRSEM image of the cross section of a 9.5YSZ:N/9.5YSZ sandwich film. Deposition conditions: $p(N_2) = 4$ Pa, $T = 500$ °C, $d = 4$ cm.

the surface topology as the result of a typical grain size in the range between 20 nm and 50 nm. From the AFM images we can conclude that PLD is a suitable method for the preparation of YSZ:N films of high surface quality. HRSEM proves that the films are virtually pore-free and adhere well to the substrate. Changes of the background gas allow the growth of bi- and multi-layers with different local composition with perfect interfaces.

4.1.3 XRD studies of nitrogen doped YSZ layer

We found that all films were crystalline as deposited, even without additional thermal post-treatment. The resulting diffraction patterns of three YSZ:N films are shown in figure 4.7. Apart from the intensive (0006) Al_2O_3-reflection at $2\theta = 41.68$ ° and the corresponding K_β and L_α reflections marked by arrows the main reflections were assigned to the cubic fluorite-type structure of YSZ. The orientation of the films is preferably in the (111) direction as this reflection is much more intense than the others. Additional (220), (331) and (420) reflections
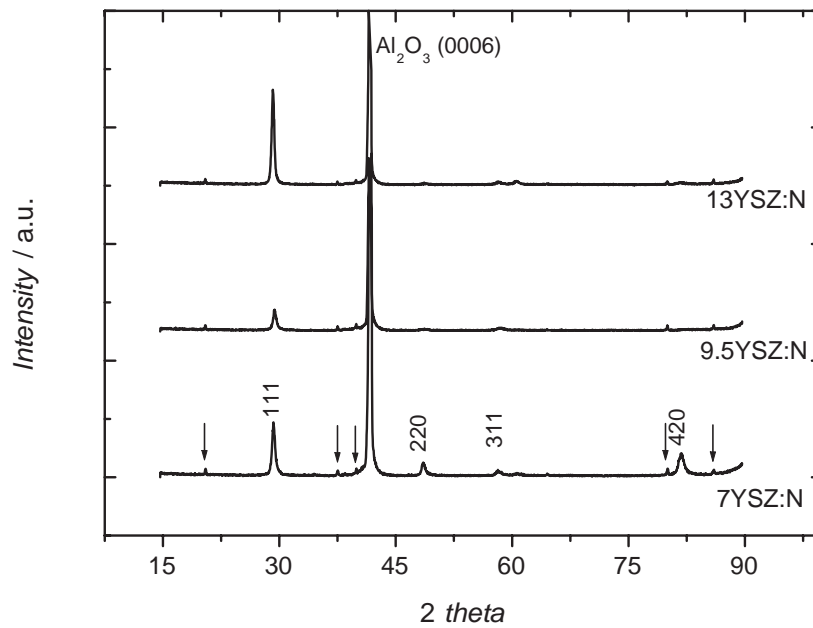
Fig. 4.7: X-ray diffraction pattern of 1 μm thin YSZ films containing 7; 9.5 and 13 mol% Y_2O_3 deposited via PLD in nitrogen ambient on 0001 sapphire substrate.

are found with much lower intensity, but being more pronounced for the 7YSZ:N sample. In fig. 4.7 the position of the main (111) peak for the nitrogen doped films is found at smaller 2θ values than those calculated for cubic YSZ free of nitrogen. This result differs from those reported by Lerch [14] on YSZ:N powders, where a shift of the reflections was towards higher 2θ. However an exact calculation of the lattice constant and the symmetry of our YSZ:N films was not possible, because of a distortion of the cubic fluorite type structure and the strong texturing. This distortion of the fluorite-type lattice might be due to the incorporated nitrogen and/or due to strain fields caused by the nano-crystalline film structure.

To demonstrate the effect of nitrogen doping we compare in fig. 4.8 the positions of the (111) reflection of YSZ, of YSZ:N and of a nitrogen-doped sample which was subsequently re-oxidized in air at 700 °C for 30 minutes. We also see the (200) reflection of the nitrogen-free YSZ film. This reflection is almost

absent in the YSZ:N films, indicating different texture of YSZ and YSZ:N films. The (111) reflection of 13YSZ:N is shifted towards a smaller 2θ value by 0.45° compared to 13YSZ. The reflection of the re-oxidized film has again the same 2θ value as the nitrogen-free film. The films deposited in different gas atmospheres
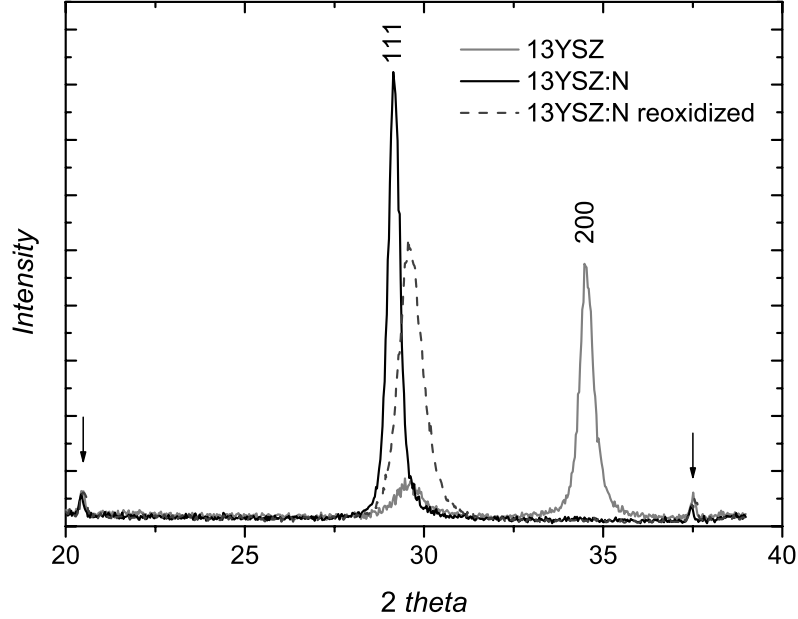
Fig. 4.8: X-ray diffraction patterns of a 13YSZ, a 13YSZ:N, and a re-oxidized 13YSZ:N (30 min at 700 °C at) film at room temperature. Deposition conditions: $p(N_2) = 4$ Pa, $T = 500$ °C, d = 4 cm.

were always crystalline, and we found significant orientation effects. When the deposition process was carried out in nitrogen, the YSZ:N films grew preferably with (111) orientation. Using Debye-Scherrer's equation one can calculate from the FWHM of the reflections an average grain size comparable to the grain size measured by AFM. The deposition in oxygen increased the intensity of the (200) reflection, but the (111) reflection is still present. The re-oxidation process of YSZ:N and loss of nitrogen does not seem to influence the orientation of the films. The (111) reflection shifts back to its position of YSZ, indicating that the nitrogen content influences the lattice parameter. As the (200) reflection does not appear upon re-oxidation, the orientation is maintained. Thus, we

can preferably grow (111) oriented YSZ films doped with nitrogen and we can subsequently oxidize the sample (removing nitrogen) retaining its orientation. The effect of the re-oxidation (de-nitridation) of YSZ:N is pronounced and shifts the reflections back to the position typical for the films deposited in oxygen atmosphere. For the YSZ prepared in oxygen atmosphere the cubic distortion reported for the YSZ:N films is noticeable but smaller compared to the YSZ:N films. The distortion is highly reduced after the re-oxidation/heat treatment.
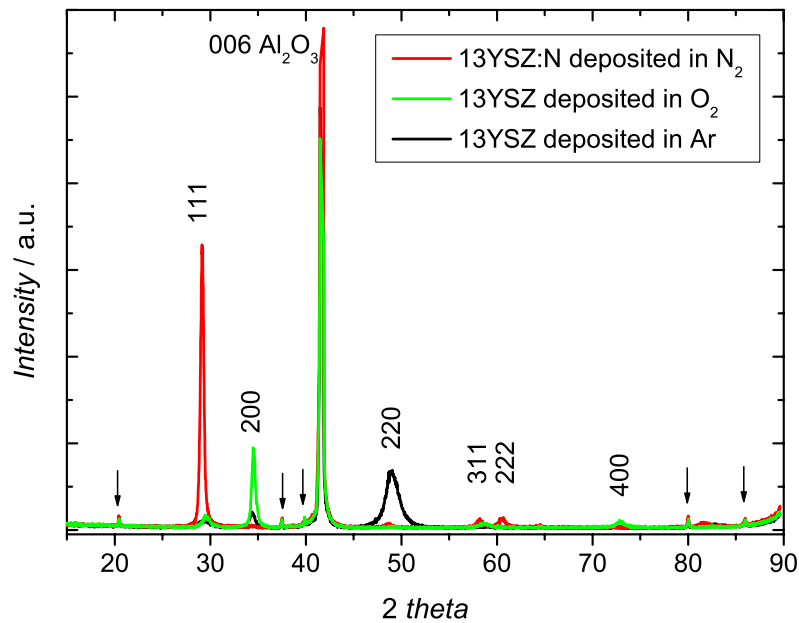
Fig. 4.9: X-ray diffraction pattern of 13mol% yttria doped zirconia films prepared in oxygen, nitrogen and respectively Ar/H_2 atmosphere.

As no systematic studies on the structure of nitrogen doped YSZ (for yttria content above 5 mol%) have been made to date, we cannot compare our results with literature data, but the distortion of the cubic structure is found in all the YSZ and YSZ:N films we have studied.

The effect of the reduction of YSZ on the cell parameters has also been studied for 13YSZ samples. In fig. 4.9 X-ray diffraction patterns of 13YSZ layers

prepared in oxygen, nitrogen and reducing (Ar/H$_2$ mixture) atmosphere are shown. Compared to the films deposited in oxygen no significant difference in the diffractograms was found for the films deposited in reducing atmosphere, but the film grew preferentially with a (220) orientation.

Summarizing, two main results are obtained: (a) A distortion of the cubic symmetry in the YSZ and YSZ:N films can be observed. This might be due to the incorporated nitrogen and/or due to strain fields caused by the nano-crystalline film structures. The distortion is highly reduced after the re-oxidation/heat treatment. (b) The deposition of films in different background gas leads to different orientations of the crystalline films.

These observations require more intensive and systematic measurements in order to understand the underlying crystallographic details.

4.2 Influence of the deposition parameters

4.2.1 SIMS analysis

The following parameters were varied, in order to investigate their influence on the nitrogen content: (a) The influence of the substrate temperature was studied at three temperatures in the temperature range from 500°C to 700 °C. We found this temperature range to be optimal for the PLD deposition process of YSZ:N in nitrogen gas. As target material for this experiment we used 9.5YSZ. The cubic lattice of this material is fully stabilized and it has found the largest application in practice. We deposited films in nitrogen atmosphere with a constant pressure of 4 Pa and 4 cm distance between the target and the substrate. (b) The nitrogen gas pressure in the deposition chamber was varied in four steps in the range from 2 Pa to 8 Pa. Lower pressures led to the deposition of strongly reduced films and were not sufficient to cause nitrogen concentrations higher than 0.5 at-%. Higher pressures resulted in a poor film quality. (c) The distance d between the target and the substrate was adjusted between 4 cm and 5 cm. (d) Finally we investigated the influence of the yttria concentration in YSZ on the nitrogen concentration in thin films at constant substrate temperature, constant d and $p(N_2)$. We applied two extreme dopant concentrations, i.e. 0 mol-% (pure

ZrO$_2$) and 13 mol-% Y$_2$O$_3$ which is the practical upper limit of yttria doping in most applications. As intermediate points we choose 7YSZ and 9.5YSZ as these concentrations are widely used in practical applications.

Influence of the deposition temperature

The influence of the temperature was studied in the temperature range of 500 °C to 700 °C as these temperature range have been found optimal for the PLD deposition process. As target we have used 9.5YSZ. We deposited the layers in nitrogen atmosphere with constant pressure of 4 Pa and 4 centimeter distance between the target and the substrate - 0001 orientated Al$_2$O$_3$. The nitrogen content in samples deposited at different temperatures was subsequently analyzed by SIMS and the depth profiles are shown in figure 4.10. We found that
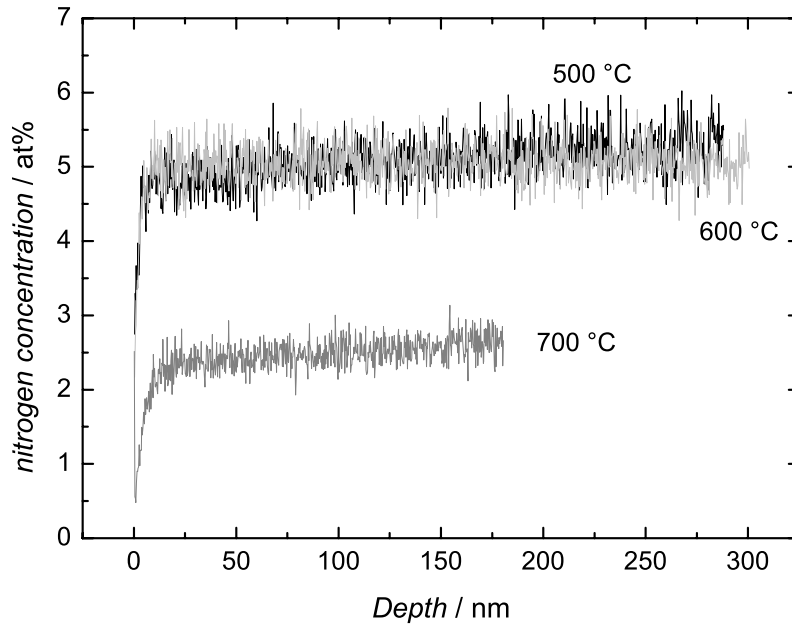
Fig. 4.10: Nitrogen depth profiles (determined by SIMS) of 9.5YSZ:N thin films deposited at different temperatures. (p(N$_2$) = 4 Pa, d = 4 cm.)

an intermediate substrate temperature around 500 °C and 600 °C leads to the highest nitrogen content of YSZ deposited in nitrogen gas. At higher tempera-

tures the nitrogen content is smaller and at lower temperatures the film quality is poor. At higher temperatures, the oxinitride is probably partially re-oxidized by oxygen impurities in the nitrogen atmosphere. In order to check this hypothesis, one ought to deposit YSZ in ultra-pure nitrogen atmospheres which is technically difficult. However, the intermediate temperature range appears to be a reasonable compromise between a declining film microstructure with decreasing substrate temperature and the decreasing nitrogen incorporation with increasing substrate temperature.

Influence of the nitrogen partial pressure and the target-substrate distance

The nitrogen pressure was varied in the PLD chamber in the range between 2 Pa up to 8 Pa. Lower pressures lead to a deposition of reduced layers and the nitrogen content drops significantly. The higher pressures result in poor layer quality and from this reason have not been investigated. Thin films deposited at different nitrogen partial pressures, keeping constant the temperature and yttria content, were analyzed by SIMS. The concentration profiles are presented in figure 4.11. We found a maximum of the nitrogen content at a nitrogen gas pressure of 6 Pa, which can easily be rationalized. With decreasing pressure the interaction between the thermal plasma and the nitrogen background gas becomes weaker and the deposited films are subject to partial reduction. With increasing pressure the interaction becomes too strong and the plasma expansion is hampered, leading to a poor film quality in general. The same dependence of the nitrogen content on the nitrogen pressure with a maximum at a pressure of 6 Pa is found for the system Ga-O-N (reported in a forthcoming study).

During the experiments on the pressure variation, we also increased the distance between the target and the substrate from 4 cm to 5 cm. This led to a significantly lower nitrogen concentration. We assume that this weaker doping effect is caused by a kind of size selection. The larger the distance the less molecular species arrive at the substrate. Larger clusters and droplets arrive at the substrate even at large distances without severe scattering on their way. And these larger clusters and particles will react less with the background gas, thus reducing the doping effect in the growing film.
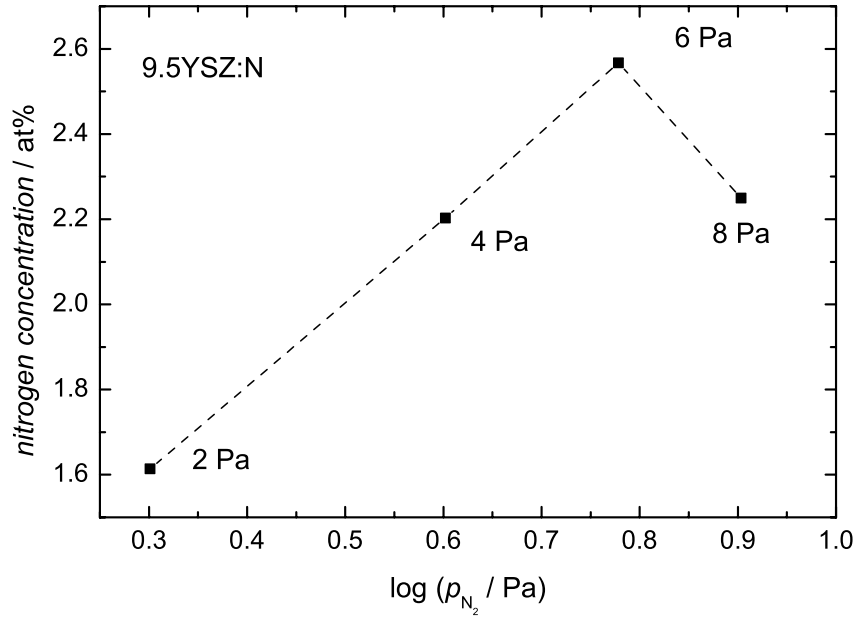
Fig. 4.11: Nitrogen concentration (determined by SIMS) in 9.5YSZ:N films deposited at different $p(N_2)$ on sapphire (0001). Deposition parameters: $T = 500$ °C, $d = 5$ cm.

In essence, also the distance between target and substrate has an optimum value. Too small distances do not allow a sufficient interaction of plasma and background gas, too large distances favor the deposition of larger clusters and droplets. In our experiments we found a distance of 4 cm as sufficient for a significant nitrogen doping.

Influence of the Y_2O_3 concentration on the nitrogen incorporation rate

The doping of pure ZrO_2 or partially stabilized YSZ bulk material (powders and single crystals) with nitrogen by thermochemical methods has already been studied extensively by Lerch [14] and Lerch et al. [4,12,13,15,16] and it has been found that nitrogen alone (i.e. anion doping) cannot fully replace the cation doping. But as in our case, Lerch et al. report an upper limit of the anion vacancy concentration in the YSZ:N compound. However, a systematic study on the nitrogen doping as a function of the cation dopant concentration has not

been performed. In fig 4.12 the nitrogen concentration is shown as a function of
the yttria content. The maximum in the nitrogen content in 7YSZ:N thin films
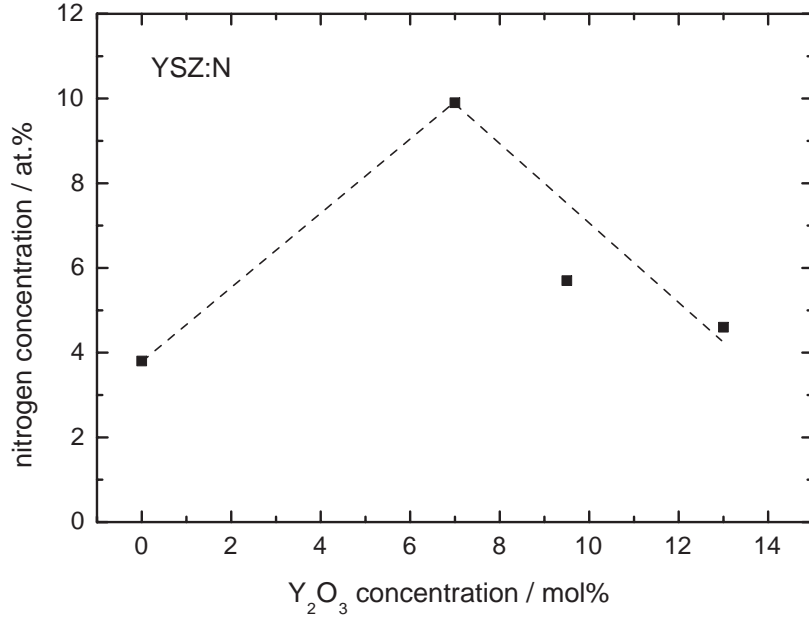
Fig. 4.12: Nitrogen concentration in YSZ:N films with different Y_2O_3 content deposited
on sapphire (0001). Deposition conditions: $T = 500\ °C$; $p(N_2) = 4$ Pa, $d = 4$ cm.

(fig. 4.12) leads to the conclusion that the total defect concentration determined
by the sum of and cation and anion dopant is an important parameter. The
fluorite-type lattice does only accommodate a limited number of anion vacancies,
and a too high defect concentration leads to a saturation effect. Practically we
observe an optimum yttria content which in our study is found in 7YSZ.

4.2.2 XPS analysis of nitrogen doped YSZ

In order to collect an integral information from a larger area and additionally to
understand more about the chemical nature of the bonds in the YSZ:N films we
investigated our films by XPS. It has been found that the 7YSZ layer properties
deviate from those with other yttria content and need additional discussion,
so we comment separately on the spectra recorded for 7YSZ. To account the

charging effects of the layers all spectra are calibrated with respect to the carbon C1s peak (E_b = 284.6 eV). In figure 4.13 the XPS spectra of a depth profiling of Y 3d; Zr 3d; O 1s; and N1s for nitrogen doped 9.5YSZ film are shown. It can
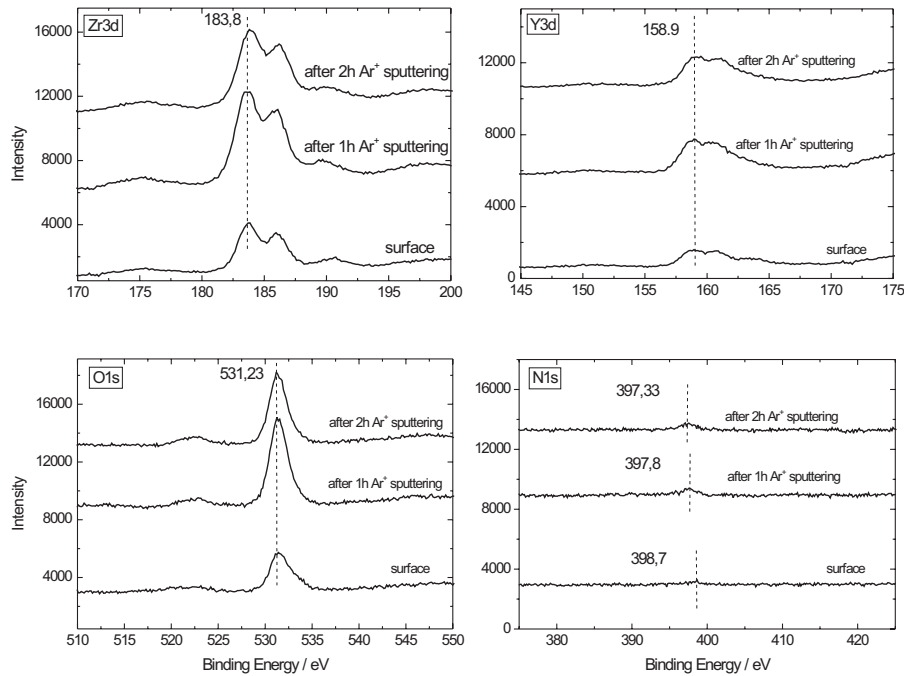
Fig. 4.13: XPS spectra of 9.5YSZ layer deposited via PLD in N_2 atmosphere at 4 Pa. *T* = 500 °C; d = 4 cm.

be seen that Y 3d; Zr 3d and O1s peak positions remain unchanged after 2h of Ar+ sputtering (corresponding to about 40 nm depth). Only the N1s peak shifts towards lower binding energies and increases in intensity with increasing depth. We assume that the surface nitrogen species have been slightly oxidized at the surface.

Nitrogen (N 1s spectra): All XPS spectra of films deposited in nitrogen (fig.4.14) show clearly the N 1s peak. In 9.5YSZ:N and 13YSZ:N the nitrogen peak is detected at 398.7 eV on the film surface and shifts towards a lower binding energy of 397.8 eV after 1 hour sputtering with Ar^+ and towards 397.3 eV after 2 hours sputtering. Thus, the binding energy gets the smaller the deeper in the film the spectra are taken. The N 1s peak for ZrO_2:N is found at a binding energy of 396.4 eV. Again 7YSZ:N shows quite different spectra: In contrast to the other

films we found a broad signal at a binding energy of approximately 402.6 eV. At the position of the nitrogen N 1s peak in 9.5YSZ:N and 13YSZ:N (397.3 eV) we found no pronounced signal. The reference value for the N 1s binding energy
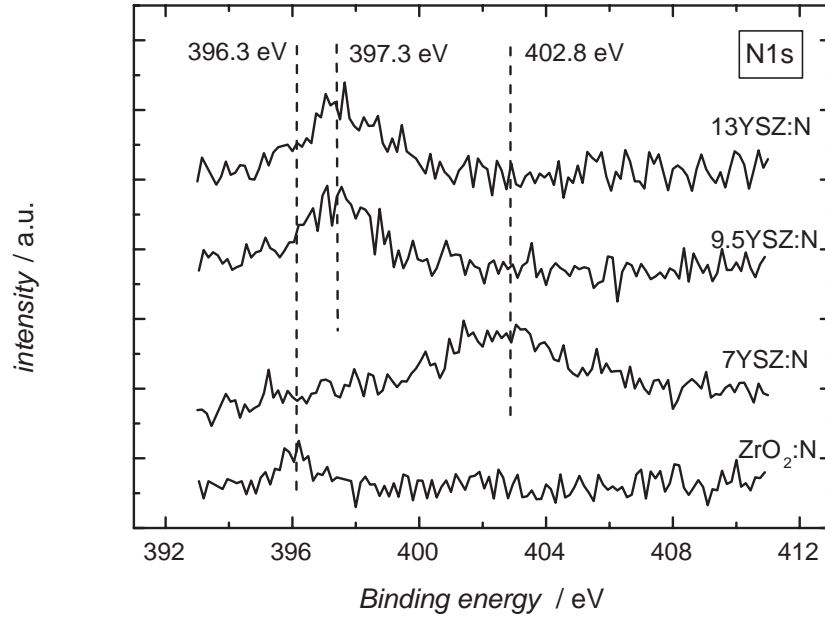
Fig. 4.14: XPS spectra of the N 1s peak in YSZ:N films of different yttria content deposited on sapphire (0001). Deposition conditions: $p(N_2) = 4$ Pa, ($T = 500$ °C, $d = 4$ cm.

of the N^{3-} state in XPS is suggested in the literature [115] as 398.5 eV for the standard compound boron nitride. As BN is a covalent rather than an ionic compound this value can only serve as a rough guide line. In other XPS studies on nitrogen containing zirconia binding energies of 396.4 eV or 396.6 eV have been reported and assigned to N^{3-} in Zr_3N_4 [116]. Soto et al. [113] suggested the value of 397.6 eV for the N^{3-} state in ZrN, whereas Milocev et al. [117,118], who investigated in situ the oxidation of ZrN to ZrO_2, have assigned the value of 397.3 eV. The same authors have suggested values of 396.3 eV and 400.05 eV for the nitrogen peaks of N-O bonds in ZrON. A higher binding energy of 403.2 eV is attributed to adsorbed N_2 species. Other authors [119,120] have registered a peak at 402.8 eV and suggested that this peak represents dinitrogen species in the solid. Finally Del Re [121] even attributed (after peak deconvolution) the

value of the N1s peak at 395.8 eV to a ZrN_2 compound. In general, the increase of the valence state of N^{3-} towards less negative values (oxidation) is always related to an increasing binding energy.

The N 1s peak positions in our spectra of thin YSZ:N films appear roughly at the same positions as reported by the other authors. However, we have to keep in mind that all data available from the literature describe pure (undoped) ZrO_2 and ZrN or Zr_3N_4. As it can be seen, the addition of Y_2O_3 to zirconia causes a shift in the Zr 3d and O 1s peaks of about 1 eV towards higher binding energies. So we can expect also a shift for the N1s peak in YSZ. We suggest that the binding energies of 397.3 eV measured on 9.5YSZ and 13YSZ represent the O-N bond in Zr(O,N) compound but not the Zr-N one. At this stage we exclude the possibility of Zr_3N_4 formation as it requires a large shift in Zr3d peak which has not been observed.

N1s spectra of 7YSZ:N: The nitrogen N 1s peak position (fig. 4.14) deviates from those recorded for ZrO_2:N, 9.5YSZ:N and 13YSZ:N. It is detected at 402.6 eV - a value very close to 402.8 eV reported by [120] for dinitrogen species. The results suggests that the high nitrogen concentration in 7YSZ:N is correlated with the presence of nitrogen species in a valence state more positive than 3−. At this stage it is still too early to conclude whether nitrogen is present as N^{3-}, N^{2-} or as already reported dinitrogen - N_2^{x-}. There are no systematic studies concerning this system and our results cannot be compared with known standards, but the existence of nitrates (i.e. N^{x+}) can be excluded because the binding energies of the nitrates are much higher (up to 10 eV) than those recorded for our films.

The main question, we cannot answer unequivocally on the basis of the present results, concerns the valence state of nitrogen in zirconia. Usually it is accepted that N^{3-} is incorporated in the anion sublattice and our results do not disagree with this hypothesis. The N 1s peak at a high binding energy in 7YSZ:N is not in agreement with the simple picture of N^{3-} ions. Rather this observation suggests the existence of nitrogen molecular ions in the YSZ lattice. We cannot exclude this possiblity, as nitrogen dianions are stable in other ionic compounds. To confirm such suggestions more detailed studies with a monochromatic X-ray source with much higher intensity and better energy resolution (synchrotron

Table 4.1: N 1s binding energies of different nitrogen containing zirconium compounds

	N 1s (E_b / eV)	compound	bond	reference
1.	398.5	BN	kovalent	[115]
2.	396.4	Zr_3N_4	Zr-N	[116]
3.	397.6	ZrN	Zr-N	[113]
4.	397.3	ZrN	Zr-N	[117, 118]
5.	396.3, 400.05	ZrON	N-O	[117, 118]
6.	403.2	N_2	kovalent	[117, 118]
7.	402.8	ZrON/TiON	M-N≡N-M *	[119, 120]
8.	395.8	ZrN_2	Zr-N	[121]
9.	396.4	ZrO_2:N	N-O	this study
10.	397.3	9.5YSZ:N, 13YSZ:N	Zr-N	this study
11.	402.6	7YSZ:N	M-N≡N-M *	this study

* dinitrogen species

radiation) are required in order to investigate in situ the changes of the nitrogen either during its incorporation (reduction) or upon oxidation. Combined with quantum mechnical calculations these experiments might clarify the valence state of nitrogen in YSZ. However, these findings should be taken as first hints, and a systematic XPS study on YSZ and YSZ:N is clearly missing.

Zirconium (Zr 3d spectra): The position of the Zr $3d_{3/2}$ peak in ZrO_2 is found at 182.4 eV in exact agreement with the literature [115], and the peak is shifted to higher binding energies in YSZ:N - respectively to 183.4 eV in 7YSZ:N; to 183.8 eV in 9.5YSZ:N and to 183.9 eV in 13YSZ:N. This shift of more than 1 eV relative to yttria free zirconia was confirmed to be reproducible.

In YSZ:N (fig. 4.15) the binding energies of the Zr 3d doublet are not shifted towards the values typical for the ZrN bond (about 180 eV) as suggested by [117, 118, 120, 122], but are closer to those assigned to the ZrON bond (182.2 eV). But even here the difference of 1.4 eV does not allow to assign the chemical bond to an oxynitride composition as reported in the literature.

The Zr $3d_{3/2}$ peak position is not shifted towards lower binding energies by the nitrogen incorporation, and thus, the reduction of Zr^{4+} can be excluded
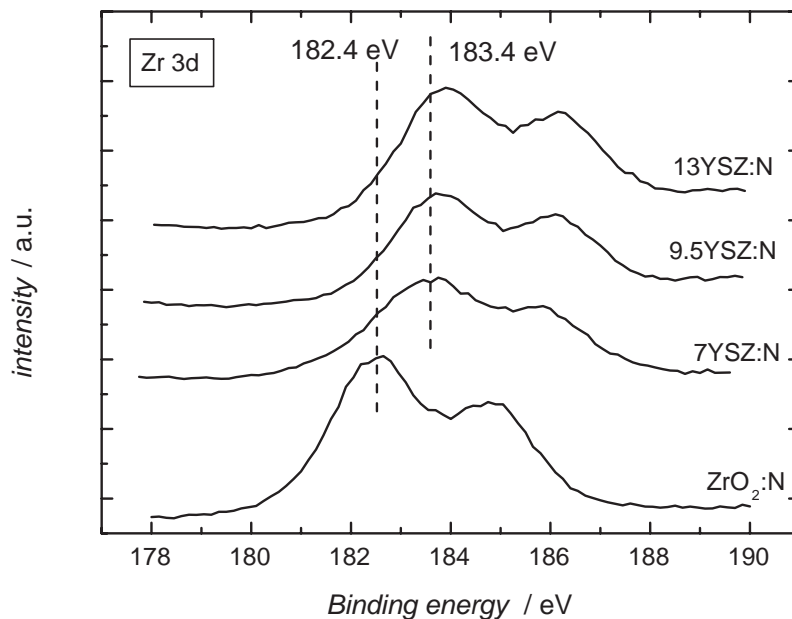
Fig. 4.15: XPS spectra of the Zr 3d doublet in YSZ:N films of different yttria content deposited on sapphire (0001). Deposition conditions: $p(N_2) = 4$ Pa, $T = 500$ °C, $d = 4$ cm.

within the limit of detection. The depth profiling of different YSZ materials upon sputtering with argon ions (up to 2 h) demonstrates that the Zr3d peak remains unchanged for each YSZ composition. The recorded higher binding energies of Zr $3d_{3/2}$ in YSZ compared to ZrO_2 has to be explained by the changes of the crystalline structure of the films and the presence of yttrium.

Oxygen (O 1s spectra): The O 1s peak of ZrO_2:N is found at a binding energy of 530.4 eV. In 7YSZ:N and 9.5YSZ:N the signal lies at about 531.2 eV and in 13YSZ the peak is found at 531.4 eV (fig. 4.16). These values are in a good agreement with those suggested in the literature (see discussion).

No comprehensive study on the XPS spectra of pure and yttria doped zirconia can be found, and different opinions about the position of the O 1s peak in pure zirconia have been published. The reported binding energies for O1s vary in the range from 529.7 eV to 530.9 eV [117,118,120,122], whereas the value suggested

Fig. 4.16: XPS spectra of the O 1s peak in YSZ:N films of different yttria content deposited on sapphire (0001). Deposition conditions: $p(N_2) = 4$ Pa, $T = 500$ °C, $d = 4$ cm.

in [115] is 531.3 eV. In our experiments the addition of yttria to ZrO_2 shifts the O1s peak towards higher binding energies by approximately 0.9 eV compared to those for the pure oxide.

Yttrium (Y 3d spectra): In figure 4.17 the Y 3d spectra of different nitrogen-doped zirconia films are shown. The Y $3d_{3/2}$ peak appears at a binding energy of 158.9 eV (E_b for pure Y_2O_3 is 158.4 eV) irrespective of the yttria content. The peak intensity increases with increasing yttria concentration. Y 3d spectra do not shift with increasing yttria content. We can definitely exclude a possible yttrium nitride formation from a further consideration because the suggested binding energies for Y $3d_{3/2}$ peak in YN are much lower (156.6 eV) [123] than those recorded for our films (the standard for pure Y_2O_3 is $E_b = 158.4$ eV).

Quantitative analysis of the XPS spectra: The element concentration within the different films is obtained by integrating the XPS peak area. The results are presented in table 4.2.
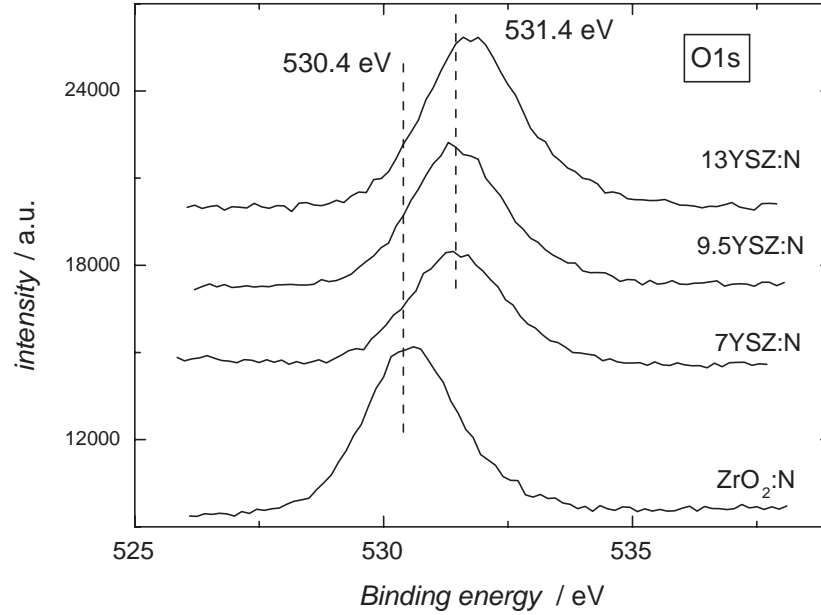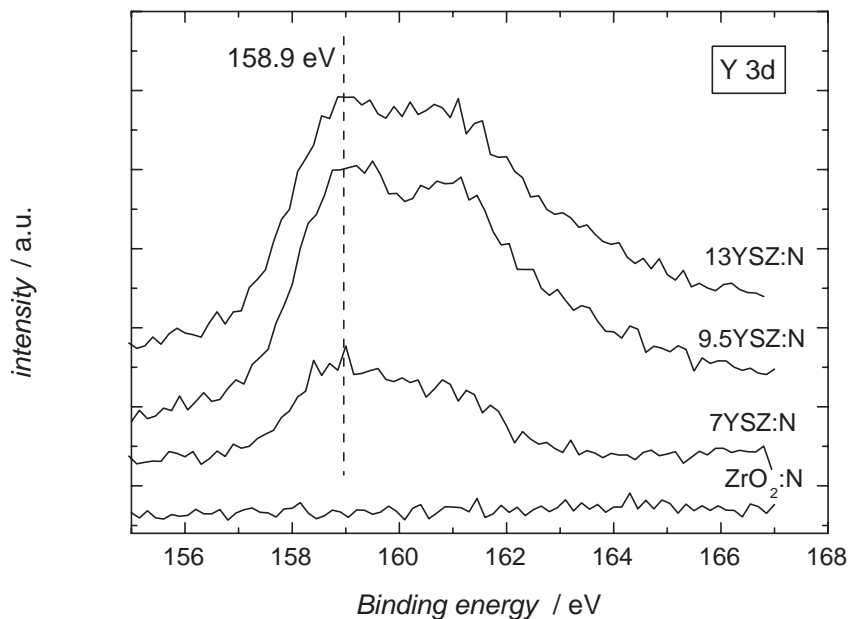
Fig. 4.17: XPS spectra of the Y 3d doublet in YSZ:N films with different yttria content deposited on sapphire (0001). Deposition conditions: $p(N_2) = 4$ Pa, $T = 500$ °C, $d = 4$ cm.

The highest nitrogen content was found in 7YSZ:N, followed by 9.5YSZ:N, 13YSZ:N and ZrO$_2$:N.

The nitrogen concentrations determined by XPS and SIMS do not agree exactly and differ by 20% up to 30%. As XPS collects the integral information from the whole surface of a sample and the concentrations given above are relative, and as SIMS data could also give an error of maximum 10%, this difference is acceptable. Nevertheless we can conclude that PLD is suitable for nitrogen doping and results in nitrogen concentrations of up to 10 at-%.

Additional information can be obtained from the relative concentration changes as determined by XPS (O 1s, Y 3d and Zr 3d). Obviously ZrO$_2$ dissolves only a small concentration of nitrogen under the given experimental conditions, and the metal/non metal ratio corresponds within the experimental to a 1:2 stoichiometry. Roughly the same 1:2 ratio is obtained for the 9.5YSZ:N and

Table 4.2: Concentration of nitrogen in YSZ:N thin films as a function of the Y_2O_3 content as evaluated from XPS deposition conditions: $p(N_2)$ = 4 Pa, T = 500 °C, d = 4 cm.

composition	N / at%	O / at%	Zr / at%	Y / at%
ZrO_2:N	1.6	63.5	34.8	-
7YSZ:N	12.1	63.7	19.7	4.6
9.5YSZ:N	7.1	58.3	23.6	10.9
13YSZ:N	6.5	56.8	23.5	13.1

13YSZ:N films, but the yttrium/zirconium ratio is unreasonably high. Clearly the 7YSZ:N film shows the highest nitrogen content, corresponding to approx. 16 % of the anions. But the metal/non metal ratio is here unreasonably small (approx. 1:2.7). Even neglecting the nitrogen, the oxygen to metal ratio is still too high. Thus, at this point we can only conclude that nitrogen has definitely been incorporated with concentrations of several per cent. The exact content cannot be given. Whereas the integration of the XPS peaks leads to some unreasonable results, the spectra themselves are reliable and give clear evidence for the homogeneous dissolution of atomic nitrogen in YSZ. Only in the case of 7YSZ:N there is additional evidence for molecular nitrogen species.

4.2.3 Optical spectroscopy on N-doped YSZ layers

All nitrogen-containing samples were transparent but of violet or dark violet color. We measured absorption spectra of YSZ:N films containing different amounts of yttria, deposited either on silica glass or on sapphire substrates. For the calibration we measured the absorption of the pure substrates as well as the absorption of YSZ deposited in oxygen and in argon atmosphere, i.e. without any nitrogen content. All spectra were collected at room temperature and at 300 °C, but no influence of the temperature on the absorption spectra was observed. In figure 4.18 the absorption spectra of YSZ, YSZ:N and ZrO_2:N films are shown. The absorption spectra of all nitrogen-doped films show a broad absorption band in the range of the visible light, with a maximum at a wavelength of approximately 500 nm. Additionally, a shift of the absorption edge towards larger wavelengths compared to samples prepared in oxygen or in
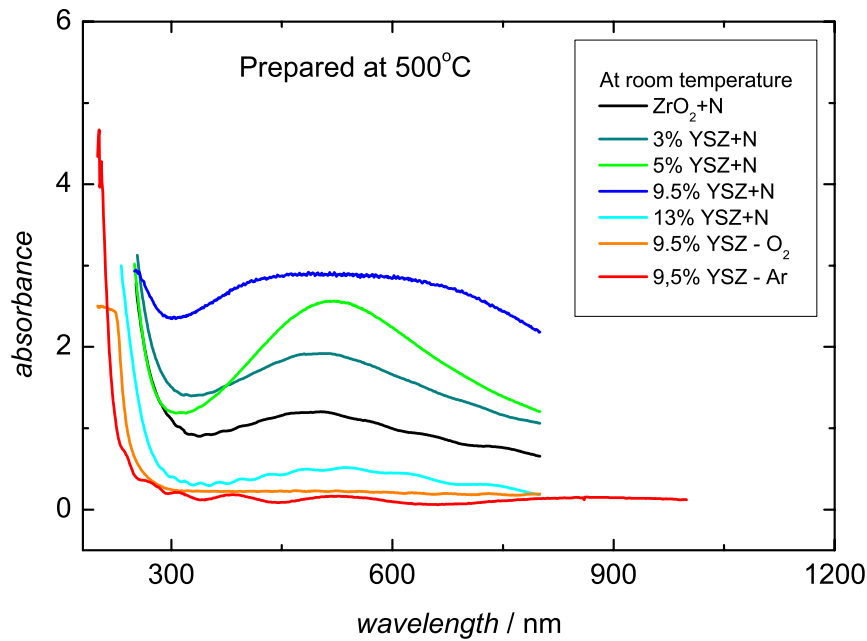
Fig. 4.18: Optical absorption spectra of ZrO_2, YSZ and YSZ:N films of variable yttria content (deposited on silica glass) at room temperature. Deposition conditions: $p(N_2)$ = 4 Pa, T = 500 °C, d = 4 cm, film thickness: 2 μm, an offset of approx. 0.5 abs. units was used)

argon is detected. The edge of the 9.5YSZ film deposited in argon is found deep in the UV range at about 200 nm. In 9.5YSZ deposited in oxygen it shifts to approximately 220 nm. The nitrogen doping shifts the absorption edge to about 250 nm. In the spectra of the other samples doped with different amounts of Y_2O_3, this shift is also observed - but as in these experiments two parameters were changed (both nitrogen and yttria concentrations), we cannot relate this effect only to the nitrogen content. The "oscillations" in the absorption spectra of 9YSZ prepared in Ar and 13YSZ:N deposited in nitrogen (see figure 4.18) can be attributed to interference effects of the films. A significantly different spectrum was recorded with the 7YSZ:N film, see figure 4.19. The optical band edge is determined as 201 nm. An absorption peak at 263 nm is registered, which is not observed in films with other yttria concentrations. In 7YSZ:N the typical broad absorption maximum is shifted to lower wavelengths and is
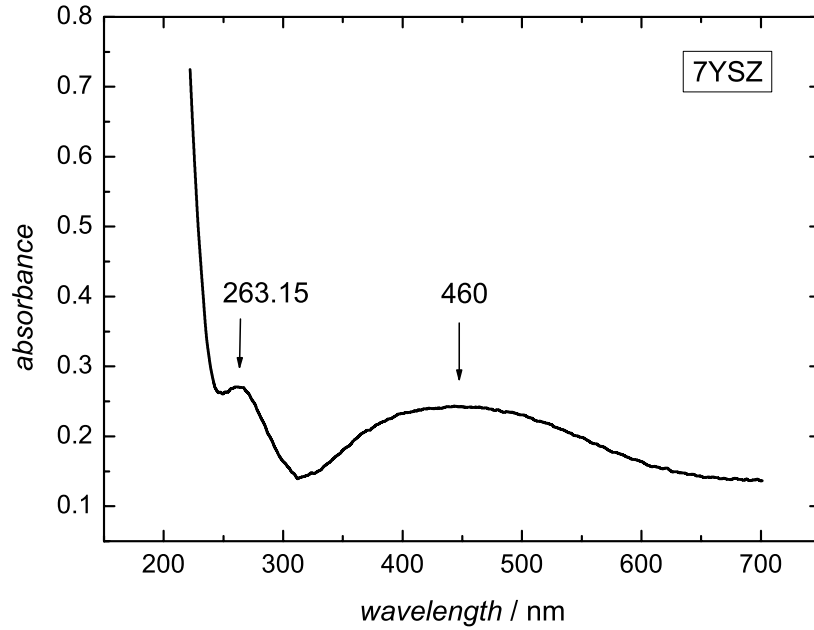
Fig. 4.19: Optical absorption spectrum of a 7YSZ:N film on sapphire (0001) at room temperature. Deposition conditions: $p(N_2)$ = 4 Pa, T = 500 °C, d = 4 cm.

centered at 455 nm.

The results from the optical spectroscopy measurements of YSZ:N show a broad absorption band around 500 nm, while the nitrogen free reference samples prepared in oxygen and argon atmospheres show practically no absorption in the UV and VIS range. Like in the SIMS and XPS studies, the nitrogen-doped 7YSZ:N sample exhibits a different behavior and shows an additional absorption maximum at 263 nm. This maximum might also be related to a second type of nitrogen differing in its charge or in its position in the lattice of zirconia. The broad absorption around 500 nm is typical for nitrogen doped and/or reduced material [124] and suggests that nitrogen energy levels are placed almost in the middle of the band gap in the non-stoichiometric zirconia. This finding is clearly supported by theoretical calculations [52].

5 Transport properties

Studies on the transport properties of cubic and tetragonal nitrogen stabilized YSZ were already published [4,6–8,12,14,51]. According to these studies YSZ:N shows not only a super ionic (oxygen) conductivity but it is also supposed to be a nitrogen ion conductor. The values for the activation energies of nitrogen ion movement determined by different methods were found to be close to 2 eV. The diffusion coefficient of nitrogen in YSZ was found to vary in the range from 10^{-13} cm^2/s to 10^{-11} cm^2/s depending on the temperature. A study on the transport properties of partially stabilized (TZP) nitrogen doped samples by micro-contact impedance measurements was also recently reported by Lee et. al [125]. The summarized results of the existing literature on the transport properties of N-doped YSZ (in both tetragonal and cubic modification), the activation energy and the diffusion coefficient of the N^{3-} ion are given in table 5.1. The reported activation energies for the nitrogen diffusion in YSZ are

Table 5.1: Activation energies and diffusion coefficients for YSZ at 1000 K

Material	Experiment	E_a / eV	D_N / $cm^2 \cdot s^{-1}$	Reference
YSZ cubic	EIS	0.84 - 1.16	-	[4]
YSZ tetr.	Diffusion (AES)	1.92	1.63×10^{-11}	[6, 7]
YSZ tetr.	EIS (Raman)	1.76	5.24×10^{-12}	[8]
YSZ cubic	^{15}N diffusion	2.1	2.084×10^{-11}	[9]

approximately twice as high as those for oxygen and the diffusion coefficient is three to four orders of magnitude lower. However, based on the extrapolation of the existing experiments at lower temperatures, at high temperatures (above approx. 1200 °C) the diffusion coefficient of nitrogen should be comparable

to the diffusion coefficient of oxygen [9, 53, 54]. In addition the diffusion of nitrogen ions in PLD deposited YSZ:N films was found to be faster compared to the samples prepared by other methods [9, 54].

Experimental details

We studied the transport properties of nitrogen-doped YSZ thin films by two point contact impedance spectroscopy as a function of the temperature and the nitrogen content. The YSZ:N films were prepared by PLD (see chap. 4) on (0001) sapphire substrates, where the nitrogen content was varied from 0 at.% (nitrogen free 9.5YSZ) up to 6 at.% nitrogen (determined by SIMS). The temperature was varied in the range of 500 °C up to 800 °C. The working electrode was a Pt micro-electrode with a geometrical surface of approx. 3×10^{-4} cm^2. The counter electrode was a platinum paste dried in air for 24 hours with a contact area of about 0.25 cm^2. Both electrodes were placed on the upper side of the samples. The conductivity of the films was calculated according to:

$$\sigma = \frac{1}{2dR} \tag{5.1}$$

where σ is the total conductivity, d is the diameter of the electrode and R is the determined DC resistance. In order to obtain a more detailed information the experimentally recorded spectra were further deconvoluted. The fit procedure was performed with the programm *EQUIVALENT CIRCUIT* written by B. Boukamp (a standard support to the impedance analyzer). A detailed discussion on the application of micro-electrodes in solid state electrochemical studies is given by Fleig [109].

5.1 Impedance spectroscopy

In figure 5.1 a typical impedance spectrum (the red circles) of YSZ:N films is presented. It shows two semicircles (the second one at the lower frequencies appears only partially) representing the bulk and the electrode impedance respectively. The dashed line (depicted also by black squares) is the fitted dispersion calculated on the basis of the equivalent circuit shown in the figure. Thus we succeeded to separate the contribution of the bulk and the grain boundaries
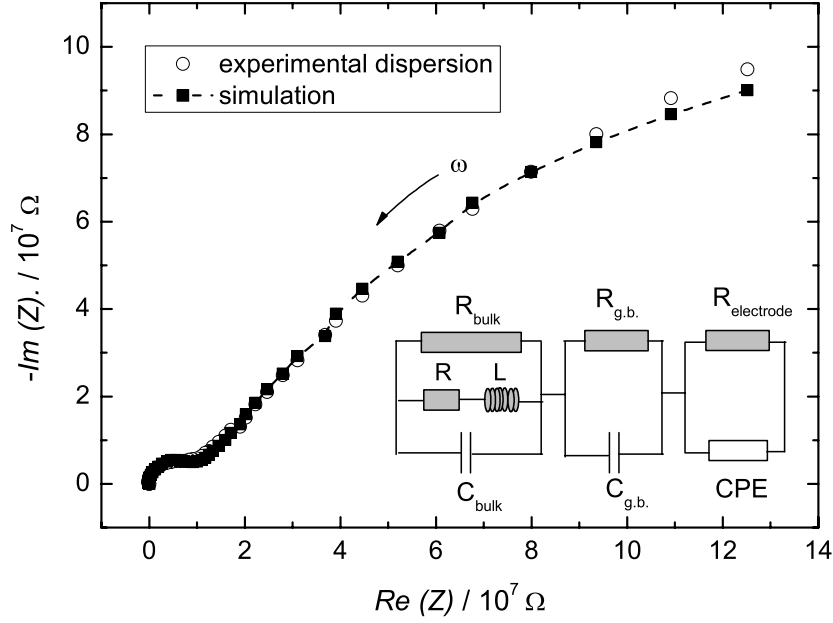
Fig. 5.1: Complex impedance plane (Nyquist plot) of 9.5YSZ:N thin film, deposited on sapphire substrate, measured on a platinum microelectrode. $T = 775$ °C, in pure N_2 $(a(O_2) = 10^{-14})$

to the total impedance of the first semicircle. An additional inductive loop at higher frequencies appears after the subtraction. The appearance of this inductive loop has been already reported by [125–128]. Boukamp [128] interpreted this loop as a result of a "crosstalk" between the reference and the working electrode in the presence of mobile ionic oxygen species in the case that both electrodes are placed close to each other. However, in our two point measurements both electrodes were more than 1 cm apart and the potential drops at a distance of $2d$ (d is the diameter of the micro-electrode). We assume as more reasonable the interpretation of Fleig [125] who suggested the heating element (beneath the sample) as an origin of the inductive loop. The fit parameters are summarized in table 5.2. As mentioned above the first two sub-elements in the equivalent circuit present in fig. 5.1 represent the contribution of the bulk and the grain boundaries. The third sub-circuit consists of a parallel connected resistance ($R_{electrode}$) and non-ideal capacity - a constant phase element (CPE). The impedance of the constant phase element is given by $Z = (A(i\omega)^n)^{-1}$, where

Table 5.2: The sub-circuit parameters calculated after deconvolution of the experimental
spectra shown in fig. 5.1

Sub-circuit 1	R_{bulk}	R	L	C_{bulk}
	$7.9 \times 10^6 \ \Omega$	$4.4 \times 10^5 \ \Omega$	1.1 H	6.8×10^{-12} F
Sub-circuit 2	$R_{g.b.}$	-	-	$C_{g.b.}$
	$7.5 \times 10^6 \ \Omega$	-	-	1.1×10^{-10} F
Sub-circuit 3	$R_{electrode}$	-	n (CPE)	A (CPE)
	$2.6 \times 10^8 \ \Omega$	-	0.75	1.1×10^{-9}

A and n are fit parameters, i is $\sqrt{-1}$ and ω is the frequency in Hz.

From the parameters attained by the deconvolution procedure it is clear that
the resistance of the "bulk" (grains) and the the grain boundaries are of the
same order (approximately equal), but the capacity of the grain boundaries is
approximately two orders of magnitude higher than the capacity of the bulk.
The impedance of a simple parallel circuit is given by the equation:

$$Z_{\text{parallel}} = \frac{1}{\frac{1}{R} + i\omega C} = \frac{R}{1 + i\omega RC} \tag{5.2}$$

Thus comparing the complex impedance of these two parallel circuits we con-
clude that the impedance of the grain boundaries is definitely smaller than those
of the bulk because of the much higher capacity, i.e. the charge stored in the
grain boundaries is definitely larger. This result confirms the results from the
SIMS analysis after nitrogen incorporation in poly-crystalline thin films (see
figure 6.24) also suggesting that nitrogen is stored in the grain boundaries.
However the effect of the grain boundaries and their contribution to the to-
tal conductivity is well known and is thoroughly discussed for different solid
electrolytes by Fleig [106–109].

In order to determine the activation energies of the ionic movement in the
YSZ:N thin films we recorded the impedance spectra at different temperatures.
The evaluation of the experimental data was carried out for the total response
of the system, i.e. $Z_{\text{bulk}} + Z_{\text{g.b.}}$ but excluding the impedance of the electrode.
In fig. 5.2 the temperature dependence of the conductivity of samples with a
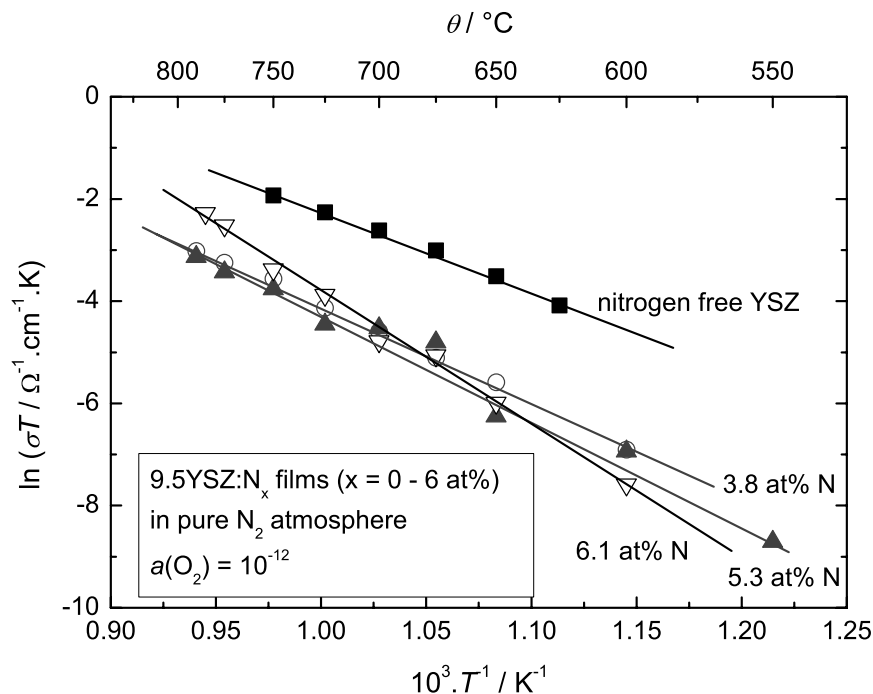
Fig. 5.2: Arrhenius plot of the temperature dependance of conductivity of different 9.5YSZ:N samples

different nitrogen content are presented. The nitrogen-free sample shows the highest conductivity and the lowest activation energy in the whole temperature range. The conductivity of the nitrogen-doped samples decreases up to temperatures of approximately 700 °C and increases above this temperature with the increasing nitrogen content. In fig. 5.3 the activation energies are present as a function of the nitrogen concentration. Their values vary from 1.3 eV for 9.5 YSZ up to 1.92 eV for 9.5YSZ:N (with 6.1 at.% nitrogen). The increase is not ideally linear but is pronounced and confirms the tendency reported already by Wendel and Lerch [4, 14]. The increase of the ionic conductivity with the nitrogen content is explained in [4, 14] as a result of the increase in the number of oxygen vacancies created by the incorporated nitrogen ion (incorporation of N^{3-} is assumed) according to equation 1.3 (see chap. 1.1, p. 3). Thus the effect of the combined doping (cation + anion) results in a creation of more oxygen vacancies and leads to a super ionic (oxygen) conductivity. However, the in-
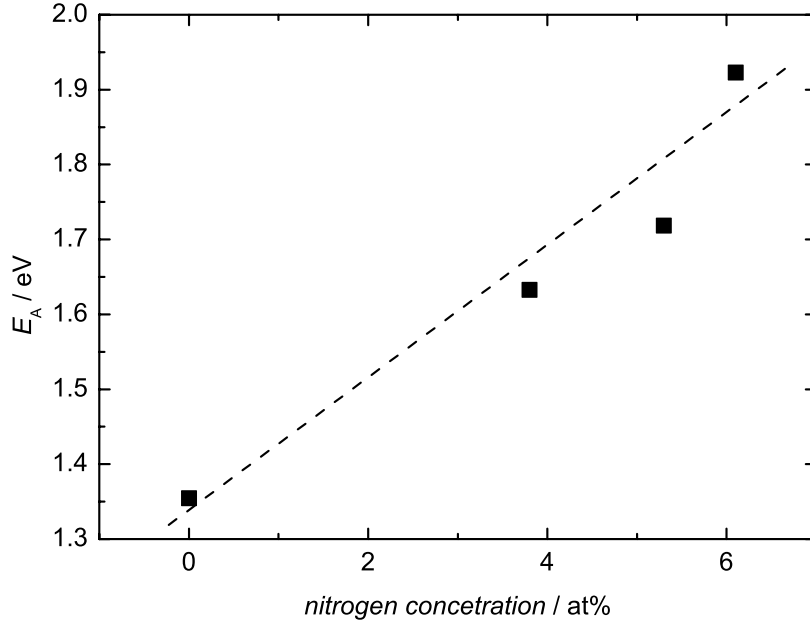
Fig. 5.3: The activation energies of the ionic transport in 9.5YSZ:N as a function of the nitrogen concentration

crease of the activation energies can be associated with a formation of clusters between the nitrogen ions and the oxygen vacancies hindering the oxygen ion or vacancy movement.

We should also mention that the conductivities measured on the thin YSZ and YSZ:N films are approximately of two orders of magnitude lower than those measured for the bulk samples, which we associate with the microstructure of the films. However no reports on the conductivity of thin YSZ:N films for a comparison were found.

Thus the nitrogen-doped zirconia films were found to show a lower total conductivity and higher activation energy than the nitrogen-free YSZ films.

In addition on the basis of the fit analysis of the recorded impedance spectra we succeeded to determine the distinct activation energies for the ionic transport in the grain boundaries and in the "bulk". In fig. 5.4 Arrhenius plot with the individual conductivities for 9.5YSZ:N sample is shown. From the values for
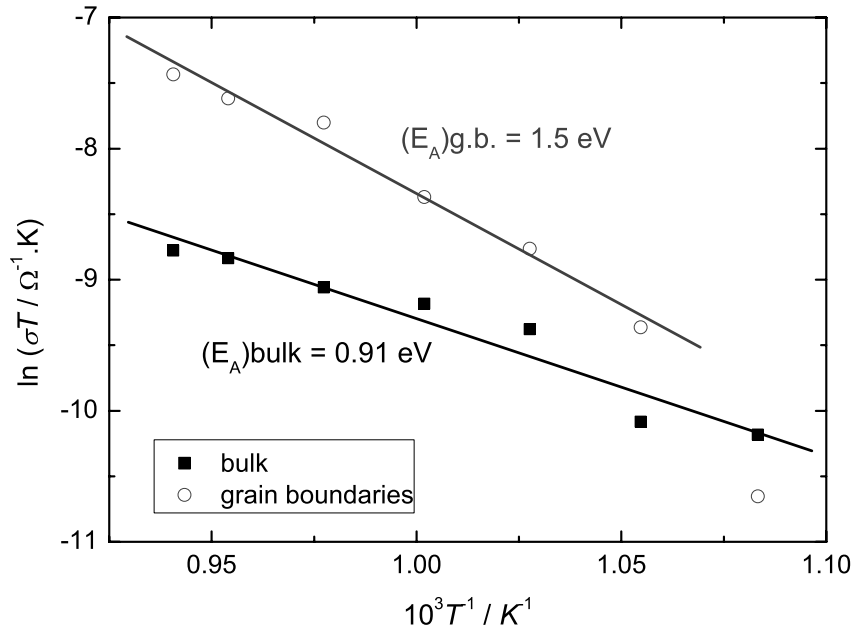
Fig. 5.4: The individual activation energies of the ionic transport in the grain boundaries and in the bulk for 9.5YSZ:N, the nitrogen concentration was 5.3 at.%

the activation energies we concluded, that the transport in the grain boundaries is definitely slower than those in the grains, thus, limiting the rate of diffusion. The variation of the nitrogen concentration in the films was found also to be an important factor. For the 9.5YSZ:N films with a higher nitrogen content (i.e. 6.1 at.%) the activation energies for both grain boundaries and bulk increase and become virtually equal ($E_A \approx 2$ eV). At lower nitrogen content (approx. 3.5 at.% nitrogen) and also in the nitrogen-free sample the separation into two sub-semicircles was not possible as they both overlay.

6 Electrode processes

The study of the electrode processes on solid oxide electrolytes is even more complicated than in liquids. The main differences origin from a difficulties by contacting the solid electrolyte, the non-defined electrode surface and the change of the chemical composition (usually reduction) of the electrolyte at higher voltages. It requires more thorough understanding of the chemical reactions coupled to the defect related properties of the material. The kinetic studies of an electrochemical reaction refers to specific working conditions, i.e. a particular electrolyte concentration, a particular electrode material, temperature (or temperature range), etc. In the case of solid oxide electrolytes the important parameters which should be initially defined and should be kept constant for all experiments are the temperature (T), the pressure (P), the structure, the chemical composition and the defect related properties of the electrolyte. We should define the base material with its crystallographic structure, the doping agent with its particular concentration and respectively the vacancy and/or interstitial ions concentration in order to perform reproducible measurements.

Below we discuss the most important factors influencing the kinetics of the nitrogen electrode, respectively its reaction mechanism. The recorded electrochemical characteristics and their interpretation depend on the following parameters.

- The composition of the electrolyte, i.e the predominant charge carriers; the conductivity, respectively the resistance (also denoted as IR drop); the strength of interaction between oppositely charged ions.

As in liquid electrolytes, we need to perform the electrochemical measurements in the solid state at maximal conductivity, respectively minimum resistance,

in order to prevent the influence of the ohmic drop (IR) and migration effects in the electrolyte. In solid electrolytes we cannot apply conductive additives (supporting electrolyte), so we need to achieve the highest possible conductivity of all charge carriers. The strength of interaction between the ions in the crystal defines the interaction with the electrode material and the adsorbed species situated between and as well determines the mobility of the ions inside the material.

- The materials of the working and counter electrodes.

The only requirements for the counter electrode material is to be stable in the particular temperature range and not to diffuse into the electrolyte, thus changing its properties (of course for metal ion conducting electrolytes as $AgCl$, $AgBr$, $CuBr$ etc. this requirement is not relevant). The electrode also should have a good adhesion to the electrolyte in order to ensure a sufficient electrical contact.

The choice of the working electrode material is most important for in the kinetic studies. Different materials usually have different catalytic properties with respect to the particular redox reaction, thus determining the rate and the mechanism. We need a chemically inert material (usually noble metals are used) which does not solve, absorb or adsorb any species. The presence of electrochemically active or even inactive species on the electrode surface will automatically reflect in a change of the current - potential characteristics. The active species can influence the rate of the reaction and the inactive species could block partially or fully the electrode surface. The selection of an electrode material being specifically active towards a certain redox reaction, thus changing its kinetics and mechanism (enhancing the reaction rate), is a powerful tool to catalyze a particular process.

- The capacity and the structure of the electrical double layer.

We have already discussed that the structure of an electrical double layer plays an important role in the kinetics of the electrochemical reactions. It is related to the overvoltage and can either lower it (attracting oppositely charged ions)

or increase it by repelling like charged ions. In addition the adsorption leads to a change in the thickness of the Helmholtz layer and as higher is the thicknes of EDL, respectively as more difficult is the electron transfer and as higher is the polarization (overvoltage) accompanying the redox processes. The specific adsorption of ionic species or gas molecules on the electrode/electrolyte interface can drastically change the EDL capacity and leads sometimes to a complete blocking of the reactive surface. In order to predict a possible adsorption or to provide optimal working conditions it is important to know the position of the potential of zero charge (pzc). This potential is also specific for each electrode/electrolyte composition. An additional problem may arise due to an adsorption of neutral species which could cause an increase of the expected limiting current as a result of synergetic effect known also as exaltation current [129]. The capacity of the electrical double layer provides an important information about the surface adsorption and the energetic barrier for the charge transfer. The change in the EDL capacity can also be used as a criterion for adsorption/desorption surface processes.

- The choice of the reference electrodes.

The selection of the reference electrode is no problem at all in liquid systems, but often causes difficulties in the case of solid electrolytes. The correct evaluation and interpretation of the experimental results depends on the stability and reproducibility of the reference electrode defined by a suitable reference reaction.

- Surface vs. bulk properties

In order to perform the experiments on the electrochemical nitrogen activity at defined and reproducible conditions on solid oxygen conducting electrolytes we should also take into account the difference between the surface and the bulk properties of the ceramics. This problem is not relevant in the classical electrochemistry of liquid electrolytes where the electrodes are immersed in the electrolyte but is quite relevant for the solids. This difference is important for a comparison between the potentiodynamic and steady state experiments, as the first "senses" only the surface concentration of the species and usually there

is no bulk "response". Only under steady state conditions we obtain results representative for the complete system.

Experimental details

The electrochemical experiments were performed with YSZ and YSZ:N films of thickness of approximately 3 μm deposited by PLD on Zr/ZrO_2 substrate of size approximately 10 mm $\times$ 10 mm, where the ZrO_2 film of thickness $\approx$ 1 μm) was previously deposited also by PLD. The yttria content in the films was in the range 3 mol-% up to 13 mol-%. The experiments with single crystals were performed with (111) orientated 9.5YSZ with a size of 10 mm $\times$ 10 mm. The working electrodes were tip micro-electrodes of silver, gold or iridium with a diameter varying in the range (depending on the experiment) between 1 μm and 100 μm or photo-lithographically printed micro-electrodes of gold and iridium with a size of 100 μm $\times$ 100 μm. As counter electrode for the thin film experiments was used the Zr/ZrO_2 substrate serving also as a reference electrode with a fixed oxygen activity. For the experiments with single crystals a Zr/ZrO_2 reference electrode was used (Zr wire covered with ZrO_2 by PLD) and as an auxiliary electrode a platinum paste painted and subsequently burned for 2 hours at 250 °C in air on the back side of the samples.

The electrochemical experiments were performed in air, or in ultra-pure nitrogen, respectively ultra-pure argon atmospheres with oxygen activity of $a_{O_2} = 10^{-14}$ measured with a YSZ oxygen sensor at the outlet of the electrochemical cell. To achieve this extremely low oxygen activity the commercial nitrogen and argon gases were purified by purging through a TiN (for argon Ti) oxygen trap heated to 450 °C.

After the experiments the samples were analyzed by SIMS, XPS, AFM and optical spectroscopy.

6.1 Definition of the initial parameters and the working conditions

The initial parameters as discussed above and the working conditions are defined in the following section. These parameters are important for the interpretation

of the current-potential experiments and for the general understanding of the complex process of electrochemical nitrogen reduction.

6.1.1 Selection of appropriate electrode materials

The material of the working electrode has been selected among the group of the noble metals as we needed a stable and reproducible surface, inert towards the surrounding environment. We have considered the noble materials in order to perform two different experiments. Firstly we intended to study whether nitrogen can be incorporated electrochemically at all, i.e. to prove its electrochemical activity and its mobility in the zirconia lattice. For this purpose we need a material showing a large overvoltage for the oxygen reaction[1] and a low overvoltage for the nitrogen reaction. We have choose three of the most often used electrode materials - gold, silver and platinum as possible candidates. Considering platinum there are two major problems using it as working electrode. Platinum is known to react with YSZ at cathodic voltages of about -1 V forming a series of Pt-Zr alloys [130]. The latter results in enlarging the real electrode surface and modifying the electrolyte at the contact point irreversibly. Secondly platinum is a well known catalyst for the oxygen reaction and adsorbs oxygen chemically. It may also form different PtO_x stable at temperatures of up to 750 °C [131, 132]. So we discarded platinum as a suitable electrode material. To choose between gold and silver we recorded the current-voltage characteristics of Au and Ag electrodes in oxygen atmosphere to test which of the both materials show larger oxygen overvoltage for the cathodic reaction. In figure 6.1 the E/I curves of micro electrodes are shown. At anodic potentials oxygen is much more easily oxidized on silver than on the gold electrode, but in the cathodic region the oxygen reduction is definitively faster on Au micro electrode and proceeds at much lower overvoltages. So we can conclude that the catalytic activity of gold for oxygen reduction at negative potentials is higher than of silver. Thus, regarding the nitrogen incorporation experiment silver appears to be the more appropriate electrode material.

---

[1]The oxygen reaction is involved as oxygen is always present in small amounts in the purified gases. Even in an ultra pure atmosphere ($a_{O_2} < 10^{-10}$) we can expect some oxygen appearing as a result of the electrode (oxygen) reaction at the anode side.
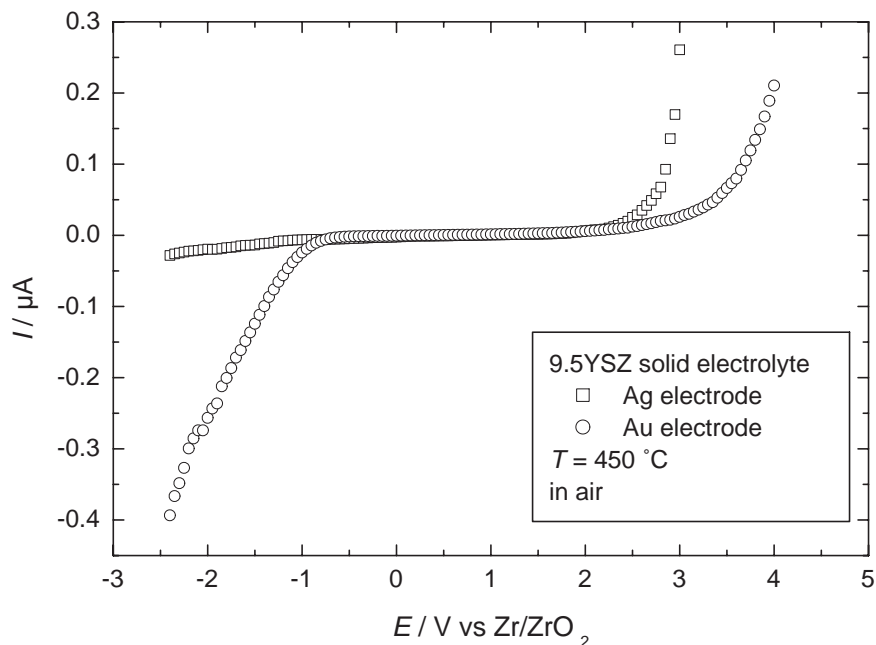
Fig. 6.1: Comparison of the electrochemical activity of Ag and Au micro electrodes for the oxygen reaction on a 9.5YSZ thin film at 450 °C.

For the kinetic experiments on the mechanism of the nitrogen reduction we found gold much more appropriate as an electrode material than all other noble metals. Silver can dissolve oxygen in its lattice and Pt, Ir, Ru and Rh posses a well known catalytic activity. Gold on the other hand is well known as an inert material which does not specifically adsorb oxygen, hydrogen or nitrogen. Thus, in our kinetic experiments we used gold micro-electrodes.

6.1.2 Selection of an appropriate vacancy concentration

The conductivity of the YSZ solid electrolytes depends strongly on the vacancy concentration, which itself is controlled by the dopant concentration (Y_2O_3). The yttria content is typically varied up to 20 mol%, where the cubic fluorite structure is fully stabilized at yttria concentrations higher than 9 mol%. According to the literature [33, 50, 133, 134] a maximum of the ionic conductivity

occurs between 7 mol% and 10 mol% yttria content. A higher concentration leads to stronger interactions between the charged vacancies, lowering their mobility. The rate of incorporation of nitrogen into the oxide itself should also depend on the vacancy concentration, i.e. on the yttria content. Thus we investigated electrolytes with 3, 5, 7 (partly stabilized) and 9.5 mol% yttria content (fully stabilized), respectively. This range of dopant concentration has been chosen as it includes the most commonly used solid electrolytes for solid oxide fuel cells and gas sensors [50, 135].

Steady state *I-E* characteristics of a silver cathode on solid electrolyte films with an Y_2O_3 content between 3 mol% and 9.5 mol% are shown in figure 6.2. In the temperature range between 500 °C and 850 °C the electrolyte doped
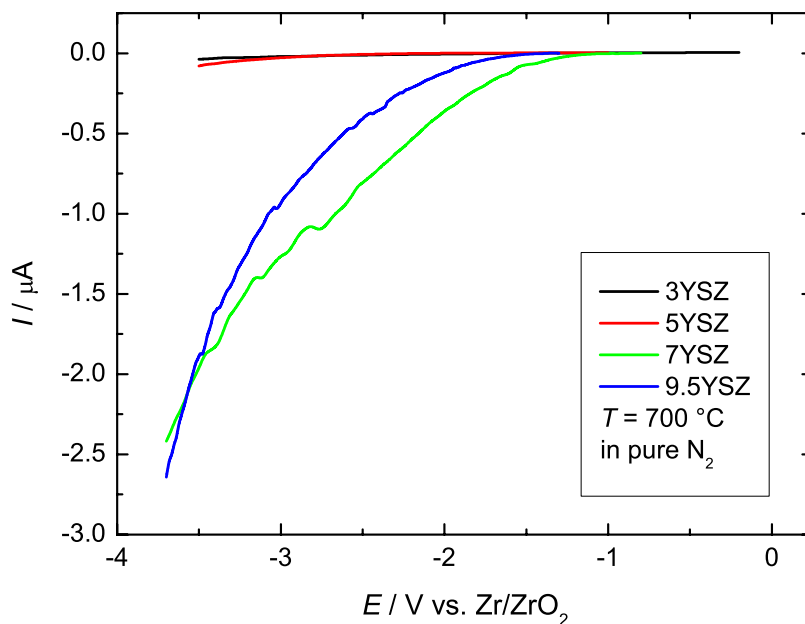
Fig. 6.2: Steady state E / i characteristics of YSZ electrolytes with different Y_2O_3 content in pure nitrogen ($a_{O_2} = 10^{-10}$)

with 7 mol% yttria shows the largest current under nitrogen atmosphere on both gold and silver electrodes. The film with 9.5 mol% yttria content shows approximately a twofold decrease (however the currents equal above E = −3.5

V), and the films with 3 mol% and 5 mol% yttria show significantly smaller currents and are not further considered in the electrochemical experiments on the kinetics of the nitrogen reaction. We assume that the higher current at the Ag (N$_2$)/ 7YSZ electrode is an indication for a faster nitrogen kinetics on 7YSZ. Obviously the oxygen vacancy concentration (as in the case of oxygen ion conduction) has an optimal value, being large enough to provide sufficient ionic mobility but still being low enough to allow the creation of new vacancies by nitrogen incorporation.

In our kinetic studies we decided to work with samples doped with 7mol% and 9.5 mol% because the first one shows the highest currents in nitrogen atmosphere and the second one has a fully stabilized fluorite-type structure and is the most commonly used material for practical applications.

6.1.3 Surface/interface characterization

The surface of the samples we used as solid electrolytes was characterized via atomic force microscopy before and after the electrochemical experiments in order to document the changes of the surface morphology. We also use AFM to estimate the contact surface area between the electrode and the electrolyte. We found two different types of interaction between the metal and the ceramic electrolyte. At lower voltages (up to approximately -2 V) we could not detect any change in the film morphology before and after the polarization. From -2 V up to -3.5 V we observe silver particles left on the surface after removal of the electrode. The AFM picture of the contact surface after 30 min polarization at -1.95 V is presented in figure 6.3. As the current density at the edges is higher than in the middle of the needle we found there more silver drops. When a voltage even more cathodic than -3.5 V was applied the electrode adhere even more to the electrolyte and by removing the tip the deposited YSZ layer was torn from the substrate as it can be seen in figure 6.4. From this image we estimated the thickness of the film (approximately 1.85 μm) and the diameter of the electrode used for the nitrogen incorporation experiment (≈ 69 μm).

In both figures (6.3 and 6.4) we found a changes of the electrolyte surface caused by the electrode-electrolyte interaction. Firstly we conclude that the
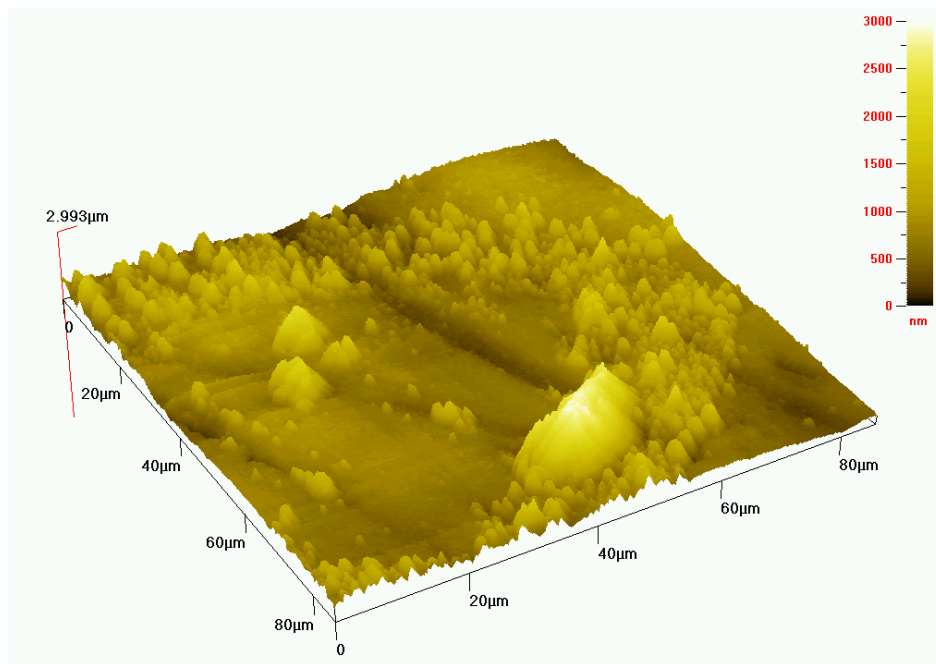
Fig. 6.3: The contact surface between Ag micro electrode and 7YSZ thin layer after 10 min polarization of −3.4 V at 700 ℃.

electrical contact between the two phases is sufficient. Secondly, one has to be very careful in applying too high cathodic voltages. This effect cannot be avoided in the steady state experiments especially at high temperatures and voltages but because of the short duartion time of the sweep it is not strongly pronounced in the potentiodynamic measurements.

6.1.4 Capacity of the electrical double layer (EDL)

The influence of the capacity and the structure of the electrical double layer on the kinetics of the electrode processes was already discussed above (p. 122). This influence was thoroughly studied for liquid electrolytes [94, 136–139] and attempts have been made to adapt or modify the theory for solid electrolytes [140–147]. The electrical double layer (EDL) is generated by the contact of two different phases. At the interface oppositely charged ions are attracted. In the case of contact between an ionic and an electronic conductor the electronic conductor (usually metal) attracts ions of opposite charge and repels those with the same charge. For the solid electrolytes it is important to note that not all
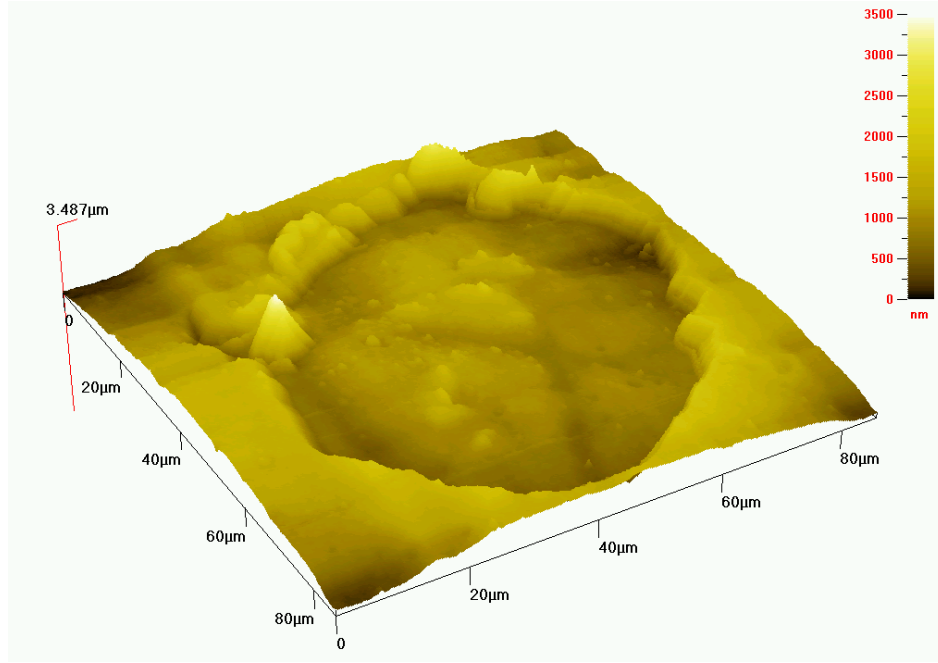
Fig. 6.4: The contact surface between Ag micro electrode and 7YSZ thin layer after 10 min. polarization of -3.55 V at 700 °C.

ions are usually able to move freely. Thus for the same charge on the electrode the capacity of the double layer will not be the same for a positive and for a negative charge of the electrode. Additionally we are not able to immerse the electrode into the solid and the contact can be quite poor. Filyaev et al. have found that the dense contact of nickel electrode to zirconia electrolyte consists of just few percents of the geometrical area of the electrode [148]. It has also been found that the capacity of the double layer of YSZ raises with increasing temperature and that the potential of zero charge (pzc) shifts to more positive values. The values for the EDL capacity of liquid silver electrode were found to vary in the range $C_{dl} = 0.3$ up to 1.5 $\mu F.cm^{-2}$ at temperatures between 900 °C and 1200 °C, where the pzc varies in this temperature range in the range $E = -1$ V up to $-0, 8$ V versus an air reference electrode (at 1 atm) [143, 149].

We have performed our measurements with two different types of Au micro-electrodes. The capacity of the EDL was measured by both AC and DC methods with needles and with photo lithographically printed micro-electrodes. The needles cannot, as discussed in section 3.2.2 (p. 84), be perfectly contacted to the

electrolyte and can probably easy adsorb gas species at the contact area. The other type of micro-electrode has an approximate thickness of 120 nm and is gas tightly printed onto the YSZ surface. They ensure a perfect electrical contact and do not leave any possibility for the gas molecules to diffuse to the electrode/electrolyte interface. On figure 6.5 the temperature dependence of the double layer capacity is plotted. We can clearly distinguish the different behav-
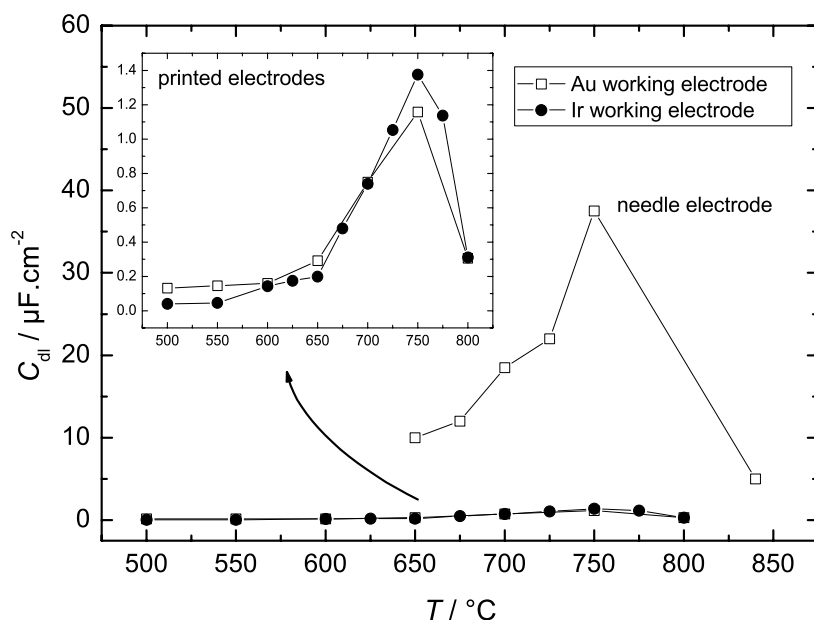
Fig. 6.5: The capacity of the electrical double layer as a function of the temperature at −□−) needle and printed gold micro-electrodes − • −) printed iridium micro-electrodes

ior of the tip electrodes (with a capacity in the maximum $C_p \approx 40\ \mu\text{F.cm}^{-2}$) and the photo lithographically printed micro electrodes with a capacity maximum of $C_p \approx 1.4\ \mu\text{F.cm}^{-2}$. The difference is explained with the ability of the gas molecules to adsorb on the electrolyte/tip micro electrode interface. This adsorption leads to this high capacity values. Additionally we should notice that in this calculation we assume that the contact area equals the geometrical surface of the needle, which usually is not always correct (see [148]) and the value of the C_{dl} should be at least 50% larger. Other authors have measured

even higher values on gold electrodes of about $C_{dl} \approx 163 \ \mu\text{F.cm}^{-2}$ [147]. The printed micro electrodes on the other hand have a perfect adhesion and we can safely assume that at least 90% from the surface has an electric contact with the oxide beneath. The measured capacities are in a very good agreement with the values ($C_{dl} \approx 1 \ \mu\text{F.cm}^{-2}$) provided by other authors [143, 146, 149].

We also find a distinct maximum of the double layer capacity at a temperature of 750 °C for both types of electrodes. Above this temperature the capacity decreases again. This behavior is independent on the electrode material and is also measured with other noble metals. The existence of this maximum we related to a saturation of the electrode surface with adsorbed species which desorb at higher temperatures. Hendriks et al. [147] report that at temperatures above 700 °C the mobility of vacancies in 8YSZ material increases which can also be an additional reason for the rise of the C_{dl} value, but cannot be the only reason because the mobility of vacancies remains high after exceeding 700 °C. The maximum of the EDL capacity indicates a change in the surface/interface adsorption/desorption conditions which influences also the other electrochemical characteristics at these temperatures and obviously plays an important role in the electrode kinetics.

6.1.5 Conductivity and IR drop in the electrolytes

The conductivity of the materials used as solid electrolytes is a parameter used for the calculations of one important characteristics - the ohmic drop. The conductivity is strongly dependent on the temperature and the dopant concentration. We have already discussed in chapter 2 the influence of the doping elements on the ionic conductivity in zirconia based electrolytes but the temperature is probably the most important parameter. Yttria stabilized zirconia is assumed to be a pure oxygen ion conductor with a transference number $t_{O^{2-}} \approx 1$. However there is also an electronic contribution. Park and Blumenthal [23] have reported a data for the partial conductivities for 8YSZ:

$$\frac{\sigma_{O^{2-}}}{(\Omega \ .cm)^{-1}} = 1.63 \cdot 10^2 \cdot \exp\left(\frac{-0.79 \ eV}{kT}\right) \tag{6.1}$$

$$\frac{\sigma_{e'}}{(\Omega \ .cm)^{-1}} = 1.31 \cdot 10^7 \cdot \exp\left(\frac{-3.68 \ eV}{kT}\right) \cdot a_{O_2}^{-1/4} \tag{6.2}$$

$$\frac{\sigma_{h\bullet}}{(\Omega \ .cm)^{-1}} = 2.35 \cdot 10^2 \cdot \exp\left(\frac{-1.67 \ eV}{kT}\right) \cdot a_{O_2}^{1/4} \qquad (6.3)$$

The calculated values for the conductivity at a temperature of 800 °C are respectively $\sigma_{O^{2-}} \approx 3.2 \times 10^{-2}$ [$\Omega^{-1}. \ cm^{-1}$]; $\sigma_{e'} \approx 8.2 \times 10^{-12}$ [$\Omega^{-1}. \ cm^{-1}$] and $\sigma_{h\bullet} \approx 3.4 \times 10^{-6}$ [$\Omega^{-1}. \ cm^{-1}$] at $a_{O_2} = 1$. Compared to liquid electrolytes the YSZ shows a relatively high ionic conductivity but it does not achieve the values typical for the strong acid or basic solutions.

As discussed in section 5 the conductivity of our YSZ and YSZ:N thin films and single crystals vary in the range of 10^{-1} [$\Omega^{-1}. \ cm^{-1}$] to 10^{-4} [$\Omega^{-1}. \ cm^{-1}$] at temperatures between 650 °C. and 850 °C.

For the electrochemical experiments it is important to know the resistance of the electrolyte in order to determine and further to subtract the IR part from the total voltage. The IR is also known as ohmic drop and appears in the Faradyic region of the current-voltage curves. The measured voltage difference between the working and the counter electrode can be written as:

$$U = \Delta\varphi_{(work-el)} - \Delta\varphi_{(count-el)} + IR_{el} \qquad (6.4)$$

where $\Delta\varphi_{(work-el)}$ and $\Delta\varphi_{(count-el)}$ are the potential difference between the electrolyte and the working/counter electrodes. Practically we should always correct the measured potential value with the IR part, but in the case of highly conducting electrolytes this term is very small and is usually neglected. In the case of YSZ electrolytes we can expect weak shape of the peaks and the voltammograms will lose their sharpness if IR is not subtracted especially in the potentiodynamic experiments (CVA, LSV). Our experiments were performed in temperature range between 600 °C and 850 °C where the resistance of YSZ films varies from 1 MΩ to 10 kΩ. In our electrochemical measurements we used micro electrodes and in spite of the large current densities the current remained small which kept the ohmic drop relatively small.

6.2 The Zr/ZrO₂ reference electrode

As in liquid electrochemistry, the choice of a reference electrode in solid-state electrochemistry is also of importance to obtain reproducible experimental results and to interpret these results correctly. In liquid systems (aqueous or

nonaqueous) different reference electrodes are used. To the most preferred reference electrodes belong: $Ag/AgCl, Hg/Hg_2Cl_2, Hg/Hg_2SO_4$ (reference electrodes of second order). Their construction is simple and does not require special equipment. Additionally the potential of these electrodes remains stable with time and it can easily be reproduced. In a variety of systems simple redox couples as $Li^+/Li; H^+/H_2; Cd^{2+}/Cd$ serve perfectly as reference if the polarization of these electrodes is kept low. They provide a reference redox reaction of first order and are more sensitive to the electrolyte composition and the surrounding environment than the reference electrodes of second order. Finding an appropriate reference system in solid-state electrochemistry is much more complicated. The complication originates mainly because there is no universal solvent and a limited number of mobile ions exist. Thus, there is a limited number of solutions of the problem with the reference electrode. Usually, because of the high resistance of electrolytes, the electrode reactions are accompanied by a high polarization, which shifts the working conditions far from equilibrium and limits the application of reference electrodes of first order with exception of Ag^+/Ag electrode in silver ion solid conductors. Presently the most employed reference seems to be platinum (or other noble metal) contacted to the solid electrolyte. Even an "absolute" scale, based on noble metal electrodes was recently suggested by Tsiplakides et al. [150, 151]. In other studies different oxide reference couples as Fe/FeO [152–154], CuO/Cu_2O [155], or some other oxide systems have been used [152, 156–161] as well a sodium based reference system was suggested [162]. The limitation of the reference electrodes of second order is the oxygen activity/potential range of stability. Usually these oxide systems are chemically stable in a potential range of approximately 500 mV. A review on specific solid state techniques, including comments on the used reference electrodes was recently published by Fleig [109].

The Zr/ZrO_2 couple has been applied as an electrode with a fixed oxygen activity for high temperature oxygen sensors [163] and as a sense electrode for an amperometric titration in molten salts [164]. The first work suggests Zr/ZrO_2 as a suitable reference electrode for determining the oxygen activity in gases and molten salts, where a special attention is paid on the dependence of transference number of O^{2-} in undoped ZrO_2 on the temperature and on the external

oxygen partial pressure. In the second paper the Zr/ZrO_2 system was applied to the molten KNO_3 salt electrolyte, in order to determine the oxygen ion activity. The dependence of the Zr/ZrO_2 potential (versus Ag/Ag^+) on the O^{2-} concentration has been studied.

Application of Zr/ZrO_2 as a reference redox couple for solid state reaction studies

In this chapter the application of Zr/ZrO_2 is considered as a reference electrode applied to solid oxide electrolytes. The system is treated as a reversible thermodynamic system. According to reaction $Zr + O_2 = ZrO_2$ (the mass-action constant and the standard free enthalpy of formation are defined as in equations 2.57 and 2.58) and the Gibbs free reaction energy can be calculated from the available thermodynamic data [55]:

$$\Delta_r G_O^o = \Delta_f G_{ZrO_2}^o - \Delta_f G_{Zr}^o - \Delta_f G_{O_2}^o \tag{6.5}$$

At 700 K this value is equated as $\Delta_r G_O^o = -912$ kJ.mol^{-1} and the reaction proceeds spontaneous to the right side of equation 6.5. The electromotive force of this reaction can be calculated according to the relation given by eq. 2.59. It should be mentioned that the calculated values for E^o can be experimentally observed only in case, that the transfer number of oxygen ions is equal or close to unity. The emf equals $E^o = 2.4$ V at 700 K. Under real conditions ZrO_2 is formed as a stable product on the metal surface, preventing the free oxygen access to the Zr-metal surface, thus lowering the rate of reaction 2.56 further in both directions. The transference number of oxygen in the ZrO_2 film influences the electromotive force of the cell according to:

$$E = -\frac{RT}{4F} \int_{\ln a_{O_2}}^{\ln a_{O_2}^*} t_{O^{2-}} d \ln a_{O_2} \tag{6.6}$$

where $a_{O_2}^*$ is the fixed oxygen activity side and the transference number of oxygen ions is defined as: $t_{O^{2-}} = \sigma_{O^{2-}}/\sigma_{total}$. At the interphase between the two phases (Zr and ZrO_2) the oxygen activity a_{O_2} is fixed at given temperature. The dependence of the cell emf on the oxygen activity, respectively of the standard emf on the temperature is given in fig. 2.10.

6.2.1 Definition and choice of the reference reaction

The main reason using a reference electrode is to provide a stable and reproducible electrode potential value (energy level). Versus this reference energy level the potential of the working electrode has to be measured. So the reference electrode should be understood not only as a simple electrode, but as an electrode reaction. This reaction must proceed in both straight and backward directions reversible, without or with negligible overvoltage. There must be only one electrochemical redox reaction taking place on a certain reference electrode system and this reaction should involve only one electron transference step as the existence and/or stability of any intermediate species will make the reaction unacceptable as reference reaction.

6.2.2 Gibbs phase rule and kinetic arguments

The Zr/ZrO$_2$ system
In order to characterize the reference system thermodynamically , the Gibbs phase rule is applied:

$$P + F = C + 2 \tag{6.7}$$

where P designates the number of phases; F - the degrees of freedom and C - the number of components involved in the system. Assuming reaction 2.56, there are three phases: $\mathrm{Zr}; \mathrm{ZrO_2}; \mathrm{O_2}$ or $P = 3$. The number of components was calculated as follows: three components ($\mathrm{O_2}; \mathrm{Zr}; \mathrm{ZrO_2}$) minus one independent equation, describing the related chemical process ($C = 2$). For the degree of freedom F one obtains:

$$F = 2 + 2 - 3 = 1 \tag{6.8}$$

Thus, if the temperature is kept constant, the oxygen activity is fixed and the system is at thermodynamic equilibrium and provides a stable electrode potential and can be used as a reference electrode.

Noble metal electrodes

Considering platinum or other noble metal as a reference electrode, the situation changes, compared to metal/metal oxide systems. If we assume, that the noble metal remains inert and does not form more or less stable surface

intermediates, applying the Gibbs phase rule to this system an important difference with the previous system appears. We have two phases: Pt, and O_2 ($P = 2$). The number of components is also two, ($C = 2$). So for the degree of freedom obtained according to eq. 6.7 is $F = 2$. This means that one have to keep two parameters constant (both temperature and pressure) in order to preserve the thermodynamic equilibrium, which is practically impossible during electrode polarization or other electrochemical experiments as the application of voltage leads automatically to a change of the oxygen partial pressure. The situation is more complicated if we also take into account that Pt is reacting with ZrO_2, forming a series of intermetallic compounds [130].

Not only thermodynamic, but also kinetic factors are playing an important role. Platinum forms oxides stable up to temperatures of approximately 750 °C [131,132]. The existence of oxides on the electrode surface polarizes the electrode and in this way disturb the equilibrium condition with the surrounding atmosphere. It is also well known that the oxygen reduction/oxidation proceeds via at least one intermediate step. Each stable intermediate valence state, excluding the initial and the end one, provides also a reaction serving temporary as a reference. After the potential required for a further proceeding of the intermediate reaction to the end state is exceeded a new redox couple begins to serve as a reference. These reasons are convincingly enough to discard the noble metals as a reference electrodes. Moreover there are a number of oxygen species detected by Luerßen et al. and Vayenas et al. on the surfaces of noble metals [165–167]. The existence of such species fails the requirement for a simple, reversible and stable electrode reaction. Working with such a reference electrode one measures the potential each time versus different reference potential, temporary determined only by the adsorbed species. An experimental confirmation of the irreversibility of the oxygen reaction are numerous voltammograms [168–172], including ours (see section 6.3.1), showing clearly the large potential difference between the oxidation and reduction peaks, which is a clear sign for irreversible process and an irreversible process cannot serve as a reference reaction.

We conclude, that neither the noble metal electrodes nor O^{2-}/O_2 redox couple can fulfil the thermodynamic and kinetic requirements for a reference electrode. They cannot provide a stable reference reaction and form different surface in-

termediates depending on the surrounding environment.

The Me/MeO$_x$ systems on the other hand ensure a stable redox reaction and being at thermodynamic equilibrium are suitable for application as reference electrodes on oxygen conducting solid electrolytes. From the commonly accessible oxides thermodynamically stable systems applicable at temperatures above 600 °C are Zr/ZrO$_2$; Hf/HfO$_2$; Y/Y$_2$O$_3$ and also Ta/Ta$_2$O$_5$.

6.2.3 Determination of the standard reference potential via UPS

From thermodynamics we can easily calculate the theoretical value of the oxygen activity at the Zr/ZrO$_2$ interface but we cannot *a priori* compare this value with the well known aqueous electrochemical potential scale (the Nernst scale) or the absolute work-function scale referred to the vacuum level (the physical scale). With the present experiment we have determined the energy required for an electron transfer from zirconium metal to the oxide or from the oxide to the metal. Practically in this way the difference in the Fermi levels between the both phases was determined, where the difference in the Fermi levels is the electrode potential as depicted in figure 6.6. Because the Fermi level for zirconium oxide
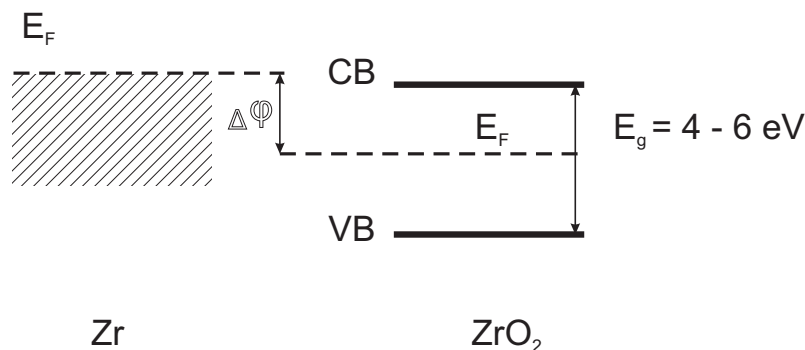
Fig. 6.6: Schematic presentation of the difference in the Fermi level of zirconium metal in contact with ZrO$_2$

lies deep in the band gap the required energy for an electron transfer between the two phases is defined as the difference in the energetic levels between the valence band of ZrO$_2$ and the Fermi level of the Zr metal.

Experimental details

Zirconium metal finely polished up to $0.02 \mu m$ was covered (by PLD) with a 20 nm thick ZrO_2 film which was analyzed by ultraviolet photoelectron spectroscopy (UPS). Before the experiment the sample was sputtered in the chamber with argon ions for one hour in order to remove from the surface the adsorbed species as water, CO_2, etc.

In figure 6.7 the resulting UPS spectrum is presented. The scan is shown
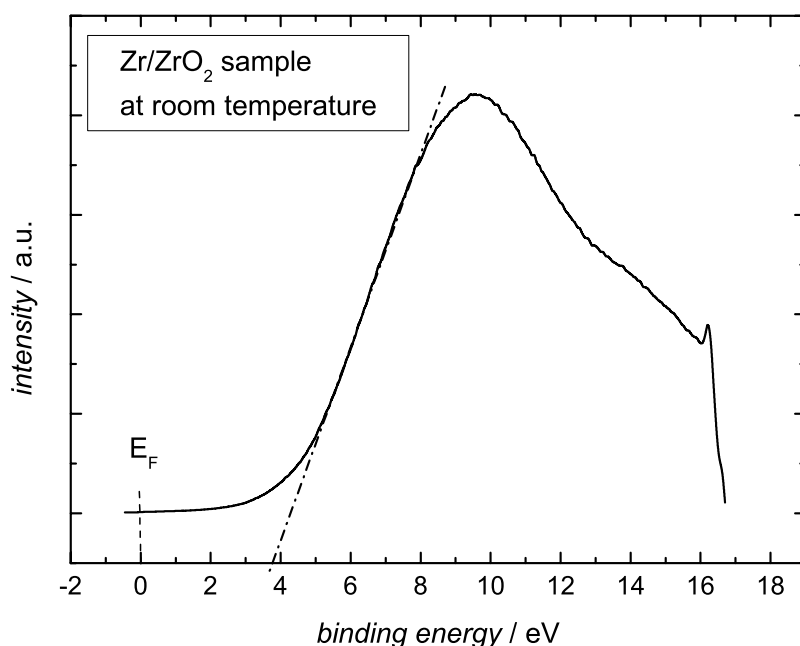
Fig. 6.7: UV photoelectron spectroscopy on Zr/ZrO_2 sample at room temperature

with a respect to the Fermi level of the metal (set as zero) and the position of the valence band is given by the intercept of the tangent of the steep emmision step with the x-axis. The energy difference is found to be 3.89 eV which is in a good agreement with the values for the ZrO_2 system reported by other authors [31,173]. The next step was to compare our experimentally determined value with the well known in the liquid electrochemistry standard hydrogen scale. The energy difference for an electron transfer of the redox couple H^+/H_2 is according to IUPAC recommendation 4.44 eV [174]. Comparing the both

values we can easily determine the position of Zr/ZrO_2 couple on the absolute electrochemical scale. $E_{abs}(Zr/ZrO_2) = 3.89 - 4.44 = -0.55$ V vs. SHE. Of course this comparison is only an approximation because the 4.44 eV for the hydrogen reaction is given only for liquid systems and we cannot compare it directly to a system in a purely gas (or vacuum) atmosphere. However this value is an orientation for the ability of Zr/ZrO_2 redox pair to share or attract electrons. Further we have defined the half cell reaction which provides the reference potential and based on the Nernst equation we have calculated the standard reference potential E°_{Zr/ZrO_2}. We define the half cell reaction as:

$$ZrO_2 + 2V_O^{\bullet\bullet} + 4e^- \rightleftharpoons Zr + 2O_O^\times \tag{6.9}$$
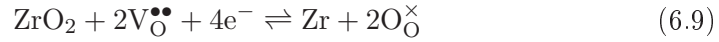
We write the reaction at equilibrium in the terms of chemical/electrochemical potentials where first equation 6.9 was rearranged, because to the structural elements (i.e. $O_O^\times$ and $V_O^{\bullet\bullet}$) no chemical potential can be assigned. Only the building units possess a chemical potential:

$$\mu^\circ_{Zr} + 2\widetilde{\mu}_{\underbrace{(O_O^\times - V_O^{\bullet\bullet})}_{(O^{2-})_O}}(ZrO_2) = \mu^\circ_{ZrO_2} + 4\widetilde{\mu}_{e^-}(Zr) \tag{6.10}$$

By rearrangement of equation 6.10 assuming that $a_{Zr} = 1$, $a_{ZrO_2} = 1$ and $a_{e^-} = 1$ we obtain

$$F\varphi(Zr) - \mu^\circ_{e^-} = -\frac{1}{4}\mu^\circ_{Zr} - \frac{1}{2}\mu_{O^{2-}} + F\varphi(ZrO_2) + \frac{1}{4}\mu^\circ_{ZrO_2} \tag{6.11}$$

$$F\underbrace{[\varphi(Zr) - \varphi(ZrO_2)]}_{\Delta\varphi} = -\frac{1}{4}\mu^\circ_{Zr} - \frac{1}{2}\mu_{O^{2-}} + \frac{1}{4}\mu^\circ_{ZrO_2} + \mu^\circ_{e^-} \tag{6.12}$$

$$F\Delta\varphi = -\underbrace{\left[\frac{1}{4}\mu^\circ_{Zr} + \frac{1}{2}\mu^\circ_{O^{2-}} - \frac{1}{4}\mu^\circ_{ZrO_2} - \frac{1}{4}\mu^\circ_{e^-}\right]}_{\frac{1}{4}\Delta_R G^\circ} - \frac{1}{2}RT\ln a_{O^{2-}} \tag{6.13}$$

or finally we obtain

$$\Delta\varphi_{Zr/ZrO_2} = \Delta\varphi^\circ_{Zr/ZrO_2} - \frac{RT}{2F}\ln a_{O^{2-}} \tag{6.14}$$

In equation 6.14 we have already experimentally determined the value for the equilibrium potential via UPS ($\Delta\varphi = -0.55$ V). The activity term we replace with the mole fraction, where the deviation from the stoichiometry δ in ZrO_2 is approximately 10^{-3} [20]. The standard electrode potential $\Delta\varphi^\circ_{Zr/ZrO_2}$

or $E^{\circ}_{\mathrm{Zr/ZrO_2}}$ of this reaction can now be estimated. $E^{\circ}_{\mathrm{Zr/ZrO_2}} = -0.57$ V vs. SHE at 700 °C. The comparison of the electrochemical and physical scales and the position of the $E^{\circ}_{\mathrm{Zr/ZrO_2}}$ standard electrode potential are shown in figure .
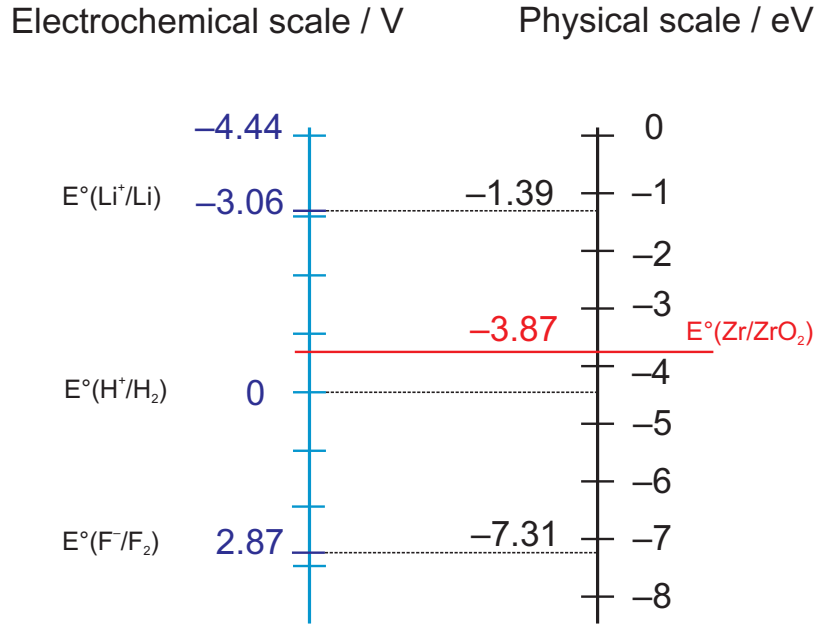
Fig. 6.8: Comparison between the electrochemical scale (left) and the physical scale (right) and the position of E°_{Zr/ZrO_2}

6.2.4 Conclusions

In this chapter were defined the boundary conditions for the electrochemical studies on the nitrogen incorporation kinetics. We have tested gold and silver as materials for the working micro electrodes , where Au was found appropriate for the kinetic studies because it does not tend to adsorb species on its surface and silver as a material with higher oxygen overvoltage. We use two different types of working electrodes - needle micro electrodes with a tip diameter between 3 μm and 60 μm and photo lithographically printed square shaped electrodes with side length of 100 μm up to 200 μm. The first type allows an easy movement and positioning of the tip on the electrolyte surface and the second type ensures a defined surface and a perfect electric contact to the oxide beneath, but its position cannot be relocated.

From series of zirconia electrolytes doped with different amounts of yttria

(in the range from 3 mol% up to 9.5 mol%) we selected YSZ doped with 7 mol%, respectively 9.5 mol% Y_2O_3. The first one shows the highest current in nitrogen atmosphere and the second one has a fully stabilized cubic structure and is widely applied in the praxis. We confirmed that by applying voltages above 2 V the metal electrode reacts with the YSZ electrolyte and either metal particles remain on the oxide surface (at voltages up to -3.4 V) or a part of the electrolyte was torn at U larger than -3.5 V.

Our experiments show that the capacity of the electrical double layer formed on the electrode/electrolyte interface should influence the kinetics of the electrochemical processes especially in the case of needle micro electrodes, where the EDL capacity exceeds 50 $\mu F.cm^{-2}$. At temperatures of about 750 °C the EDL capacity reaches a maximum for both types of working electrodes. This maximum is associated with adsorption/desorption phenomena involving gas molecules of the surrounding environment but also ionic species from the electrolyte.

In order to obtain a qualitative current-voltage characteristics we have determined the conductivity ($\sigma_{O^{2-}} = 10^{-1}$ [$\Omega^{-1}.cm^{-1}$] $\div 10^{-4}$ [$\Omega^{-1}.cm^{-1}$]) of our materials where the measured resistance vary in the range 1 MΩ $\div$ 10 kΩ depending on the temperature and the dopant concentration. On the basis of these results the ohmic drop in the oxide electrolytes (IR) can be calculated and subtracted from the potential-current characteristics in order to improve the peak sharpness. We keep in any case the IR drop low because of the small electrode surface but its subtraction from the E/I curves helps for a clearer presentation.

Finally we suggest to apply the Zr/ZrO_2 couple as a reference electrode instead of noble metal electrodes. The advantages of Me/MeO_x are the constant oxygen activity at the metal/oxide interface and the stable and reproducible electrode potential. We have used UV photoelectron spectroscopy to determine the exact value of Zr/ZrO_2 reference couple: $E^{\circ}_{Zr/ZrO_2} = -0.59$ V at room temperature vs. the standard hydrogen electrode scale or -3.87 eV vs the absolute physical scale. On the other hand we show that from thermodynamic and also kinetic reasons the noble metal electrodes are not appropriate to be used as reference electrodes.

6.3 Electrochemical studies on the nitrogen reaction

It is not only of theoretical but also of practical importance to find out whether molecular nitrogen is electrochemically active. As discussed in section 1.1 nitrogen is usually treated as an inert gas and only the report from Wilcockson [19] leaves the door for further discussions open. The nitrogen molecule ($N - N$ distance 1.0976 Å) is very stable. Its dissociation energy corresponds to 945.33 kJ/mol or 9.79 eV. The dissociation constant for: $N_2 \rightarrow 2N$ is $K_d = 10^{-160}$ [132]. So practically we cannot expect the existence of free nitrogen atoms even at elevated temperatures. The study of the electrochemical nitrogen reaction on oxygen conducting electrolytes is even more complicated, because it proceeds simultaneously with the oxygen redox reaction and in the case of very low oxygen partial pressures an electron exchange between the electrode and the solid electrolyte takes place (reduction of the electrolyte).

We have studied the nitrogen reaction by potentiodynamic and as well by steady state electrochemical methods. In order to distinguish the nitrogen signals from those of the possible simultaneously proceeding concurrent redox processes on the current-potential curves the electrochemical characteristics of the oxygen reaction and those of electron exchange between YSZ and the working electrode in argon atmosphere were firstly determined and just after the studies on the nitrogen reaction were performed. In order to obtain a direct confirmation of the nitrogen incorporation, the surface of the electrolyte beneath the electrode contact was analyzed after electrochemical polarization by SIMS.

6.3.1 The oxygen reaction

The oxygen reaction of yttria stabilized zirconia has been thoroughly studied with a variety of solid electrolytes and electrode materials. In most studies the Pt or Ag (i.e. noble metals) reference electrode are used. If we directly accept the reaction characteristics from the existing literature this could lead to wrong assumptions concerning the reaction potentials reflecting in incorrect interpretation of the experimental results. We performed potentiodynamic and

steady state polarization measurements in order to determine the potentials of oxygen reduction respectively oxidation on micro electrodes with Zr/ZrO_2 reference electrode.

Experimental details

We performed potentiodynamic (CVA, LSV) and steady state (galvanostatic and potentiostatic) electrochemical experiments on the oxygen reaction with gold micro-electrodes on approximately 3 μm thick 9.5YSZ films, deposited by PLD on a Zr/ZrO_2 substrate used as both reference and counter electrode. The sweep rate for LSV and CVA was varied in the range 100 mV.s^{-1} up to 1 V.s^{-1}. The applied voltages were in the range $\pm$ 6 V, and the temperatures varied between 400 °C and 700 °C.

Dynamic electrochemical measurements(CVA)

In fig. 6.9 the first two sweeps from the cyclovoltammogram of a gold working electrode on 9.5YSZ in air are presented. The measurements started at highly positive potentials ($E = 4.3$ V vs Zr/ZrO_2) where the lattice O^{2-} ions are oxidized to molecular oxygen. In the cathodic sweep this oxygen is reduced again to O^{2-}. The peak potential of the reduction reaction: $O_2 + 4e^- \rightarrow 2O^{2-}$ is registered at $E = -0.85$ V. Beside this peak no other reactions are detected up to potentials of about -6 V. On the reverse (anodic) sweep a peak associated with oxygen adsorption on the electrode surface appears at potentials $E = 1.65$ V followed by an increase of the anodic current due to oxygen evolution. This voltammogram shows no significant differences with those well known from the liquid electrochemistry. It demonstrates clearly that the oxygen reaction is completely irreversible (charge transfer controlled) since the potential difference between the cathodic and anodic peak potential is much larger (over 2.5 V) than those required from the criterium for reversibility of the system given as $E_p^a - E_p^c = \frac{2.3RT}{nF}$ in [96]. In the second cycle of the cathodic sweep the oxygen reduction peak is at the same potential position ($E = -0.85$ V), but the current of the peak is much lower. As in the first cycle no other cathodic peaks are present in the whole potential range. A further increase of the number of cycling results in voltammograms absolute identical with those from the second
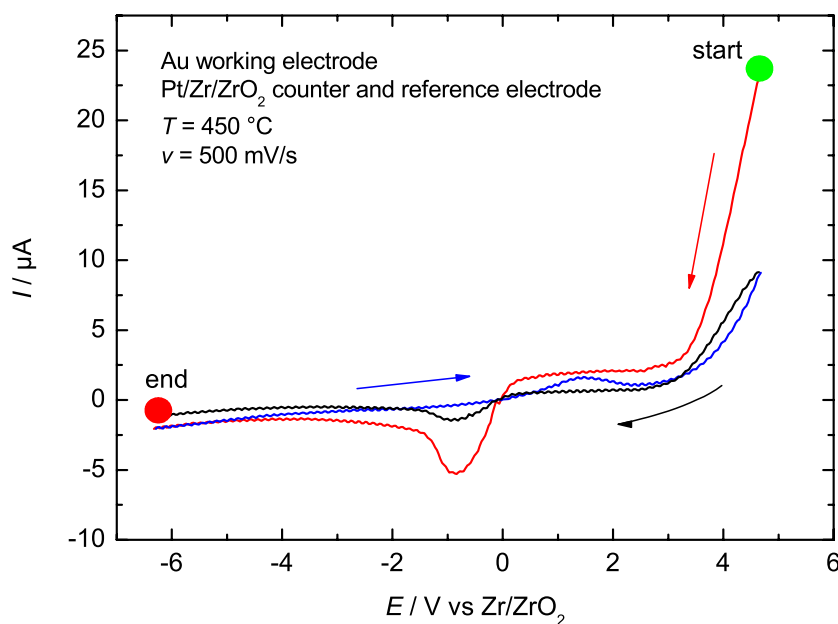
Fig. 6.9: Cyclovoltammogram of a gold micro-electrode on a 9.5YSZ thin film in oxygen atmosphere. $T = 450$ °C; sweep rate $v = 500$ mV.s^{-1}

cycle.

The difference between the first and the following sweeps is not surprising, as the starting potential is highly positive and the equilibration time of the potentiostat was set to 10 seconds. During these 10 sec we saturate the electrode surface with oxygen molecules which are subsequently reduced in the cathodic sweep resulting in high current peak values. On the reverse (anodic) scan oxygen molecules are also produced, but as the sweep rate was 500 mV.s^{-1} their quantity is much lower compared to those at the initial conditions. The lower oxygen amount on the electrode surface results in lower reduction currents on the cathodic scans of the second and following cycles. When the experimental conditions are not changed in the following runs the form and position of the voltammograms remain constant.

The experiments with a variation of the sweep rate shown as expected a negative shift in the oxygen reduction peak potential by increasing the sweep

rate. However, as these results are going out of the scope of this work they are not analyzed or discussed further.

Steady state electrochemical measurements

The steady state galvanostatic experiments on gold electrodes demonstrate that the oxygen reduction reaction, respectively the oxygen limited current appears at potentials between -1 V and -1.5 V versus Zr/ZrO_2 reference electrode. Figure 6.10 presents the current-voltage of a gold working electrode dependence on 9.5YSZ solid electrolyte. A plateau associated with the limited current of
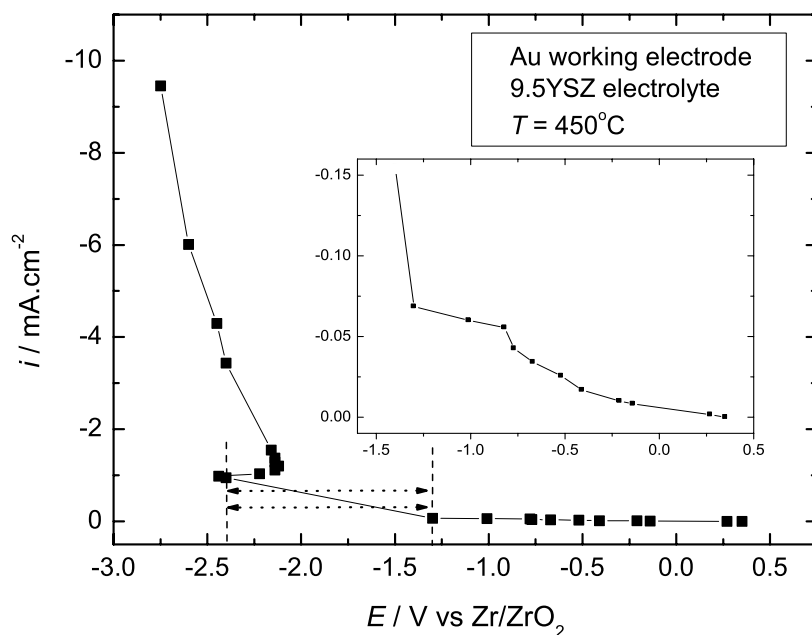
Fig. 6.10: Galvanostatic current-potential curve at a gold electrode on 9.5YSZ in oxygen atmosphere. $T = 450$ °C

the oxygen reduction can be seen at about -1 V. A further increase of the current does not lead to a large potential shift and corresponds to enhanced oxygen incorporation rate, as no reduction of the material has been detected. We observed that within the current range from 0.06 mA to 0.9 mA the potential

values were not stable and oscillated continuously with a constant rate between -1.3 -2.4 V. If the current exceeds 0.9 mA the potential characteristics become stable with the time again. The origin of these oscillations is not clear. As possible explanation we suggest that in this region because of charge transfer or diffusion problems we gather a certain amount of oxygen atoms and/or molecules at the electrode/electrolyte interface. The created layer acts as an insulator and shifts the potential towards more negative values. When the potential required for the reduction and incorporation (diffusion in the bulk) is achieved the surface amount of accumulated oxygen is consumed and the potential shifts back to its initial value. This procedure is repeated until the current is high enough to ensure a regular consumption of the adsorbed species.

On the $\eta / \log i$ plot (fig. 6.11) two Tafel regions can be identified. The first region is found at potential values up to -1 V and the second region is found at values above -2 V. In both regions the high values for the Tafel constant
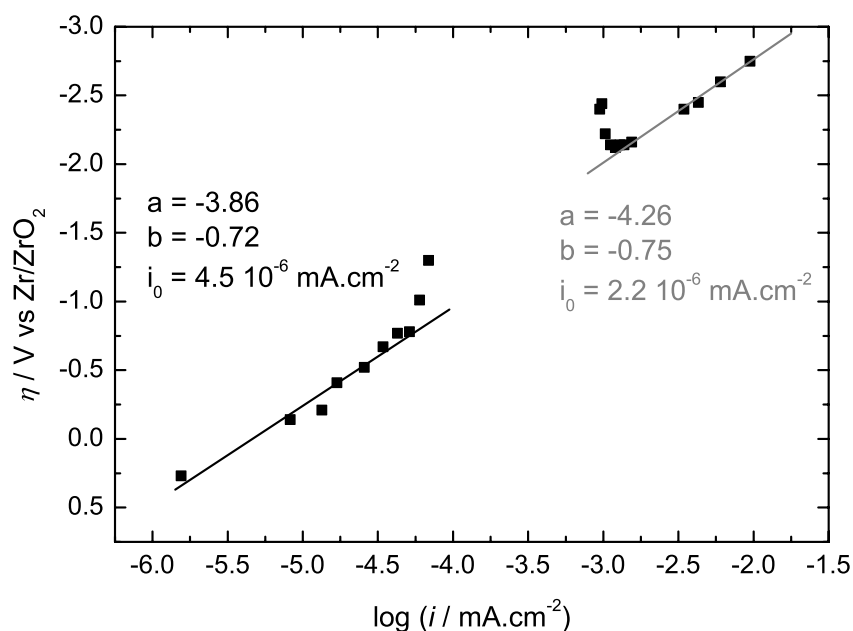
Fig. 6.11: Tafel plot of the current voltage characteristics of a gold electrode on 9.5YSZ in oxygen atmosphere. $T = 450$ °C

b suggest that the process is diffusion controlled or at least controlled by both the charge transfer and diffusion. The oxygen diffusion from the gas phase to the reactive electrode/electrolyte interface cannot be the limiting factor (the gas diffusion is fast) so the diffusion of the oxygen species into the bulk remains to limit the current. As the operating temperatures are relatively low to ensure the maximum ion conductivity of YSZ we can expect that the process of diffusion in the bulk is limiting the overall process.

The results of the steady state polarization measurements seems to disagree with the CVA experiments demonstrating clearly a serious difficulties in the electron exchange. But comparing the both methods we should keep in mind that during the potentiodynamic measurements (higher sweep rates) we may not detect the diffusion limits as the reactance time is short and thus we determine only the charge transfer resistance. So the results from both measurements are not in conflict and we can assume that the oxygen reduction process is limited in real-time conditions by the diffusion of O^{2-} species from the electrode surface into the bulk.

In the same system and under the same conditions we investigated the oxygen evolution process. It starts at potentials of about 1 V. The steady state galvanostatic curve shows higher Faradaic currents in the order of potentials above 1.3 V.

A plateau associated with the limited current of oxygen evolution is found at 1.9 V, followed by a rapid increase of the current. Because of the large plateau (about 1 V) we can confirm the results obtained by the CVA experiments suggesting that the oxygen species are firstly adsorbed on the electrode/electrolyte interface and later at higher potentials oxygen gas molecules are evolved. However such a mechanism is well known in the liquid electrochemistry and can also be expected on solid electrolytes. The slope on the Tafel plot shown on fig. 6.13 suggests an oxidation process controlled also by diffusion. The limiting factor may be as in the case of the reduction process the diffusion of the O^{2-} from the bulk towards the electrode surface, but it can also be the evolution or recombination of the oxygen atoms/molecules from the electrode in the gas phase. From this study alone it is difficult to conclude which of these both steps is exactly the slowest, respectively we do not offer a concrete mechanism of the

oxygen evolution. We investigated the oxygen reaction and we have determined the potentials at which the oxygen process takes place and the kind of its control only in order to distinguish the oxygen from the nitrogen process.
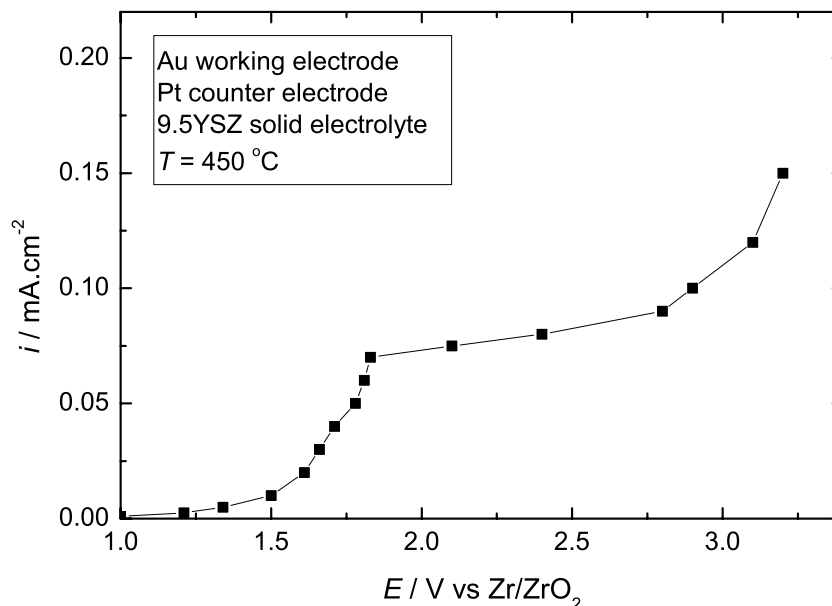
Fig. 6.12: Anodic galvanostatic current voltage characteristics of 9.5YSZ at gold electrode in oxygen atmosphere. $T = 450$ °C

Conclusions

From both cathodic and anodic experiments we can conclude that the oxygen reaction proceeds in both directions under diffusion control. Of course we cannot exclude (because of the low exchange current densities) that both the diffusion and the charge transfer are determining the reaction rate (mixed control). However the diffusion of the lattice O^{2-} ions into the bulk material at these temperatures seems to be the limiting factor of the overall electrochemical process. The experiments performed at higher temperatures (up to 800 °C) do not show large deviations in the potential peak positions but the current densities were larger. In our further studies on the nitrogen electrochemical reaction we expect to detect the oxygen impurities (if any) resulting in a reduction peak at potential position of about -1 V vs. Zr/ZrO_2 reference electrode.
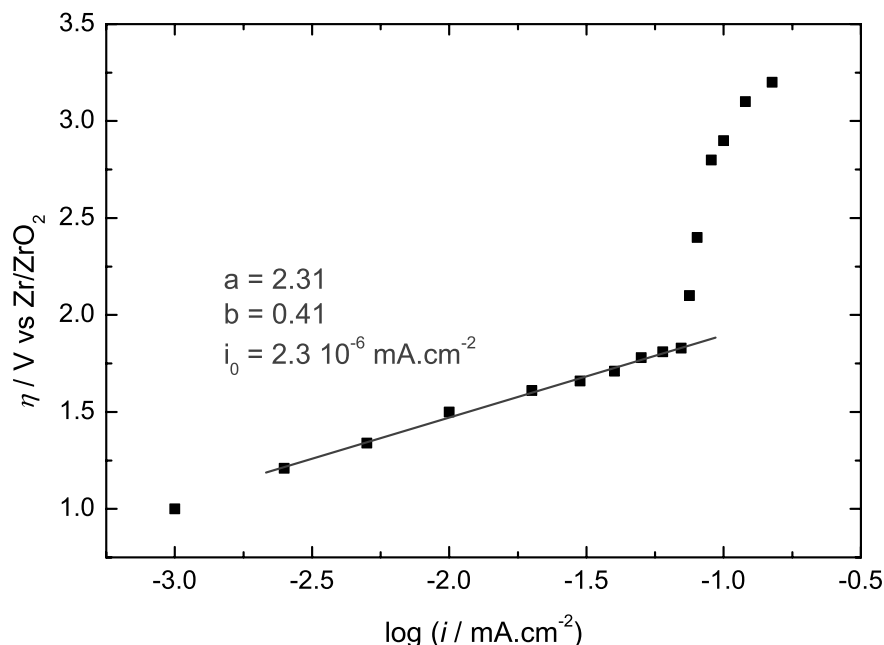
Fig. 6.13: Tafel plot of the anodic current voltage characteristics of 9.5YSZ at gold electrode in oxygen atmosphere. $T = 450$ °C

6.3.2 Electrochemical nitrogen reduction

The process of electrochemical reduction of nitrogen is pretty complicated. As discussed in section 2.5 a reduction process involving simple nitrogen species (N^{3-}) was reported only in [57] and [58] for high temperature nitrogen ion containing melt electrolytes purged with gaseous nitrogen. We performed studies of the molecular nitrogen reduction for the first time on oxygen conducting electrolyte.

Experimental details

We performed potentiodynamic (CVA, LSV) and steady state (galvanostatic and potentiostatic) electrochemical experiments on the nitrogen reaction with gold micro-electrodes on approximately 3 μm thick 7YSZ films, deposited by PLD on a Zr/ZrO$_2$ substrate used as both reference and counter electrode. The sweep rate for LSV and CVA was varied in the range 100 mV.s^{-1} up to 1 V.s^{-1}.

The applied voltages were in the range from 1 V to -4 V and the temperatures varied between 600 °C and 700 °C. The nitrogen reduction reaction was studied in a pure nitrogen atmosphere with $a_{O_2} = 10^{-14}$. As inert atmosphere a pure argon ($a_{O_2} = 10^{-13}$) was used.

Dynamic electrochemical experiments (CVA, LSV)

The cyclovoltammetry and linear sweep voltammetry have found a wide application in kinetics studies and electrochemical characterization of all kind of redox systems (see section 3.1.3, p. 72). In figure 6.14 the cyclovoltammogram on 7YSZ electrolyte at gold micro electrode is presented. The temperature is 700 °C and the cell is thoroughly purged with ultra pure nitrogen (a flow rate of 4 sccm) where oxygen activity measured at the gas outlet is extremely low - $a_{O_2} = 10^{-14}$. It can be seen that the voltammogram has quite complicated form. At least four cathodic peaks (the lack of sharpness is due to the IR of the electrolyte) have been detected on the forward sweep. However no anodic peaks were registered on the reverse sweep, which is a clear criterium that all cathodic peaks are definitely irreversible. The absence of anodic peak on the voltammogram shows that the polarization of the cathodic reaction was too high and the oxidation potentials of the reaction lie out of the potential range of the sweep. Our LSV experiments on the nitrogen oxidation show peaks at potentials of approximately 2.5 V.

To confirm that the cathodic peaks are really associated/related to the nitrogen reduction and no other processes like for example the electrolyte reduction are involved we have performed measurements in pure argon atmosphere ($a_{O_2} = 10^{-13}$). This CV curve is shown on fig 6.15 below, but it is also shown for comparison in fig. 6.14. On the curve recorded in pure argon (i.e. in really inert atmosphere) the currents are of about one order of magnitude lower than those in nitrogen. It starts at equilibrium potentials of about E = -2.5 V. This value is very close to the theoretical predictions for the potential of electrolyte decomposition. No peaks can be seen on the voltammogram and the current rises approximately exponentially with the increase of the potential. It should be mentioned that the current corresponding to the potential at equilibrium
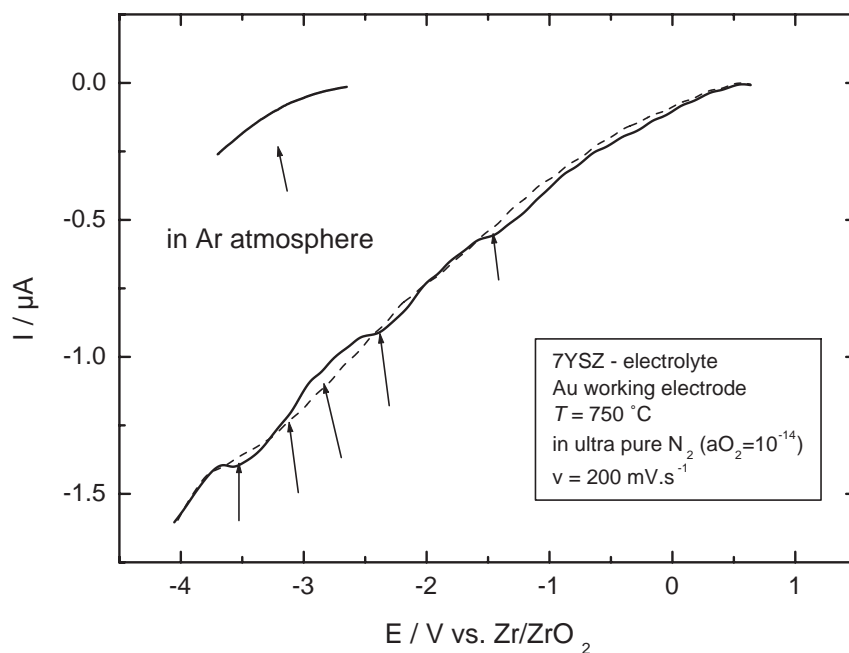
Fig. 6.14: Cyclovoltammogram on 7YSZ at gold micro electrode in ultra pure nitrogen atmosphere. $T = 700$ °C; N_2 flow rate = 4 sccm; $a_{O_2} = 10^{-14}$; sweep rate v = 200 mV.s^{-1}

conditions (the initial potential) does not equal zero as it should be expected. It starts at a non-zero value, decreases and just after reaching zero starts to increase. We can explain this behavior with a difference in the concentration of the adsorbed species on the electrode/electrolyte interface (the first two or three atomic layers) compared to the bulk material, where the regular distribution of the defect species is governed by the electro neutrality conditions in one homogenous environment. The higher surface concentration causes a higher reduction current. However the experiments performed in Ar confirm that the peaks recorded in the CV curve (fig. 6.14) are associated with the nitrogen electrochemical reduction.

It can be seen that on the cyclic voltammograms the cathodic and the anodic part of the curve overlay. This overlapping causes difficulties for the determination of the exact position of the recorded peaks. Additionally the reverse sweep
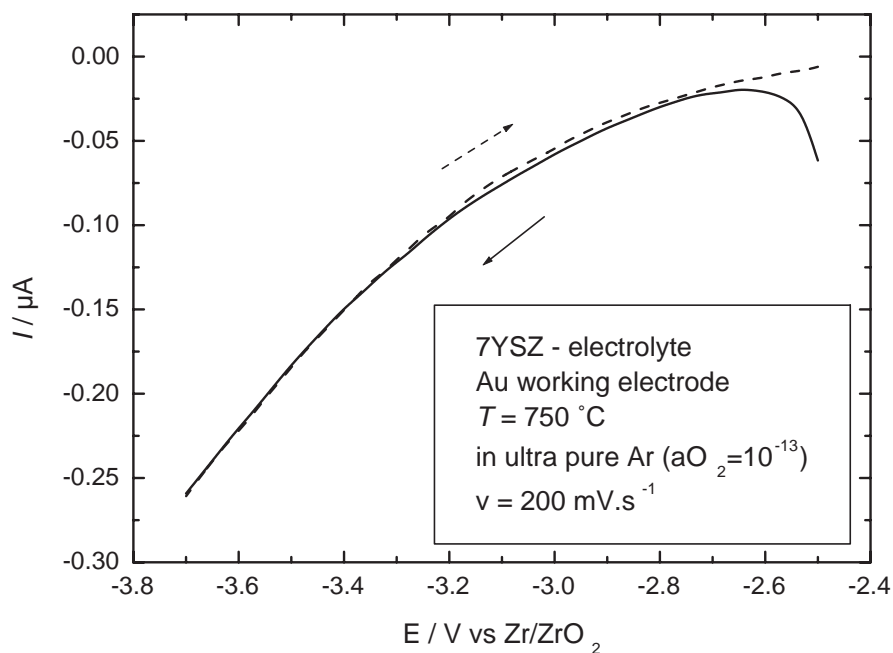
Fig. 6.15: Cyclovoltammogram on 7YSZ at gold micro electrode in ultra pure argon atmosphere. $T = 700$ °C; Ar flow rate = 4 sccm; $a_{O_2} = 10^{-13}$; sweep rate $v = 200$ mV.s^{-1}

does not provide any useful information as no peaks appeared. For these reasons we discuss in the further analysis only the forward scan, i.e the linear sweeps (LSV). Another advantage of LSV is that during the experiments it is not possible to oxidize the lattice O^{2-} ions (only cathodic potentials were applied) thus forming unexpected oxygen species. In figure 6.16 linear sweep voltammograms on zirconia electrolytes with 3, 5, 7, 9.5 and 13 mol% Y_2O_3 are shown. We determine the potential positions of the four peaks recorded at sweep rate of 100 mV.s^{-1}, present in table 6.3.2. During the experiments we acknowledge

	peak 1	peak 2	peak 3	peak 4
E_p	-2.7 V	-2.85 V	-3.11 V	-3.4 V

no oxygen peak (expected in potential range between $E = -0.8$ V and -1.5

V). So we can be sure that the oxygen reaction does not influence the recorded electrochemical characteristics.
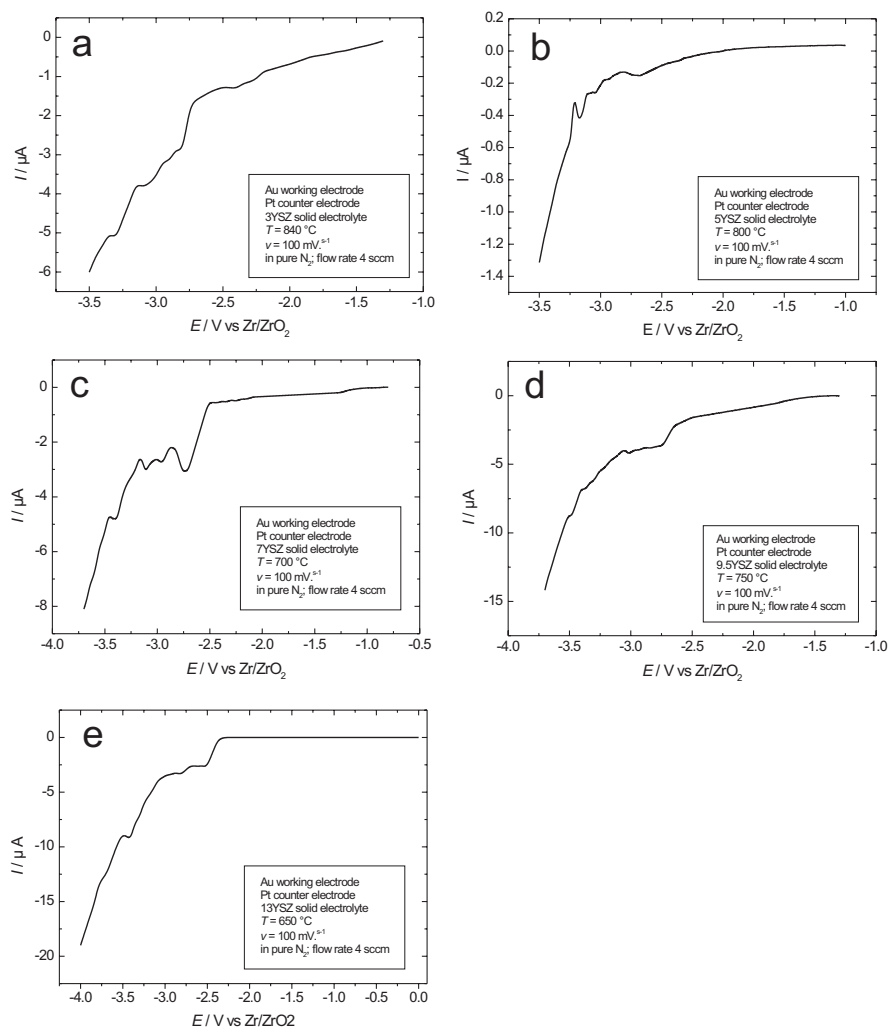
Fig. 6.16: Linear sweep voltammograms on micro electrodes in ultra pure nitrogen atmosphere after IR correction. N_2 flow rate = 4 sccm; $a_{O_2} = 10^{-14}$; sweep rate $v = 100$ mV.s^{-1}

a) 3YSZ at 840 °C; b) 5YSZ at 800 °C; c) 7YSZ at 700 °C; d) 9.5YSZ at 750 °C; e) 13YSZ at 650 °C

The analysis of the voltammograms recorded at various sweep rates (up to 500 mV.s^{-1}) are performed according to the criteria given in chapter 3.1.3. However
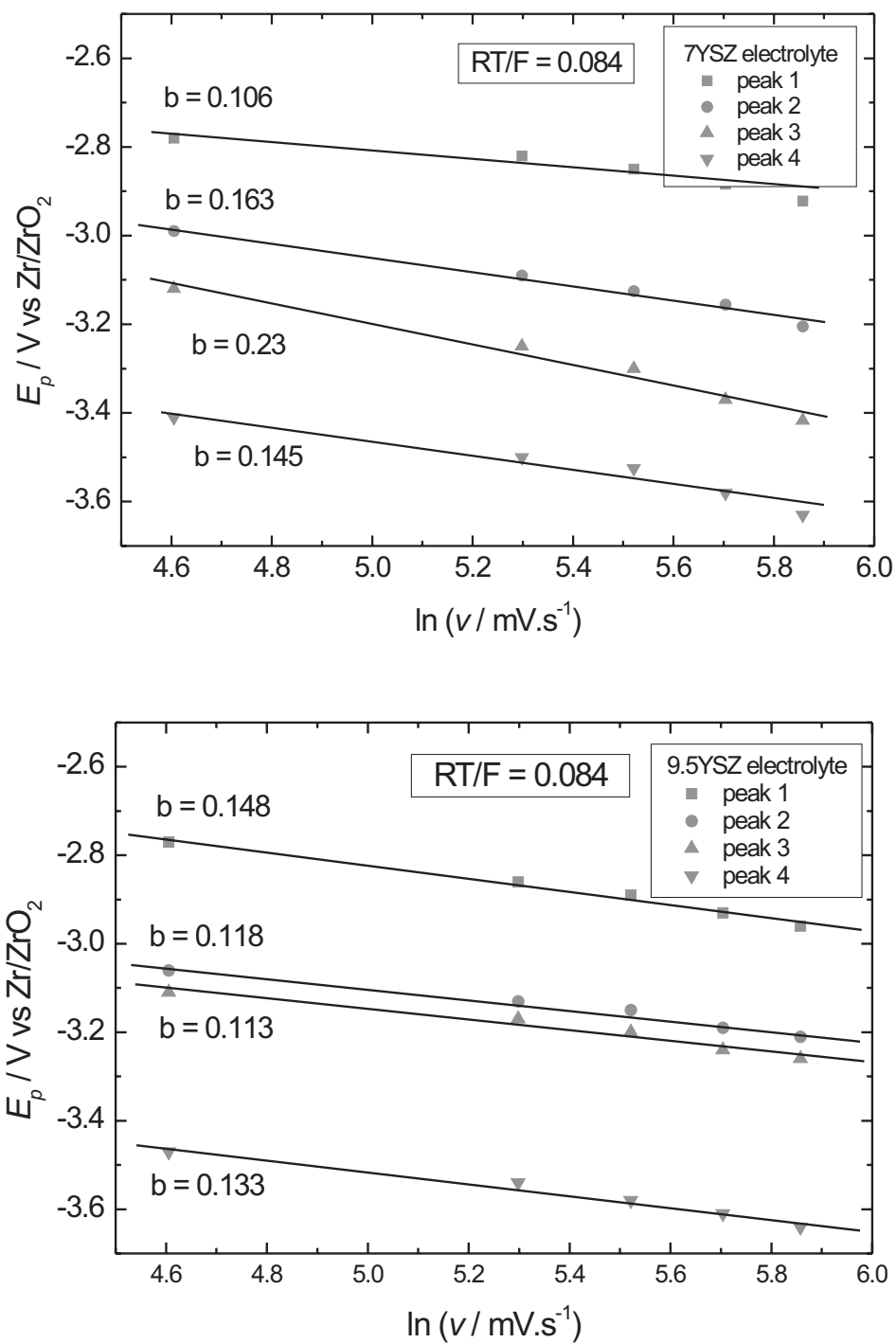
Fig. 6.17: $E_p/\ln v$ plot for 7YSZ (left) and 9.5YSZ (right) on gold micro electrode at temperature 700 °C in pure nitrogen ($a_{O_2} = 10^{-14}$)

because we changed the position of the micro-electrode for each new sweep rate (in order to eliminate the influence of nitrogen incorporated during the sweeps) the real electrode surface may vary and cannot be defined exactly, respectively no current density can be calculated we do not use the plot i_p vs. $v^{1/2}$ as a criteria for reversibility/irreversibility. Additionally the diffusion coefficient of nitrogen ions is still not precisely determined and the transfer coefficients are not known so we cannot calculate the theoretical slopes for this dependence to compare them with the experimental ones. However as already mentioned the absence of anodic peaks on the reverse scan of CV's is a clear diagnostic that the processes are controlled by the charge transfer and not by the diffusion. Further in order to determine the Tafel constant b, respectively the parameter αn $\left(b = \frac{2.3RT}{\alpha nF}\right)$ we plot the peak potential versus logarithm of the sweep rate (E_p vs. $\ln v$). From the slope of the line the Tafel constant b was calculated. On figure 6.17 $E_p/\ln v$ plots for all four peaks on 7YSZ and 9.5YSZ electrolyte are present. The values for b vary in the range between 106 mV and 230 mV for this temperature. If we take into account that $\frac{RT}{F} = 0.084$ the values for αn_α can be calculated. Assuming one or maximum two electron exchange per single act we calculate a transfer coefficient for each the individual steps between 0.4 and 0.6 which value is usual for the transfer coefficient in the electrochemically controlled kinetics.

Determination of the activation energies

As next step we have performed measurements at different temperatures in the range 500 °C ÷ 840 °C in order to determine the activation energies of the individual steps. It has been already discussed (see chapter 2.6.1) that the chemical reaction rate can be expressed in electrical units: $v = i/nF$. So plotting the dependence of the peak current on the temperature in Arrhenius ($\log i$ vs $1/T$) coordinates we calculated the activation energies. In figure 6.18 Arrhenius plots for 7YSZ and 9.5YSZ solid electrolytes are given. Two regions can be clearly distinguished on both graphs. The first one is up to temperatures of approximately 750 °C. The Arrhenius plots consist of straight lines with slopes corresponding to the activation energies of the individual steps of the nitrogen electrochemical reduction. The second region is at temperatures above 750 °C
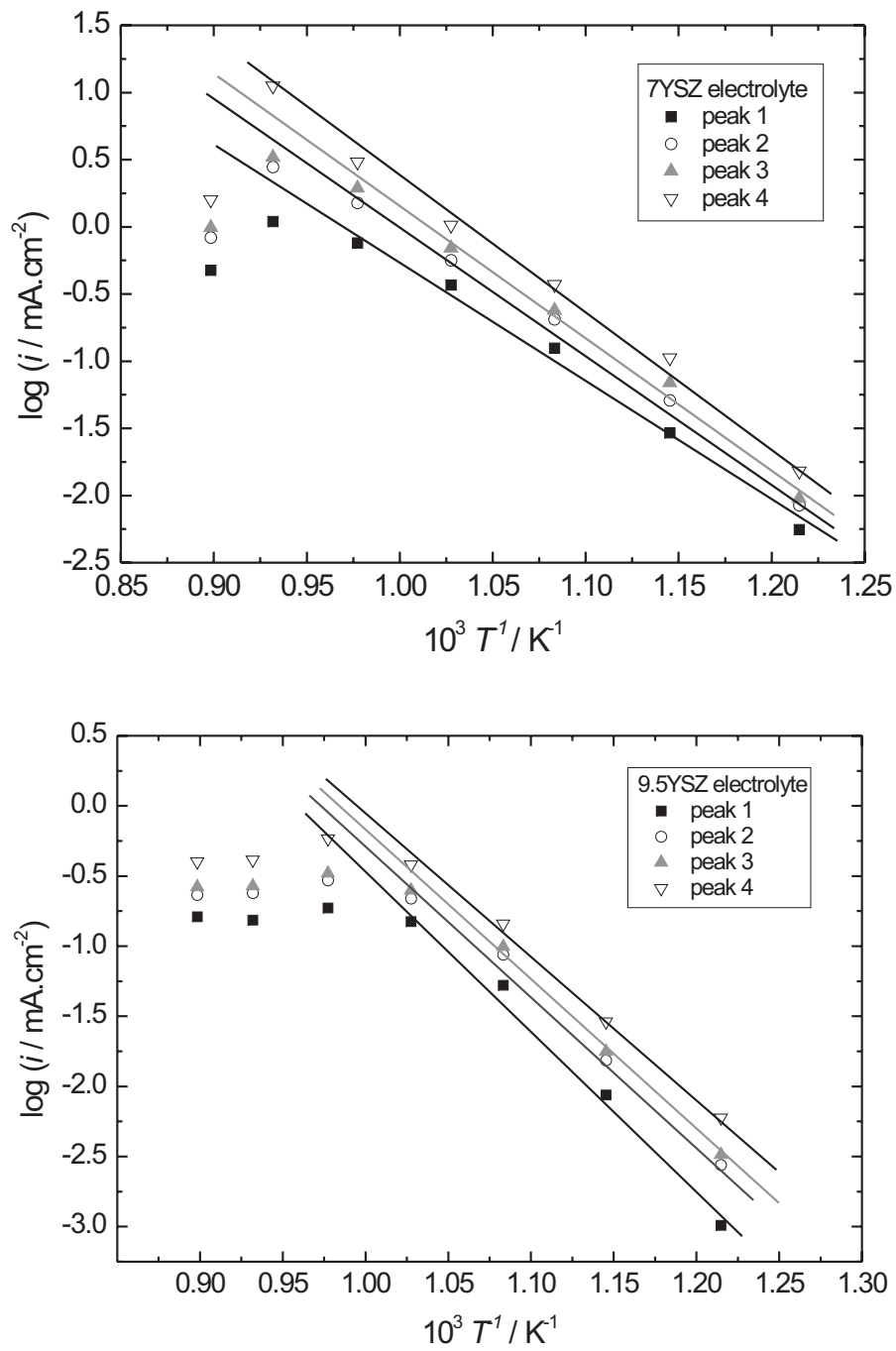
Fig. 6.18: Arrhenius plot for 7YSZ and 9.5YSZ on gold micro electrode

up to 840 °C. In this region we calculate negative slopes, respectively negative activation energies, because the current decreases with increasing temperature. To explain this result we suggest that in this region the nitrogen molecules had become enough thermal energy to desorb from the electrode surface in the gas phase, thus lowering the rate of the electrochemical reaction. The latter results in negative slopes of the activation energies. The temperature range near 750 °C seems to be a very special region for the YSZ/Me(N_2) system. Exactly at these temperatures we measure a maximum in the double layer capacity (see chapter 6.1.4). Above 750 °C this capacity also decreases. As N_2 molecules are electrically neutral species their adsorption at the electrode/electrolyte interface causes an increase in the capacity of EDL and respectively their desorption should decrease it. So both capacity measurements and temperature dependent experiments (Arrhenius plot) confirm our suggestion that at temperatures of about 750 °C a maximum concentration of adsorbed species is achieved. Above these temperature these species are desorbed or at least leave the electrode/electrolyte interface.

Further we have compared all the activation energies in order to determine the step controlling the overall reduction process i.e. we calculate the activation energies for all four peaks recorded on zirconia electrolyte with different Y_2O_3 concentration and we have compared them as individual and absolute values. Figure 6.19 presents the variation of individual peak activation energies as a

function of dopant amount. The individual peak values vary in the range of 1 eV up to 3.06 eV. For the sample doped with 3 mol% yttria the highest activation energy is required for the fourth step of the reduction process $E_A = 3.08$ eV. It is followed by the second, third and the first steps with decreasing energy values respectively. The sample doped with 5 mol% Y_2O_3 shows the largest deviation in the peak activation energies of the individual steps. The first one consists of only 1 eV, followed by second, third and the fourth steps, where the highest activation is needed for the last one $E_A = -2.02$ eV. The most favorable energetic conditions for the nitrogen reaction are measured for the 7YSZ sample. The first peak (E $= -2.7$ V) requires activation of only 1.89 eV and the highest energy required is for the second peak at potential of -3.0 V: $E_A = 1.94$ eV. The 9.5YSZ electrolyte has much higher value of the first peak
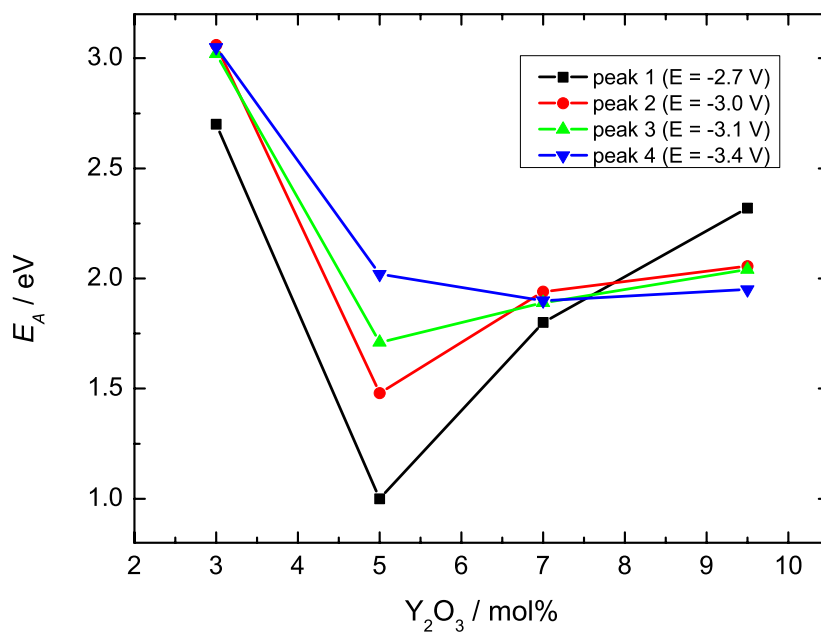
Fig. 6.19: Dependence of the individual peak activation energies at gold micro electrodes on YSZ electrolyte as a function of Y_2O_3 content

(E_A = 2.32 eV) but it is the highest one compared with the other three peaks. They are characterized by approximately equal activation energies of 2.0 eV. In table 6.1 the calculated values of the activation energies as a function of yttria content for the different peaks are summarized. The individual values of the activation energies provide an information about the maximal energy required to proceed the overall reaction and respectively which of the individual step is determining the reaction rate. Additionally we can compare this energy for zirconia containing different Y_2O_3 amount and choose the most appropriate solid electrolyte.

As already mentioned above the most favorable electrolyte we found to be 7YSZ. Its activation energy of the second step of 1.94 eV is the lowest activation energy (compared to the samples with other yttria content) determining the overall reaction rate. Further followed the 5YSZ with 2.02 eV, 9.5YSZ with 2.32 eV and at the end is 3YSZ with 3.08 eV. We also can see that the reaction

Table 6.1: Activation energies of the different electrochemical reduction steps as a function of Y_2O_3 content in zirconia

	3YSZ	5YSZ	7YSZ	9.5YSZ
peak 1	2.7 eV	1 eV	1.8 eV	2.32 eV
peak 2	3.06 eV	1.48 eV	1.94 eV	2.06 eV
peak 3	3.02 eV	1.71 eV	1.89 eV	2.04 eV
peak 4	3.08 eV	2.02 eV	1.87 eV	1.95 eV

proceeds with different rate determining steps depending on the Y_2O_3 concentration. Thus for the 3YSZ and 5YSZ the last step determines the overall rate whereas for 9.5YSZ and 7YSZ the first, respectively the second one is the limiting factor. It looks perhaps surprising, that the electrolyte with the highest vacancy concentration (9.5YSZ) requires higher activation energies for nitrogen reduction than those with 5 mol% and 7 mol% yttria. However the change of the double layer capacity as a function of the dopant concentration may answer explain this result. It is well known that the capacity and the structure of the EDL are related to the overvoltage. As higher is the capacity as higher is the activation energy of the reaction and as higher is the overvoltage required to keep a constant reaction rate. The double layer capacity for the 9.5YSZ has the highest value compared to the electrolytes doped with 3, 5 and 7 mol% yttria. That is the reason why the activation energy is high and may be exactly that is the reason the first step to be the limiting one. Of course in the case of 3YSZ the high activation energies are related to the high resistivity of the material and the low vacancy concentration. Also we should clearly distinguish the electrochemical reduction, which is a surface/interface process and diffusion in the bulk. The potentiodynamic measurements are sensitive to surface reactions and not to the slower diffusion processes.

Conclusions

To summarize the results from the cathodic potentiodynamic measurements: We detect the electrochemical signals of the reduction process of molecular nitrogen. At least four peaks were registered in the potential range between E =

-2.5 V and -3.5 V versus Zr/ZrO_2 reference electrode. All the individual steps are irreversible. The charge transfer of these individual stages is characterized by values for the transfer coefficient α of approximately 0.5.

The measurements performed at different temperatures allow to calculate the activation energies of the individual steps and as well to determine the activation energy of the step controlling the rate of the overall reaction. In Arrhenius plot two regions were distinguished: below and above 750 °C. At temperatures below 750 °C the values determined for the individual peaks depending on the Y_2O_3 content in the ZrO_2 electrolyte vary between 1 eV and 3.08 eV, where the most favorable condition is obtained for 7YSZ. At temperatures above 750 °C the activation energies become negative. We interpret this result with desorption of nitrogen atoms/molecules and/or other species from the electrode/electrolyte interface. These results supported the conclusions from the measurements of the double layer capacity showing a maximum at 750 °C thus suggesting the adsorption/desorption processes at this temperature.

Steady state electrochemical measurements

In contrast to potentiodynamic methods the steady state polarization measurements are not appropriate for direct detailed studies of all the individual electrochemical steps especially if they do not proceed with comparable rates. But as already discussed in section 3.1.3 the advantage of this method is the completeness and integrity of the information which we extract from the current-voltage dependencies. In contrast to CVA the electrochemical response originates not only from the concentration of species in the vicinity of the surface but also from the bulk of material.

We have studied the electrochemical nitrogen reduction in the temperature range between 650 °C and 700 °C. This region has been chosen in order firstly to ensure a high ionic conductivity and secondly to avoid any undefined experimental conditions due to adsorption/desorption processes taking place at temperatures around 750 °C (see 6.3.2) which will influence the recorded electrochemical characteristics. In figure 6.20 the steady state potential-current curve of a gold micro-electrode on 7YSZ is shown as a function of time. This
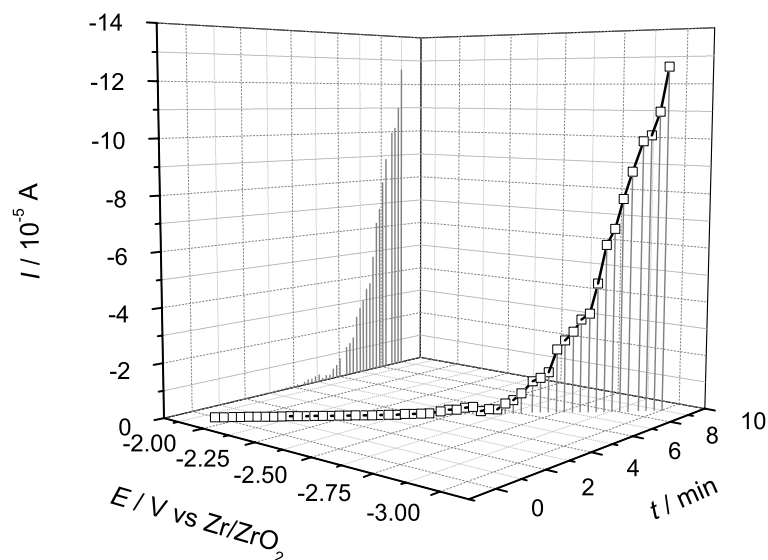
Fig. 6.20: Steady state potential-current curve of a gold micro electrode on 7YSZ in pure nitrogen. $T = 700$ °C, $a_{O_2} = 10^{-14}$

presentation of the results has the advantage that it also depicts the current-time dependence giving an impression for the charge used for the process. The charge can be further calculated by integration of the area beneath the I/t curve. In contrast to the steady state curve in oxygen the E/I dependence in nitrogen starts at much lower (more negative) potential values. Due to the reduced oxygen content in the working atmosphere the oxygen species do not contribute to the potential determining reaction (at least not so strong) and the electrochemical equilibrium is shifted to the next redox couple. Additionally the polarization (the overvoltage) of the reaction is extremely high (about 600 mV) which is a sign for a large capacity of the electrical double layer and leads to the conclusion of reaction rate controlled totaly by the charge transfer kinetics.

On the curve two plateaus can be distinguished. Each of these plateaus represents a limited current of the overall electrochemical reaction. The first one appears in potential range between $E = -2.78$ V up to $E = -2.82$ V

and the second one in the range of $E = -2.94$ V up to $E = -2.96$ V. A further increase of the potential does not change the form of the curve. At potential values above -2.5 V according to the thermodynamical calculations the process of reduction of the electrolyte can also appear. However its rate is much lower than those of the nitrogen reaction but in long lasting experiments (exceeding 40 min.) this reaction should not be neglected. In our experiments taking over 40 minutes we detect an increase of the electric conductivity of the samples. The latter is most probably a result of the substitution of oxygen by nitrogen resulting in ZrN formation (ZrN is an electronic conductor) and/or due to the reduction of YSZ. Both factors can contribute to increase the overall conductivity but a detailed spatially resolved analysis on eventual change in the structure of the material were not possible.

More detailed information on the redox processes was obtained by presenting the experimental data in Tafel plot as shown on figure 6.21 below. On the Tafel plot we can clearly define three regions. The first one at the beginning ($E = -1.9$ V up to $E = -2.2$ V) is characterized by negligible Faradaic current (non-Tafel region), where the potential - current dependence is still not exponential but linear (see chapter 2.6.1, p. 47). The second region is the most extended one between $E = -2.2$ V and $E = -2.85$ V. It is a typical Tafel region with a slope of 225 mV. The third and the last one is in the potential range $E = -2.85$ V and $E = -3.08$ V. It is characterized by a higher slope and the electrochemical process is controlled by diffusion or has a mixed control. From the results presented in the Tafel plot we draw the following conclusions: *The electrochemical process* of nitrogen reduction occurs under charge transfer control. *A Tafel slope* of $b = 225\ mV$ was determined. *The exchange current* density was calculated according to the relation $i_0 = exp(-a/b)$ and has extremely low values: $i_0 = 6.57 \times 10^{-18}\ A.cm^{-2}$ which experimentally proofs that the nitrogen molecules have a negligible self-incorporation rate into zirconia solid electrolyte, predicted also by the thermodynamic calculations in chapter 2.3. To calculate the transfer coefficient α we take into account that at this temperature the constant RT/F has the value of 84 mV and for the parameter αn the value of 0.86 was obtained.However on the basis of this value alone we still cannot make any conclusions concerning the energetic barrier of the process
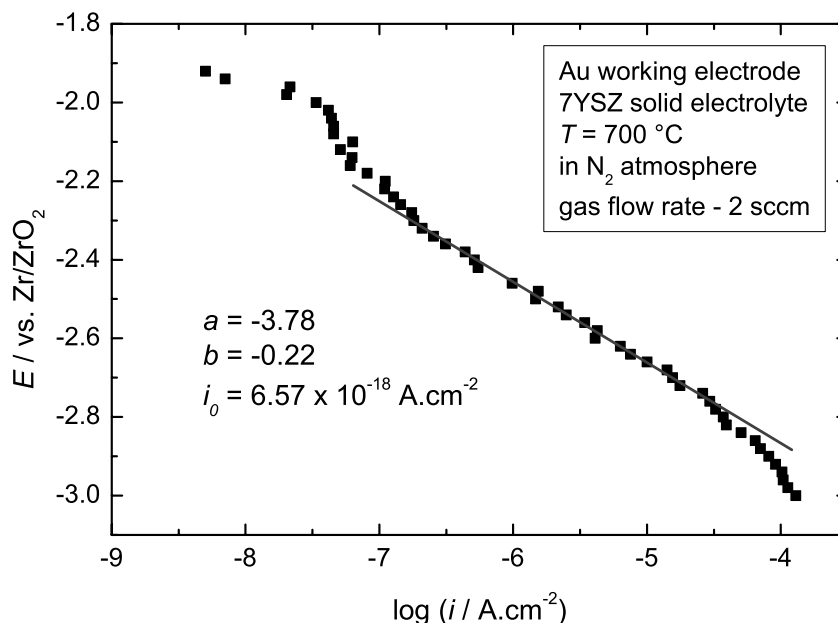
Fig. 6.21: Tafel plot of steady state potential-current curve on 7YSZ at gold micro electrode in pure nitrogen. $T = 700$ °C, $a_{O_2} = 10^{-14}$

because we do not know the number of the exchanged electrons at this step.

Mechanism of the electrochemical nitrogen reduction

In order to study the mechanism of the electrochemical nitrogen reduction we combined the steady state polarization measurements with the concept for the stoichiometric number as described in section 2.6.3, p. 51. We plot together the anodic and the cathodic polarization curve in logarithmic coordinates as a function of the overpotential. The anodic curve was recorded on a sample of nitrogen doped 7YSZ solid electrolyte prepared via pulsed laser deposition at gold micro electrodes. In order to prevent any oxidation reaction of the molecules from the gas phase (oxidation of N_2 to N^{x+} species) we have performed the measurements in pure argon atmosphere ($a_{O_2} = 10^{-13}$) at the same temperature (700 °C) as the cathodic curve was recorded. As the N_2/N^{3-} redox couple has more negative standard electrochemical potential than the O_2/O^{2-} couple,

N^{3-} ions should be preferably oxidized. Because of the complexity of the nitrogen reaction we have additionally subtracted from the anodic curve of N-doped 7YSZ sample the $I - E$ curve of an electrolyte which does not contain nitrogen ions. So we assume that the recorded current-voltage dependence is a result of the electrochemical oxidation of nitrogen. The combined anodic/cathodic Tafel plot is shown on figure 6.22. According to the theory of the single step electron

$a = 1.06$
$b = 0.165$
$i_0 = 3.76 \times 10^{-7}$ A.cm^{-2}

$a = -3.78$
$b = -0.22$
$i_0 = 6.57 \times 10^{-18}$ A.cm^{-2}
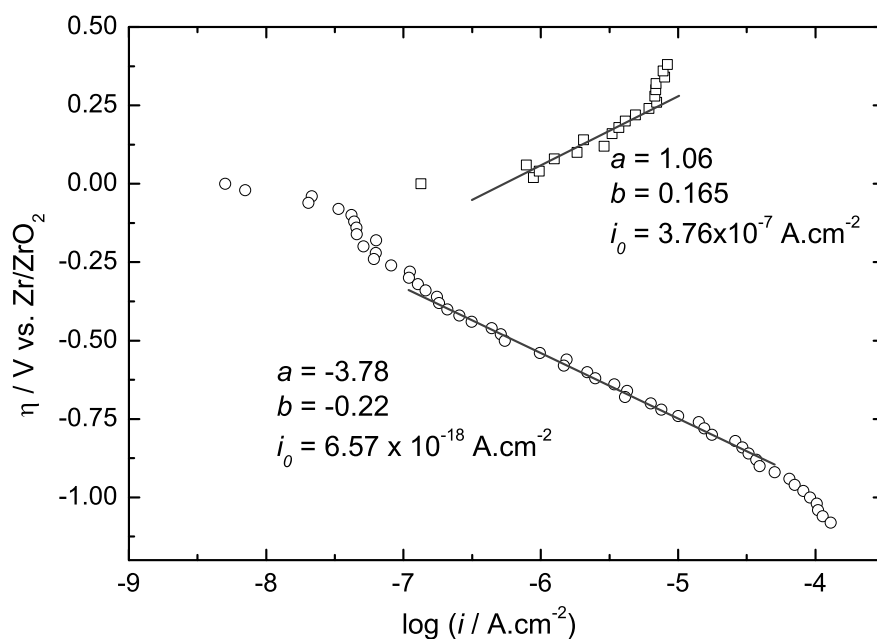
Fig. 6.22: Mixed anodic and cathodic Tafel plot of steady state potential-current curve of a gold micro-electrode. The anodic curve was taken in pure argon on a N-doped 7YSZ sample. The cathodic curve on 7YSZ in pure nitrogen. $T = 700$ °C

transfer (see chapter 2.6.1) both tangents (cathodic and anodic) to the Tafel slopes should cross in one point at $\eta = 0$, thus determining the exchange current density. For such simple processes the exchange currents of the anodic and the cathodic reactions are equal. In graphic 6.22 this is obviously not the case as the both reactions have different exchange currents and do not cross at $\eta = 0$. The latter is an evidence for a multi-step charge transfer reaction. It can be seen that the anodic exchange current is much larger (of approximately ten orders of magnitude) than the cathodic one which demonstrates that nitrogen ions are

much faster oxidized as nitrogen molecules are reduced and incorporated. Thus the electrochemical reduction of nitrogen is found to be complicated, where the charge transfer is controlling the kinetics of the overall reaction. From the Tafel slope we cannot calculate the transfer coefficient α or β for the cathodic, respectively anodic reaction, but the apparent transfer coefficients α_c and α_a as defined in section 2.6.2 (p. 50). From the relations $b_c = \frac{2.3RT}{\alpha_c F}$ and $b_a = \frac{2.3RT}{\alpha_a F}$ we have calculated the apparent transfer coefficients: $\alpha_c = 0.86$ and $\alpha_a = 1.17$. Assuming a multi-step electrochemical process we apply the concept of stoichiometric number for the overall redox reaction: $N_2 + 6e^- \rightleftharpoons 2N^{3-}$, which involves the exchange of six electrons. In general it is energetically highly unfavorable that all six electrons are transferred by a single elementary act. Such reactions involving the transfer of more than two or three electrons in a single act are extremely rare and we neglect the possibility that all six electrons in the nitrogen electrochemical reduction are transferred in one single step. To understand the mechanism of the reaction and to suggest a reasonable reaction route we have to evaluate the stoichiometric number of the rate determining step which controls the overall reaction rate. Equation 2.138 relates the apparent transfer coefficients and the total number of exchanged electrons to the stoichiometric number ν as: $\nu(\alpha_c + \alpha_a) = n$. From the Tafel slope shown on fig. 6.22 the apparent transfer coefficients α_c and α_a equal to 0.86 and 1.17 respectively. We also assumed that the total number of exchanged electrons $n = 6$, and substituting these values in eq. 2.138 we obtain:

$$\alpha_c + \alpha_a = \left(\frac{m}{\nu} + \alpha_{RDS}\right) + \left(\frac{n-m}{\nu} - \alpha_{RDS}\right) \qquad (6.15)$$

or

$$\nu = \frac{n}{\alpha_c + \alpha_a} = \frac{6}{0.86 + 1.17} \approx 3 \qquad (6.16)$$

where α_{RDS} is the transfer coefficient of the rate determining step. The value obtained is the number of repetitions of the slowest step (RDS) in order to proceed from nitrogen molecule to the final product $2N^{3-}$. In the reaction rout the rate determining step should be repeated 3 times i.e. $\nu = 3$. An additional criterium in the evaluation of the reaction parameters is the ratio $\frac{\alpha_c}{\alpha_a}$. From this ratio we calculated, according to $\frac{\alpha_c}{\alpha_a} = \frac{m+\alpha}{n-m-\alpha}$, the number of steps before (m) and after $(n-m-\nu)$ the rate determining step (see eq. 2.145, p. 56).

Because nitrogen can exist as an anion in all possible valence states (-1; -2, -3) and because the single electron transfer is the mostly energetic favorable we assume that in each of the intermediate steps only one electron is transferred.

$$\frac{\alpha_c}{\alpha_a} = \frac{\left(\frac{m}{\nu} + \alpha_{RDS}\right)}{\left(\frac{n-m}{\nu} - \alpha_{RDS}\right)} \tag{6.17}$$

If we substitute for simplicity in this equation α_c/α_a by c and assume a transfer coefficient value of the single electron transfer process in the rate determining step $\alpha_{RDS} = 0.5$ we can solve the equation in respect to m and obtain:

$$m = \left(\frac{c}{1+c}\right) \cdot n - \alpha_{RDS} \cdot \nu = \left(\frac{0.74}{1+0.74}\right) \cdot 6 - 0.5 \cdot 3 \approx 1 \tag{6.18}$$

According to equation 6.18 one step precedes the rate determining step ($m = 1$) and two steps follow it ($n - m - \nu = 2$).

To summarize the results from the steady state polarization experiments: We conclude that the process of electrochemical nitrogen reduction is a multi step charge transfer process. The evaluation of the experimental data suggests that the rate determining step is repeated three times to obtain as a final product $2N^{3-}$. The rate determining step is preceded by one and followed by two other steps under the assumption that in all the steps only one electron is transferred.

The next step is to suggest possible intermediate species. As discussed above the dissociation energy of the nitrogen molecule is extremely high (see page 143) and we do not suppose that nitrogen atoms can exist alone and participate in the electrochemical reduction. It is energetically more favorable that the nitrogen molecule are partially reduced forming intermediate species of the type N_2^- and/or N_2^{2-}. Interestingly the existence of N_2^{2-} has been proven by Auffermann et al. and Prots et al. as being the anion within SrN_2 [175,176], and it has been found to be relatively stable. The set of possible reaction routes is formulated under the following assumptions:

1. Only nitrogen molecules (and not atoms) are participating in the reaction leading finally to the formation of N^{3-}. Thus we neglect N-atoms as stable intermediates.

2. We assume that the only possible stable intermediates are N_2^- and N_2^{2-} as the acquisition of more than two electrons by the nitrogen molecule will

result in energetically unstable composition which will decompose very fast.

The reactions listed below described not all the possible reactions, but we have selected only those involving the transfer at least one but no more than four electrons per single act.

$$N_2 + e^- \rightleftharpoons N_2^- \tag{6.19}$$

$$N_2^- + e^- \rightleftharpoons N_2^{2-} \tag{6.20}$$

$$N_2 + 2e^- \rightleftharpoons N_2^{2-} \tag{6.21}$$

$$N_2^{2-} + 4e^- \rightleftharpoons 2N^{3-} \tag{6.22}$$

$$N_2^{2-} + 3e^- \rightleftharpoons N^{3-} + N^{2-} \tag{6.23}$$

$$N_2^{2-} + 2e^- \rightleftharpoons N^{3-} + N^- \tag{6.24}$$

$$N_2^{2-} + 2e^- \rightleftharpoons N^{3-} + N \tag{6.25}$$

$$2N_2^{2-} + 4e^- \rightleftharpoons 2N^{3-} + N_2^{2-} \tag{6.26}$$

$$2N_2^{2-} + 3e^- \rightleftharpoons 2N^{3-} + N_2^- \tag{6.27}$$

$$2N_2^{2-} + 2e^- \rightleftharpoons 2N^{3-} + N_2 \tag{6.28}$$

$$2N_2^{2-} + e^- \rightleftharpoons N^{3-} + N_2^{2-} + N \tag{6.29}$$

$$N_2^{2-} + e^- \rightleftharpoons N^{3-} + N_2^- + N^- \tag{6.30}$$

$$3N_2^{2-} + 4e^- \rightleftharpoons 2N^{3-} + 2N_2^{2-} \tag{6.31}$$

$$3N_2^{2-} + 4e^- \rightleftharpoons 3N^{3-} + N_2^- + N \tag{6.32}$$

$$3N_2^{2-} + 3e^- \rightleftharpoons 3N^{3-} + N_2 + N \tag{6.33}$$

$$3N_2^{2-} + 3e^- \rightleftharpoons 2N^{3-} + N_2^{2-} + N_2^- \tag{6.34}$$

$$3N_2^{2-} + 2e^- \rightleftharpoons 2N^{3-} + 2N_2^- \tag{6.35}$$

$$3N_2^{2-} + 2e^- \rightleftharpoons 2N^{3-} + N_2^{2-} + N_2 \tag{6.36}$$

$$3N_2^{2-} + e^- \rightleftharpoons 2N^{3-} + N_2^- + N_2 \tag{6.37}$$
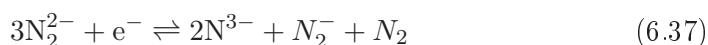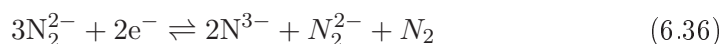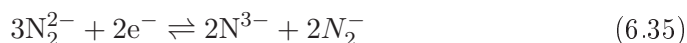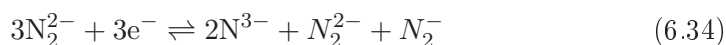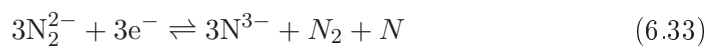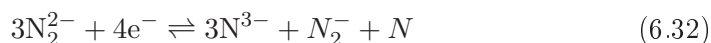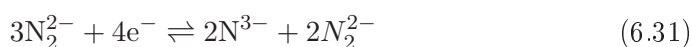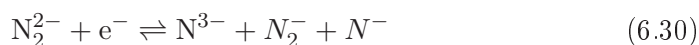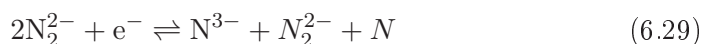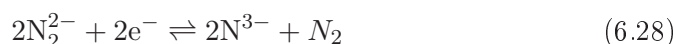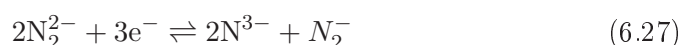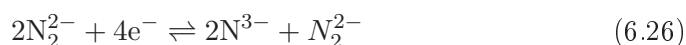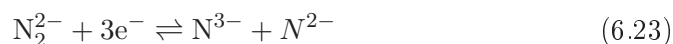
We have formulated eighteen possible reactions involving the formation and the consumption of the both possible intermediate species N_2^- and N_2^{2-}. From these eighteen equations we can eliminate equations 6.23, 6.24, 6.25, 6.29, 6.30, 6.32

and 6.33 because they involve either the formation of atomic nitrogen or a single charged nitrogen atoms which is highly improbable. Additionally equations 6.22, 6.26 and 6.31, respectively 6.27 and 6.34 as well equations 6.36 and 6.28 are equal and only one of each group remain, and as a final result we reduce the possible equations to a set of eight electrochemical steps representing the most probable pathways.

$$
\begin{array}{rlll}
1) & N_2 + e^- & \rightleftharpoons & N_2^- \\
2) & N_2^- + e^- & \rightleftharpoons & N_2^{2-} \\
3) & N_2 + 2e^- & \rightleftharpoons & N_2^{2-} \\
4) & N_2^{2-} + 4e^- & \rightleftharpoons & 2N^{3-} \\
5) & 2N_2^{2-} + 3e^- & \rightleftharpoons & 2N^{3-} + N_2^- \\
6) & 2N_2^{2-} + 2e^- & \rightleftharpoons & 2N^{3-} + N_2 \\
7) & 3N_2^{2-} + 2e^- & \rightleftharpoons & 2N^{3-} + 2N_2^- \\
8) & 3N_2^{2-} + e^- & \rightleftharpoons & 2N^{3-} + N_2^- + N_2
\end{array}
$$
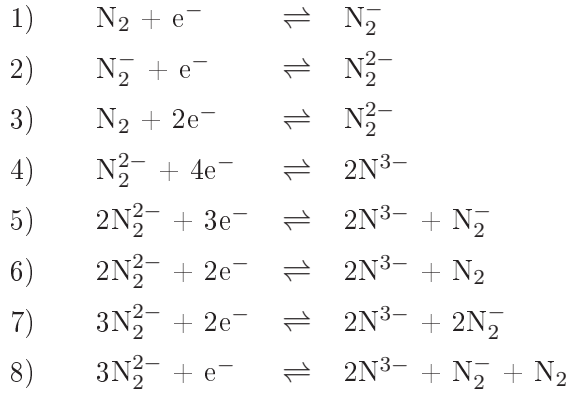
According to equation 2.134 (see page 52) we can calculate the number of independent solutions:

$$P = S - I = 8 - 2 = 6 \tag{6.38}$$

The six possible reaction routes are further reduced on the basis of the experimental results i.e. the parameters m, ν and $n - m - \nu$. The steady state condition require that the sum of all intermediates along the particular pathway equals zero. We denote $N_2^- = 1$ and $N_2^{2-} = 2$, and for species 1 it follows:

$$\sum_{s=1}^{8} \nu_{s,1} b_{s,1} = \nu_{1,1} - \nu_{3,1} + \nu_{5,1} + \nu_{7,1} \cdot 2 + \nu_{8,1} = 0 \tag{6.39}$$

We define a matrix with the possible values for the coefficients $\nu_{s,1}$ (for the s values the numbers of eqs. 1 - 8 are used) which fulfill the requirements of equation 6.39. As discussed in section 2.6.3 we can apply any linear mathematical operation valid for vectors on these solutions and it will be automatically valid, but it is important to take care that there is a physical meaning behind this operations. We can sort out different routes for production and consumption of N_2^-, but it is clear that reaction (1) cannot be excluded as it is the only reaction which creates N_2^- species directly from N_2. So all routes with $\nu_{1,1} = 0$ are excluded from further considerations. The other solutions are all possible and on this stage we cannot further reduce their number. In the second step

Table 6.2: Possible values for the coefficients $\nu_{s,1}$ according the solutions of equation 6.39

	$\nu_{1,1}$	$-\nu_{3,1}$	$\nu_{5,1}$	$2\,\nu_{7,1}$	$\nu_{8,1}$
1.	1	1	0	0	0
2.	1	2	1	0	0
3.	1	2	0	0	1
4.	1	3	1	0	1
5.	1	3	0	1	0
6.	2	3	0	0	1
7.	2	3	1	0	0

we analyze the second intermediate species. The steady state condition is here formulated as:

$$\sum_{s=1}^{8} \nu_{s,2} b_{s,2} = \nu_{2,2} + k_{3,2} - \nu_{4,2} - \nu_{5,2} - \nu_{6,2}\cdot 2 - \nu_{7,2}\cdot 3 - \nu_{8,2}\cdot 3 = 0 \quad (6.40)$$

The possible mathematical solutions for this equation are given in the table below. We neglected the term $\nu_{2,2}$ corresponding to N_2^{2-} created in reaction

Table 6.3: Possible values for the coefficients $\nu_{s,2}$ according to the solutions of equation 6.40

	$\nu_{3,2}$	$-\nu_{4,2}$	$-2\,\nu_{5,2}$	$-2\,\nu_{6,2}$	$-3\,\nu_{7,2}$	$-3\,\nu_{8,2}$
1.	1	1	0	0	0	0
2.	2	0	1	0	0	0
3.	2	0	0	1	0	0
4.	3	1	0	1	0	0
5.	3	1	1	0	0	0
6.	3	0	0	0	1	0
7.	3	0	0	0	0	1

(2), otherwise we have no step before the RDS or we should propose another step to be the rate determining involving species of the type N_2^{x-} with $x > 2$ which do not correspond to our initial conditions and experimental results.
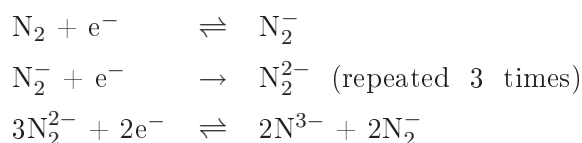
The analysis of the possible reaction routes involving the formation and consumption of the two most probable intermediate species N_2^- and N_2^{2-} alone suggest more alternative solutions. To reduce their number we take into account our experimental results and the calculated reaction parameters (m, *and* ν). We should mention that in the calculation of the steps before (m) and after ($n-m-\nu$) the rate determining step we have assumed that all individual steps involve only a single electron exchange. In the step before the RDS (m) it is reasonable to expect only single electron transfer because as the experimental results suggest we have one step before RDS. If two electrons are transferred during this first step we should expect as a second charge transfer act (the RDS) a step involving a creation of intermediate species of the type N_2^{3-}. As we already discussed the energy of such a molecular ion will be too high, i.e this species will not be a stable intermediate and it cannot polarize the electrode. In other words such a reaction cannot be a rate determining step.

As the total number of exchanged electrons is six we expect that in the steps after the RDS two additional electrons are exchanged leading to $2N^{3-}$ formation. We cannot experimentally determine by the steady state measurements if these two electrons are transferred in a single act or in two steps. In this case we have to refer to the potentiodynamic experiments (section 6.3.2, p. 151). We detect four peaks where for 7YSZ electrolyte, where the second one has the highest activation energy i.e. determines the overall reaction rate. Two peaks are detected after the RDS and one before. So these experiments confirm our suggestion for single electron transfer steps.

In table 6.3 we point out the minimum set of independent solutions for the second intermediate. As the stoichiometric number is three ($\nu = 3$) only routes 4 to 7 fulfill the steady state condition requirement. As discussed above we can multiply the coefficients of the pathways 1 to 3 achieving $\nu_{3,2} = 3$, but this does not result in a new independent solution. We can further reduce the number of the probable reaction routes as route 4 and route 5 are not in agreement with our initial assumptions (i.e. the value for n), and route 7 (reaction 8) involves only one electron exchange, whereas our results suggest two steps after the rate determining step and the number of electrons cannot be lower than two. After this the only remaining route is route 6 {3 0 0 0 1 0} suggesting reaction

(7) to be the pathway for the overall reaction. Except the final product $2N^{3-}$ as a side product $2N_2^-$ ions are created which can further participate in N_2^{2-} formation.

Referring again to table 6.2 we are now able to propose a reaction route for the N_2^- formation involving reaction (7) and we can safely conclude that the only possible route for these species is route 5 {1 3 0 1 0}, which involves their formation as a result of reactions (1) and (8) and their consumption by reaction (3). As a possible mechanism of the reaction of electrochemical reduction of molecular nitrogen to N^{3-} on gold electrode we suggest on the basis of our analysis the following route:

$$N_2 + e^- \quad \rightleftharpoons \quad N_2^-$$
$$N_2^- + e^- \quad \rightarrow \quad N_2^{2-} \quad \text{(repeated 3 times)}$$
$$3N_2^{2-} + 2e^- \quad \rightleftharpoons \quad 2N^{3-} + 2N_2^-$$

The most probable mechanism of the overall reaction of the electrochemical nitrogen reduction on 7YSZ solid electrolyte at gold electrodes proceeds via three steps: N_2^- formation, its reduction to N_2^{2-} which is the rate-determining step and the final step to form N^{3-} (the third stage) anion. In this final step N_2^- is also produced which leads to a feedback step. The reaction route is graphically presented in figure 6.23.
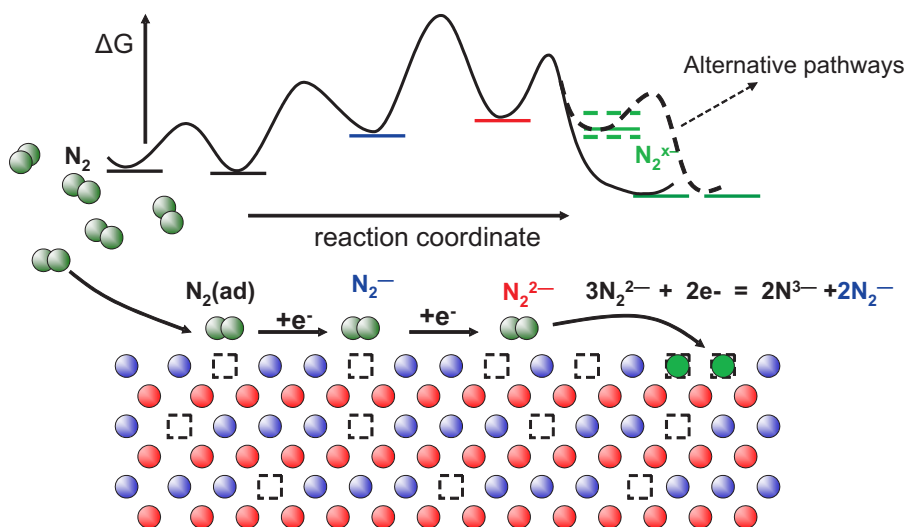
Fig. 6.23: Schematic presentation of the reaction route of the reduction of molecular nitrogen to nitrogen ion.

To summarize briefly the analysis and considerations: We have applied the concept of the stoichiometric number to the study of the mechanism of electrochemical nitrogen reduction and incorporation. Two species have been chosen as the most probable intermediates - N_2^- and N_2^{2-}. We have formulated a set of chemical equations which represent different possible reaction routes for the overall reaction involving the formation and consumption of these intermediates. Taking into account the experimentally determined stoichiometric number ν and the number of steps before and after the rate determining step (calculated on the basis of the results provided by the steady state polarization measurements) we suggest a mechanism of the overall reaction of the electrochemical nitrogen reduction on 7YSZ solid electrolyte at gold electrodes, where the rate determining is the second reduction step and it should be repeated three times in order to let the overall reaction proceed once.

6.3.3 SIMS analysis on the local nitrogen incorporation

In order to confirm by a direct analytical method the incorporation of nitrogen ions into zirconia and also to determine at what potential value the incorporation starts we have analyzed the oxide surface beneath the micro electrode and its vicinity after polarizing the electrode by secondary ion mass spectrometry (SIMS).

Experimental details

We performed the experiments of the nitrogen incorporation into YSZ electrolyte with 7YSZ thin films deposited by PLD and with (111) orientated 9.5YSZ single crystals. The working electrodes were of silver or gold. The working temperatures were between 600 °C and 700 °C. The applied voltages were in the range $E = -1.0$ V up to $E = -3.55$ V. The experiments in nitrogen atmosphere were carried out for 10 min and in air for 30 min. The nitrogen incorporation was proven after the experiments by SIMS.

Electrochemical nitrogen incorporation in thin films and single crystals

Based on the potentiodynamic curves (see figures 6.14 and 6.16) we have firstly tried to incorporate nitrogen into 7YSZ films at highly negative potential ($E =$

-3.55 V), where on the voltammograms the mostly negative peak can be found. After 10 min. polarization time the micro electrode position was changed and potential of -3.55 V was applied for 5 min. The third position of the electrode was at -3.5 V for 10 min. After the experiment we have analyzed the electrolyte surface with SIMS to detect if the nitrogen was incorporated during the polarization. Figure 6.24 shows a combined image of nitrogen distribution on the surface (SIMS mapping) and an optical picture of the analyzed surface taken by an interference microscope, where the position of the nitrogen signal is related to the position of the micro electrode. The SIMS distribution profile
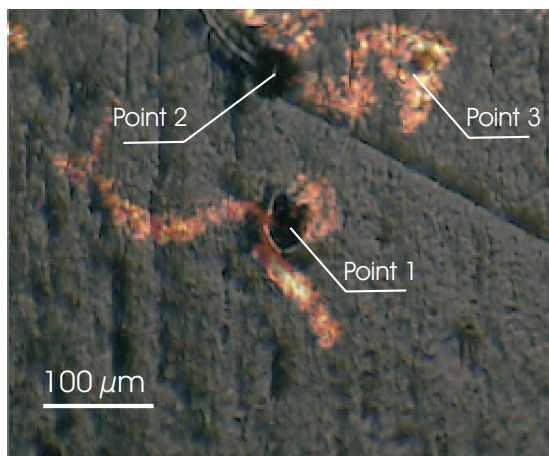
Fig. 6.24: Nitrogen distribution on 7YSZ surface after electrochemical polarization in pure nitrogen atmosphere ($a_{O_2} = 10^{-14}$) at 650 °C (the bright color corresponds to higher nitrogen content).
Point 1: $E = -3.55$ V for 10 min.; Point 2: $E = -3.55$ V for 5 min.; Point 3: $E = -3.5$ V for 10 min.

indicates clearly the incorporated nitrogen. The optical image (displayed as a background) shows that the electrolyte material have been torn by the micro electrode for Point 1 and Point 2 and for this reason the nitrogen signal comes only from the near edge positions. At Point 3 (E $= -3.5$ V) the material beneath the electrode had not been damaged and we observe a homogeneous distribution of the nitrogen signal. It can be seen especially for Point 1 and Point 2 that the nitrogen ions diffuse faster via the grain boundaries, where the bright colored

lines (corresponding to a higher nitrogen content) mark the diffusion pathway. In order to confirm diffusion through the bulk material we have repeated the experiment at the same conditions as Point 3 ($E = -3.5$ V; t = 10 min) but the electrolyte was a single crystalline (111) orientated 9.5YSZ. The SIMS analysis confirms clearly the nitrogen incorporation. Both SIMS ion images proof the ni-

^{90}Zr^{14}N
Ion intensity

^{90}Zr^{14}N / ^{96}Zr^{16}O
plus average filter

100 µm
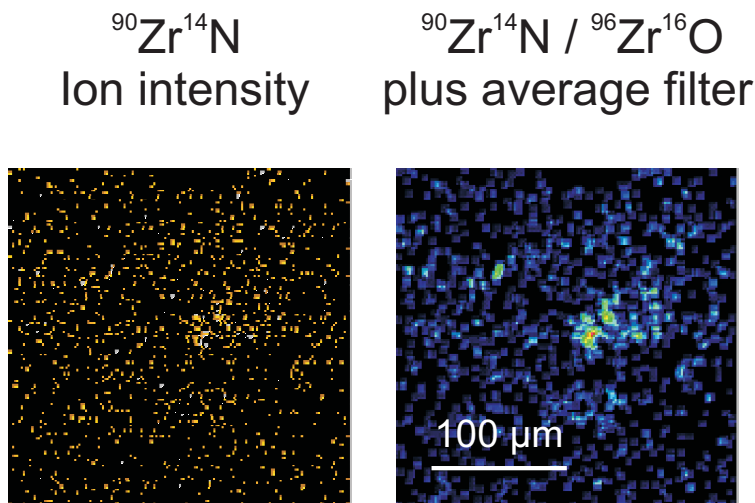
Fig. 6.25: Nitrogen distribution on (111) orientated 9.5YSZ single crystal surface after electrochemical polarization E = -3.5 V for 10 min. in pure nitrogen atmosphere ($a_{O_2} = 10^{-14}$) at 650 °C (the bright color corresponds to higher nitrogen content).

trogen incorporation into the single crystal. The position of the micro electrode can also be determined as the intensity of the signal is higher, respectively the color is brighter. Practically with the experiments on the single crystalline sample and the thin PLD layer we confirm definitely that the nitrogen is not only electrochemically active as demonstrated in the electrochemical experiments but can be incorporated into the oxide. Additional experiments performed at potential values of $E = -1.0$ V, $E = -1.5$ V, $E = -2.0$ V, $E = -2.5$ V, $E = -3.0$ V and $E = -3.5$ V show that the incorporation starts at $E = -2.5$ V with increasing intensity of the nitrogen signal by increasing the applied voltage but the strongest signal (corresponding to the highest nitrogen concentration) was obtained for the sample polarized at -3.5 V.

Finally we studied how strong the oxygen reaction influences the nitrogen incorporation. For this reason we have applied a voltage of -3.5 V to a 9.5YSZ single crystalline samples (random orientation) in both air and argon atmospheres,

where the both working and counter electrodes (macro electrodes from silver paste) were positioned on the sample surface as shown on figure 6.26. It can be
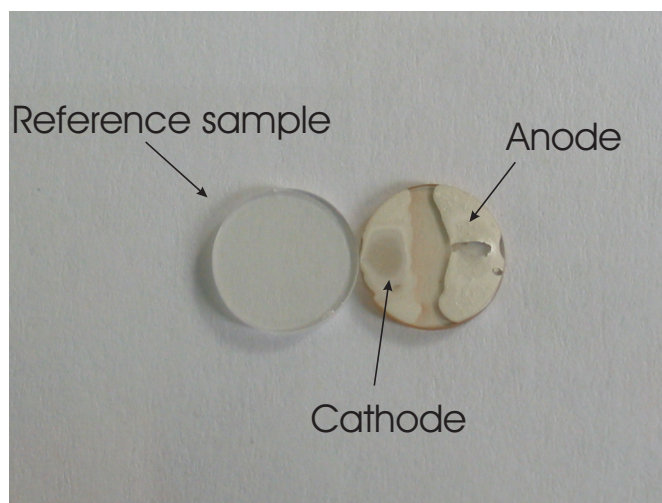
Fig. 6.26: Random orientated 9.5YSZ single crystals. On the left is the reference sample. On the right is the sample polarized (E = -3.5 V) for 30 min at 700 °C in open air conditions

seen that the sample polarized in air had changed its color from transparent (see the reference sample) to pale yellow-red. The sample was analyzed by SIMS to determine if there is a chemical change in the YSZ crystal (i.e. if nitrogen from the air was incorporated). The nitrogen signal recorded at the both sides of the sample, approximately 1 μm away from each electrode is presented in figure 6.35. The difference in the intensity of the ^{96}ZrN signal on the anodic side (going down to the background level) and on the cathodic side is clearly demonstrated. It is more pronounced at a depth up to 250 nm. The both signals become practically identical at a depth of approximately 1 μm. Of course we expected that the nitrogen concentration will decrease in the depth as the both electrodes are placed on the upper side of the crystal and we observe the electrochemical reaction and the following ion diffusion only in the first few hundred nanometers on the sample surface. In spite of the relatively low total intensity of the nitrogen signal we should remind that the experiment run for only thirty minutes and the working temperatures are not as high as in the usual application of YSZ as electrolyte in the fuel cells.

An additional information we obtain from the optical absorption spectra
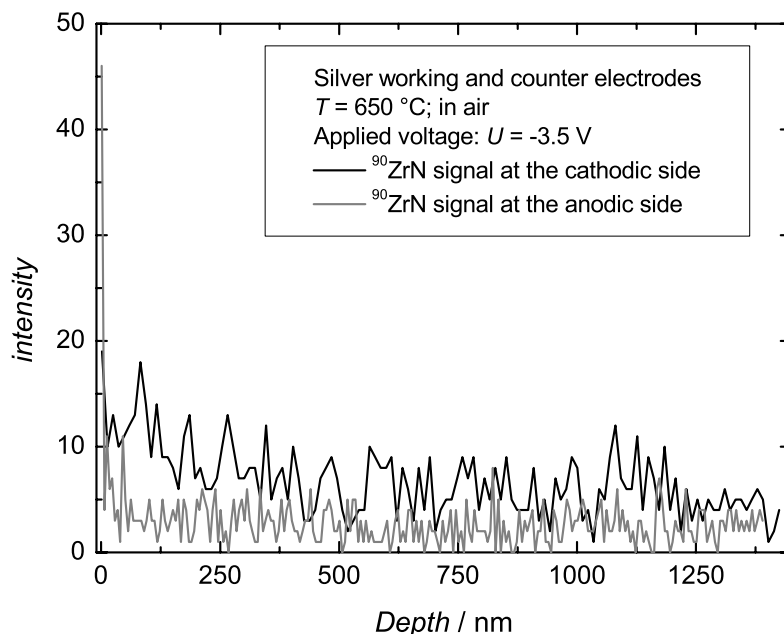
Fig. 6.27: SIMS analysis on the cathodic and anodic side after 30 min. polarization (E = -3.5 V) at 700 °C in open air conditions

shown in fig. 6.28. The intensity of absorption was measured at the cathodic and the anodic side of the single crystal polarized in air as well of a reference sample (only heated in air) and a sample polarized at the same conditions but in pure argon atmosphere. The spectrum of the sample polarized in air near the cathodic side is different than the spectra at the anodic side and of the reference. An absorption in the range between 380 nm and 640 nm was observed with a broad maxima at approximately 470 nm. The sample polarized in argon was completely black and almost not transparent, showing a broad absorption in the whole visible spectrum and as the absorption intensity was much higher this spectrum is not shown in fig. 6.28.

As we discussed in section 4.2.3 (p.110) the maximum at around 500 nm was assigned to nitrogen doped and/or reduced YSZ samples where a clear distinction between both have not been made. However, because our experiment was carried out in air and no visible blackening of the material was observed we

assign this absorption to the incorporated nitrogen.
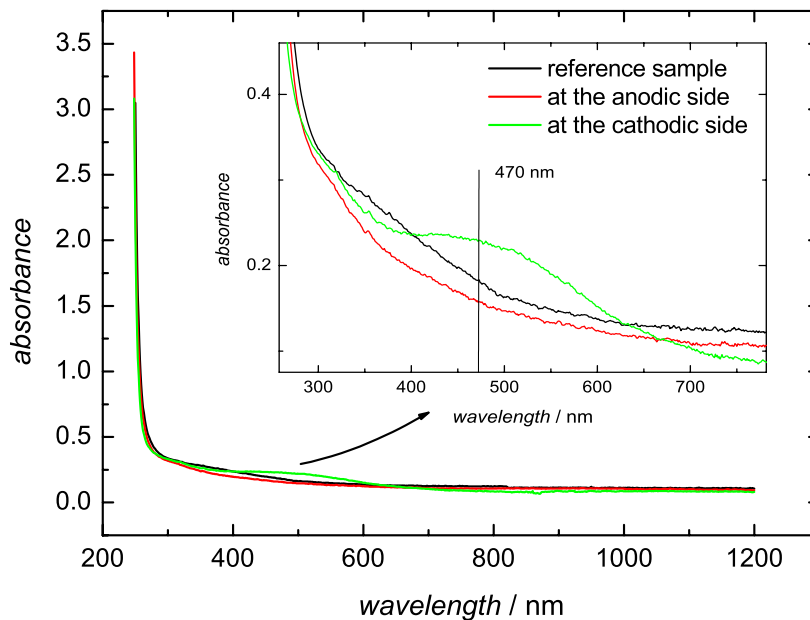
Fig. 6.28: Optical absorption spectra of a reference sample and the cathodic and anodic
side of the single crystal after 30 min. polarization (E = -3.5 V) at 700 °C in open air
conditions

So nitrogen seems to be incorporated in YSZ material when the equilibrium potential of the redox couple N^{3-}/N_2 is exceeded. Moreover according to our preliminary galvanostatic experiments the initial presence of N^{3-} in the YSZ (i.e a material initially doped with nitrogen) leads to a shift in the equilibrium electrode potential thus accelerating the nitrogen reaction rate. Oxygen on the other hand plays an important role not only as a concurrent reaction, but it also prevents the reduction of zirconia at these extremely negative potentials.

6.3.4 *In-situ* XPS study on the electrochemical nitrogen reduction

The electrochemical reduction of nitrogen was studied *in-situ* during electrode polarization by XPS experiments (μ-ESCA beam line) at the synchrotron ELET-TRA in Trieste, Italy. A detailed description of the experimental setup and some

technical details are given in [177] The beam line provides a unique possibility to follow the reduction steps involving species of different valence state.

Experimental details

For our experiment we used an iridium micro-electrode placed on a (111) 9.5YSZ single crystal as gold was found too soft and the contact to the crystal was not good. The counter electrode was a platinum paste burned on the back side of the sample. The working temperature was approximately $T = 500$ °C. The voltage was varied in the range $U = 0$ V up to $U = -3$ V. The nitrogen partial pressure in the XPS-chamber was 10^{-5} Pa.

No nitrogen signal can be detected at voltages up to -1.5 V. When -1.5 V is exceeded a peak at biding energies of 397.2 eV appears. Typical N 1s spectra are shown in fig. 6.29.
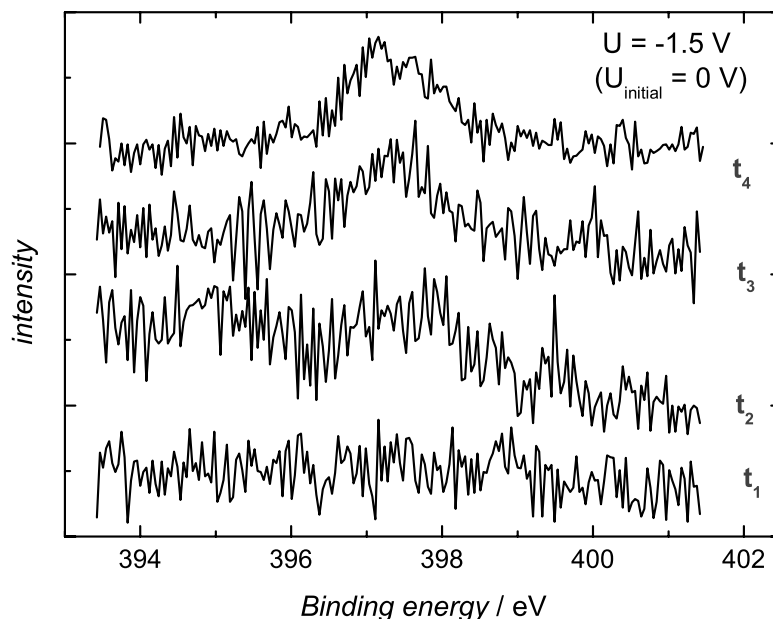
Fig. **6.29**: N 1s consecutive XPS spectra at iridium micro-electrode after applying a voltage of $U = -1.5$ V. t - the time ($t_1 > t_2 > t_3 > t_4$), $T = 500$ °C, $p(N_2) = 10^{-5}$ Pa

As discussed in chapter 4 at these binding energies nitrogen is supposed to exist as N^{3-} ion most probably participating in a Zr-(O-N) bond. The intensity

of the signal increases with the time and it can be seen that the last spectrum (at t_4) shows two components. The first one appears at binding energy of 397.2 eV and the second one at 397.9 eV. This splitting of the nitrogen peak was confirmed later by experiments at higher voltages where this effect was more pronounced. The appearing of the N 1s peak is reversible and after switching the voltage off the peak disappears completely with the time. In fig. 6.30 the decrease of the intensity of N 1s signal is shown after the applied voltage of -1.5 V was switched off. In this way we have reduced nitrogen at the electrode
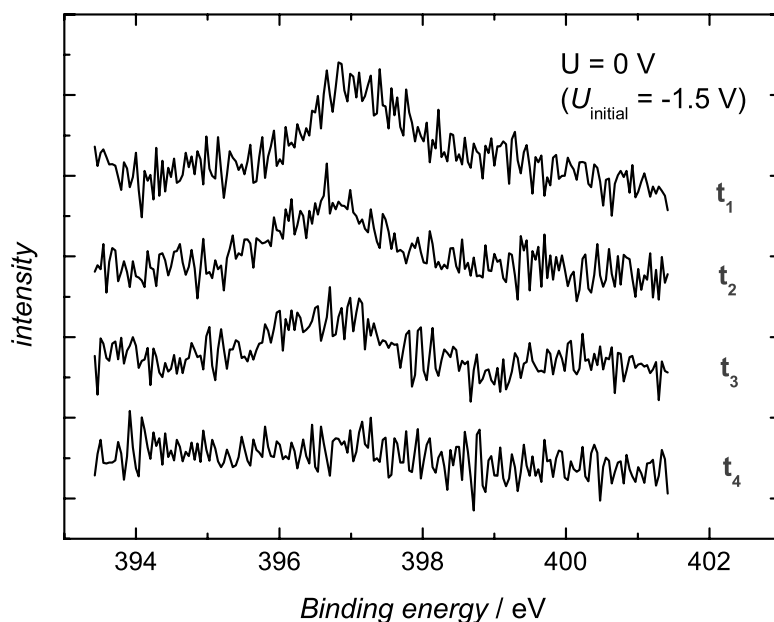
Fig. 6.30: N 1s consecutive XPS spectra at iridium micro-electrode after switching the applied voltage of $U = -1.5$ V off. t - the time (t$_1$>t$_2$>t$_3$>t$_4$), $T = 500$ °C, $p(N_2) = 10^{-5}$ Pa

and nitrogen species have been detected on the surface but it has not been incorporated in the YSZ single crystal and desorbs from the surface if the electric filed is not present. Applying more negative voltage to the micro-electrode the intensity of the nitrogen peak increases as shown in fig. 6.31 but the process remains reversible until a voltage of -2.5 V was achieved. Above this voltage the nitrogen peak remains constant as position and intensity after switching the

voltage off. In fig. 6.31 we also register the existence of at least one another
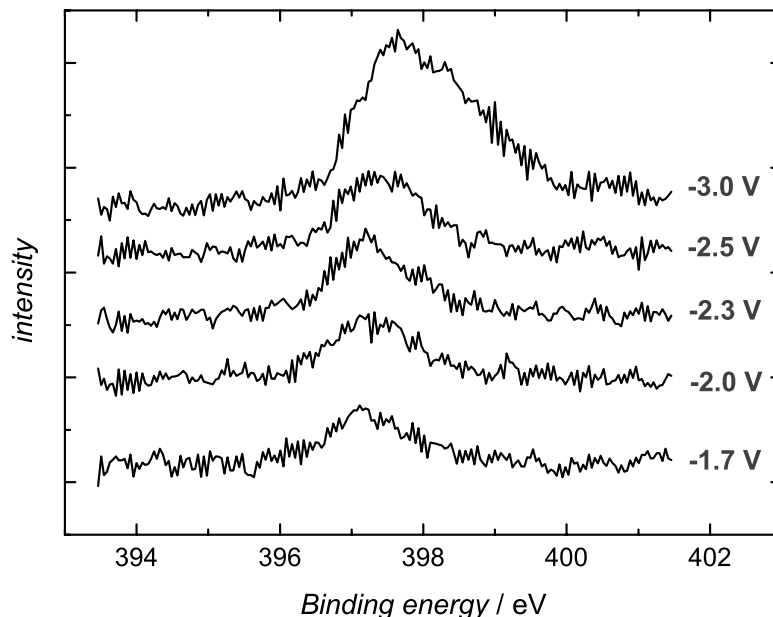
Fig. 6.31: N 1s spectra at iridium micro-electrode at different voltages, $p(N_2) = 10^{-5}$ Pa, $T = 500\ ^{\circ}C$

peak component at higher biding energies. It is especially pronounced for the spectra recorded at -3.0 V. As reference data are not available at this point we cannot identify the surface species and we cannot conclude about the charge they carry. However, it is clear that the shift of the peak position towards higher binding energies is related to a decrease of the negative charge. As the second component is much more pronounced at higher negative voltages we exclude the possibility that nitrogen can be present at -3 V in a valence more positive than at -1.5 V or -2.7 V. In addition, according to our conclusions from the steady state electrochemical experiments the limiting factor for the reduction is the charge transfer i.e. not all ions/molecules at the electrode/electrolyte interface can react. Thus we suggest that the peak at this binding energies may represent negatively charged molecular anions.

In order to study in more details the nitrogen speciation we improved the

time resolution. All spectra shown in figures 6.29- 6.31 are a sum of at least three consecutive sweeps. The time necessary to collect these sweeps depends on the energy resolution, the step and the scan range. However at least five minutes are required for one integral scan. Recording each individual spectrum we improve the time resolution at least by a factor of three. Individual N 1s spectra recorded consecutively upon polarization of -3 V are shown in figure 6.32. Two different nitrogen species can be clearly distinguished. The first
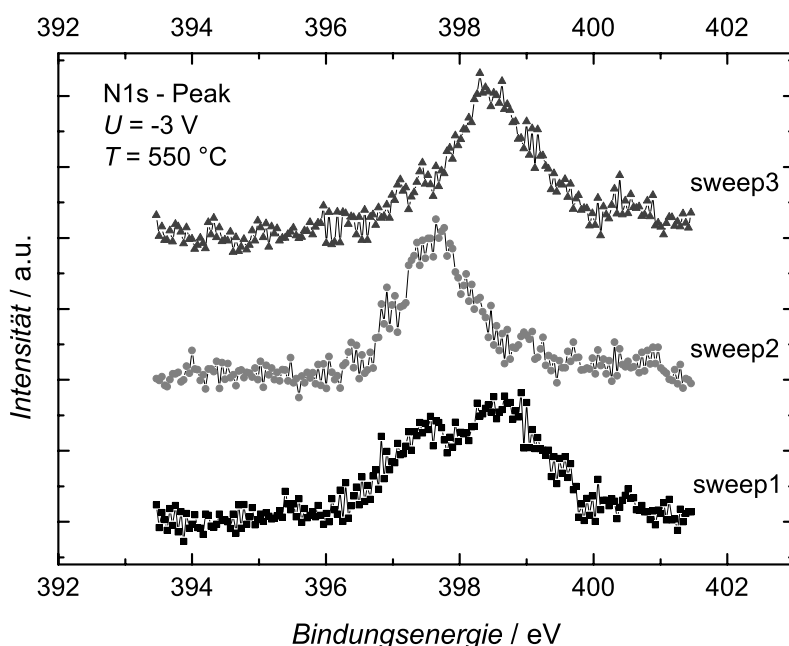
Fig. 6.32: N 1s spectra of three consecutive sweeps. $U = -3$ V, $p(N_2) = 10^{-5}$ Pa, $T = 500$ °C

one at a binding energy of 397.5 eV and the second one at binding energy of 398.5 eV. However a shoulder at higher binding energies can be seen for the second peak and we suppose that both peaks consist of more than one component. As mentioned above the lack of reference data makes the fitting procedure extremely difficult and a deconvolution of the N 1s spectra as well a clear interpretation is still missing. However the results suggest that nitrogen is reduced upon the electrochemical polarization and exists in differently charged

states. These states are different from those without applied electric field where the N 1s peak appears at binding energy of 396.9 eV. Thus, we can differentiate between nitrogen ions being already incorporated in the YSZ and those being reduced but still not incorporated at the moment of the scan, i.e. we assume that the experiments displays the chemical shift of nitrogen proceeding through an intermediate state(s) upon electrochemical reduction.

In addition we record the N 1s spectra at the iridium micro-electrode during the polarization process in order to study wether nitrogen species are reduced at the metal surface rather than at the triple phase boundary. However no nitrogen was detected. We also confirmed that no chemical reaction between reduced YSZ and molecular nitrogen takes place. A reduced, nitrogen free YSZ crystal was exposed at the same temperature to nitrogen atmosphere, but as no nitrogen peak was detected we exclude a chemical reaction between reduced YSZ and nitrogen. Thus we report for the first time the electrochemical activity of molecular nitrogen, where more than one nitrogen species were detected.

One of the advantages of the μ-ESCA beam line is the possibility for a direct chemical imaging of the surface in a given range of binding energies i.e. we can reproduce the distribution of an element on the surface. We have studied the N 1s distribution near to the electrode edge. In the XPS image shown in fig. 6.33 each point depicts the intensity of the N 1s peak, related to its concentration. It can be seen that the most intensive signal is recorded at and near to the micro-electrode and it decreases moving away from the electrode. The dark spot in the middle on left axis is the iridium electrode, where no nitrogen signal was detected. The nitrogen signal decreases constantly away from the electrode/electrolyte interface, and it disappears completely about 2.7 mm away from the electrode edge. After the experiments the sample was analyzed by SIMS in order to obtain an information on the nitrogen depth distribution. In figure 6.34 images of the surface and the depth profiling of the nitrogen signal are shown. The surface distribution image (fig.6.34a) reproduces the XPS results confirming a high nitrogen concentration exactly at the point of contact. The intensity of the signal decreases away from the electrode and goes back to the background level at a distance of 2.7 mm. The images (*b* and *c*) show the vertical nitrogen distribution (a slice in XZ, respectively YZ direction).
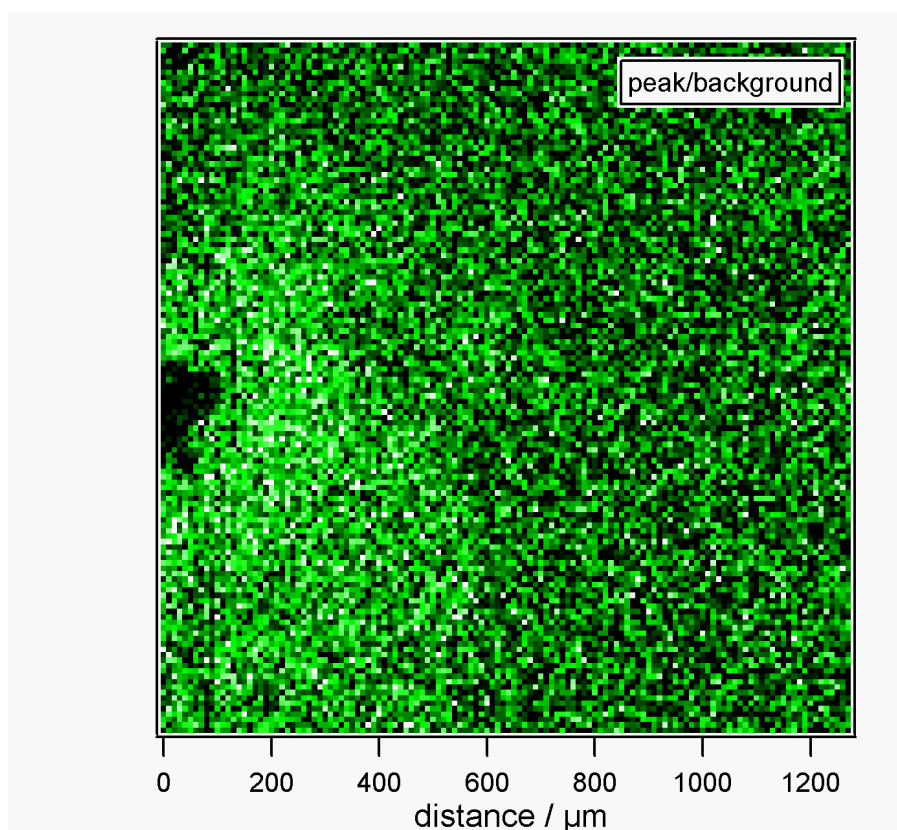
Fig. 6.33: XPS image of the N 1s distribution near to the electrode edge during nitrogen incorporation. $U = -3$ V, $p(N_2) = 10^{-5}$ Pa, $T = 500$ °C

Both figures clearly show the highest intensity of the nitrogen signal beneath the electrode. The results suggest that nitrogen had moved under influence of the applied electric field throughout the YSZ crystal and the most intensive nitrogen signal is observed below the electrode/electrolyte interface. Thus we confirm that nitrogen migrates in YSZ under the condition of an applied electric field.

To summarize - we confirmed the electrochemical activity of nitrogen by *in-situ* XPS experiments. At least two different nitrogen species were detected during cathodic polarization but an exact interpretation is still missing. No chemical reaction between reduced YSZ and nitrogen gas, and no nitrogen species on the iridium micro-electrode were detected. The SIMS analysis confirmed the nitrogen incorporation into YSZ and shows clearly that the migration of nitrogen occurs only beneath the point contact between the micro-electrode and YSZ
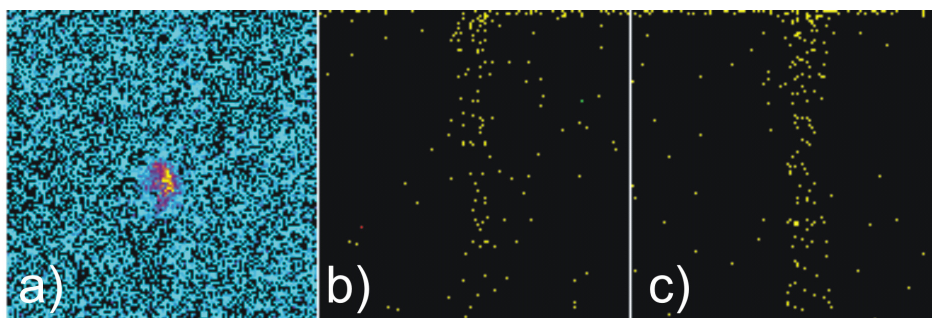
Fig. 6.34: SIMS image of nitrogen distribution around the electrode after cathodic polarization. The field of view of each image is 251×251 μm^2. **a)** a XY surface image; **b)** a XZ depth profile; **c)** a YZ depth profile

single crystal.

6.3.5 Nitrogen incorporation from ammonia gas phase

We concluded from our electrochemical studies that the electrode kinetics is rate determining for the complete process of nitrogen reduction and not the diffusion in the bulk. We have performed additional incorporation experiments in ammonia gas phase. In ammonia nitrogen is present in N^{3-} state and according to the conclusions from the previous experiments it should be incorporated much easier into zirconia, as we do not have any kinetic difficulties due to the redox process.

Experimental details

In this experiment a voltage of -1.5 V was applied to a gold electrode on a 9.5YSZ (111) orientated single crystals at a temperature of 700 °C for 10 min. The samples were exposed at 10^5 Pa ammonia atmosphere.

After the experiments the color of the samples had changed, more pronouncedly around the electrode, from fully transparent to pale yellow or even slightly orange. The sample was analyzed by SIMS and the results are presented in figure 6.35.

The ion image (a) confirms the incorporation of nitrogen under these experimental conditions. The intensity of the nitrogen signal is much more pronounced in the area near and at the electrode edge. So we can definitely conclude that
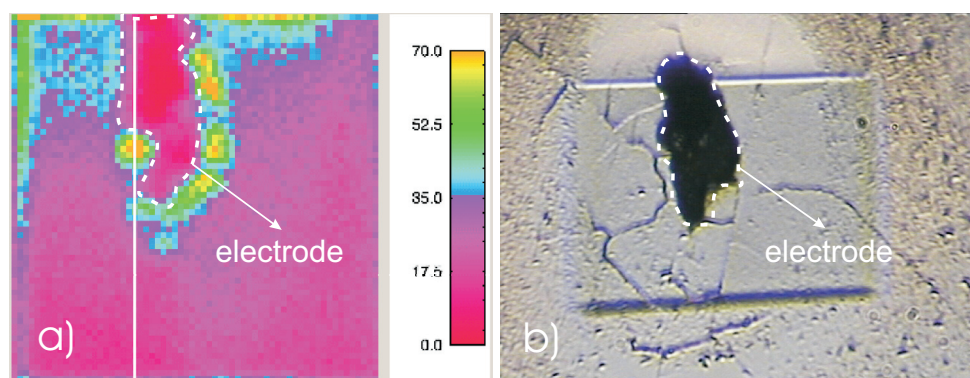
Fig. 6.35: SIMS analysis of electrode area beneath the contact between the gold electrode and (111) orientated 9.5 YSZ single crystal after 10 min. polarization (E = -1.5 V) at 700 °C in pure ammonia, $p(NH_3)$ = 1 atm   a) ion image   and   b) optical image with the depth crater

we have incorporated nitrogen at much lower voltages compared to the process of the reduction of molecular nitrogen. The low voltages at which nitrogen have been incorporated from ammonia phase are especially convenient, because they lay much lower (about 1 V difference) than the thermodynamic decomposition voltage of the YSZ electrolyte. Of course we should not forget that the atmosphere is strongly reducing which additionally contributes to the applied voltage but no visible reduction (blackening) of the single crystals was observed.

To summarize - the electrochemical experiments in NH_3 support our conclusions for a charge transfer control of the reduction process of molecular nitrogen at the electrode and demonstrate a possibility for electrochemical incorporation of N^{3-} ions into YSZ at voltages much lower than its decomposition voltage. In spite of the reduction behavior of ammonia gas no visible reduction of zirconia single crystals was observed during and after the experiments.

6.3.6 The dependence of the equilibrium potential of N^{3-}/N_2 electrode on the nitrogen partial pressure

In our kinetic studies we found that the electrochemical reduction of nitrogen molecules is an irreversible process. However we tested the behavior of the system $Au(N_2)/7YSZ : N/ZrO_2/Zr$, where enough time for equilibration of the potential determining reaction was left. The application of thin electrolyte

films (the thickness of the 7YSZ layer was up to 1 μm) minimizes the diffusion pathway of the ions from the electrolyte surface to the reference electrode thus lowering the response time of the reference system. Additionally the long equilibration time ensures enough time for the ions to diffuse under the chemical potential gradient thus minimizing the diffusion potential contribution to the total *emf* of the cell.

Experimental details

We used the electrochemical cell $Zr/ZrO_2/7YSZ:N/Au(N_2)$ to study if the nitrogen activity will influence the emf of the cell. The temperature was 700 °C and the nitrogen partial pressure was varied by mixing with argon in ratios 0.125/0875, 0.275/0.725, 0.575/0.425 and 0.725/0.275. The equilibration time for the emf was typically 10 min.

The dependence of the equilibrium potential at a gold electrode (versus Zr/ZrO_2 reference) on the applied different nitrogen partial pressures was measured and the experimental results are plotted in fig. 6.36. The partial pressure of the nitrogen was adjusted by mixing with argon in different ratios, thus providing the required N_2 partial pressure. The time for equilibration was not fixed but we waited until the potential value remained stable with the time. Usually about 15 min. were necessary to achieve a stable potential. According to the Nernst equation we have plotted the measured potential value versus the logarithm of the nitrogen pressure expecting experimental points laying on a straight line with a slope of $2.3RT/nF$ and the intercept with the potential axes shows the standard equilibrium potential. The slope of the line on figure 6.36 was found to be 0.0284 V and the intercept with y-axes $E = 0.976$ V. The theoretical value for the pre-exponential factor in the Nernst equation for six electron exchange reversible process involving a redox reaction of nitrogen molecules at temperature of 700 °C is 0.031 V. The same calculation for the redox reaction regarding the participation of N-atoms (i.e. 3 electron exchange process) is 0.0643 V. Comparing these values, the experimentally determined one is close to the 6 electron exchange reaction. The deviation from the theoretical value may be caused by the lower nitrogen mobility (compared with oxygen). Thus, in spite of the long equilibration time it is probable that the concentration of N^{3-} is not constantly distributed throughout the whole layer which leads to an
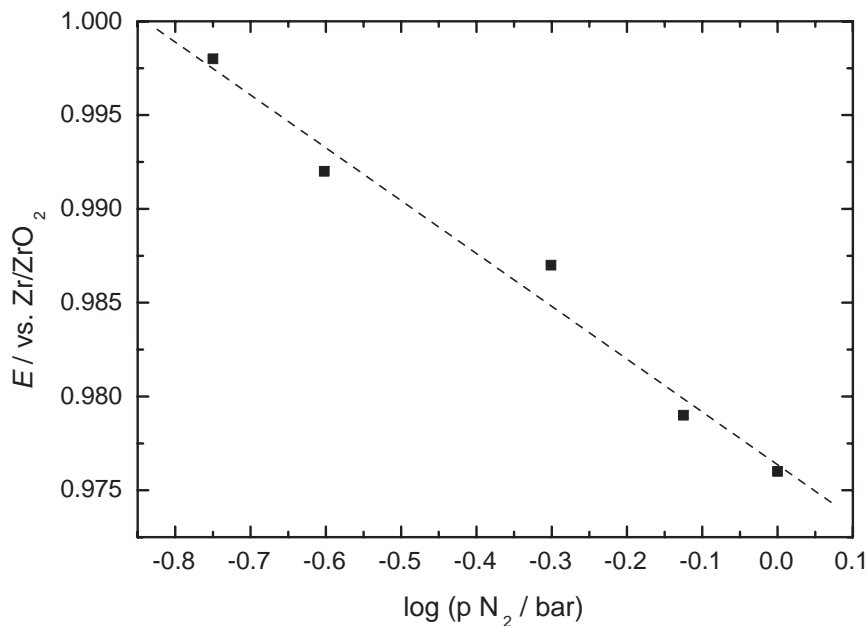
Fig. 6.36: Dependence of the equilibrium potential of Zr/ZrO_2 reference on the nitrogen partial pressure at gold electrode on 7YSZ:N. $T = 700$ °C

additional contribution by the diffusion potential. As a second point we should not forget that the nitrogen redox reaction is not the only potential determining reaction. Even if we completely ignore oxygen in the gas phase, in 7YSZ the oxygen ions are also involved in the equilibration of the open circuit potential resulting in a mixed potential involving at least three different species - N_2, N^{3-} and O^{2-}. Nevertheless this experiment provides an evidence that the Zr/ZrO_2 reference electrode could be efficiently used to detect deviations in nitrogen partial pressure if the oxygen content in the surrounding gas atmosphere is held constant.

7 Summary and conclusions

On the theoretical analysis:

In the present work an analysis of the defect structure of pure ZrO_2, nitrogen-doped $ZrO_{(2-\delta)(1-x)}N_{4x/3}$, YSZ and YSZ:N is presented. On the basis of appropriate Brouwer approximations, defect models and the related Kroeger-Vink diagrams for each of these materials have been constructed. Nitrogen can be incorporated into zirconia either at strongly reducing conditions characterized by an electron excess (this condition can be achieved either by lowering the oxygen partial pressure or by cathodic polarization) or at extremely high nitrogen pressures. The nitrogen ion concentration in the oxide remains constant only at fixed thermodynamic variables, i.e temperature, oxygen activity, nitrogen activity. Thus unlike yttria, nitrogen cannot be used as a dopant in a large range of experimental conditions but only in a controlled atmosphere - at least under equilibrium conditions.

The analysis of the thermodynamics of an electrochemical cell of the type $M/MX/X_2(Me)$, where X is non-metal component, M is a reactive metal and Me is a inert metal, shows that the standard free enthalpy of formation at T = 0 K of the compound MX can experimentally be determined by plotting the measured *emf* value versus the logarithm of the activity of the non-metal component at different temperatures. In this plot all isotherm lines cross in an invariant point with the coordinates $-\Delta_r H^\circ / nF$ on the x-axis and $\Delta_r S^\circ / R$ on the y-axis. Diagrams for the cells $Zr/ZrO_2/O_2(Me)$ and $Zr/ZrN/N_2(Me)$ were constructed on the basis of theoretical values.

On the experiments:

The design of the experimental setup for high temperature electrochemical experiments was shown. The electrochemical cell we have constructed is equipped

with four micro-manipulators for a precise positioning of the micro-electrodes on the surface of the solid electrolytes and ensures a gas tight atmosphere and working temperatures up to 840 °C. The cell ensures the required experimental conditions to preserve the extremely low oxygen activities in the supplied gas.

On the PLD preparation of YSZ:N thin films:

The pulsed laser deposition technique is found to be appropriate for the incorporation of nitrogen (supplied as a background gas) into zirconia. The influence of the deposition parameters on the surface morphology, the structure and the nitrogen content was systematically studied.

The AFM and HRSEM images shows a fine structured films with an average grain size of approximately 30 nm. The grain size depends on the preparation of the substrate and raw substrate surface resulted in larger grain size. We found that the YSZ:N films almost reproduce the surface of the substrate.

The effect of nitrogen incorporation influences strongly the orientational structure of the films. Thus we found that all YSZ:N films deposited in nitrogen atmosphere show mainly (111) orientation and the other reflexes are almost missing. The re-oxidation of these samples leads to a loss of nitrogen but the (111) orientation was retained. The deposited in oxygen atmosphere YSZ films had a (200) orientation, but the other reflexes of the cubic structure are also present, whereas the films deposited in argon have (220) main orientation. Thus by PLD we can deposit YSZ films with a selective orientation. In addition we found that the YSZ:N films show a small distortion of the cubic cell parameters, more pronounced for the YSZ:N films and less pronounced for films deposited in oxygen or in argon atmospheres. The distortion of the cell constant suggests a possible regularity in the order of the nitrogen ions in the lattice but it also can be a result of the nano-sized grain structure.

We found the nitrogen concentration in YSZ:N depends on various deposition parameters. Based on the SIMS analysis as most suitable working temperature we suggest the range between 500 °C and 600 °C. Above these temperatures the nitrogen content in the films drops at least twofold and at lower temperatures the quality of the films is poor. The concentration of the cation dopant (i.e. yttria) was also found to influence the incorporation of nitrogen. The de-

pendence proceeds through a maximum, where the highest amount of nitrogen was measured in 7YSZ:N. The distance between the target and the substrate is reciprocally proportional to the nitrogen content. The highest nitrogen concentration was found for a 4 cm distance. The pressure of nitrogen gas in the deposition chamber is also found to be important. The nitrogen content depends strongly on the gas pressure, and a maximum is found at 6×10^{-4} Pa. The application of higher or lower gas pressures in the deposition chamber results in lower nitrogen concentrations.

The XPS studies on ZrO_2:N and YSZ:N films show that the binding energies of N 1s peak are found at positions typical for the three valent nitrogen ions. However in 7YSZ:N the position of the peak is shifted to much higher binding energies (BE = 402.3 eV) suggesting that nitrogen exists either in higher than $3-$ valence state or as dinitrogen molecular species. The quantitative XPS analysis confirmed the conclusions made by the SIMS analysis and the highest nitrogen content was found in 7YSZ:N samples.

The optical absorption microscopy also found a difference in the behavior of 7YSZ:N samples. Two absorption peaks were registered - at approximately 263 nm and 455 nm, whereas the other nitrogen-doped samples show only a maximum at approx. 500 nm. The first maximum for 7YSZ:N at the lower wavelengths might be related either to a different charge or to a different position of the nitrogen ions. However the second absorption maximum suggests that the nitrogen energy levels are placed almost in the middle of the band gap of the oxide material.

On the transport properties:

The results from the AC conductivity measurements with YSZ:N thin films as a function of the nitrogen content show in the complex impedance plane (after a deconvolution of the spectra), that for films with higher nitrogen content the ion transport in the grain boundaries is limiting the diffusion. The experiments in a pure nitrogen atmosphere at temperatures up to approximately 700 °C show that the total ion conductivity decreases by increasing nitrogen concentration, whereas above this temperature the ion conductivity increases with the nitrogen content. The activation energies increase with the nitrogen content starting with

1.3 eV for a nitrogen-free YSZ and increasing to a value of 1.94 eV for zirconia doped with 6 at.% nitrogen.

On the electrode processes:

The current study demonstrates that the most appropriate electrolyte for the electrochemical experiments on the nitrogen reduction is 7YSZ showing the highest conductivity in pure nitrogen atmosphere. In addition, sliver was chosen as a working electrode material for the nitrogen incorporation experiments and gold for the kinetic studies.

We found a maximum in the capacity of the electrical double layer at temperatures of 750 °C suggesting that adsorption/desorption processes take place. Of this reason the working temperature was limited to approximately 700 °C. We also found that the electrode material reacts with the electrolyte at applied voltages higher than 2 V.

The analysis of different reference electrodes shown that according to the Gibbs phase rule and also of kinetic reasons, noble metal electrodes cannot provide a stable reference reaction and their use in the kinetic studies must be restricted. Metal/metal oxide electrodes (and particulary Zr/ZrO_2) fulfill the thermodynamic and kinetic requirements and were further used as reference electrodes in our studies. Via UPS the position of the Fermi-level in the Zr/ZrO_2 system was determined and in this way its reference potential.

In the CV and LSV studies four irreversible peaks related to the nitrogen redox process were detected, suggesting a charge transfer control of the overall process. The calculated activation energies are of order up to 2 eV confirming the irreversibility of the process. Depending on the yttria content these values suggested different reductions steps to control the overall process. In the Arrhenius plot at temperatures above 750 °C we determined negative values for the activation energies, explained with a desorption processes at the electrode/electrolyte interface. This conclusion is supported also by the measurements of the capacity of the EDL showing a maximum at this temperature.

The steady state polarization measurements allowed us to suggest a multi-step charge transfer mechanism of the nitrogen electrochemical reduction at

gold micro-electrodes, with a rate determining step: $N_2^- + e^- = N_2^{2-}$ and stoichiometric number $\nu = 3$. One step precedes and two follow the rate determining step. Thus we suggested for the first time a mechanism of the electrochemical reduction of molecular nitrogen on solid electrolytes at high temperatures.

The nitrogen incorporation into YSZ thin films and single crystals was confirmed by SIMS analysis. Nitrogen was incorporated into YSZ at potentials above -2.5 V but the process becomes significant at potentials above -3 V. In the single crystals the distribution of nitrogen is homogeneous around the electrode/electrolyte contact, whereas in poly-crystalline samples at higher voltages (i.e. $E = -3.55$ V) nitrogen diffuses faster along the grain boundaries. Additional polarization experiments in air show clearly that nitrogen can be incorporated into YSZ even from the air without visible reduction of the zirconia electrolyte.

The electrochemical activity of nitrogen was uniquely confirmed by *in-situ* XPS experiments. During cathodic polarization of iridium micro-electrode on YSZ single crystal we detected at least two different nitrogen species. We detected a reversible reduction of nitrogen molecules to ions above potentials of -1.5 V but the incorporation starts after exceeding potentials of -2.5 V. The distribution of nitrogen ions was homogeneous around the micro-electrode with decreasing intensity of the signal away from it.

Considering the nitrogen-doped zirconia as a possible nitrogen ion conductor or as a possible material for nitrogen sensors two factors contribute to the overall process: the surface reaction and the diffusion into the bulk. The polarization experiments in ammonia gas phase show that nitrogen (present as N^{3-} ion) was incorporated at voltages of -1 V which are much lower than the decomposition voltages of YSZ and the voltages required for incorporation from N_2-atmosphere. Thus we suggest that the surface reaction (i.e. the electrochemical process) of molecular nitrogen limits the overall process.

The experiments and results reported in this work trace the first steps on the way to the nitrogen electrochemistry.

List of publications based on results presented in this thesis

I. Valov, C. Korte, R. A. De Souza, M. Martin and J. Janek, *Electrochemical Incorporation of Nitrogen into a Zirconia Solid Electrolyte*, Electrochemical and Solid-State Letters, **9(5)**, F23-F26, 2006

Ilia Valov and Jürgen Janek, *Kinetic studies on the electrochemical nitrogen reduction and incorporation into yttria stabilized zirconia*, Solid State Ionics, **in press** 2006 (doi:10.1016/j.ssi.2005.11.021)

I. Valov, R. A. De Souza, C. Z. Wang, A. Börger, C. Korte, M. Martin, K.-D. Becker and J. Janek, *Preparation of nitrogen-doped YSZ thin films by pulsed laser deposition and their characterization*, Journal of Materials Science, **in press** 2006

M.A. Taylor, M. Kilo, C. Argirusis, G. Borchardt, I. Valov, C. Korte, J. Janek, T.C. Rödel and M. Lerch, *Nitrogen tracer diffusion in yttria doped oxonitride*, Defect and Diffusion Forum, **237-240**, 479-484, 2005

I. Valov, V. Rürup, R. Klein, C. Rödel, M. Dogan, H. D. Wiemhöfer, M. Lerch and J. Janek, *Ionic and Electronic Conductivity of nitrogen-doped YSZ single crystals*, **in preparation**

I. Valov, B. Luerssen, E. Mutoro, S. Günther, R.A. De Souza, L. Gregoratti, M. Martin and J. Janek, *In-situ XPS study on the electrochemical nitrogen reduction at Ir(N_2)/YSZ triple phase boundary*, **in preparation**

Bibliography

[1] M. Jansen and H. P. Letschert, "Inorganic yellow-red pigments without toxic metals," *Nature* **404**, pp. 980–982, 2000.

[2] E. Guenther and M. Jansen, "Optical properties of $Ta_{3-x}Zr_xN_{5-x}O_x$ semiconductor pigments," *Materials Research Bulletin* **36**, pp. 1399–1405, 2001.

[3] Z. T. P. Zu, G. Wong, M. Kawazaki, A. Ohtomo, H. Koinuma, and Y. Segawa, "Ultraviolet spontaneous and stimulated emission from ZnO microcrystallite thin films at room temperatures," *Solid State Communications* **103**(8), pp. 459–463, 1997.

[4] J. Wendel, M. Lerch, and W. Laqua, "Novel Zirconia-Based Superionic Conductors: The Electrical Conductivity of Y-Zr-O-N Materials," *Journal of Solid State Chemistry* **142**, pp. 163–167, 1999.

[5] R. Schloegel, "Catalytic synthesis of ammonia - a "never-ending story"?," *Angewandte Chemie Int. Ed.* **42**, pp. 2004–2007, 2003.

[6] J.-S. Lee, T.-J. Chung, and D.-Y. Kim, "Electrical and microstructural characterization on nitrogen-stabilized zirconia," *Solid State Ionics* **136–137**, pp. 39–44, 2000.

[7] T.-J. Chung, J.-S. Lee, and D.-Y. Kim, "Surface nitridation of yttria-doped tetragonal zirconia polycrystals (y-TZP): Microstructural evolution and kinetics," *Journal of the American Ceramic Society* **82**(11), pp. 3193–3199, 1999.

[8] G. Deghenghi, T.-J. Chung, and V. Sergo, "Raman investigation of the nitridation of yttria-stabilized tetragonal zirconia," *Journal of the American Ceramic Society* **86**(1), pp. 169–173, 2003.

[9] M. Kilo, I. Valov, J. Janek, M. Lerch, and G. Borchardt, "Diffusion und reaktion in dotierten zirkoniumoxonitriden," *Zeitschrift fuer Anorganische und Allgemeine Chemie* **630**, p. 1734, 2004.

[10] S. Gutzov and M. Lerch, "Optical properties of europium containing zirconium oxynitrides," *Optical Materials* **24**(3), pp. 547–554, 2003.

[11] R. Sharma, D. Naedele, and E. Schweda, "In situ studies of nitridation of zirconia (ZrO$_2$)," *Chemistry of Materials* **13**, pp. 4014–4018, 2001.

[12] J. Wrba and M. Lerch, "Phase Relationships in the ZrO$_2$-Rich Part of the Systems Y-Zr-N-O, Ca-Zr-N-O, and Mg-Zr-N-O Up to Temperatures of 1150 °C," *Journal of the European Ceramic Society* **18**, pp. 1787–1793, 1998.

[13] M. Lerch and O. Rahaeuser, "Subsolidus phase relationships in the ZrO$_2$-rich part of the ZrO$_2$ − Zr$_3$N$_4$ system," *Journal of Materials Science* **32**, pp. 1357–1363, 1997.

[14] M. Lerch, *Neue Anionendefizit-Materialien Auf der Basis Von ZrO$_2$ Synthese, Charakterisierung und Eigenschaften Von Ternaeren und Quaternaeren Nitridoxiden Des Zirconiums.*, Habilitationsschrift, 1997.

[15] M. Lerch, J. Lerch, and K. Lerch, "Kinetic and thermodynamic studies on the incorporation of nitrogen into zirconia," *Journal of Materials Science Letters* **15**(24), pp. 2127–2129, 1996.

[16] M. Lerch, "Nitridation of zirconia," *Journal of the American Ceramic Society* **79**(10), pp. 2641–2644, 1996.

[17] B. A. Shaw, Y. Cheng, and D. P. Thompson, "Nitrogen stabilization of tetragonal zirconias," *British Ceramic Proceedings (Engineering Ceramics: Fabrication Science and Technology)* **50**, pp. 143–152, 1993.

[18] L. Pichon, T. G. A. Straboni, and M. Drouet, "Nitrogen and oxygen transport and reactions during plasma nitridation of zirconium thin films," *Jounal of Applied Physics* **87**(2), pp. 925–932, 2000.

[19] A. Wilcockson and R. Casselton, "Zirconium oxynitride formation during electrolysis of stabilized zirconia," *Journal of the American Ceramic Society* **53**(5), p. 293, 1970.

[20] J. Xue, "Non stoichiometry and point defect structure of monoclinic and tetragonal zirconia $ZrO_{2+\delta}$," *Journal of the Electrochemical Society* **138**(2), pp. 36C–40C, 1991.

[21] K. Sasaki and J. Maier, "Re-analysis of defect equilibria and transport parameters in Y2O3 - stabilzed ZrO2 using EPR and optical relaxation," *Solid State Ionics* **134**, pp. 303–321, 2000.

[22] V. R. PaiVerneker, A. N. Petelin, F. J. Crowne, and D. C. Nagle *Physical Review B* **40**, pp. 8555–8557, 1989.

[23] J.-H. Park and R. N. Blumenthal, "Electronic transport in 8 mole percent $Y_2O_3 - ZrO_2$," *Journal of the Electrochemical Society* **136**(10), pp. 2867–2876, 1989.

[24] V. V. Roddatis, D. Su, E. Beckmann, F. C. Jentoft, U. Braun, and R. S. J. Krohnert, "The structure of thin zirconia films obtained by self-assembled monolayer mediated deposition: TEM and HREM study.," *Surface and Coatings Technology* **151**–**152**, pp. 63–66, 2002.

[25] A. S. Gandhi and V. Jayaram, "Plastically deforming amorphous $ZrO_2 - Al_2O_3$," *Acta Materialia* **51**, pp. 1641–1649, 2003.

[26] L. K. Lenz and A. H. Heuer, "Stress-induced transformation during sub-critical crack growth in partially stabilized zirconia.," *Journal of the American Ceramic Society* **65**(11), pp. C192–C194, 1982.

[27] S. Namba and H. Tamura, "Transparent semiconducting oxide films. III. zirconium dioxide film," *Rikagaku Kenkyusho Hokoku* **36**, pp. 368–371, 1960.

[28] A. V. Byalobzheskii and V. D. Valkov, "The effects of the semiconductor properties of oxide films on the electrochemical behaviour of metals in electrolytes when under the influence of ultraviolet light," *Doklady Akademii Nauk SSSR* **134**, pp. 121–124, 1960.

[29] L. P. Srivastava and T. F. Archbold, "Semiconductor behaviour of zirconium oxide," *High Temp. Mater., Proc. Symp. Mater. Sci. Res., 3rd*, pp. 365–371, 1972.

[30] S. Rengakuji, Y. Nakamura, T. Yamazaki, K. Mitsunari, C. Shimasaki, and A. Yamada, "Preparation of TiO_2, ZrO_2 and $TiO_2 - ZrO_2$ films by

sol-gel process and their application to methane gas sensors," *Kyoiku Kenkyu Ronbunshi* **7**(2), pp. 121–126, 1998.

[31] L. Soriano, M. Abbate, J. Faber, C. Morant, and J. Sanz, "The electronicstructure of ZrO_2: Band structure calculations compared to electron and x-ray spectra," *Solid State Communications* **93**(8), pp. 659–665, 1995.

[32] A. Foster, V. Sulimov, F. L. Gejo, A. Shluger, and R. Nieminen, "Modelling of point defects in monoclinic zirconia," *Journal of Non-Crystalline Solids* **303**, pp. 101–107, 2002.

[33] J. Nowotny, M. Rekas, and T. Bak, "Defect chemistry and defect-dependent properties of undoped and stabilized zirconia. bulk vs interface," *Key Engineering Materials* **153–154**, pp. 211–240, 1998.

[34] D. L. Douglass and C. Wagner, "The oxidation of oxygen-deficient zirconia and its relationship to the oxidation of zirconium," *Journal of the Electrochemical Society* **113**(7), pp. 671–676, 1966.

[35] A. Saiki, H. Funakubo, N. Mizutani, K. Shinozaki, T. Bak, J. Nowotny, M. Rekas, and C. C. Sorrel, "Charge transfer between oxygen and zirconia.," *Journal of Thermal Analysis and Calorimetry,* **57**, pp. 875–881, 1999.

[36] S. Ramanathan, C.-M. Park, and P. C. McIntyre, "Electrical properties of thin film zirconia grown by ultraviolet ozone oxidation," *Journal of Applied Physics* **91**(7), pp. 4521–4527, 2002.

[37] X. Zhao and D. Vanderbilt, "Phonons and lattice dielectric properties of zirconia," *Physical Review B* **65**, pp. 075105–1–075105–10, 2002.

[38] A. Cristensen and E. A. Carter, "First-principles characterization of a heteroceramic interface: ZrO_2 (001). deposited on an $\alpha - al_2o_3$ (1102) substrate," *Physical Review B* **62**(24), pp. 16968–16983, 2000.

[39] F. Schneider, *Eigenschaften der N^{3-} -Ionen im System Zr-O-N*. PhD thesis, Justus-Liebig-Universitaet Giessen, 2004.

[40] T. Smith, "Diffusion coefficients and vacancy concentrations for the zirconium-zirconium dioxide system," *Journal of the Electrochemical Society* **112**(6), pp. 560–567, 1965.

[41] P. Kofstad and D. J. Ruzicka, "On the defect structure of ZrO_2 and HfO_2," *Journal of the Electrochemical Society* **110**(3), pp. 181–184, 1963.

[42] A. Kumar, D. Rajdev, and D. L. Douglass, "Effects of oxide defect structure on the electrical properties of ZrO_2," *Journal of the American Ceramic Society* **55**, pp. 439–445, 1972.

[43] F. A. Kroeger, "Electronic conductivity of calcia-stabilized zirconia," *Journal of the American Ceramic Society* **49**(4), pp. 215–218, 1966.

[44] D. J. Poulton and W. W. Smeltzer, "Oxygen diffusion in monoclinic zirconia," *Journal of the Electrochemical Socitey* **117**(3), pp. 378–381, 1970.

[45] M. Kilo, M. A. Taylor, C. Argirusis, and G. Borchardt, "Cation self-diffusion of ^{44}Ca,^{88}Y and ^{96}Zr in single-crystalline calcia- and yttria-doped zirconia," *Journal of Applied Physics* **94**(12), pp. 7547–7552, 2003.

[46] M. Kilo, G. Borchardt, B. Lesage, O. Kaitasov, S. Weber, and S. Scherrer, "Cation transport in yttria stabilized cubic zirconia: ^{96}Zr tracer diffusion in $(Zr_xY_{1-x})O_{2-x/2}$ single crystals with $0.15{\leq}x{\leq}0.48$," *Journal of the European Ceramic Society* **20**, pp. 2069–2077, 2000.

[47] J. B. Goodenough, "Oxide-ion electrolytes," *Annual Review of Materials Research* **33**, pp. 91–128, 2003.

[48] A. T. Tham, C. Rödel, M. Lerch, D. Wang, D. S. Su, A. Klein-Hoffmann, and R. Schlögl, "Electron microscopy investigations on structures of ZrO_2-rich phases in the quasibinary system ZrO_2-Zr_3N_4," *Crystal Research and Technology* **39**(5), pp. 421–428, 2004.

[49] A. T. Tham, C. Rödel, M. Lerch, D. Wang, D. S. Su, A. Klein-Hoffmann, and R. Schlögl, "A TEM study on ZrO_2-rich phases in the quasibinary system ZrO_2-Zr_3N_4: Comparison between fast and slowly cooled samples," *Crystal Research and Technology* **40**(3), pp. 193–198, 2005.

[50] J. P. Goff, W. Hayes, S. Hull, M. T. Hutchings, and K. N. Clausen, "Defect structure of yttria-stabilized zirconia and its influence on the ionic conductivity at elevated temperatures," *Physical Review B* **59**(22), pp. 14202–14219, 1999.

[51] A. Feder, J. Alcala, L. Llanes, and M. Anglada, "Microstructure, mechanical properties and stability of nitrided y-TZP," *Journal of the European Ceramic Society* **23**, pp. 2955–2962, 2003.

[52] T. Bredow, "Nitrogen substitution in cubic zirconia." manuscript for Physical Review B, 2006.

[53] M. Kilo, M. A. Taylor, C. Argirusis, G. Borchardt, M. Lerch, O. Kaitasov, and B. Lesage, "Nitrogen diffusion in nitrogen-doped yttria stabilised zirconia," *Physical Chemistry Chemical Physics* **6**, pp. 3645–3649, 2004.

[54] M. Taylor, M. Kilo, C. Argirusis, G. Borchardt, I. Valov, C. Korte, J. Janek, T. Roedel, and M. Lerch, "Nitrogen tracer diffusion in yttria doped zirconium oxonitride," *Defect and Diffusion Forum* **237–240**, pp. 479–484, 2005.

[55] I. Barin, *Thermodynamical Data of Pure Substances*, VCH - Weinheim, 1995.

[56] A. Bard, R. Parsons, and J. Jordan, *Standard Potentials in Aqueous Solutions*, IUPAC (Marcel Dekker), New York, 1985.

[57] Y. Ito and T. Goto, "Thermodynamic and kinetic properties of the N_2 gas electrode in a molten $LiCl - KCL - Li_3N$ system," *Molten Salt Forum* **5–6**, pp. 279–286, 1998.

[58] T. Goto and Y. Ito, "Electrochemical reduction of nitrogen gas in a molten chloride system," *Electrochimica Acta* **43**(21–22), pp. 3379–3384, 1998.

[59] K. J. Walsh and P. S. Fedkiw, "Nitric oxide reduction using iridium electrodes on yttria-stabilzed zirconia," *Solid State Ionics* **104**, pp. 97–108, 1997.

[60] A. Oda, N. Imanaka, and G.-Y. Adachi, "New type of nitrogen oxide sensor with multivalent cation- and anion-conducting solid electrolytes," *Sensors and Acuators B* **93**, pp. 229–232, 2003.

[61] J. Butler, "A kinetic theory of reversible oxidation potentials at innert electrodes," *Transactions of the Faraday Society (London)* **19**, pp. 734–739, 1924.

[62] J. Butler, "The mechanism of overvoltage and its relation to the combination of hydrogen atoms at metal electrodes," *Transactions of the Faraday Society (London)* **28**, pp. 379–382, 1932.

[63] T. Erdey-Gruz and M. Volmer, "Zur theorie der wasserstoffueberspannung," *Transactions of the Faraday Society (London)* **150A**, pp. 203–213, 1930.

[64] J. Tafel, "über die polarisation bei kathodischer wasserstoffentwicklung," *Z.Phys.Chemie(Leipzig)* **50**, pp. 641–752, 1905.

[65] J. Horiuti and M. Polanyi, "Grundlinien einer theorie der protonuebertragung," *Acta Physicochimica U.S.S.R.* **11**(4), pp. 505–532, 1935.

[66] B. Damaskin and O. Petrii, *Introduction in the Electrochemical Kinetics*, Vishaia Shkola, Moscow, 1975.

[67] J. Bockris and S. Khan, *Surface Electrochemistry*, Plenum Press, New York, 1993.

[68] J. Horiuti and M. Ikusima, "The mechanism of the hydrogen electrode process on platinum," *Proc. Imp. Acad. Jap* **15**(2), pp. 39–44, 1939.

[69] J. Horiuti, "A method of statistical mechanical treatment of equilibrium and chemical reactions," *J. Res. Catalysis, Hokkaido Univ.* **1**(1), pp. 8–79, 1948.

[70] J. Horiuti, "Theory of reaction rates as based on the stoichiometric number concept," *Ann. N. Y. Acad. Sci.* **213**(1), pp. 5–30, 1973.

[71] A. Riddiford, "Stationary current-voltage curves for complex electrode processes," *J. Chem. Soc. (London)* , pp. 1175–1183, 1960.

[72] R. Ehrenburg, "Stoichiometric number of an electrochemical reaction," *Elektrochimija* **10**(3), pp. 457–464, 1974.

[73] R. Ehrenburg, "Application of the stoichiometric number method to investigation of multistep reactions," *J. Res. Catalysis, Hokkaido Univ.* **28**(3), pp. 137–146, 1980.

[74] W. Losew, M. Dembrowski, A. Molodow, and W. Gorodezki, "Radiochemische miethode zur untersuchung der kinetik von elektroden-

prozessen an metallelektroden," *Electrochimica Acta* **8**(5), pp. 387–397, 1963.

[75] V. Losev, A. Molodov, and V. Gorodetzki, "Influence of a following diffusion step on the kinetics of moderately rapid electrode processes," *Electrochimica Acta* **12**(5), pp. 475–484, 1967.

[76] V. Losev and A. Molodov, "Criteria of the presence of disproportionation in multistep processes," *Elektrochimija* **4**(11), pp. 1366–1370, 1968.

[77] R. Parsons, "Electrode reaction orders, transfer coefficients, and rate constants," *Pure and Appl. Chem.* **52**, pp. 233–240, 1979.

[78] A. Frumkin, "The stoichiometric number for the reaction of the electrochemical desorption of hydrogen.," *Doklady Akademii Nauk SSSR* **119**(1), pp. 318–321, 1958.

[79] L. Krishtalik, "Stoichiometric number of the electrode reaction.," *Elektrochimija* **1**(3), pp. 346–349, 1965.

[80] J. O. Bockris and A. Reddy, *Modern Electrochemistry*, vol. 2, Plenum Press, New York, 1970.

[81] J. Bockris and E. Potter, "The mechanism of the cathodic hydrogen evolution reaction," *J. Electrochem. Soc.* **99**, pp. 169–186, 1952.

[82] M. Enyo and T. Yokoyama, "The reaction order and general equations for electrode kinetics," *Electrochimica Acta* **16**(2), pp. 223–243, 1971.

[83] I. Morcos and E. Yeager, "Kinetic studies of the oxygen—peroxide couple on pyrolytic graphite," *Electrochimica Acta* **15**(6), pp. 953–975, 1970.

[84] C. Athanasiou, G. Karagiannakis, S. Zisekas, and M. Stoukides, "Electrode polarization at the O_2 (g), Pd/YSZ interface," *Solid State Ionics* **136–137**, pp. 873–877, 2000.

[85] S. Wang, X. Lu, and M. Liu, "Electrocatalytic properties of $La_0.9Sr_0.1MnO_3$-based electrodes for oxygen reduction," *Journal of Solid State Electrochemistry* **6**, pp. 384–390, 2002.

[86] C. Belouet, "Thin film growth by the pulsed laser assisted deposition technique," *Applied Surface Science* **96–98**, pp. 630–642, 1996.

[87] D. B. Chrisey and G. K. Hubler, eds., *Pulsed Laser Deposition of Thin Films*, John Wiley & Sons, Ltd, New York, 1994.

[88] R. A. De Souza, J. Zehnpfenning, M. Martin, and J. Maier, "Determining Oxygen Isotope Profiles in Oxides with Time-of-Flight SIMS," *Solid State Ionics* **176**, pp. 1465–1471, 2005.

[89] J. Vickerman, A. Brown, and N. Reed, eds., *Secondary Ion Mass Spectrometry: Principles and Applications*, Clarendon Press, Oxford, 1989.

[90] R. Wilson, F. Stevie, and C. Magee, *Secondary Ion Mass Spectrometry: A Practical Handbook for Depth Profiling and Bulk Impurity Analysis*, Wiley, New York, 1989.

[91] G. Ertl and J. Küppers, *Low Energy Electrons and Surface Chemistry*, VCH Verlaggeselschaft mbH, 1985.

[92] S. Huefner, *Photoelectron Spectroscopy, Principles and Applications*, Springer Verlag, 2003.

[93] J. R. Macdonald, ed., *Impedance Spectroscopy*, John Wiley & Sons, New York, 1987.

[94] P. Delahay, *Double Layer and Electrode Kinetics*, John Wiley & Sons Inc, 1965.

[95] L. Antropov, *Theoretical Electrochemistry*, Vuishaija Shkola Publ., Moscow, 1969.

[96] A. J. Bard and L. R. Faulkner, *Electrochemical Methods*, ch. Potential Sweep Methods, p. 241.
John Wiley & Sons Inc, New York, second ed., 2001.

[97] J. Randles, "Cathode-ray polarograph. II. Current-voltage curves," *Transactions of the Faraday Society* **44**, pp. 327–338, 1948.

[98] A. Sevcik, "Oscillographic polarography with periodical triangular voltage," *Collection of Czechoslovak Chemical Communications* **13**, pp. 349–377, 1948.

[99] Z. Galus, *Fundamentals of Electrochemical Analysis*, John Wiley & Sons, New York, 2nd ed., 1994.

[100] R. Marcus, "Chemical and Electrochemical Electron-Transfer Theory," *Annual Review of Physical Chemistry* **15**, pp. 155–196, 1964.

[101] R. Marcus, "On the Theory of Electron-Transfer Reactions. VI. Unified Treatment for Homogeneous and Electrode Reactions," *The Journal of Chemical Physics* **43**(2), pp. 679–701, 1965.

[102] J. Fleig, "On the current-voltage characteristics of charge transfer reactions at mixed conducting electrodes on solid electrolytes," *Physical Chemistry Chemical Physics* **7**(9), pp. 2027–2037, 2005.

[103] J. Winkler, P. Hendriksen, N. Bonanos, and M. Mogensen, "Geometric Requirements of Solid Electrolyte Cell with a Reference Electrode," *Journal of the Electrochemical Society* **145**(4), pp. 1184–1192, 1998.

[104] A. Hashibon, S. Raz, and I. Riess, "Preferred position for the reference electrode in solid state electrochemistry," *Solid State Ionics* **149**, pp. 167–176, 2002.

[105] J. Schultze and V. Tsakova, "Electrochemical microsystem technologies: from fundamental research to technical systems," *Electrochimica Acta* **44**(21–22), pp. 3605–3627, 1999.

[106] J. Fleig and J. Maier, "Point contacts in solid state ionics: finite element calculations and local conductivity measurements," *Solid State Ionics* **86–88**, pp. 1351–1356, 1996.

[107] J. Fleig, S. Rodewald, and J. Maier, "Spatially resolved measurements of highly conductive and highly resistive grain boundaries using microcontact impedance spectroscopy," *Solid State Ionics* **136–137**, pp. 905–911, 2000.

[108] J. Fleig, S. Rodewald, and J. Maier, "Microcontact impedance measurements of individual highly resistive grain boundaries: General aspects and application to acceptor-doped $SrTiO_3$," *Journal of Applied Physics* **87**(5), pp. 2372–2381, 2000.

[109] J. Fleig, "Microelectrodes in Solid State Ionics," in *Advances in Electrochemical Science and Engineering*, R. C. Alkire and D. M. Kolb, eds., **8**, Wiley-VCH, 2003.

[110] R. Vispute, V. Talyansky, R. Sharma, S. Choopun, M. Downes, T. Venkatesan, Y. Li, L. Salamanca-Riba, A. Iliadis, K. Jones, and J. McGarrity, "Advances in pulsed laser deposition of nitrides and their integration with oxides," *Applied Surface Science* **127–129**, pp. 431–439, 1998.

[111] Z. Zhang, P. VanRompay, J. Nees, R. Clarke, X. Pan, and P. Pronko, "Nitride film deposition by femtosecond and nanosecond laser ablation in low-pressure nitrogen discharge gas," *Applied Surface Science* **154–155**, pp. 165–171, 2000.

[112] A. Phani and J. Krzanowski, "Preferential growth of Ti and TiN films on Si (111) deposited by pulsed laser deposition," *Applied Surface Science* **174**, pp. 132–137, 2001.

[113] G. Soto, W. de la Cruz, and M. Farias, "XPS, AES, and EELS characterization of nitrogen containing thin films," *Journal of Electron Spectroscopy and Related Phenomena* **135**, pp. 27–39, 2004.

[114] J. Zhu, T. Li, B. Pan, L. Zhouand, and Z. Liu, "Enhanced dielectric properties of ZrO_2 thin films prepared in nitrogen ambient by pulsed laser deposition," *Journal of Physics D: Applied Physics* **36**(4), pp. 389–393, 2003.

[115] B. V. Crist, *Handbook of Monochromatic XPS Spectra: The Elements and Native Oxides*, John Wiley & Sons, Ltd, 2000.

[116] P. Pietro, L. Galan, and J. Sanz, "Electronic structure of insulating zirconium nitride," *Physical Review B* **47**(3), pp. 1613–1615, 1993.

[117] I. Milosev, H.-H. Strehblow, M. Gaberscek, and B. Navinsek, "Electrochemical Oxidation of ZrN Hard (PVD) Coatings Studied by XPS," *Surface and Interface Analysis* **24**, pp. 448–458, 1996.

[118] I. Milosev, H.-H. Strehblow, and B. Navinsek, "Comparison of TiN, ZrN and CrN hard nitride coatings: Electrochemical and thermal oxidation," *Thin Solid Films* **303**, pp. 246–254, 1997.

[119] L. L. Gendre, R. Marchand, and Y. Laurent, "A New Class of Inorganic Compounds Containing Dinitrogen-Metal Bonds," *Journal of the European Ceramic Society* **17**, pp. 1813–1818, 1997.

[120] H. Wiame, M.-A. Centeno, S. Picard, P. Bastians, and P. Grange, "Thermal Oxidation under Oxygen of Zirconium Nitride Studied by XPS, DRIFTS, Tg-MS," *Journal of the European Ceramic Society* **18**, pp. 1293–1299, 1998.

[121] M. D. Re, R. Gouttebaron, J.-P. Dauchot, P. Leclere, G. Terwagne, and M. Hecq, "Study of ZrN layers deposited by reactive magnetron sputtering," *Surface and Coatings Technology* **174–175**, pp. 240–245, 2003.

[122] X. Guo, Y.-Q. Sun, and K. Cui, "Darkening of zirconia: A problem arising from oxygen sensors in practice," *Sensors and Actuators B* **B 31**, pp. 139–145, 1996.

[123] W. D. L. Cruz, J. Diaz, L. Mancera, N. Takeuchi, and G. Soto, "Yttrium nitride thin films grown by reactive laser ablation," *Journal of Physics and Chemistry of Solids* **64**, pp. 2273–2279, 2003.

[124] T. He and K. D. Becker *Ber. Bunsenges. Phys. Chem.* **99**, p. 658, 1995.

[125] J.-S. Lee, J. Fleig, J. M. A. T.-J. Chung, and D.-Y. Kim, "Microcontact impedance spectroscopy in nitrogen-graded zirconia," *Solid State Ionics* **176**, pp. 1711–1716, 2005.

[126] C.-N. Cao, "On the Impedance Plane Displays for Irreversible Electrode Reactions Based on the Stability Conditions of the Steady State - I. One State Variable Besides Electrode Potential," *Electrochimica Acta* **35**(5), pp. 831–836, 1990.

[127] C.-N. Cao, "On the impedance plane displays for irreversible electrode reactions based on the stability conditions of the steady state - II. two state variables besides electrode potential," *Electrochimica Acta* **35**(5), pp. 837–844, 1990.

[128] B. A. Boukamp, "Interpretation of an "inductive loop" in the impedance of an oxigen ion conducting electrolyte/metal electrode system," *Solid state ionics* **143**, pp. 47–55, 2001.

[129] Y. I. Kharkats, "Theory of the exaltation effect and the effect of correlation exaltation of migration current.," *Journal of Electroanalytical Chemistry and Interfacial Electrochemistry* **105(1)**, pp. 97–114, 1979.

[130] W. Weppner, "Formation of intermetallic pt-zr compounds between pt electrodes and ZrO_2-based electrolytes, and the decomposition voltage of yttria-doped ZrO_2," *Journal of Electroanalytical Chemistry* **84**, pp. 339–350, 1977.

[131] T. Chao, K. J. Walsh, and P. S. Fedkiw, "Cyclic voltametric study of the electrochemical formation of platinum oxide in a Pt/yttria stabilized zirconia cell," *Solid State Ionics* **47**, pp. 277–285, 1991.

[132] A. Holleman and E. Wiberg, *Lehrbuch der Anorganischen Chemie*, p. 1592.
Walter de Gruyter, Berlin, 1995.

[133] I. R. Gibson, G. Dransfield, and J. T. S. Irvine, "Influence of Yttria Concentration upon Electrical Properties and Susceptibility to Ageing of Yttria-stabilised Zirconias," *Journal of the European Ceramic Society* **18**, pp. 661–667, 1998.

[134] Y. Yamamura, S. Kawasaki, and H. Sakai, "Molecular dynamics analysis of ionic conduction mechanism in yttria-stabilized zirconia," *Solid State Ionics* **126**, pp. 181–189, 1999.

[135] M. de Ridder, *The Rate-Limiting Factor of Thte Solid Oxide Fuel Cell.* PhD thesis, University of Eindhoven, 2002.

[136] A. Frumkin, "Wasserstoffüberspannung und Struktur der Doppelschicht," *Zeitschrift für Physikalische Chemie A (Leipzig)* **164**(A), pp. 121–133, 1933.

[137] A. Frumkin, *Electrode Processes*, Nauka, Moscow, 1987.

[138] S. Trasatti, "Structure of the Metal/Electrolyte Solution Interface: New Data for Theory," *Electrochimica Acta* **36**(11/12), pp. 1659–1667, 1991.

[139] R. D. Levie, "On Impedance Measurements: The Determination of the Double Layer Capacitance in the Presence of an Electrode Reaction," *Electrochimica Acta* **10**, pp. 395–402, 1965.

[140] R. Armstrong and B. Horrocks, "The double layer structure at the metal-solid electrolyte interface," *Solid State Ionics* **94**, pp. 181–187, 1997.

[141] V. Chebotin and L. Solovieva, "Theory of the electrical double layer in

solid electrolytes. I. Zero charge potentials.," *Elektrokhimiya* **11**(8), pp. 1189–1197, 1975.

[142] V. Chebotin and L. Solovieva, "Theory of the electrical double layer in solid electrolytes. II. Differential capacitance.," *Elektrokhimiya* **11**(8), pp. 1198–1204, 1975.

[143] I. Remez, V. Chebotin, L. Solovieva, and S. Karpachev, "Temperature dependence of the potential minimum capacitance and zero charge in solid oxide electrolytes," *Elektrokhimiya* **11**(2), pp. 296–297, 1975.

[144] V. Chebotin, I. Remez, L. Solovieva, and S. Karpachev, "Electrical Double Layer in Solid Electrolytes - Theory: Oxide Electrolytes," *Electrochimica Acta* **29**(10), pp. 1381–1388, 1984.

[145] M. Cappadonia, H. T. V. der Heyden, and U. Stimming, "The capacity of the $Hg/HClO_4 \cdot 5.5H_2O$ interface in the liquid-liquid, solid-liquid and solid-solid state. Temperature and potential dependence," *Solid State Ionics* **94**, pp. 9–16, 1997.

[146] B. Kuzin and D. Bronin, "Electrical Double Layer Capacitance of the $M, O_2/O^{2-}$ Interfaces ($M = Pt, Au, Pd, In_2O_3$; O^{2-} = Zirconia-Based Electrolyte)," *Solid State Ionics* **136–137**, pp. 45–50, 2000.

[147] M. Hendriks, J. T. Elshof, H. Bouwmeester, and H. Verweij, "The electrochemical double layer capacitance of yttria-stabilized zirconia," *Solid State Ionics* **146**, pp. 211–217, 2002.

[148] A. Filyaev, S. Karpachev, and I. Remez, "Double-layer capacity and Faraday impedance on a liquid drop electrode in a soild zirconium dioxide-calcium oxide electrolyte," *Elektrokhimiya* **6**(2), pp. 283–285, 1970.

[149] I. Remez, S. Karpachev, L. Solovieva, V. Chebotin, and A. Filyaev, "Capacity of an electric double layer in solid oxide electrolytes," *Elektrokhimiya* **11**(2), pp. 292–295, 1975.

[150] D. Tsiplakides and C. Vayenas, "Electrode work funktion and absolute potential scale in solid-state electrochemistry," *Journal of the Electrochemical Society* **148**(5), pp. E189–E202, 2001.

[151] D. Tsiplakides and C. Vayenas, "The absolute potential scale in solid state electrochemistry," *Solid State Ionics* **152–153**, pp. 625–639, 2002.

[152] S. T. Keqin Huang and Q. Liu, "The diffusivity and solubility of oxygen in reference electrodes $Ni - NiO$, $Co - CoO$, $Fe - FeO$ and $Mo - MoO_2$ systems," *Solid State Ionics* **61**(4), pp. 355–359, 1993.

[153] E. Jacobsson and E. Rosen, "Thermodynamic studies of high temperature equilibriums. 25. solid state emf studies of the systems iron-ferrous oxide, nickel-nickelous oxide, and cobalt-cobaltous oxide in the temperature range 1000-1600," *Scandinavian Journal of Metallurgy* **10**(1), pp. 39–43, 1981.

[154] C. Gatellier, D. Henriet, and M. Olette, "Thermodynamic activity of the constituents of the solid-state iron-nickel system determined by an electrochemical method," *Comptes Rendus des Seances de l'Academie des Sciences, Serie C: Sciences Chimiques* **271**(7), pp. 453–456, 1970.

[155] S. Lubke and H.-D. Wiemhofer, "Electronic conductivity of gd-doped ceria with additional pr-doping," *Solid State Ionics* **117**, pp. 229–243, 1999.

[156] F. Li, Y. Tang, and L. Li, "Distribution of oxygen potential in ZrO_2 - based solid electrolyte and selection of reference electrode for oxygen sensor," *Solid State Ionics* **86**–**88**(2), pp. 1027–1031, 1996.

[157] X. Lu, F. Li, L. Li, and G. Zhou, "Study on exchange current density of ZrO_2 solid electrode at high temperature," *Wuji Cailiao Xuebao* **12**(4), pp. 531–535, 1997.

[158] P. V. Manen, R. Weewer, and J. de Wit, "High temperature cyclic voltammetry on Metal/Metal oxide systems," *Journal of the Electrochemical Society* **139**(4), pp. 1130–1134, 1992.

[159] S. Aronson and J. Clayton, "Thermodynamic properties of nonstoichiometric urania-thoria solid solutions," *Journal of Chemical Physics* **32**, pp. 749–754, 1960.

[160] T. Tran and M. Brungs, "Applications of oxygen electrodes in glass melts. part 1. oxygen reference electrode," *Physics and Chemistry of Glasses* **21**(4), pp. 133–140, 1980.

[161] S. Matsubara, R. Tagami, T. Den, K. Nakamoto, and I. Katayama, "Oxygen sensor with zirconia solid electrolyte and indium-based reference electrode," *Jpn. Kokai Tokkyo Koho* **patent**, p. 3, 1993.

[162] H. Schettler, J. Liu, W. Weppner, and R. Huggins, "Investigation of solid sodium reference electrodes for solid-state electrochemical gas sensors," *Applied Physics A: Solids and Surfaces* **A57**(1), pp. 31–35, 1993.

[163] K.-I. Kawamura, A. Kaimai, Y. Nigara, T. Kawada, and J. Mizusaki, "A novel oxygen sensor based on a Metal/Metal oxide scale system," *Journal of Electroceramics* **2**(3), pp. 151–156, 1998.

[164] A. Baraka, A. Abdel-Rohman, and E. El-Taher, "The use of a Zr/ZrO_2 electrode as an indicator electrode in the potentiometric acid-base titrations in fused KNO_3," *Materials Chemistry and Physics* **9**, pp. 583–595, 1983.

[165] B. Luerssen, H. Fischer, J. Janek, and S. Guenther, "In situ microspectroscopy of polarised Pt/YSZ electrodes," in *Solid State Ionics: The Science and Thechnology of Ions in Motion*, B. Chowdari, ed., pp. 139–149, Elsevier, 2004.

[166] B. Luerßen, S. Guenther, H. Marbach, M. Kiskinova, J. Janek, and R. Imbihl, "Microspectroscopy at a moving reduction front in zirconia solid electrolyte," *Physical Chemistry Chemical Physics* **4**(12), pp. 2673–2679, 2002.

[167] S. Ladas, S. Kennou, S. Bebelis, and C. Vayenas, "Origin of non-faradaic electrochemical modification of catalytic activity," *Journal of Physical Chemistry* **97**(35), pp. 8845–8848, 1993.

[168] R. Imbihl and J. Janek, "Patially resolved measurements of electrochemically induced spillover on porous and microstructured Pt/YSZ catalysts," *Solid State Ionics* **136–137**, pp. 699–705, 2000.

[169] M. W. Breiter, K. Leeb, and G. Fafilek, "Voltammetric studies of the Au/YSZ interface at temperatures between 300 and 600 °C," *Journal of Electroanalytical Chemistry* **436**, pp. 155–159, 1997.

[170] M. W. Breiter, K. Leeb, and G. Fafilek, "Voltammetric studies of the Pt/YSZ interface at temperatures between 300 and 600 °C," *Journal of Electroanalytical Chemistry* **434**, pp. 129–137, 1997.

[171] S. G. Neophytides, D. Tsiplakides, and C. Vayenas, "Temperature-

programmed desorption of oxygen from Pt films interfaced with Y_2O_3 - doped ZrO_2," *Journal of Catalysis* **178**(2), pp. 414–428, 1998.

[172] S. G. Neophytides and C. Vayenas, "TPD and cyclic voltammetric investigation of the origin of electrochemical promotion in catalysis," *Journal of Physical Chemistry* **99**(47), pp. 17063–17067, 1995.

[173] M. Kurahashi and Y. Yamauchi, "A metastable de-excitation spectroscopy (MDS) study on oxygen adsorption on a polycrystalline zirconium surface," *Surface Science* **420**, pp. 259–268, 1999.

[174] S. Trasatti, "The absolute electrode potential: An explanatory note," *Journal of Pure & Applied Chemistry* **58**(7), pp. 955–966, 1986.

[175] G. Auffermann, U. Schmidt, B. Bayer, Y. Prots, and R. Kniep, "Speciation of nitrogen - $[N^{3-}]$ and $[N_2^{2-}]$ in binary compounds," *Analytical and Bioanalytical Chemistry* **373**, pp. 880–882, 2002.

[176] Y. Prots, G. Auffermann, M. Tovar, and R. Kniep, "Sr_4N_3: A hitherto missing member in the nitrogen pressure reaction series $Sr_2N \rightarrow Sr_4N_3 \rightarrow SrN \rightarrow SrN_2$," *Angewandte Chemie International Edition* **41**(13), pp. 2288–2290, 2002.

[177] B. Luerssen, *In situ-mikroskopische Untersuchungen an Pt/YSZ-Elektroden.*

PhD thesis, Justus-Liebig Universtity, 2003.

A Symbols and units

Constants

ϵ_0	permittivity of free space, $8.8542 \cdot 10^{-12}$ A^2 s^4 m^{-3} kg^{-1}
π	Pi, 3,14159
c	velocity of light in vacuum, $2.9979 \cdot 10^8$ m s^{-1}
e	electronic charge, $1.6022 \cdot 10^{-19}$ C
F	Faraday-Konstante, 96485 C mol^{-1}
h	Planck constant, $6.6262 \cdot 10^{-34}$ J s
k	Boltzmann constant, $1.381 \cdot 10^{-23}$ J K^{-1}
N_A	Avogadro's number, $6.022 \cdot 10^{23}$ mol^{-1}
R	gas constant, 8.31441 J K^{-1} mol^{-1}

Symbols

α	transfer coefficient
α_c	apparent transfer coefficient of the cathodic reaction
α_a	apparent transfer coefficient of the anodic reaction
α_{RDS}	apparent transfer coefficient of the rate determining step
φ	Galvani potential [V]
ϕ	electric potential [V]
μ	chemical potential [J.mol^{-1}] or [J]
$\widetilde{\mu}$	electrochemical potential [J.mol^{-1}] or [J]
δ	diffusion layer thickness [m]
δ	deviation from stoichiometry
$\aleph$	transmission coefficient
η	overpotential [V]

ν	stoichiometric number
σ_i	conductivity of species i $[\Omega^{-1}.\text{cm}^{-1}]$

A	area $[\text{m}^2]$
c_{ox}	concentration of oxidized species $[\text{mol/l}^1]$ or $[\text{mol/cm}^3]$
c_{red}	concentration of reduced species $[\text{mol/l}^1]$ or $[\text{mol/cm}^3]$
C_{dl}	capacity of the electrical double layer $[\text{F/m}^2]$ or $[\mu\text{F/cm}^2]$
c^0	volume concentration of species $[\text{mol/l}^1]$ or $[\text{mol/cm}^3]$
c^s	surface concentration of species $[\text{mol/l}^1]$ or $[\text{mol/cm}^3]$
D_i	self-diffusion coefficient $[\text{m}^2/\text{s}]$ or $[\text{cm}^2/\text{s}]$
D_{Ox}	diffusion coefficient of oxidized species $[\text{cm}^2/\text{s}]$
D_{Red}	diffusion coefficient of oxidized species $[\text{cm}^2/\text{s}]$
E	cell potential, half cell potential, electromotive force (emf) $[\text{V}]$
E°	standard value for E $[\text{V}]$
E_{A}	activation energy $[\text{eV}]$
E_{g}	energy of the band gap $[\text{eV}]$
E_F	Fermi level $[\text{eV}]$
E_p	peak potential $[\text{V}]$
G	Gibbs free energy $[\text{J/mol}]$
H	enthalpy $[\text{J/mol}]$
I	current $[\text{A}]$
I_p	peak current $[\text{A}]$
i	current density $[\text{mA/cm}^2]$ or $[\text{A/m}^2]$
i_0	exchange current density $[\text{mA/cm}^2]$ or $[\text{A/m}^2]$
i_d	diffusion current density $[\text{mA/cm}^2]$ or $[\text{A/m}^2]$
i_p	peak current density $[\text{mA/cm}^2]$ or $[\text{A/m}^2]$
J	flux density $[(\text{m}^{-2}.\text{s}^{-1})]$
k	rate constant
m	Masse $[\text{kg}]$
n	number of exchanged electrons
p	pressure $[\text{Pa}]$
Q	electric charge $[\text{A.s}]$
R	resistance $[\Omega]$

S	entropy [J/mol.K]
T	temperature [K]
t	time [s]
t_i	transference number of species i [s]
U	voltage [V]
v	potential sweep rate [V/s]
Z	impedance [Ω]

Kroeger-Vink notation

S_σ^q	general formula
S	symbol of chemical element or vacancy
q	relative charge
σ	apparent sub-lattice

Samples

$V_O^{\bullet\bullet}$	positively double charged vacancy in oxygen sublattice
$O_O^\times$	neutral (relatively) oxygen ion in oxygen sublattice
Y_{Zr}'	negatively single charged yttrium ion in zirconium sublattice
$Zr_I^{\bullet\bullet\bullet\bullet}$	positively fourfold charged zirconium ion at interstitial position

Abbreviations

AC	alternate current
AFM	atomic force microscopy
CE	counter electrode
CVD	chemical vapor deposition
CV	cyclic voltamperometry
DC	direct current
EDL	electrical double layer
IR	infra-red light
LSV	linear sweep voltamperometry

OHP	outer Helmholz plane of EDL
PLD	pulsed laser deposition
RDS	rate determining step
RE	reference electrode
SIMS	secondary ion mass spectrometry
SOFC	solid oxide fuel cell
UHV	ultra high vacuum
UPS	ultra-violet photoelectron spectroscopy
UV	ultra-violet light
WE	working electrode
XPS	X-ray photoelectron spectroscopy
YSZ	yttria-stabilized zirconia
YSZ:N	yttria-stabilized zirconia doped with nitrogen

Curriculum Vitae

Name :		Ilia Valov
Address:		Aulweg 13, 35392 Gießen
Date of birth:		12th of April 1972
Birthplace:		Sofia, Bulgaria

Education

Secondary school:	1986 - 1990	English language secondary school
Higher (University):	1990 - 1998	University of Chemical Technology and Metallurgy - Sofia
Diploma thesis:		Study of the kinetics of the electrochemical reactions of arsenic in diluted solutions
Educational degree:		M.Sc. in materials science
Specializations:	1993 - 1995	Environmental Protection and Sustainable Development
	1995-1998	Electrochemistry and Protection from Corrosion
Work experience:	1998-2002	research associate in Institute of Physical Chemistry Bulgarian Academy of Science
	since 09/2002	researcher in Institute of Physical Chemistry Justus-Liebig-University Giessen
Submission of the Dr.rer.nat. thesis:	24.04.06	Nitrogen doped zirconia: preparation, characterization and electrode processes